

Unclassified

ESC-TR-96-115

Project Report
STK-249
Volume I

Proceedings of the 1997 Space Control Conference

19970331 092

L.B. Spence
Editor

25-27 March 1997

Lincoln Laboratory
MASSACHUSETTS INSTITUTE OF TECHNOLOGY
LEXINGTON, MASSACHUSETTS



Prepared with partial support of the Department of the Air Force
under Contract F19628-95-C-0002.

Approved for public release; distribution is unlimited.

Unclassified DTIC QUALITY INSPECTED 4

Prepared with partial support of the Department of the Air Force under Contract F19628-95-C-0002.

This report may be reproduced to satisfy needs of U.S. Government agencies.

The ESC Public Affairs Office has reviewed this report, and it is releasable to the National Technical Information Service, where it will be available to the general public, including foreign nationals.

This technical report has been reviewed and is approved for publication.

FOR THE COMMANDER



Gary Tutungian
Administrative Contracting Officer
Directorate of Contracted Support Management

Non-Lincoln Recipients

PLEASE DO NOT RETURN

Permission is given to destroy this document
when it is no longer needed.

Unclassified

MASSACHUSETTS INSTITUTE OF TECHNOLOGY
LINCOLN LABORATORY

**PROCEEDINGS OF THE 1997
SPACE CONTROL CONFERENCE**

PROJECT REPORT STK-249
VOLUME I

25-27 MARCH 1997

The fifteenth Annual Space Control Conference (formerly called Space Surveillance Workshop) held on 25-27 March 1997 was co-hosted by MIT Lincoln Laboratory and Phillips Laboratory and provided a forum for space control issues. This *Proceedings* documents some of the presentations, with minor changes where necessary.

Approved for public release; distribution is unlimited.

LEXINGTON

MASSACHUSETTS

Unclassified

PREFACE

The Fifteenth Annual Space Control Conference sponsored by ESC will be held on 25, 26 and 27 March 1997. The purpose of this series of conferences is to provide a forum for the presentation and discussion of space surveillance issues.

This *Proceedings* documents those presentations from this conference that were received in time for pre-conference publication. The papers contained were reproduced directly from copies supplied by their authors (with minor mechanical changes where necessary). It is hoped that this publication will enhance the utility of the conference.

Dr. Lee B. Spence
Editor

TABLE OF CONTENTS

Satellite Drag Model Calibration and Feedback for Precision Low Earth Orbit Determination	1
<i>Frank A. Marcos & E.C. Robinson - Phillips Laboratory</i> <i>J.N. Bass - Radex, Inc.</i> <i>Donald Larson - SAIC</i> <i>Joseph J. Liu - AFSWC</i>	
SBV Data Collections in Support of Space Control	11
<i>Thomas P. Opar - MIT Lincoln Laboratory</i>	
The Transportable Optical System (TOS)	25
<i>Eric C. Pearce - MIT Lincoln Laboratory</i>	
Sensor Suite for the Advanced Electro-Optical System (AEOS) 3.6-Meter Telescope	31
<i>Michael L. Vigil, David J. Witte, Paul D. LeVan - Phillips Laboratory</i> <i>David E. Briscoe - Logicon RDA</i>	
Infrared Focal Plane Arrays for Ground- and Space-Based Space Surveillance	41
<i>Paul D. LeVan, K.A. Shrock & J.E.Hubbs - Phillips Laboratory</i>	
MWIR Background Phenomenology Characterization	43
<i>Hsiao-hua K. Burke, Thom Opar, Michael Jordan & Peter Tennyson - MIT Lincoln Laboratory</i>	
Applying Electro-Optical Space Surveillance Technology to Asteroid Search and Detection	51
<i>Herbert E.M. Viggh, Grant H. Stokes, Frank C. Shelly & J.Scott Stuart - MIT Lincoln Laboratory</i>	
Remote Sensing and Characterization of Anomalous Debris	63
<i>R. Sridharan, W. Beavers, R. Lambour & J. Kinsky - MIT Lincoln Laboratory</i> <i>E. Stansbery - NASA Johnson Space Center</i>	
Radar Measurement Campaigns in Europe	75
<i>R. Jehn - European Space Operations Centre</i> <i>D. Mehrholz, L. Leushacke - Research Establishment for Applied Sciences</i>	

Calibrating the Naval Space Surveillance Fence Using Simultaneous Satellite Laser Ranging Data	83
<i>G. Charmaine Gilbreath - US Naval Research Laboratory</i>	
<i>Paul Schumacher, Jr. & Edward D. Lydick - US Naval Space Command</i>	
<i>Mark A. Davis - Allied Signal Technical Services</i>	
<i>John M. Anderson - USAF Starfire Optical Range</i>	
TRADEX Space Surveillance Improvements, Results and Plans	95
<i>Raymond A. LeClair, Aaron J. Seltzer & Stephen M. Hunt - MIT Lincoln Laboratory</i>	
<i>Stephen W. Six, C. Eston Green and Dominic S. Balesteri - Raytheon Range Systems Engineering</i>	
Geosynchronous Satellite Monitoring Using GEODSS Photometric Signatures	103
<i>Timothy P. Wallace, M.A. Kosik & M.A. Rawizza - MIT Lincoln Laboratory</i>	
A Fragmentation Event Detection System	111
<i>George Zollinger & R. Sridharan</i>	
Orientation Vector Estimation for Sub-Components of Space Object Imagery	119
<i>Xun Du, Jun Xiao, Stanley C. Ahalt - Ohio State University</i>	
<i>Capt. Bruce Stribling - Phillips Laboratory</i>	
Data Fusion Experiments with Metric and Photometric Observations	129
<i>James Dick, G. Appleby & A. Sinclair - Royal Greenwich Observatory</i>	
<i>P. Liddell & P. Seidman - Defence Research Agency</i>	
<i>D. Holland - Ministry of Defence</i>	
The Midcourse Space Experiment (MSX)	135
<i>Col. William C. Smith - BMDO</i>	
<i>Cathy S. Mansperger - Photon Research Assoc.</i>	
Spacecraft Identification by Multispectral Signature Analysis Using Neural Networks	143
<i>Col. Conrad J. Poelman & S.R. Meltzer - Phillips Laboratory</i>	

Satellite Drag Model Calibration and Feedback for Precision Low Earth Orbit Determination

F. A. Marcos (PL/GPI), J. N. Bass (Radex, Inc), D. Larson (SAIC), J. J. Liu (AFSWC)
and E. C. Robinson (PL/GPD)

ABSTRACT

Atmospheric drag is the largest uncertainty in determining orbits of low altitude satellites. Deficiencies in operational satellite drag models persist due to empirical model limitations as well as inadequacies of proxy indices used as model drivers. Satellite drag errors result in degraded accuracy, requirements for frequent updates and inadequate predictions of true positions for catalog maintenance, collision avoidance and re-entry operations. The concept of improving specification/calibration and short-term forecasts of the state of upper atmospheric variability with atmospheric density values derived from AFSPC tracking has been demonstrated. Operational application of this technique promises to provide significant improvements in low earth, precision orbit determination and prediction.

1. INTRODUCTION

Orbit prediction over periods ranging from a fraction of a day to more than a year are used in Air Force Space Command (AFSPC) space surveillance operations. The main problem facing orbital analysts today is precision orbit determination of satellites operating in an environment of moderate to significant atmospheric drag. The dominant and most difficult component to predict in the orbit propagation model is the drag force. The drag is predominantly due to changes in neutral atmospheric density. AFSPC has a goal of knowing the density to within 5%, in the altitude region 90 - 500 km, compared to the current model accuracy of about 15%. As a result, drag model parameters, such as the AFSPC ballistic coefficient ($C_d A/m$) exhibit wide variations from one orbital element correction to the next. Orbits experiencing significant drag consequently have degraded accuracy, require frequent orbit determinations and do not sufficiently predict true positions.

To circumvent limitations of current operational satellite drag models, the operational model description of upper atmosphere density global structure is improved through assimilation of satellite drag observational data. This paper summarizes initial results based on four satellites that were of high interest to AFSPC: Long Duration Exposure Facility, Solar Max Mission, Salyut 7 and Solar Mesosphere Explorer, in orbits near 400-500 km altitude during 1988-1989 (Snow and Liu, 1991). Under a study initiated in 1993, variations in the ballistic coefficients of these satellites were shown to be predominantly due to density model errors (Bass et al, 1996). Corrections to the operational J70 density model, needed to provide a best fit to the tracking observations for a single satellite (LDEF) were determined. These corrections were used to modify J70 to generate revised time-dependent global density fields. These atmospheric characteristics are then used to improve the orbit determination for the other three satellites.

Data assimilation into numerical models for initialization has been successfully used in the meteorological community. These techniques are devised to integrate data from different instruments with measurements almost arbitrarily distributed in space and time so that the maximum amount of information on the system under consideration is retrieved (Daley, 1991). Requirements for operational implementation of Space Surveillance Network data are examined together with the need for solar and geomagnetic forecasts to propagate satellite orbits ahead. There have been limited studies published regarding use of drag measurements in a feedback mode. These include the study of two satellites at the same inclination, 50 km different in altitude, (Nouel et al, 1993) and the recently published Russian Space Surveillance System orbit determination techniques using satellite drag measurements (Nazarenko, 1996).

2. ATMOSPHERIC VARIATIONS

Figure 1 illustrates that Earth's thermosphere is controlled mainly by the sun. Solar EUV radiation is the dominant heat source. However, during geomagnetically active times the Joule heating at high latitudes can be more than ten times greater than that of the local EUV. Thus the dynamic structure of the thermosphere is dependent on the

relative heating due to solar EUV radiation at low latitudes and to auroral processes, associated with the solar wind, at high latitudes. A less significant energy source, waves propagating up from the lower atmosphere, further modulates the thermosphere.

Ideally, forecasts of upper atmosphere density would be made on the basis of physical models of solar behavior and solar terrestrial interactions. Physical models that describe the theory of mechanisms leading to atmospheric density changes are being developed under PL technology transition programs. The complete solar observational data sets needed to achieve the full accuracy of these models are also being addressed both by PL and the National Space Weather Program. Further discussion is outside the scope of this paper.

Empirical models used to represent neutral upper atmospheric variability are mainly of two types: those based mainly on satellite drag data (e. g. Jacchia, 1970) developed between 1964 and 1977, and those, denoted MSIS (Mass Spectrometer and Incoherent Scatter) based mainly on measurements of atmospheric composition by satellites and of temperature by ground-based radars (e.g. Hedin, 1991) developed between 1977 and 1991. In general, the Jacchia-type models are used by the operational community for satellite drag while the MSIS models are used mainly by the scientific community for temperature and composition studies. In the empirical models the solar EUV radiation is parameterized by the F10.7 solar radio flux and the geomagnetic activity by the Kp index. The known thermospheric density variations represented in all recent empirical models are: (1) solar flux (solar cycle and daily component), (2) geomagnetic activity, (3) local time, (4) day of year, (5) latitude, and (6) longitude. Wave features are not included. Table 1 summarizes typical empirical model output magnitudes and time scales for density changes at various altitudes between 150 and 800 km.

Statistical comparisons of the numerous empirical models indicate that they are equally effective in specifying satellite drag (Liu et al, 1982; Marcos, 1990). Their statistical error is typically 15% one sigma in the altitude region of about 150 - 250 km. Significant advances in understanding the morphology of drag variations have not resulted in commensurate quantitative improvements in satellite drag modeling. Part of the difficulty in reducing empirical model errors is that the primary variations in the thermosphere were already accounted for in the early Jacchia models. Recognized limitations of empirical models include (1) use and prediction of proxy indicators F10.7 and Kp to represent solar and geophysical influences, (2) relatively coarse spatial resolution, (3) simplified physics, (4) lack of time-dependent waves and neutral winds and (5) limitations of accuracy and extent of the data base and on the extrapolation procedures to extend the model to data-sparse regions.

3. DATA ANALYSIS

Ballistic coefficients from four satellites, in orbits near 400 - 500 km at the same time during 1988-1989, were analyzed by Snow and Liu, (1991) using both Special Perturbations and a semi-analytic theory. The satellites were the Long Duration Exposure Facility (LDEF), Solar Maximum Mission (SMM), Salyut 7, and Solar Mesosphere Explorer (SME). The inclinations were 28.5 degrees for LDEF and SMM, 51.6 degrees for Salyut and 97.7 degrees for SME. The satellites were selected as good candidates for analysis because of an abundance of tracking data and minimal area-to-mass variations. Figure 2 shows the ballistic coefficient vs time obtained for each satellite using the AFSPC operational version of the J70 model. Each data point represents a weighted average, over about 5 days, of the ratio of the "actual" drag to the J70 model predicted drag. If the J70 model correctly describes the forces acting on the satellite, gives the best fit to the observations, and the area-to-mass ratio remains constant, then the ballistic coefficient would remain constant. All four satellites show similar variations in the ballistic coefficient. Two major features are a long term trend particularly evident during the first 90 days of data and short-term variations with periods of several days. Similar variations were obtained using the Jacchia (1964) and MSIS (1977) density models, although the actual value of ballistic coefficient is model-dependent. As a result of reviewing procedures used to derive the ballistic coefficients, it was determined that the cause was not due to observational errors (station bias, sensor calibration drifts, data reduction), processing errors or orbital propagator theoretical limitations.

An analysis was made to determine the effect of approximations to the actual model inputs for F10.7 and Kp. The models use both a daily solar flux and a long-term average (typically 3 solar rotations). In practice, forecasting of F10.7 and the Kp index depends on identification of past patterns of behavior of the indices themselves and correlations with other solar measurements. Extrapolations into the future are made on the basis of these patterns

and relations. The long term average of F10.7 has been a persistent source of concern since it involves predicting well beyond current capabilities (see eg Heckman, 1991; Jablonski, 1992). The need arises because the short- and long-term variations affect the thermosphere differently. These terms are attributed to two components: short-term variations due to active solar regions and long-term variations related to the solar disk 11-year cycle. In the Jacchia model for example the coefficient for the long-term variation is over twice that of the daily variation. Averaging over several rotations, centered on the day of interest, is used to filter out the shorter term variations affecting the thermosphere at the time of interest. To circumvent this unattainable forecasting need, some users (including AFSPC) substitute the 90 days up to the day of interest. This results in using an average solar flux different than that on which the model is based. Further, for the geomagnetic activity index input a value estimated from a single station, rather than the globally averaged Kp value on which the model is based, is used. Re-computation of the ballistic coefficients using solar and geophysical inputs required by the model (Bass et al, 1995) modified the ballistic coefficients (Figure 3) but did not significantly change their original characteristics. Consequently, additional factors are involved in the observed short- and long-term trends.

Based on analyses of the amplitudes and periods, the short-term variations were assumed related mainly to imperfections in the F10.7 representation of EUV. Both temporal scale and magnitude of the short-term variations supported this hypothesis. Spectral analysis of the ballistic coefficient data showed a dominant 27-day peak. The amplitudes of the peaks were from a few percent up to about 30%. Comparisons of satellite measurements of solar EUV with daily F10.7 values (Hedin, 1984) during solar cycle 21 (Figure 4) showed that errors in the estimated heat input to the thermosphere could account for these variations. Geomagnetic effects also contribute to the short term variations.

Semi-annual effect modeling errors were examined as the cause of the long-term variation. The upper atmosphere semi-annual variation has density maxima in April and October and minima in January and July. The data sets in Fig 2 start near the 1988 July minimum. Year-to-year variations in this effect are observed in satellite drag data as shown by Figure 5 (Jacchia et al, 1969). However, only an average variation is given in empirical models since the physics of this phenomenon is not yet fully understood. Figure 6 shows the semi-annual variation extracted from the LDEF data for the period 1988-89 (Bass et al 1996). The July minimum in 1988 was about 50% lower than that predicted by J70 in 1988 but close to the model prediction in 1989. The very low ballistic coefficients at the start of the Snow & Liu (1991) data are attributed mainly to errors in modeling the semi-annual variation. In 1989 the semi-annual variation was closer to model predictions.

4. RESULTS OF ATMOSPHERIC CALIBRATION

Having established that the ballistic coefficient data are largely explainable in terms of neutral density variability, the next step was to use the data as density corrections to the operational model. LDEF ballistic coefficients, determined from least-squares differential correction at every track of data, were used to calibrate the J70 model. Each LDEF ballistic coefficient value change was assumed to represent the J70 model deficiency, as averaged over all longitudes and local times and 28.5 degrees of latitude for a period weighted toward the end of a five day fit span. Two techniques were used to determine a time-dependent correction to the J70 model, which was then used in a feedback mode to LDEF and the other three satellites. The first technique took advantage of the small range of altitudes represented by the four satellites studied, by multiplying the J70 model densities by a factor yielding LDEF ballistic coefficients which best fit the ideal long-term average value. The second technique was more rigorous and systematic. It consisted of adjusting the key J70 model parameter, exospheric temperature, by determining corrections to the short-term (daily) and long-term (semi-annual) temperature components. This approach promises to permit extrapolation of J70 model corrections to other latitudes, local times and altitudes.

Both techniques were employed to compute a J70 model correction database, which was then used to modify the J70 model values in the TRACKS orbit determination and prediction software. Using the J70 model correction database, orbital elements, including ballistic coefficients, were redetermined for all four satellites. Either technique seems to provide a corrected J70 model value which gives an improved backcast of the "actual" density over the locations and time periods covered, and thus circumvents errors in model inputs and model inadequacies. Figure 7 shows the before and after ballistic coefficients for LDEF. As expected, the standard deviation is dramatically reduced for the LDEF data. Application of the LDEF corrections to the other three satellites also

provided significant error reductions. Results for the four satellites, using both the straight forward density factor (DF) and the temperature correction (TC) techniques, are given in terms of standard deviation in Table 2 (Bass et al 1996). For LDEF the standard deviation is reduced from 12.1 to 2.3%. For SMM, in a similar orbit, the standard deviation is reduced from 9.5 to 3.4%. Smaller, but important error reductions are found for the Salyut 7 and SME data sets. By examining sub-sets of these satellites, increased improvement in orbit determination (as measured by reduction in standard deviation) was observed. The Salyut satellite was subject to thrusting around day 200 as seen in Fig 1. By starting the data set at day 250 instead of day 200, the standard deviation was reduced by 50%. SME experienced a large change in drag, relative to the other satellites around day 500. Eliminating data after that period reduced the standard deviation from 14.9 to 6.2%. The straight forward density factor method is expected to be a good first order correction for these data sets with relatively little altitude differences, and is approximately equivalent to modifying the model heat input. Typically, at 400 km, a 20% change in the daily F10.7 results in density changes within $17\% \pm 2\%$ for all latitudes and local times. For the same change of F10.7 averaged over three solar rotations, the density values are within $41\% \pm 5\%$. The global accuracy can obviously be improved by using data from satellites at other orbit altitudes and inclinations with appropriate data ingestion schemes to guide the J70 corrections using the more general approach of a correction to the exospheric temperature. In addition to improving the specification of satellite positions, preliminary tests show that the calibration technique leads to improving short-term prediction capability by 15-30%.

5. CONCLUSIONS

Satellite orbital forecasts depend on the accuracies of satellite orbit determination and of the force model (including its inputs). Satellite drag is the dominant term in the force model for low-earth orbit satellites. Exploiting Space Surveillance Network tracking data for a time-dependent correction to operational satellite drag models has demonstrated remarkable success in improving orbit determination and prediction. While the approach has been demonstrated with AFSPC's operational version of the J70 model, it can be applied to other density models. The technique can be improved using data with greater spatial and temporal coverage. For short-term forecasts, less than a day, the technique has already demonstrated potential prediction improvements during geomagnetically quiet conditions. Predictions on this time scale during geomagnetic storm conditions can benefit from use of physical models under development by PL. For longer periods, an integrated program under a National Space Weather Program is planned to provide an eventual capability to accurately specify and forecast atmospheric heating inputs.

REFERENCES

- Bass, J. N., M. J. Kendra, J. M. Griffin, D.R. Larson, Computer-efficient models of thermospheric density and composition: Application of satellite data in near real time, Scientific Report, PL-TR-95-2040, 14 March 1995.
- Bass, J. N., M. J. Kendra, J. M. Griffin, D.R. Larson, N. Ericson and T. Killeen, Computer-efficient models of thermospheric density and composition: Application of satellite data in near real time, Final Report, PL-TR-96-2150, 15 June 1996.
- Daley, R., Atmospheric Data Analysis, Cambridge University Press, Canada, 1991.
- Heckman, G., Predicting solar and geomagnetic activity in the 90's, AAS 91-490, Durango, CO, 1991.
- Hedin, A. E., "Correlations between thermospheric density and temperature, solar EUV flux, and 10.7-cm flux variations", *J. Geophys. Res.*, Vol. 89, 1984, p. 9828.
- Hedin, A. E., "Extension of the MSIS thermosphere model into the middle and lower atmosphere", *J. Geophys. Res.*, Vol. 96, 1991, p. 11591.
- Hedin, A. E., J. E. Salah, J. V. Evans, C. A. Reber, G. P. Newton, N. W. Spencer, D. C. Kayser, D. Alcayde, P. Bauer, L. Cogger, and J. P. McClure, "A global thermospheric model based on mass spectrometer and incoherent scatter data MSIS 1. N₂ density and temperature", *J. Geophys. Res.*, Vol. 82, 1977, p. 2148.
- Jablonski, C., Confidence in atmospheric density forecasts, AAS 92-181, Colorado Springs, CO, 1992.
- Jacchia, L. G., Revised Static Models of the Thermosphere and Exosphere with Empirical Temperature Profiles, SAO Special Report No. 313, 1970.

Jacchia, L. G., J.W. Slowey and I. G. Campbell, "A study of the semi-annual density variation in the upper atmosphere from 1958 to 1966, based on satellite drag analysis", *Planet. Spa. Sci.*, vol 17, p.49, 1969.

Liu, J.J.F., R. G. France and H.B. Wackernagel, "An analysis of the use of empirical atmospheric density models in orbital mechanics", *Proceedings of a workshop on satellite drag*, Space Environment Laboratory, J. A. Joselyn, ed., Boulder, CO, 1982.

Marcos, F. A. "Accuracy of atmospheric drag models at low satellite altitudes", *Adv. Space Res.*, Vol 10, 1990, p. (3) 417.

Nazarenko, A.I., Technology of evaluation of atmospheric density variation based on the Space surveillance System's orbital data, *U.S.A. Russian Second Space Surveillance Workshop*, ed. by P. K. Seidelman, I. Wytrzyaszczak, and B. Kaufman, Poznan, Poland, 1996.

Nouel, F., M. Deleuze, C. Valorge, and P. Laudet, *Improvements of the ERS1 orbit precision by using the drag effect on SPOT 2*, AAS 93-601, Victoria, B.C., Canada, 1993.

Snow, D. E. and J. J. F. Liu, *Atmospheric variations observed in orbit determination*, AAS 91-492, Durango, CO, 1991.

TABLE 1 Thermospheric density variability as a function of altitude

Effect	150 km	200 km	400 km	800 km	Time Scale
1. Flux (Solar Cycle)	1.16	1.76	8.60	21.3	Years
2. Flux (Daily)	1.00	1.01	1.12	1.30	Day
3. Geomagnetic Activity	1.25	1.35	1.60	2.00	Hours
4. Local Time	1.10	1.25	2.10	3.30	Hours
5. Semi-Annual	1.15	1.15	1.50	1.80	Months
6. Latitude	1.10	1.15	1.60	1.90	Months
7. Longitude	1.02	1.02	1.05	1.15	Day

TABLE 2 Comparison of standard deviations obtained for original and corrected ballistic coefficients for each of four satellites

SATELLITE	DAYS	CORRECTION	# POINTS	STD. DEVIATION
LDEF	184-726	DF	3836	.121
	184-726		3835	.023
SOLAR MAX	184-684	DF	4428	.095
	184-684		4390	.034
SME	184-726	DF	3499	.187
	184-726		3455	.121
SME	184-480	DF	1688	.149
	184-480		1690	.062
SALYUT 7	184-726	DF	3597	.181
	184-726		3586	.119
SALYUT 7	250-727	DF	3143	.144
	250-726		3129	.071
LDEF	184-726	TC	3856	.121
	184-726		3802	.027
SME	184-726	TC	3499	.188
	184-726		3450	.046

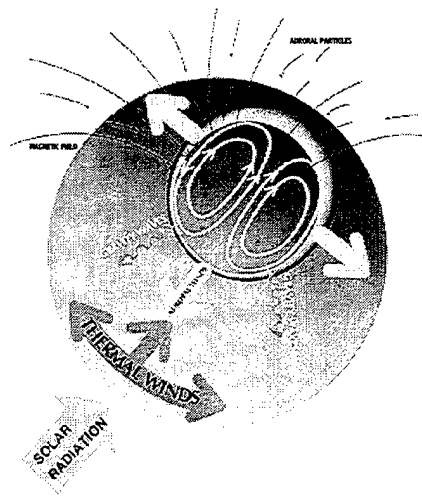


FIGURE 1 Schematic representation of solar electromagnetic and solar wind influence on thermosphere dynamics.

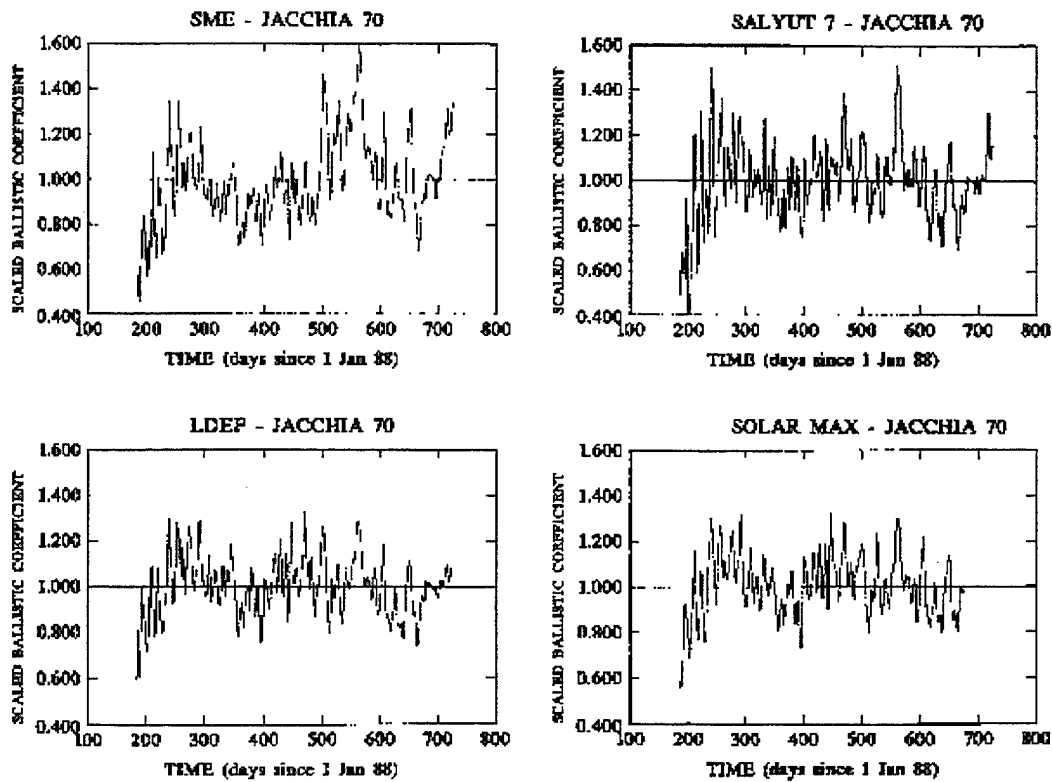


FIGURE 2 Time histories of ballistic coefficients, using J70 model, for LDEF, SMM, Salyut 7 and SME respectively. Data are scaled by dividing by the mean ballistic coefficient for each data set.

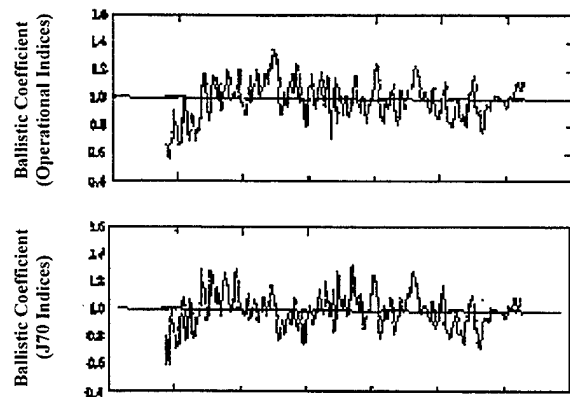


FIGURE 3 Demonstration of effect on scaled ballistic coefficients using operational (top) and model-required (bottom) solar and geomagnetic inputs.

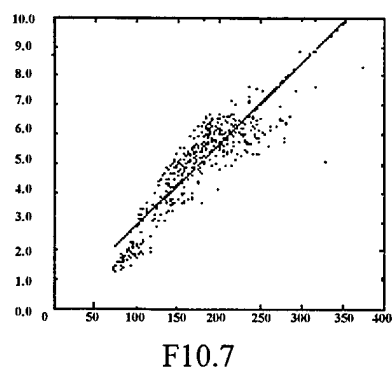


FIGURE 4 Scatter plot of daily F10.7 values vs satellite measurements of solar EUV flux.

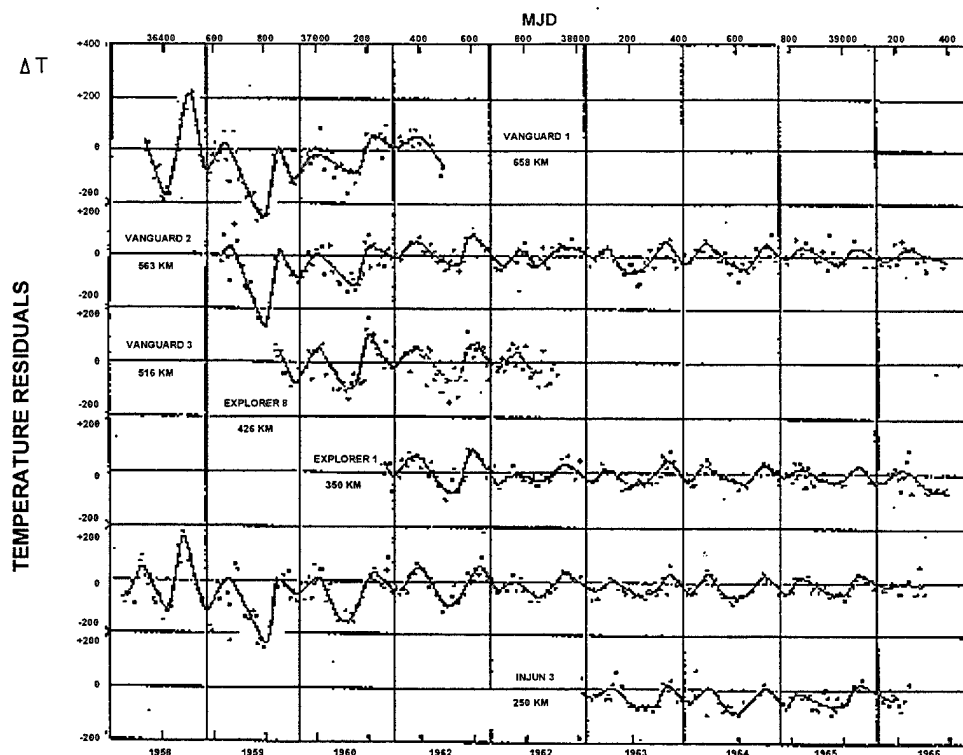


FIGURE 5 Semi-annual temperature variation from the drag of six artificial satellites, arranged in order of decreasing perigee height

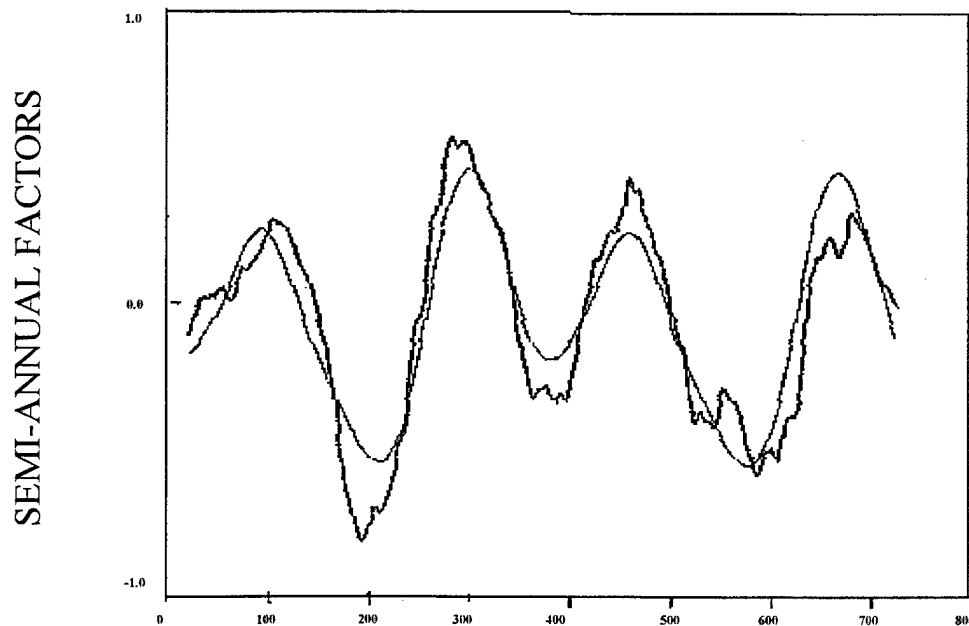


FIGURE 6 Comparison of the semi-annual temperature factor for J70 and that derived from LDEF data

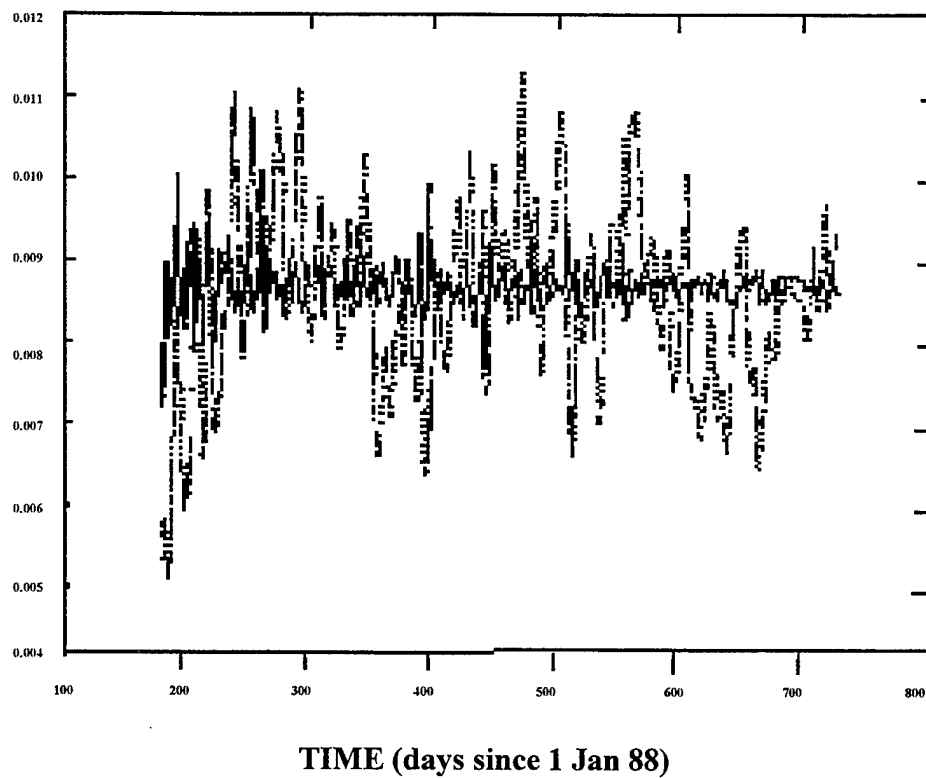


FIGURE 7 Comparison of original LDEF ballistic coefficient data to value using corrected J70 densities.

SBV Data Collections in Support of Space Control¹

Thomas P. Opar

I. INTRODUCTION

This paper is a compilation of some of the early results of the Space-Based Visible (SBV) sensor on the Midcourse Space Experiment (MSX). This paper includes an initial assessment of the SBV sensor performance and some examples of data taken from various target missions in support of Space Control Missions. The first section of the paper is an overview of the sensor characterization results, while the second is a brief overview of some of the Space Control missions supported by SBV.

II. SBV SENSOR CHARACTERIZATION

The performance of the SBV sensor quantified in terms a number of calibration and characterization parameters. There are five major categories of performance metrics being monitored, namely:

1. System Noise - the focal plane noise and dark current levels are tracked both for the purposes of performance estimation, calibration adequacy, and long term radiation damage.
2. The Out-of-Field Radiance (OFVR) Rejection is monitored to check for mirror contamination. OFVR is the dominate background source for low tangent altitude observations.
3. Radiation effects - characterization of the short term affects of passage through the South Atlantic Anomaly (SAA Focal plane event statistics are calculated. The number, type, and strength of the focal plane events as a function of location within the SAA are computed
4. Radiometric Calibration - this entails a detailed determination of the focus, throughput, total system point source response of the sensor system. The ultimate goal is the conversion factor between photons at the aperture to focal plane counts.
5. Goniometric Calibration - is the mapping between focal plane row and column position to angular position relative to the bosesight.

Each of these items is addressed in turn.

II.1 System Noise

The SBV system noise is determined through temporal analysis of cover closed images. In a typical sensor noise characterization experiment, the camera collects full frame data with a 0.625 s exposure at high gain. The temporal average and variance frame is created from a set of individual, time sequence of images. (This set of images is termed a "frameset" throughout this paper.) The spatial average of the temporal variance frame is recorded as the sensor noise. The first sensor characterization measurement after launch indicated a system level of 0.78 rms counts, corresponding to 5 rms electrons. Four months later this number had increased to 0.86 rms counts, corresponding to 5.5 rm electrons. The increase in noise is thought to be due to some of the long term effects of radiation on the focal plane.

The CDR goal for the sensor noise is 10 rms electrons or 1.56 rms counts at high gain.

¹ This work was sponsored by the BMDO under Contract F19628-95-C-0002. Opinions, interpretations, conclusions, and recommendations are those of the authors and are not necessarily endorsed by the United States Air Force.

II.2 OFVR Performance

One of the critical functions of a space-based surveillance system is to detect and track targets at low line of sight tangent altitudes. One of the primary background noise sources for these observations is Non-Rejected Earth Radiance (NRER). NRER is due to non-specular scattering within the optics. Contamination of the mirror surfaces is a potential cause of increased NRER.

SBV is routinely collecting image data using constant tangent altitude scans above an illuminated earth. Images taken from these data collection events clearly show evidence of a gradient in the background due to NRER. Figure 1 is such an image. In this case a temporal average of sixteen frames is created. The earth is at the bottom of the page. The line of sight tangent altitude at the bottom of the image is 100 km. The long streaks through the image are stars that move during the exposure time. The gradient in brightness in the image is due to Non-Rejected Earth Radiance (NRER).

The average focal plane signal versus tangent altitude is plotted in the curve at left of Figure 1. The data for this plot is a composite across all four CCDs with tangent altitudes ranging from 100 up to 430 km. Overlaid upon the data is the SBV NRER model. The three curves are for three different contamination parameters.

In terms of detection sensitivity, this background profile indicates that a 24 cm diameter specular sphere with 80% reflectance should produce an $SNR = 6.0$ on the focal plane. The CDR goal for this figure of merit is 68 cm.

II.3 Radiation Effects

One of the major radiation environments that SBV must endure is that of the South Atlantic Anomaly. (SAA) The SAA is a potential well in the earth's magnetic field. Energetic charged particles are trapped in this well. These charged particles are responsible for the radiation events seen on the focal plane. Figure 2 is a cover closed image taken at the beginning of a pass through the South Atlantic Anomaly. A frameset of sixteen frames is processed to show the pixels "lit up" by particle interactions with the focal plane. The dark points and streaks are caused by radiation events.

This is a relatively benign radiation event rate. Only 960 pixels were affected during the 16 frames. At the deepest pass through the SAA for which data was collected over 55,000 pixels suffered a radiation event with 5,000 pixels receiving two (an effective rate of 3750 pixel /s)

Future space bases surveillance sensors will fly in a high radiation environment and will be using large format focal plane arrays. The primary difficulty with the radiation events is that in single frames they provide a significant source false target reports. Radiation events can be removed in a number of ways: shielding, bulk filtering based on signal levels or shape, temporal processing, or through the track initiator. These approaches tradeoff between weight, power, and computational complexity.

II.4 Radiometric Calibration

Radiometric calibration of the SBV sensor is performed through the use of a set of calibrated star fields, namely the Landolt Special Areas². The Landolt Special Areas are comprised of roughly twenty stars with well-known magnitude and color in approximately distributed within a 1° by 1° area. Fortunately, these stars fall ideally within the dynamic range of the SBV sensor. Figure 3 is an image of Landolt SA-114 as seen by SBV. This is a high gain image at 0.625 second exposure time.

² Ref to Landolt

In addition to radiometric calibration, the Landolt field observations provide data which serves to characterize the sensor Point Response Function (PRF). The PRF can be quantified in terms of the "Ensquared Energy" or "Straddle Factor". The Ensquared Energy is the fraction of the total signal from a point source target that falls into the pixel centered on the point source. The SBV CDR goal is for this value to be between 60% and 80%. The Straddle Factor is the average signal from a point source that when it falls anywhere within a pixel. The Straddle Factor for SBV is on the order of 50%. Both of these figures of merit are a measure of the optical focus. Larger values of either indicate better focus. Long term monitoring of these parameters can be used to indicate if any changes in focus or focal plane response is occurring. Analysis of data from the first four months of on-orbit operation indicates no change in these parameters has occurred.

Since visible surveillance sensors will be used in support of object classification or discrimination and may be fused with infrared, these sensors must be accurately calibrated. As stated previously, the SBV sensor has a radiometric calibration procedure utilizing well-calibrated stars. The accuracy achieved is very good and capable of supporting discrimination and space object identification missions.

The radiometric calibration performance of the instrument is exemplified in Figure 4. The chart on the left is a plot of the SBV magnitude (an logarithmic based unit of intensity with large numbers for dim objects and small numbers for brighter objects) versus the measured signal level for a set of calibration stars. The precision of the calibration is roughly 0.5%. The right hand side chart on Figure 4 is an extrapolation of the absolute accuracy. The rms magnitude error is plotted versus object magnitude. The SBV goal was to achieve a 20% accuracy at 12th magnitude. It has achieved the goal at about 14th magnitude and at the design point has an accuracy of 5%.

II.5 Goniometric Performance

The Goniometric Performance of the sensor is also determined using star fields. There are other papers in these proceedings which deal with the goniometric performance more completely. As is shown the pointing accuracy of instrument is at the 5 μ rad level,

II.6 Performance Summary

The initial on-orbit performance is summarized in Table 1. The various figures of merit for each of the five performance assessment areas are listed.

Table 1
SBV On-Orbit Performance Parameters

System Noise	0.8 +/- 0.1 dn @ High Gain
Dark Current	< 18.0 electrons / pixel / s
OFVR Performance	24 cm. Specular sphere @ 100 km tangent altitude
Ensquared Energy (CCD #3)	66%
Point Source Sensitivity @ SNR = 6.0	15.7 SBV magnitude
Radiometric Calibration Constant	401.6 +/- 2.0 dn/s @ 12.0 magnitude
Angular Measurement Accuracy	5 μ rad

II. SBV OBSERVATIONS SUPPORTING SPACE CONTROL MISSIONS

To date SBV has participated in a large number of data collection events in support of Space Control missions. Table 2 is a synopsis of the various types of target phenomenology that has been collected to date. Six types of target mission data has been collected. There have been three instances of the TMD Surrogate Targets, four target missions, and at least two space shuttle observations with plumes .

All instruments were on during each of these data collection events so they offer the opportunity for intersensor fusion.

Hard targets were both observed both as individual resolved target and as closely spaced pairs and clumps. TCMP - 2B was the only mission in which none of the hardbody targets were ever resolved. The hardbody targets include launch vehicles, attitude control systems, replica decoys, spherical balloons, reference spheres, along with undetermined deployment hardware, fuel fragments, and other debris.

In all missions, except the Multi-Services Launch System MSLS demo flight, some type of plume events are detected. The plumes may be hot gases from the launch vehicles (as is the case with MDT II and Red Tigress), the PBV (MDT II) or cold gas from various Attitude Control System (Red Tigress & TCMP).

The targets and plumes have been observed both Above the Horizon (ATH) or Below the Horizon (BTH). Only the TMD Surrogate Target were completely BTH all others were mostly ATH with some BTH observations near launch or re-entry.

Table 2
SBV Observations in Support of Space Control Missions

Mission	Hardbody Targets		Plumes		Backgrounds	
	CSO	Resolved	Cold	Hot	ATH	BTH
TMD Surrogate(3)	Y	Y	N	?	N	Y
TCMP 2B	Y	N	Y	N	Y	N
MDT II	Y	Y	N	Y	Y	N
MSLS	Y	Y	N	N	Y	Y
Red Tigress 3	Y	Y	Y	Y	Y	Y
Space Shuttle (2)	N	Y	N	Y	Y	N

There are already some lessons learned from the visible portion of the MSX data with regards to the space control missions, and the utility of visible sensors in particular:

1. The visible sensor offers spectral diversity. The visible phenomenology is inherently different from the IR, reflection rather than self-emission. This difference makes it more difficult to design a credible, lightweight decoy that is effective in the sunlit conditions for both IR and visible sensors. On the other hand, it is possible to do so for IR sensors alone. (Note, lightweight objects are not credible IR decoys under non-illuminated conditions.)
2. The inherent sensitivity in the visible portion of the wavelength provides detection at long range, thereby increasing the battlespace for more effective resource allocation.
3. Due to its shorter wavelength, visible sensors may be able to detect Closely Spaces Objects(CSO) at an earlier time than IR sensors, thereby improving performance.
4. As stated previously the cold gas ACS plumes that are evident in a number of missions provide insight into the offense operations. Maneuvers and/or deployment events may be identified by the presence or absence of plumes.

Figure 5 illustrates some of these threat complex characterization concepts. One form of threat complex characterization is signature analysis for the purpose of monitoring maneuvers or deployments.. The plot on the right of Figure 5 is the signature from the TCMP target complex. It should be noted that all the objects in TCMP were CSOed throughout the entire flight. The signature is that of a Closely Spaced Object and it provides a number of interesting features which should be exploitable:

1. A maneuver of the booster,
2. Various object deployments,
3. Attitude Control Systems firings.

Figure 6 is a set of images taken during the MSX Dedicated Target II (MDT II) mission. This set of images shows the diversity of the phenomenology that an SBV-like sensor can exploit. It obviously can detect launch and upper stage plumes at high ranges, detect warm plumes from Attitude Control Systems, detect threat objects and deployment debris, and finally detect plumes as they interact with the atmosphere at low altitudes.

Figure 7 is an image taken late in the flight of the MSLS Demo. There are six objects in the "zoomed" image. The objects include; two large spherical balloons, two small balloons, a RV mass replica, and the bus. Figure 8 is an accompanying chart which shows the signatures extracted during the mission. There are some items of note:

1. Prior to 1500 s is a CSO pair consisting of two objects. One of the objects has a significant signature modulation, while the second does not.
2. The signal levels from two objects are essentially identical which indicates that they are most likely the same object class,
3. The fall off of the signatures near 1600 s TAL is due to approach of the terminator.
4. There are a few "negative spikes" in the signature. Two are clearly seen at 1025 s TAL and 1100 s TAL. These are an artifact of the point source detection routine background estimator. A bright star passed through the background estimator at this time. The background was overestimated which causes the algorithm to underestimate the point source intensity.
5. The sun - target - sensor phase angle change is primarily responsible for the rolloff of the balloon signatures as the terminator is approached.

III. SUMMARY

The SBV instrument is on-orbit, exceeding its CDR goals and providing useful insight into issues associated with space-based visible space control sensors. Some of results of the analysis of the SBV data and their implications are:

1. Radiation events constrain space-based data collection and processing. Future system at similar altitudes will experience similar radiation events. The intended use of large format, spatial arrays indicates the need for some type of radiation event mitigation. The mitigation is a tradeoff between weight, power, and computational complexity.
2. Warm and cold gas plumes can be detected by staring visible sensors. Plume observations provide insight into the threat complex and its intentions. Utilization of plume information should be possible within the space control context.
3. Visible sensors can be easily and accurately calibrated both radiometrically and goniometrically. The calibration of an SBV-like sensor is both stable and repeatable.
4. As the SBV data show, high quality, durable, large format array, visible sensors can be built and flown in space and operated for long duration.

Figure 1: SBV OFVR PERFORMANCE

- NRER PERFORMANCE MAINTAINED AT LOW TANGENT ALTITUDES
- ROLLOFF WITH ALTITUDE BETTER THAN EXPECTED

EARTHLIMB IMAGE
CCD #4 @ 0.625 s High Gain

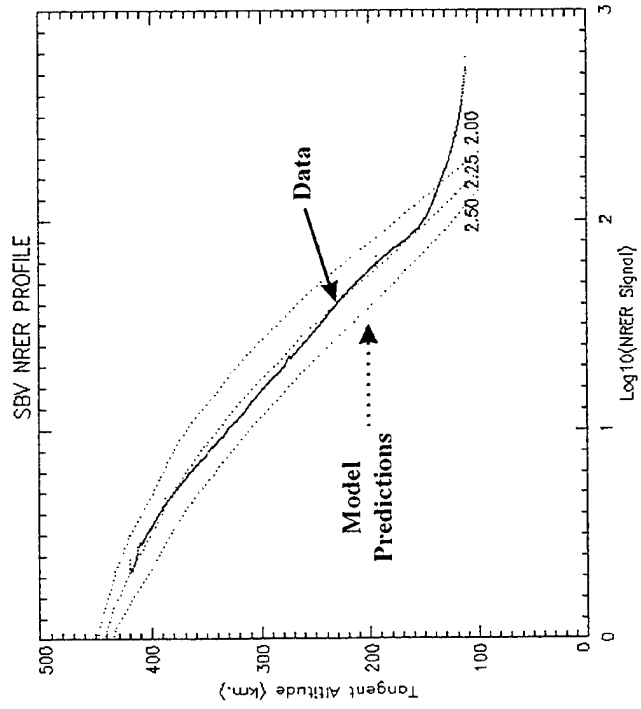
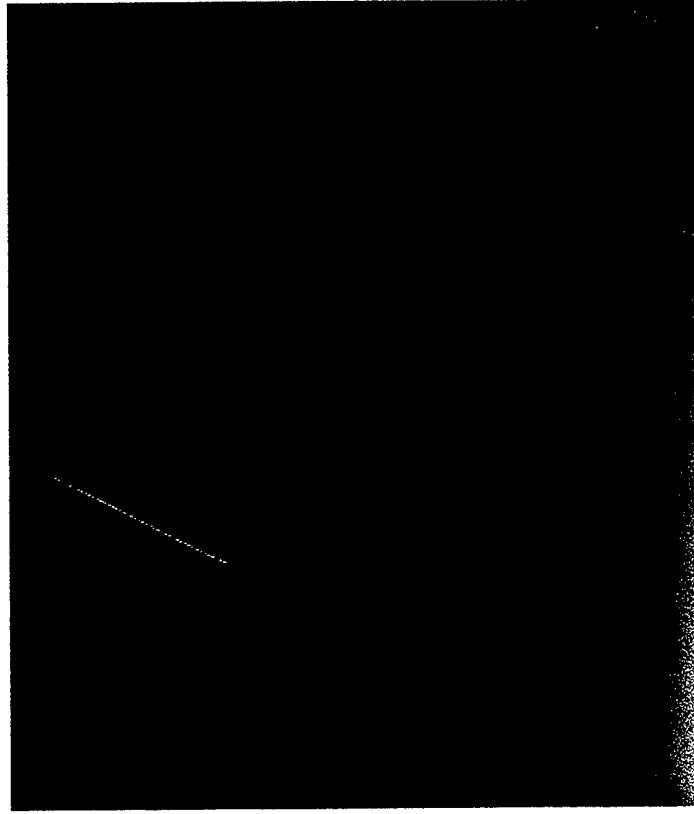
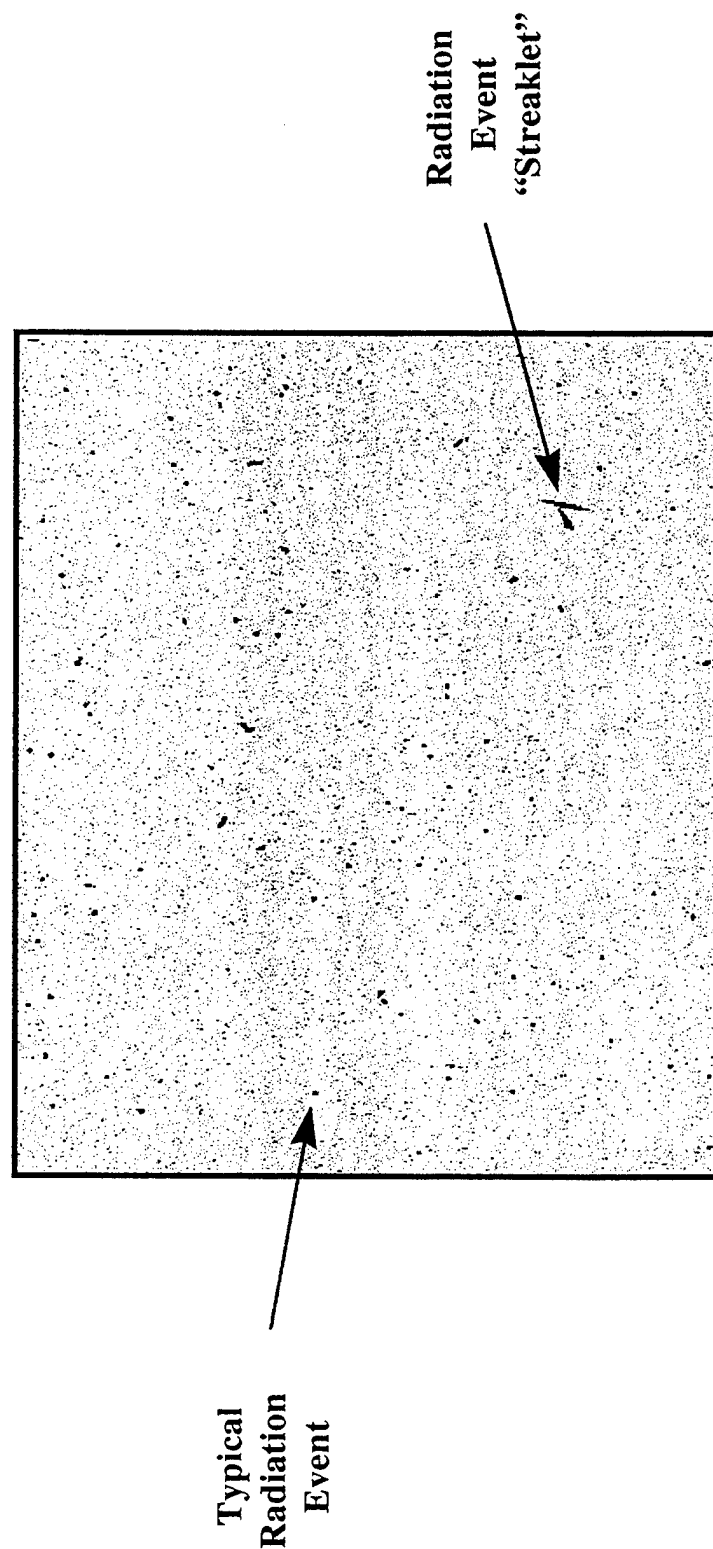


Figure 2: SBV IMAGE OF SAA RADIATION EVENTS



- Cover Closed Image
- Maximum Value Frame Displayed
- Negative Image of Radiation Events
- 60 pixels / s Affected

**Figure 3: SBV STELLAR CALIBRATION IMAGE
LANDOLT SA -114**

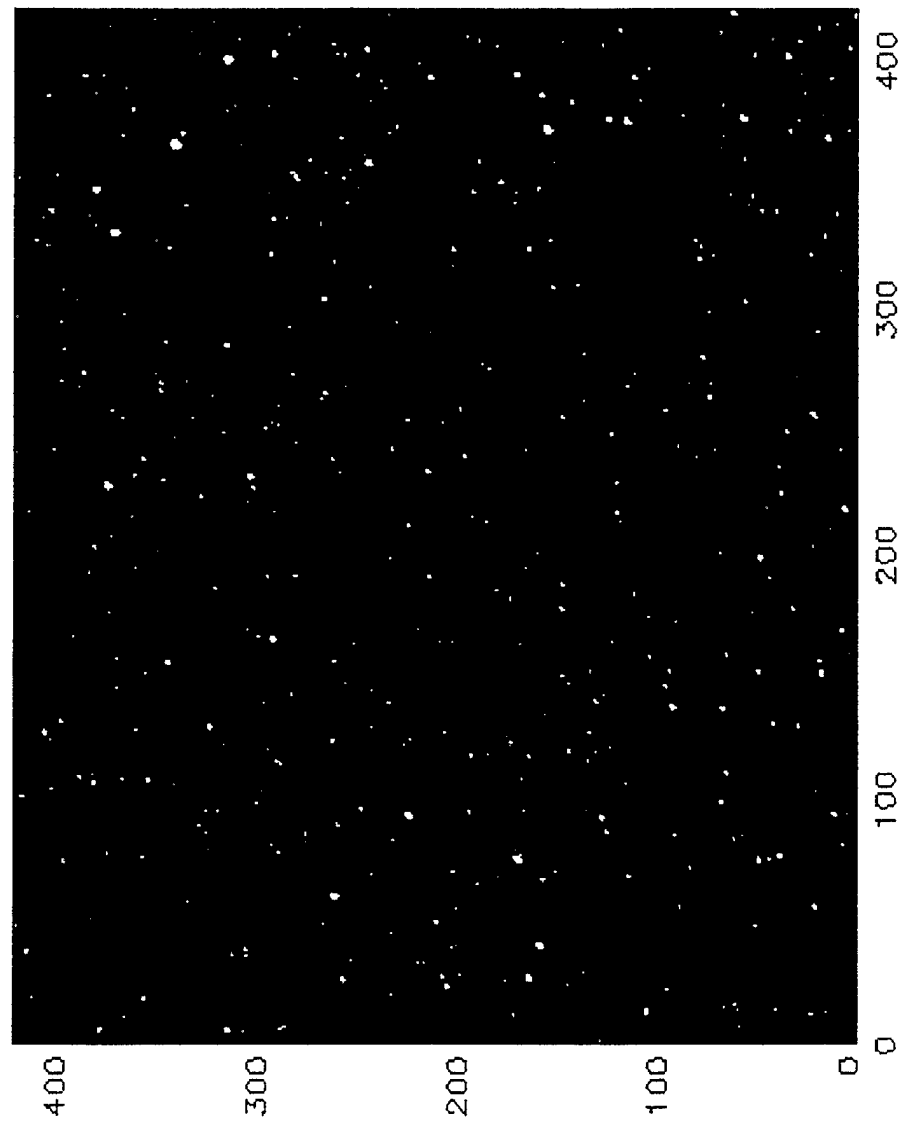
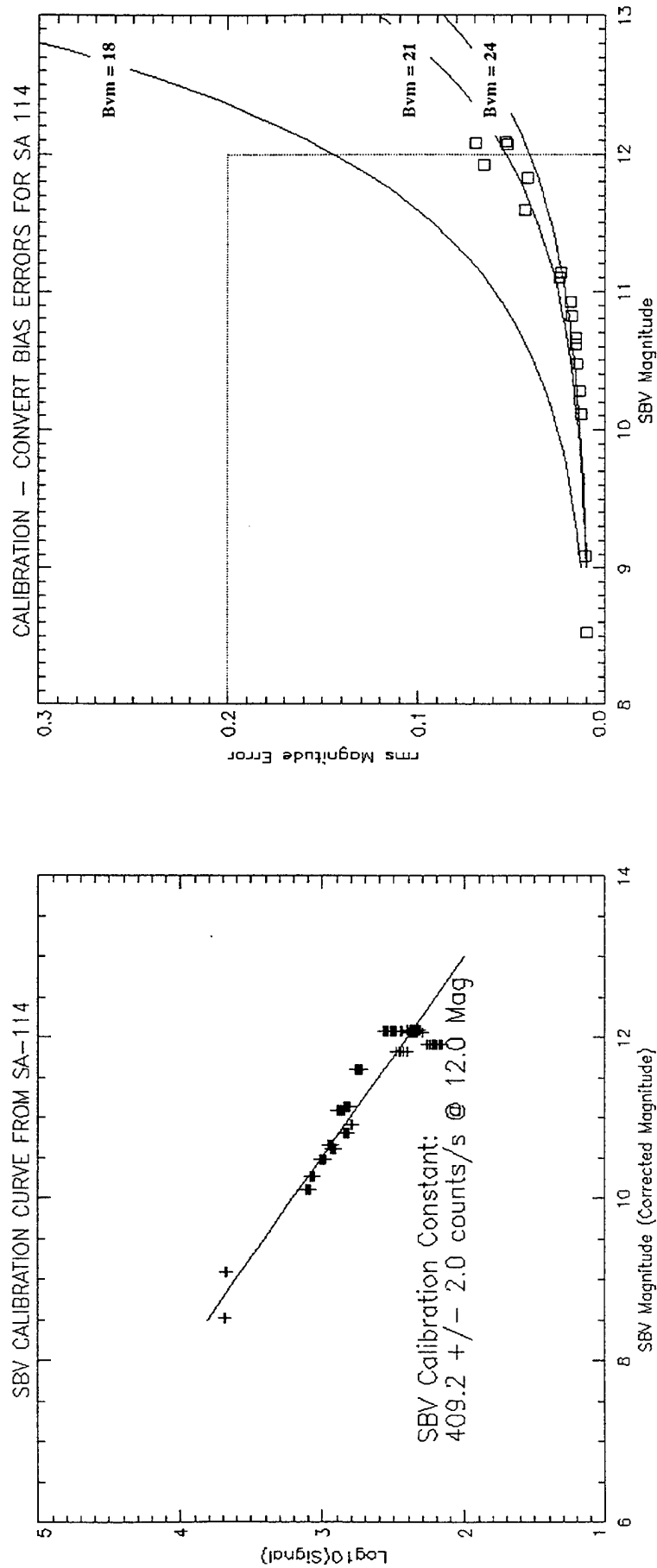
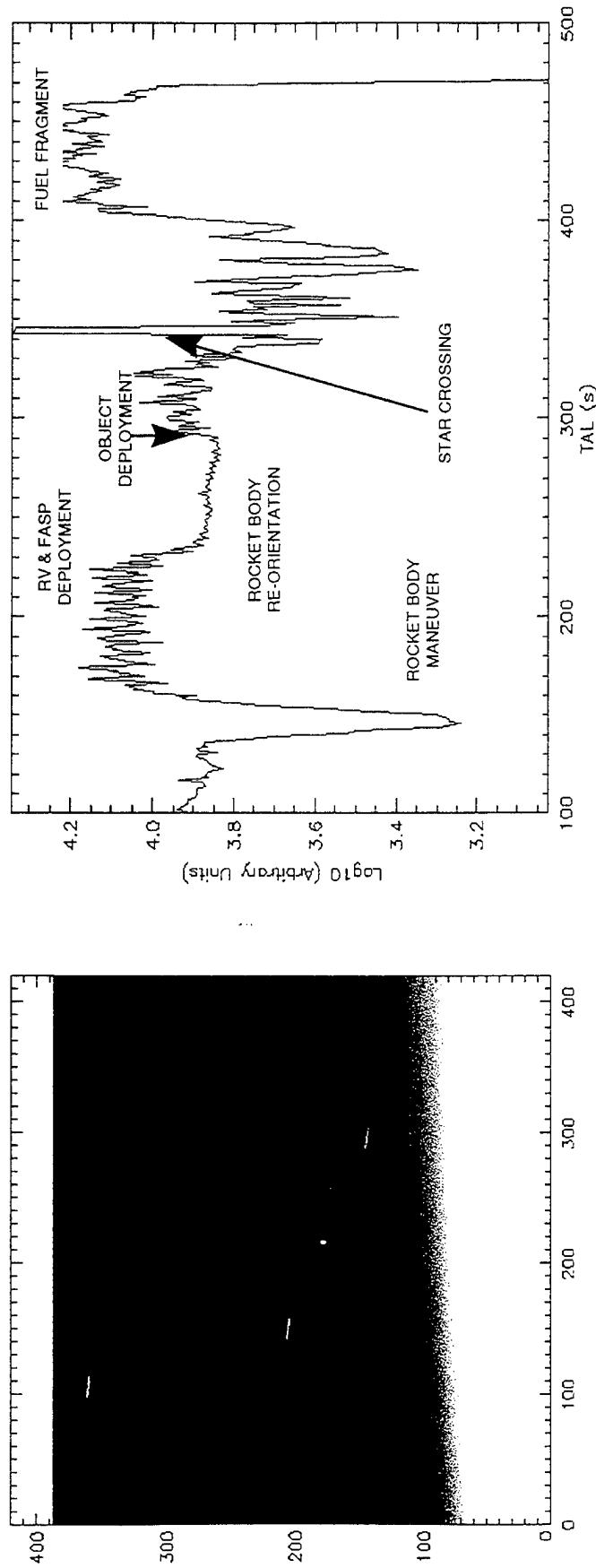


Figure 4: SBV RADIOMETRIC CALIBRATION



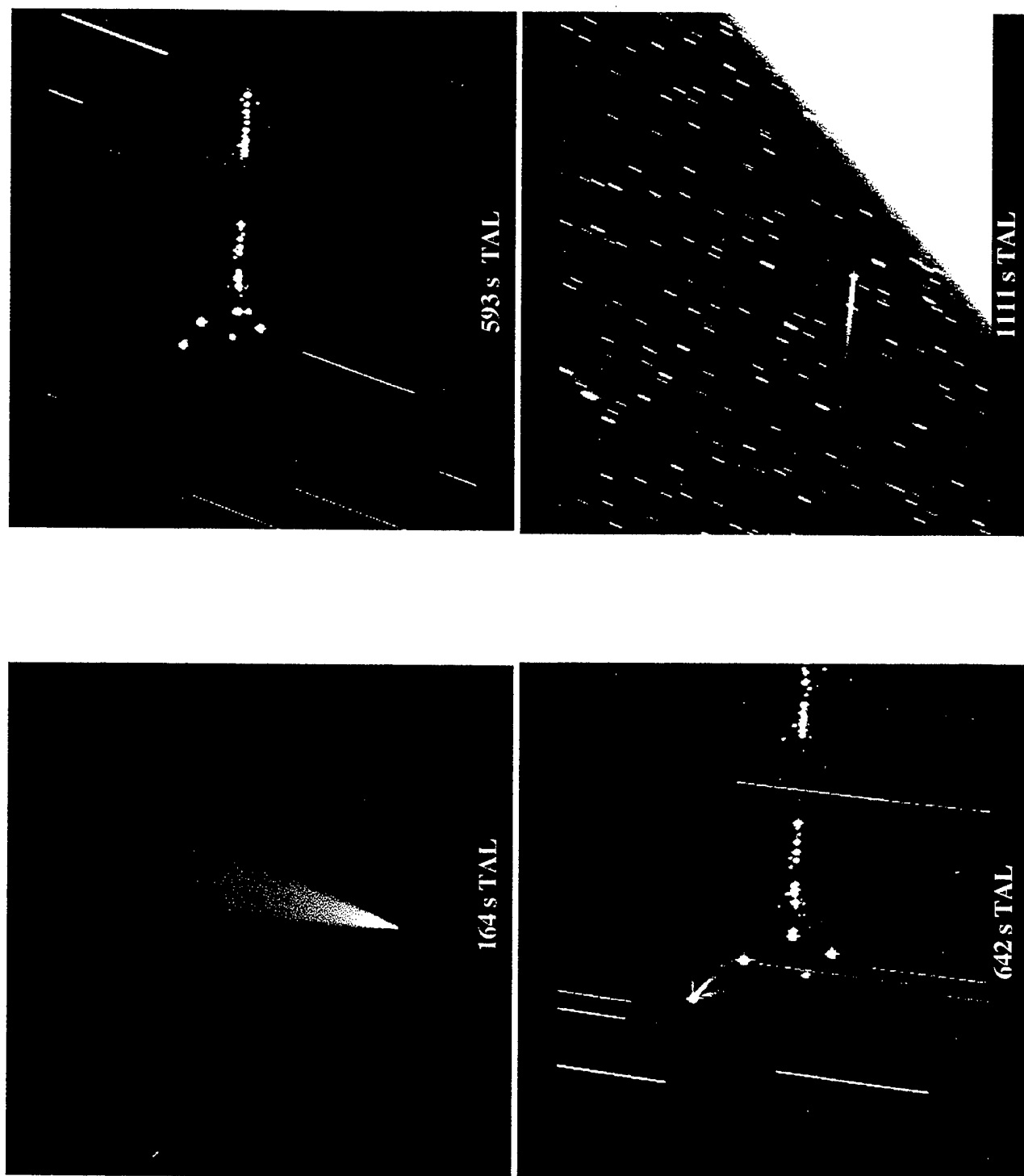
- RADIOMETRIC CALIBRATION FROM STAR FIELD OBSERVATIONS
- SBV GOAL IS 20% ACCURACY FOR 12TH MAGNITUDE STAR
- ACHIEVED 5 %

Figure 5: MSX/SBV OBSERVATIONS OF TCMP-2B



- COMPLEX DETECTED AT HIGH RANGE & LOW TANGENT ALTITUDE
- THREAT COMPLEX CHARACTERIZATION VIA DETECTION OF
 - OBJECT DEPLOYMENTS
 - ATTITUDE SYSTEM PLUMES

Figure 6: SBV OBSERVATIONS OF MDT II



**Figure 7: SBV OBSERVATIONS OF MSLS
ZOOM FACTOR 5 IMAGE @ 1600 S TAL**

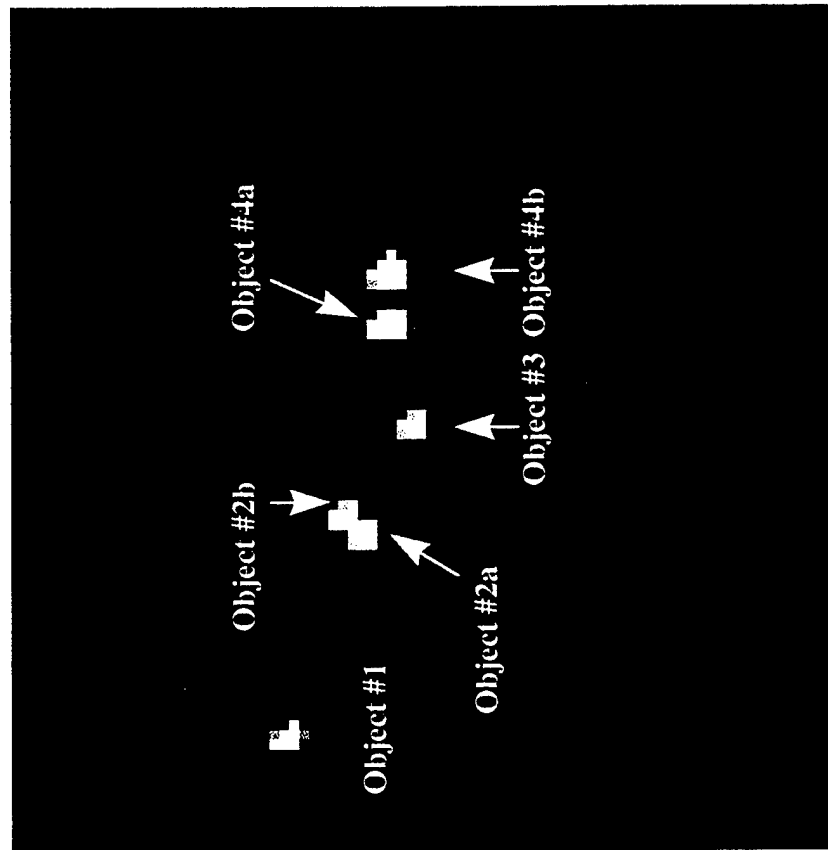
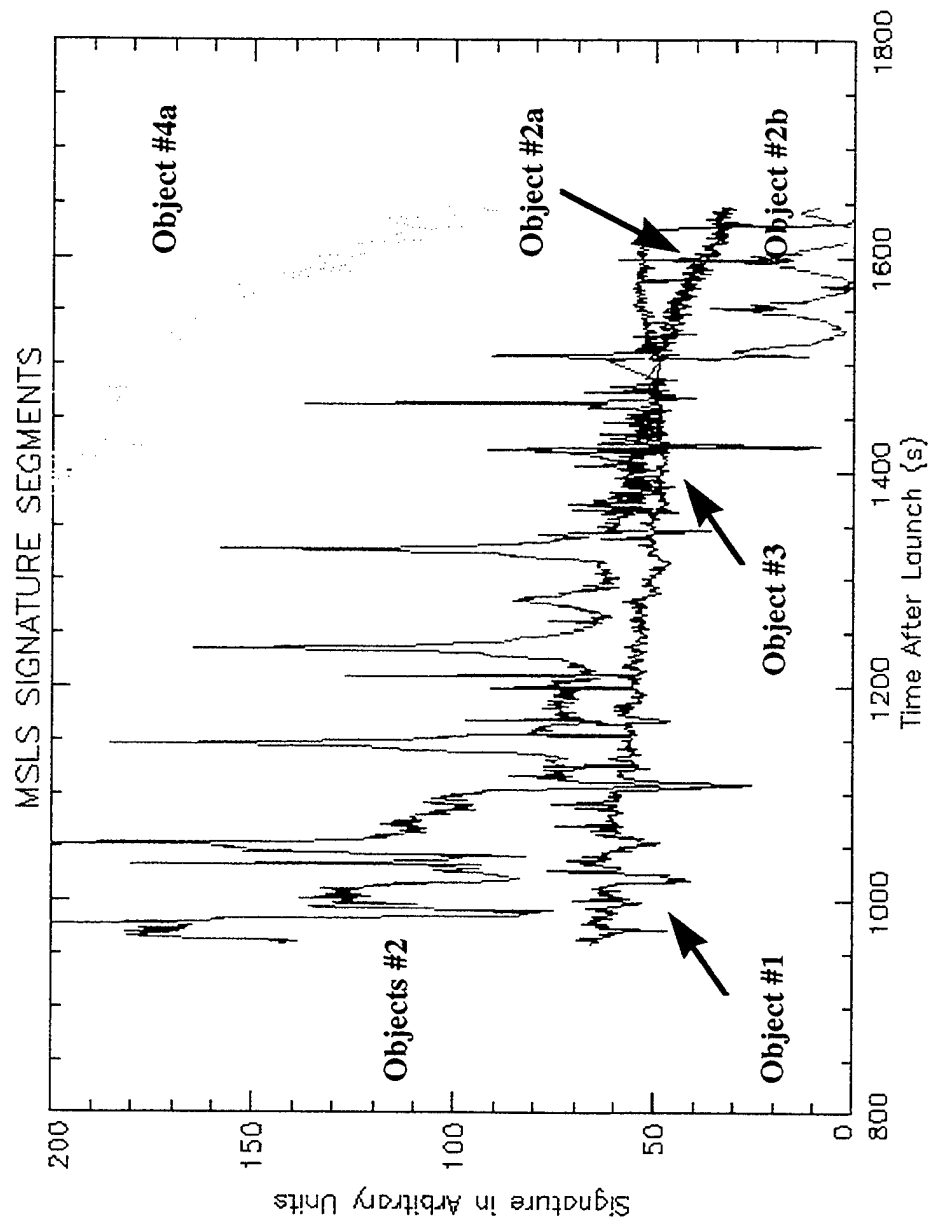


Figure 8: MSLS SIGNATURE SEGMENTS



The Transportable Optical System (TOS)*

E.C. Pearce (MIT Lincoln Laboratory)

ABSTRACT

The Transportable Optical System (TOS) is an operational prototype of a passive, ground based, electro-optical deep space surveillance system. The system has both a metric and photometric (SOI) capability. The operational concept of TOS is to use the sensor as a gap-filler for deep space sensor coverage. TOS will be used as a path finder sensor until replaced by a more permanent sensor. The TOS system was originally developed by MIT Lincoln Laboratory (MIT/LL) at its Experimental Test System (ETS) near Socorro, New Mexico. The initial version of the system was deployed to San Vito, Italy in 1990. Recently, the system has been extensively refurbished with new control computers, a state-of-the-art frame transfer CCD camera, and a unique CCD photometric capability. The system consists of a windowed 56 cm (22 in.) f/2.3 Ritchy-Chretien telescope mounted on a light-weight azimuth/elevation NIKE-AJAX mount. The system is controlled from a 20'x8' operations shelter which is located nearby. When disassembled for shipping, TOS fits onto a single flatbed truck and can be shipped by a single C-141 aircraft. The TOS system is capable of tracking over 40 objects per hour under operational conditions, a throughput comparable to an entire 3 telescope GEODSS site today.

1. INTRODUCTION

The Transportable Optical System (TOS) is an operational prototype of a passive, ground based, electro-optical space surveillance system. The system collects both metric and photometric (SOI, Space Object Identification) observations of orbiting satellites, new domestic and foreign launches, uncorrelated targets (UCTs), and other targets as tasked by the Space Control Center (SCC), Alternate Space Control Center (ASCC), or the Combined Intelligence Center (CIC). The operational concept of TOS is to use the sensor as a gap-filler for deep space sensor coverage [1]. TOS will be used as a path finder sensor until replaced by a more permanent sensor. The TOS system was originally developed by MIT Lincoln Laboratory (MIT/LL) at its Experimental Test System (ETS) near Socorro, New Mexico. The initial version of the system was deployed to San Vito, Italy. The site was deactivated in 1994, and TOS was returned to the ETS. Currently, MIT/LL is completing a refurbishment of TOS prior to its expected redeployment to the host country.

TOS is a deployable electro-optical space surveillance system performance comparable to the Ground Based Electro-Optical Space Surveillance (GEODSS) System. The system consists of a windowed 56 cm (22 in.) f/2.3 modified Ritchy-Chretien telescope mounted on a light-weight azimuth/elevation NIKE-AJAX mount. The system can be seen in Figure 1 as it is assembled at the ETS. Here, the telescope is surrounded by its plywood shelter and is covered by a clam-shell tent when not operating. When the system is operationally deployed, a traditional astronomical dome shelters the telescope. The telescope is equipped with a state-of-the-art frame transfer CCD camera. The sensor has a

* The work was sponsored by the Department of the Air Force under Contract F19628-95-C-0002.

field of view of 1.54° diagonal. In the foreground is the $20' \times 8'$ operations shelter which contains the operator console and control computers. The telescope control system is based on Motorola 68040 single board computers on a VME bus. The data processing system is based on Datacube MAX-200 image processing hardware. When disassembled for shipping, TOS fits onto a single flatbed truck. A single C-141 flight is required for air shipment. Once on location, TOS can be ready for operation in as little as 72 hr.

The TOS refurbishment has been comprehensive. The original 18 mm target intensified SIT camera has been replaced with a 40 mm frame transfer CCD, increasing both the search rate and sensitivity of the system. An optical window has been added to the telescope to provide environmental protection. The control computers have been upgraded to Motorola 68040, and modern graphical user interface (GUI) using multiple X-terminals has been installed. Moreover, the original micro-Vax based image processor has been replaced by a VME based Datacube image processor and fully integrated with the X-terminal GUI interface. Finally, a unique CCD photometry capability has been added, providing TOS with the operational capability to collect SOI (space object identification) data at 100 Hz.

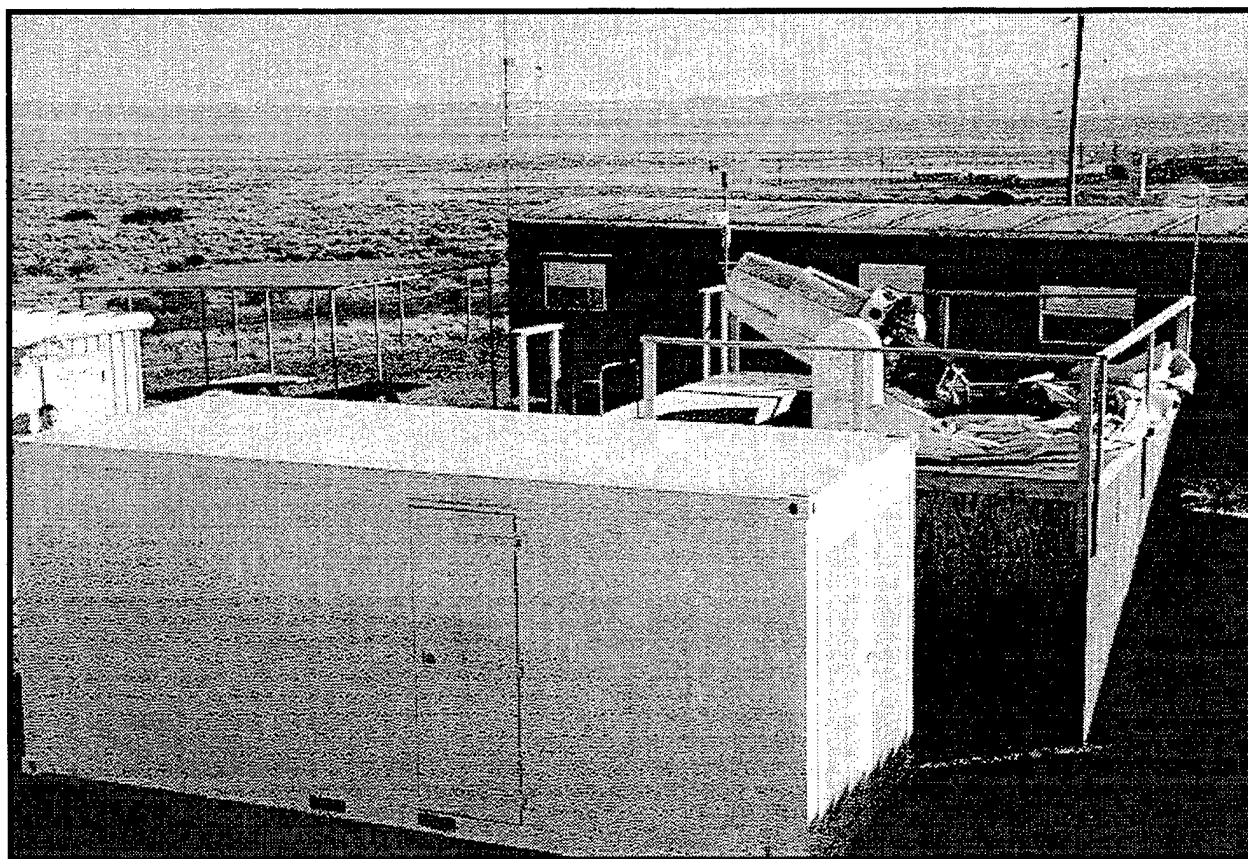


Figure 1. Elevated View of the TOS at the ETS in Socorro, New Mexico.

This Report will give an overview of the refurbished TOS system and its technical capabilities, while attempting to focus on its more unique attributes such as its dynamic scheduler, automated metric tracking capability, CCD camera and photometer.

2. SYSTEM OVERVIEW AND TECHNICAL PERFORMANCE

TOS is a small, transportable optical space surveillance system with performance that matches, and in many cases exceeds, the performance of the current GEODSS system. Table 1 shows the key performance specifications of the refurbished TOS system as demonstrated during system test.

Table 1. TOS Technical Performance Specifications.

TPM	Demonstrated Performance	Comments
Pointing Accuracy	+8.6 arcsec RMS	Significantly exceeds goal.
Metric Accuracy	± 6.0 arcsec @ 2σ	Significantly exceeds GEODSS capability.
Search Rate	403 deg ² /hr	Improved 4 _x with CCD camera
Detection Sensitivity	16.5 m _v @ SNR=6 in 1 s	Mission ready, 17.0 achievable by deploying without window.
Metric Throughput	57.8 Trk/hr (ideal) ~43 Trk/hr (operational)	Significantly exceeds goal. Exceeds current operational capacity of two GEODSS main telescopes.
SOI Accuracy	± 0.07 m _v	Significantly exceeds goal. Operational real-time displays very effective.
SOI Data Rate	100 Hz	Twice goal rate.

Figure 2 shows a comparison of the performance of the refurbished TOS system to the current GEODSS system. The TOS system is approximately 0.7 magnitude (2 times) more sensitive than the current Ebsicon equipped GEODSS main telescope, despite the much smaller TOS aperture (56 cm vs. 102 cm). The two sensor systems have comparable search rates. Most dramatic, however, is that the TOS sensor has a significantly higher capacity. During testing at the ETS, the TOS system was able to

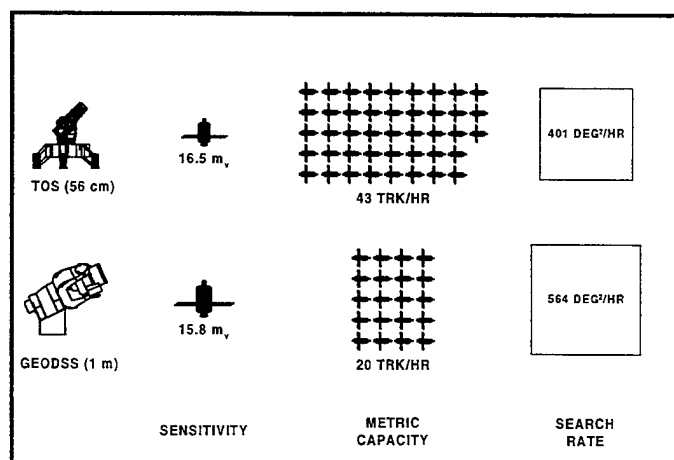


Figure 2. Comparison of TOS vs. GEODSS Performance.

make nearly 60 acquisitions per hour (5 observation tracks). Under operational conditions, the system realizes about 43 acquisitions per hour. This capacity is over twice the operational capacity of the current GEODSS main telescope. The substantial improvement in sensor capacity is largely due to a combination of TOS's real time dynamic scheduler and automation of metric tracking. During the metric mission, the sensor requires little or no operator interaction (during system test, the sensor operated for a one hour period with no operator interaction at all). Finally, the metric data produced by TOS using is single star calibration technique and physical mount modeling is 2-4 times as accurate as typical GEODSS data.

3. THE CCD CAMERA AND PHOTOMETER

The replacement of the original TOS camera with a state-of-the-art CCD camera and associated Datacube image processor were key to the refurbishment effort. The CCD camera uses a 40 mm back illuminated frame transfer CCD developed by MIT Lincoln Laboratory in 1992. The chip uses a unique correlated double sampling readout electronics and four parallel ports to achieve very low noise ($12 e^-$

RMS) and high frame readout rate. The chip has been integrated into a thermoelectrically cooled camera designed and built by Photometrics Inc. of Tucson, AZ.

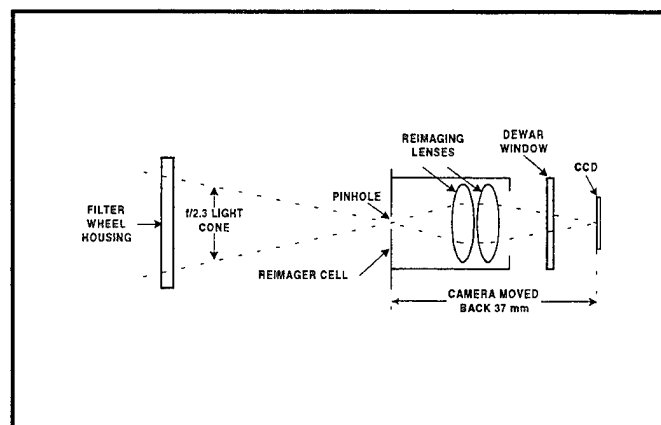


Figure 3. Reimaging Optical System.

only a small fraction of the CCD array (see Figure 3). By scanning the camera continuously in a manner similar to the time delayed integration (TDI) techniques used on fixed search telescopes, an effective frame rate of 100 Hz is achieved (see Figure 4).

The system operates by first getting an object in track in the center of a specified 54×54 pixel area of the CCD. Then the camera is moved back approximately 37 mm and the reimaging optics assembly is swung into place. With the new camera position, the focused image is now centered on a 0.1 mm pinhole. The image of the object and the pinhole are projected on the 54×54 pixel area of the CCD and the system collects the photometric (SOI) data. The TOS system uses an adaptation of traditional all-sky photometry. Currently, all calibrated photometry is done with a Johnson V filter [2]. The system is also capable of taking multi-color data using Johnson B or R filters, or using no filter at all to obtain maximum signal.

A CCD photometry (SOI) capability has been added to TOS during the refurbishment effort. Although later MIT/LL prototype CCDs developed for the GEODSS program have small 32×32 photometric arrays specifically designed for high bandwidth SOI data collection, the smaller format TOS camera does not. In order to allow TOS to gather high bandwidth photometric data, a reimaging optical system and pinhole assembly was designed to illuminate

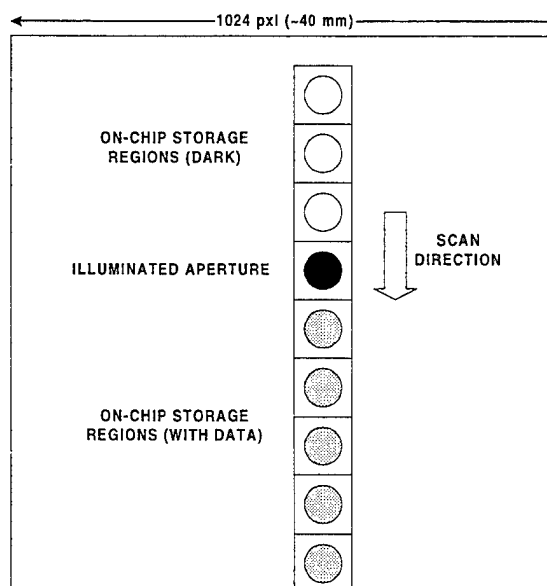


Figure 4. TOS CCD Photometry Focal Plane.

The refurbished TOS system provides a complete operational SOI data collection capability, including graphical SOI signature editing and message preparation tools. The signature show below was collected during system test and has been regenerated here in the SOI Editor from the original SIGTRANS message. This object is a discarded rocket body from an early INTELSAT launch in a near geosynchronous orbit.

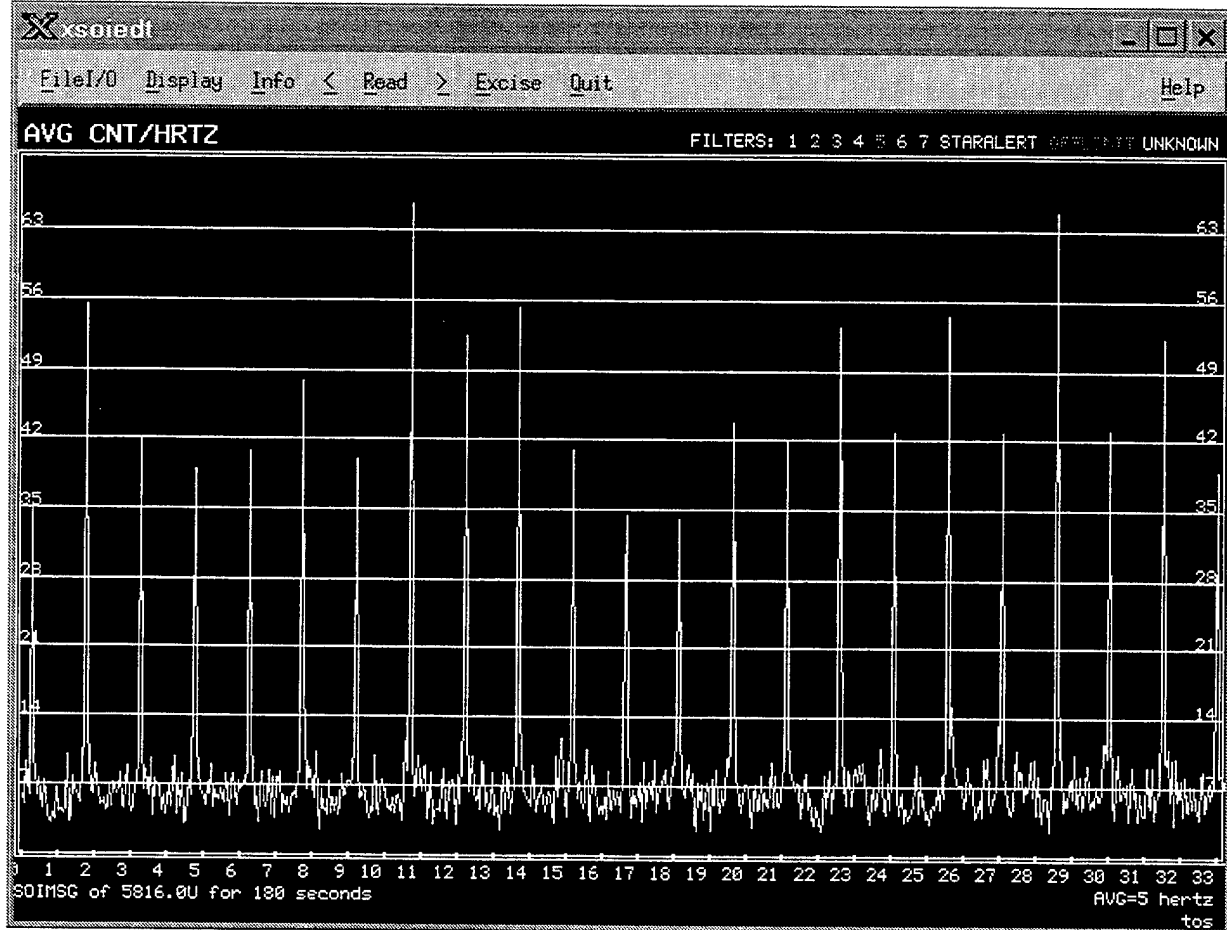


Figure 5. Sample Signature of SCC 5816 Collected by the TOS CCD Photometer.

4. CONCLUSION

The refurbishment of the TOS system is now complete and the system is awaiting deployment to the Mediterranean area near the end of CY'97. The system has surpassed performance expectations in several key areas. TOS is capable of tracking nearly 60 objects per hour under ideal conditions, a capacity comparable to an entire three telescope GEODSS site. Additionally, and operational SOI capability has been added to the system with a 100 Hz data rate. The introduction of the frame transfer CCD camera increased both the search rate and sensitivity substantially.

However, the most significant enhancements in the refurbished system is the automation of metric data acquisition and addition of standard X-window graphical user interfaces. During the metric mission, the system can be left unattended for extended periods of time while the system continues to automatically schedule, acquire, and track tasked satellites. With the operator fatigue factor eliminated, the

system realizes a much higher percentage of its ideal tracking capacity during operations. Clearly, with the successful demonstration of TOS, future electro-optical sensors will migrate towards fully autonomous, unmanned operation.

5. REFERENCES

1. AFSPC/DOY, "Concept of Operations for the Transportable Optical System (TOS)," Headquarters, Air Force Space Command Space Control Mission Area Team (DOY), Peterson AFB, Colorado Springs, CO (3 January 1996).
2. C. W. Allen, *Astrophysical Quantities*, 3rd Ed., Athlone Press (1973) p 202.

6. ACKNOWLEDGEMENTS

The culmination of the TOS refurbishment in the successful DT&E Demo Two was the result of an exceptional effort by a diverse team of individuals. This team includes Frank Shelly and Julie Johnson (software), David Beatty and Lee Ramzel (hardware engineering), Mike Bezpalko (documentation and operations), Matthew Blythe (operations), and Robert Irelan (opto-mechanical integration). Additional contributions from Eugene Rork (optics and astronomical techniques), and Bob Weber are also gratefully recognized.

Sensor Suite for the Advanced Electro-Optical System (AEOS) 3.6-Meter Telescope

Michael L. Vigil, David J. Witte, Paul D. LeVan
Air Force Phillips Laboratory, Lasers & Imaging and Space & Missile Directorates
3550 Aberdeen Ave. SE
Kirtland AFB, NM 87117-5776
(vigil@plk.af.mil, witted@plk.af.mil, levan@plk.af.mil)

David E. Briscoe
Logicon RDA
P.O. Box 9377
Albuquerque, NM 87119-9377
(dbriscoe@logicon.com)

ABSTRACT

The Phillips Laboratory Advanced Electro-Optical System (AEOS) comprises an observatory facility, a united computer network, a 3.63 meter telescope, and an associated sensor suite that will become operational beginning with a radiometer in September 1997, followed by a longwave infrared imager in January of 1998, and a visible imager later in 1998. Space Object Identification (SOI) is the primary mission for AEOS; however, astronomical applications and other visiting experiments are readily supported by the system design. The AEOS sensor suite functions derive from Air Force Space Command requirements, and incorporate high resolution imagery and multi-band radiometry performed over a broad range of wavelengths. Data collection capabilities are optimized for the rapid temporal variations in observed target brightness that arise from both intrinsic target variability and changing atmospheric characteristics during the course of an observation.

Multi-spectral photometry/radiometry over the 0.4-23 μm spectral region constitutes the principal observational technique for spatially unresolved targets. Thermal infrared wavelengths, i.e., 4-23 μm , permit observation of targets that are in the shadow of the earth, and provide temperature measurements on all targets. High resolution visible to near-infrared imagery (0.7-1.0 μm), approaching the diffraction limit, is collected on sunlit targets via an adaptive optics (A/O) system. Simultaneous LWIR (8-13 μm) imagery is obtained with an infrared sensor that shares the high-resolution NIR imager's field of view through a dichroic beamsplitter. In order to minimize the thermal background, the LWIR imager is located close to the telescope, upstream of the A/O system. The LWIR resolution approaches the diffraction limit, due to the decreased impact of atmospheric turbulence at those wavelengths.

1. INTRODUCTION

AEOS construction is underway at the Maui Space Surveillance Site (MSSS) next to the Air Force Maui Optical Station (AMOS) and the Maui Optical Tracking and Identification Facility (MOTIF) at the rim of the Haleakala caldera. This site offers many qualities favorable to high resolution imaging and infrared observing. Atmospheric turbulence for the MSSS is characterized by atmospheric seeing frequently in the range of one to two seconds of arc. The high altitude of

the site (>10,000 feet MSL) provides the low atmospheric water vapor content essential to observing in the long wave infrared.

Congressional approval for an upgrade of the AMOS to include a 4 meter class telescope (the Advanced Electro-Optical System, or AEOS), and the associated sensor suite, was granted to the Air Force Phillips Laboratory in 1991. The telescope is based on a similar design by Contraves USA, Pittsburg, PA, for a 3.5 meter telescope currently in use at the Phillips Laboratory's Starfire Optical Range, Kirtland AFB, NM. AEOS will be the Air Force's largest optical telescope devoted to space surveillance.

2. AEOS MISSION REQUIREMENTS

As an integral part of the MSSS, AEOS will support the missions of that site. Space surveillance is the primary mission, and includes space object identification (SOI) and metric data collections. System-level performance for meeting Space Object Identification (SOI) requirements is the principal basis of the AEOS sensor designs. AEOS will collect imagery, radiometry, thermometry, and metric data. Top level requirements include angular resolution, source brightness thresholds, and temperature resolution. Temporal variations in target brightness, either intrinsic to the target or due to atmospheric variations during tracking, also constitute a significant driver of sensor designs. A simultaneous imaging capability between the visible and thermal infrared wavelength regions is key for meaningful comparisons between these wavebands. The need to minimize thermal background from telescopic and sensor fore optics provides a constraint on LWIR sensor location and design.

3. AEOS MISSION SENSOR SUITE

The AEOS Mission Sensor Suite comprises three resident sensors, developed as part of the AEOS project: the Radiometer, the LWIR Imager, and the Visible Imager. Table 1 describes these three mission sensors, as well as the Acquisition Sensors mentioned above.

	Tertiary Mirror Position						
	Acquisition		Trunnion			Coude	
	WFOV	NFOV	Radiometer			LWIR Imager	Coude Imager
Aperture (CM)	20	58	363			363	363
Spectral Range ⁽¹⁾ (microns)	0.4 - 0.9	0.4 - 0.9	0.4-1.0	2 - 5.5	8 - 14 17 - 23	8.1 - 9.1 10.1-12.9	0.7 - 0.9
Detector (Pixel) FOV (μrad)	94	16/4.4	2.0	1.5	2.0	0.74	0.10/0.60
Field of View (μrad) ⁽²⁾	1.1 Deg	0.2 Deg	256	192	256	>140	51/300
Detector Type	ICCD	ICCD	Array	Array	2 Arrays	2 Arrays	Array
Array Size (Pixels) (size used)	512 ²	512 ²	128 ²	128 ²	128 ²	>200 ²	512 ²
Max. Frame Rate (FPS)	RS-170	RS-170	1000	60	200	>60	<5
Detector Material	Gen III ICCD	Gen III ICCD	Si	InSb	Si:As	Si:As	Si
Oper. Temp.	TBD	TBD	-40C	-70K	10K	10K	-40C

⁽¹⁾ Filter wheels allow for sub bands

⁽²⁾ All designed for f/200 secondary
Excludes A/O sensors

Table 1. AEOS Mission Sensors and Acquisition Sensors

3.1 Radiometer

The AEOS Radiometer is being developed by Mission Research Corporation, in Santa Barbara, CA, and Logan, UT. The primary purpose of the radiometer is to simultaneously collect radiometric data in 4 bands, covering the visible out through 23 microns. The radiometer is located on the trunnion (see Figure 1), close to the telescope primary mirror. The radiometer contains 4 focal planes: Visible (0.4-1.0 μm); MWIR (2.0-5.5 μm); LWIR (8-14 μm); and VLWIR (17-23 μm). The simultaneous photometry and radiometry provided in these wavelength regions result in high temporal resolution, multi-spectral target signatures. Although the basic requirements for the sensor could be met with single detector elements, the chosen design concept uses arrays for all channels. The system has been optimized for radiometric performance rather than imaging; however, both image data and conventional signature data are available from the sensor.

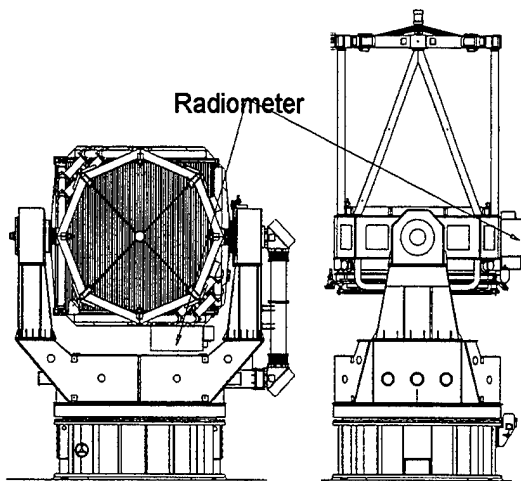


Figure 1:
Location of Radiometer on Telescope Trunnion

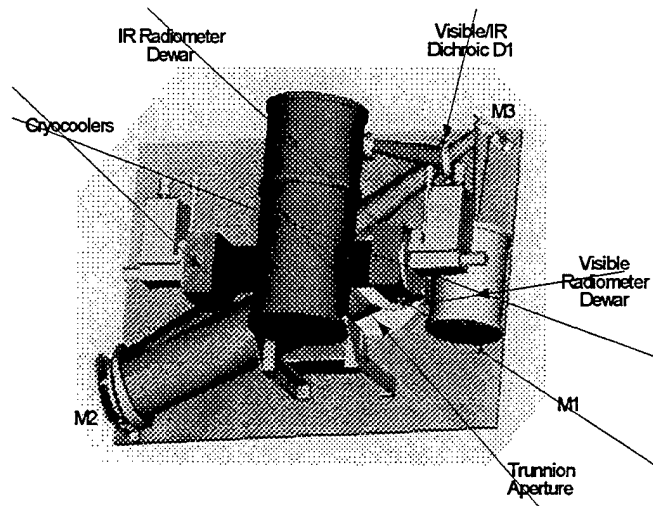


Figure 2:
Radiometer Optical Design

3.1.1 Sensor Configuration

The optical design is shown in Figure 2. The four arrays share a common line of sight by the use of dichroic elements. The first, uncooled dichroic reflects the infrared to a cryogenic housing and transmits the visible energy to a second vacuum housing. The visible FPA is contained in this second housing, and is cooled to -40 °C. This design choice to separate the visible from the IR was selected based on IR window material options for transmission from 2.0 through 23 microns. Within the cryogenic housing, two cold dichroics direct the three IR bands to their respective FPAs. The MWIR array is maintained at 60K, and the long wave arrays (Si:As) are operated at approximately 10K. Each array's temperature is controlled by on-chip thermal feedback loops. The optical design is close to diffraction limited for all IR channels--the visible channel is limited by the atmosphere.

3.1.2 Spectral Range

The full spectral ranges of the four radiometer channels are listed above. Each channel has two dedicated filter wheels; the first contains neutral density filters, while the second contains spectral bandpass filters. Standard astronomical band filters will generally be used for radiometric measurements, although certain non-standard bands that better support temperature determination will also be employed. The four focal planes, shown in Table 1, were selected from available, off-the-shelf devices. For the visible channel, the David Sarnoff Research Center high speed 512x512 array was selected based on high frame rates, low noise, and competitive cost. The driving requirement is for greater than 500 frames per second with total noise less than 30 rms electrons. The MWIR array selected is the Hughes SBRC low background InSb 256x256 array. The LWIR and VLWIR channels both employ the Rockwell Si:As HF-16 array with improved excess low frequency noise (ELFN) characteristics.

3.1.3 Background Subtraction

The use of LWIR and VLWIR bands necessitates a technique for background subtraction. The sensor developer has proposed a novel signal processing approach for removal of the background structure and detector responsivity non-uniformity. The approach is to use a circular scan around the object and co-add the frames to pixel-level resolution. The scanning is performed by the steerable telescope secondary mirror under the control of the radiometer through the Observatory Control System (OCS). The radiometer will have access to the real-time position of the secondary via OCS. The data is also spatially filtered as it is processed in real-time.

3.1.4 Sensitivity

The sensitivities of the four radiometer channels depend upon a number of parameters including effective integration time (bandwidth), total field of view (i.e., number of pixels required to encompass the target extent), spectral bandpass, and background level. The infrared channels will be background-limited over all background levels likely to be encountered at the MSSS. Representative sensitivities for favorable viewing conditions, expressed as noise equivalent flux density (NEFD) per root bandwidth, are as follows: Visible – 2×10^{-20} ; MWIR – 4×10^{-20} ; LWIR – 1×10^{-19} ; and VLWIR – 2×10^{-19} , all in units of $\text{W-cm}^{-2}\text{-Hz}^{-1/2}$ referenced to the AEOS telescope aperture.

3.1.5 Internal Calibration

The radiometer is equipped with internal calibration sources that support the spectral range of all detectors. The visible source is a NIST-traceable tungsten-halogen lamp with a stable power supply. The expected uncertainty is <3%. The IR detectors are calibrated with a blackbody source. Both sources are controlled with variable apertures, variable temperatures and relay optics. The uniformity correction may be based on the calibration data but that is yet to be determined. Once installed, the internal calibration will be combined with stellar calibration data. The calibration will be conducted periodically throughout the night.

3.2 LWIR Imager

The AEOS LWIR Imager is a dual-FPA sensor presently under development and scheduled for integration at the MSSS in early 1998. It will provide both background-limited sensitivity and virtually diffraction-limited imaging performance in the 8-13 μm region. The sensor is being developed within the Electro-Optical Systems segment of Hughes Aircraft Company in El Segundo, California. For the SOI mission, the primary data products of interest from this sensor are spatially-resolved temperature maps derived from band-ratios or other multi-band temperature estimators. Radiometrically-calibrated radiance maps with absolute accuracies of 10% or better are also required.

3.2.1 Sensor Configuration

As shown in Figure 3, the sensor assembly attaches to the yoke tine of the AEOS telescope gimbal. The sensor's data processing system is remotely located in the AEOS Control Room. A dichroic beamsplitter located along the coudé path between mirrors M4 and M5 intercepts the f/200 beam and reflects thermal IR energy into the LWIR Imager. The dichroic transmits visible and shorter IR energy to the AEOS Adaptive Optics system and the high-resolution Visible/NIR Imager. This permits simultaneous collection of visible and LWIR image data. The dichroic is removable from the coudé path for missions that do not require the LWIR Imager. The LWIR beam is re-imaged by a warm Three Mirror Anastigmat (TMA) off-axis telescope. The TMA output is directed into a cryogenically-cooled, vacuum enclosure containing spectrally-selective optics, calibration sources, and the two FPAs.

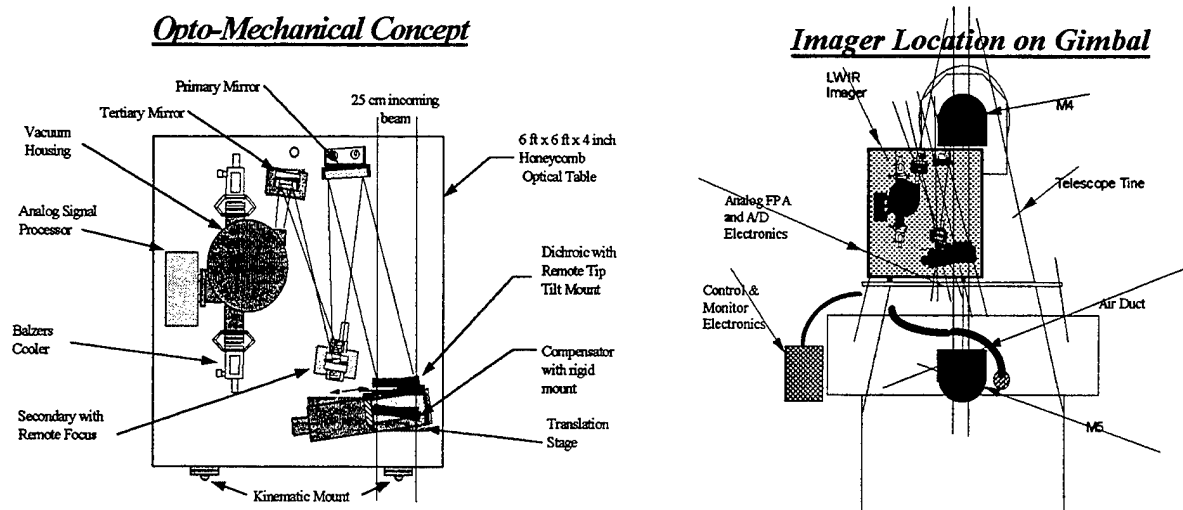


Figure 3. AEOS LWIR Imager

3.2.2 Spectral Range

The principal spectral region in which the LWIR Imager collects data is the 8-13 μm atmospheric window, i.e., the astronomical N band. This region affords the highest SNRs over the 200-350 Kelvin temperature range exhibited by most space objects. The sensor's two FPAs are identical 240x320 element blocked impurity band (BIB) Si:As arrays. The full astronomical N band is divided by a dichroic beamsplitter centered on the 9.6 μm ozone absorption band so that one FPA receives energy below 9 μm , while the other receives energy above 10 μm , allowing accurate determinations of LWIR color temperature for targets with rapid temporal brightness variations. Because of the broad spectral response of the Si:As detectors, the short wavelength FPA is also capable of background-limited data collection within the MWIR (3-5 μm) region. Blocking filters are used with each FPA to limit their long-wavelength responses and thereby minimize the extraneous background flux at the detectors. Each FPA has a dedicated filter wheel that holds up to six spectral filters for selection of specific measurement sub-bands. The filter wheel position may be changed in less than 0.5 seconds to permit rapid multi-spectral sampling.

3.2.3 Spatial Response

The angular instantaneous and total fields of view (IFOV and TFOV) of the two FPAs are identical. The IFOV of a single detector is 0.74 μrad in object space, which, given the 50 μm detector pitch, corresponds to operation at $f/19$. The 0.74 μrad IFOV provides Nyquist sampling of the diffraction-limited spatial frequency cutoff D/λ for wavelengths $\geq 8 \mu\text{m}$. This design will support developing algorithms in the area of "Super Resolution". Atmospheric turbulence, i.e., "seeing," prevents diffraction-limited imaging whenever the atmospheric coherence length, r_0 , is smaller than the telescope diameter. At the MSSS site, the value of r_0 in the visible, $r_0(\lambda=0.5 \mu\text{m})$, typically ranges from 5 cm to 20 cm, with a median value of around 8 cm. The value of r_0 scales with wavelength as $\lambda^{6/5}$, so at 8 μm this range corresponds to $r_0(8 \mu\text{m}) = 1.4 \text{ m}$ to 5.6 m with a median value of 2.2 m. The r_0 values for longer wavelengths are correspondingly larger. For example, $r_0(12 \mu\text{m})$ exceeds the 3.63 m AEOS telescope diameter whenever $r_0(0.5 \mu\text{m})$ exceeds the median value of 8 cm. Similarly, to have $r_0(8 \mu\text{m})$ exceed the telescope diameter, $r_0(0.5 \mu\text{m})$ must exceed 13 cm. Thus, under many but not all conditions, the LWIR Imager will achieve at- or near-diffraction-limited performance with both FPAs.

3.2.4 Sensitivity

The LWIR Imager will achieve near background-limited performance over the entire range of background levels likely to be encountered at the MSSS site. The background level varies substantially depending upon the site temperature and atmospheric conditions. Because AEOS is intended primarily for nighttime operation, the temperature of the warm optics (i.e., AEOS telescope, coudé path mirrors, LWIR dichroic, and TMA) will typically be around 0-5 $^{\circ}\text{C}$. Atmospheric thermal emission (i.e., sky radiance) contributes to the total background and, indeed, becomes the dominant source at larger zenith angles. For near-zenith viewing through a cold, dry atmosphere (i.e., low background condition), the NEFD, referenced to the AEOS telescope aperture, will be approximately $5 \times 10^{-19} \text{ W/cm}^2$ or lower, depending upon the specific spectral bandpass. This is the NEFD for a single frame collected with a 13 msec integration time.

3.2.5 Calibration

In order to meet the SOI mission requirements for radiometric and thermometric accuracy, a comprehensive calibration methodology has been developed for the LWIR Imager. The Hughes sensor design includes unique approaches for performing the functions of FPA non-uniformity, background subtraction, drift correction, and absolute responsivity determination. Two high-uniformity, high-accuracy blackbody sources developed by Hughes are included in the sensor design. These sources will be used to perform non-uniformity correction to extremely high precision ($< 0.1\%$), monitor drift, and assist in absolute responsivity determination. Atmospheric attenuation and telescope emission must be characterized independently on a per mission basis. Stellar sources will be employed for this purpose using standard astronomical approaches.

3.3 Visible Imager

The primary purpose of the visible imager is to collect high resolution imagery with nearly diffraction-limited performance on targets bright enough (i.e., $M_V = 8$ th magnitude or brighter) to allow atmospheric turbulence compensation by the adaptive optics (A/O) system. The visible imager is being developed by Hughes Danbury Optical Systems (HDOS), Danbury, CT, and will be integrated with the A/O system also being designed by HDOS. The sensor operates in the $0.7\text{--}1.0\ \mu\text{m}$ region with the A/O on-line. Increased throughput and spectral range is possible when the wavefront sensor is by-passed. Blur due to tracking is minimized by image rotation and atmospheric dispersion corrections. The sensor also includes accommodations for a speckle imaging upgrade envisioned for use in the near future.

3.3.1 Sensor Configuration

Figure 4 illustrates the A/O bench layout, and shows the location of the visible imager (shown as "Main Instrument"). The sensor's processing subsystem is remotely located in the AEOS Control Room. The input to the visible imager is a collimated 20 mm beam that has been corrected for atmospheric aberrations by the deformable mirror (DM) when it is on-line. With the DM off-line, e.g., for dim targets, the visible imager can operate independently of the A/O; beam collimation is maintained in this mode. In either mode, the collimated beam is transmitted through bandpass and/or neutral density filters, and then through derotation and dispersion correction optics. The beam is then focused onto the visible imager 512×512 FPA through one of three remotely-selectable lenses based on the required field of view. A translatable mirror will allow the focused beam to be optionally directed to a speckle imager, once that upgrade is implemented.

3.3.2 Spectral Range

The normal operational bandpass of the visible imager CCD is $0.7\text{--}1.0\ \mu\text{m}$, because shorter wavelengths are reserved for the A/O tracking and deformable mirror sensors. The sensor's silicon FPA has a peak quantum efficiency of 45% @ $0.7\ \mu\text{m}$, and useable response out to $1.05\ \mu\text{m}$. The entire bandpass or any desired sub-band is available via filters mounted in two six-position filter wheels. The filter wheel position can be switched in less than 2 seconds.

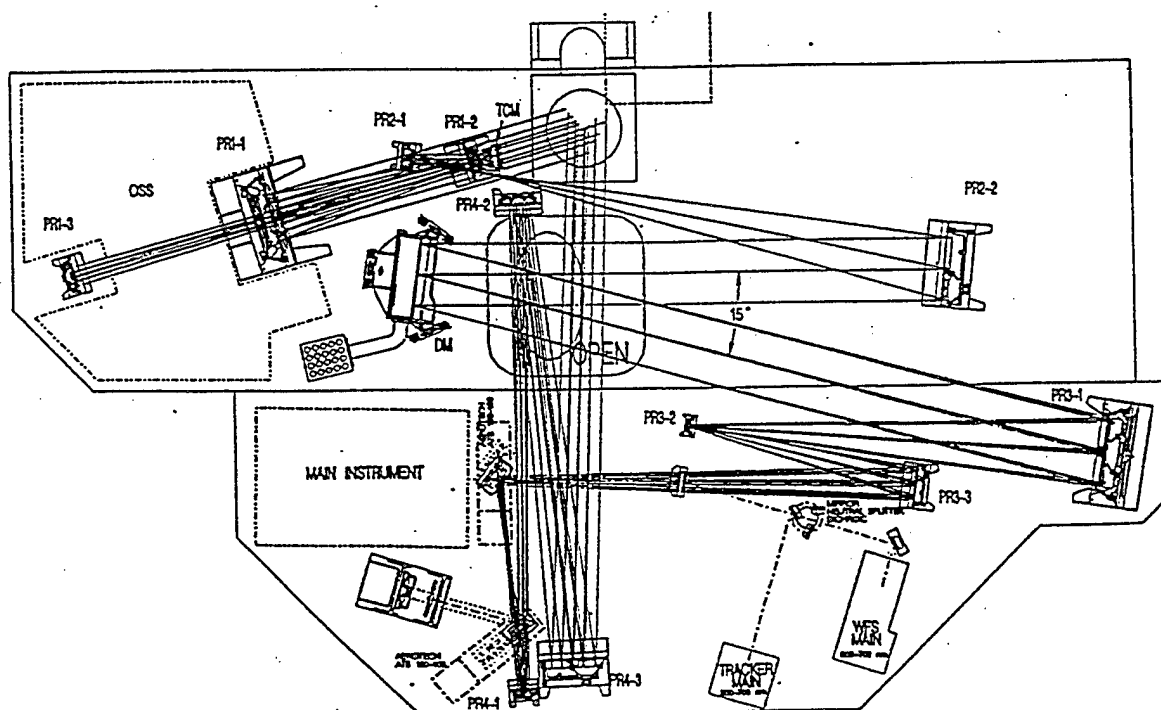


Figure 4. AEOS Visible Imager and A/O Bench

3.3.3 Spatial Response

With the adaptive optics system on-line, resolution approaching the $0.2 \mu\text{rad}$ diffraction limit of the 3.63 m telescope will be achieved. With the narrowest FOV optics selected, the IFOV is $0.1 \mu\text{rad}$ in object space, which provides Nyquist sampling of the diffraction-limited spatial frequency cutoff. For larger TFOVs, the spatial-frequency spectrum will be under-sampled. The variable FOV optics provide TFOVs of $51 \mu\text{rad}$, $120 \mu\text{rad}$, and $300 \mu\text{rad}$, with respective IFOVs of $0.1 \mu\text{rad}$, $0.24 \mu\text{rad}$, and $0.6 \mu\text{rad}$. With the adaptive optics system off-line, seeing is limited by atmospheric turbulence, and will typically be in the range of one to three arcseconds ($5\text{-}15 \mu\text{rad}$).

3.3.4 Sensitivity

The A/O provides atmospheric compensation for targets with visual magnitudes ranging from $M_V = -2$ to $+8$, but the visible imager itself is capable of much greater sensitivity. For short integration times, i.e., less than one second, the visible imager can detect targets as dim as $M_V = +16$. Longer integration times provide improved sensitivity. The CCD is cooled thermo-electrically to -40°C to minimize dark current, permitting integration times of several minutes. Optical throughput can also be increased within the sensor by selecting the wider TFOV lens and/or by rotating the filter wheel to an unfiltered position. Algorithms for background and dark current offset correction are applied to further enhance sensitivity.

3.3.5 Calibration

The relation of visible imager output signals to known power sources establishes the necessary reference for measuring radiant power confidently. Measurements utilizing a combination of stellar sources and an on-board reference source are made to meet radiometric requirements. Using standard astronomical approaches, stellar sources are used to characterize atmospheric attenuation and telescope transmission. Methodologies using the on-board source are applied for the characterization and correction of sensor artifacts such as non-uniformity, non-linearity, background subtraction, and drift correction.

4. CONCLUSION/SUMMARY

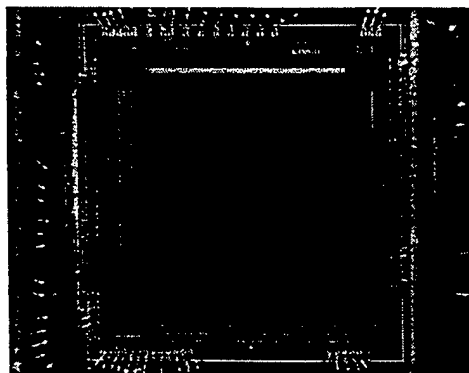
AEOS will be the Air Force's premier electro-optical space surveillance system. The 3.6 meter collecting aperture, combined with state-of-the-art sensors, atmospheric compensation, and pointing and tracking, will significantly enhance and extend the present MSSS capabilities. Although built primarily to support operational Space Command requirements, the AEOS design is intended to readily accommodate other applications and visiting experiments.

Infrared Focal Plane Arrays for Ground- and Space-based Space Surveillance

P. D. LeVan, K. A. Shrock (Phillips Laboratory), and J. E. Hubbs (Phillips Laboratory / Ball Aerospace)

Abstract: Several programs for infrared focal plane array (FPA) development, technically monitored by Phillips Laboratory, have a strong potential for space surveillance applications. For example, FPAs fabricated with impurity band conduction, arsenic-doped-silicon ("IBC silicon") are optimal for many applications in the MWIR, the LWIR, and even the VLWIR. The IBC silicon FPAs enjoy a high efficiency of conversion of incident photons into signal electrons, high pixel response uniformity, and an overall level of sensitivity approaching the background limit. This FPA technology has been sponsored by Phillips Laboratory for both high and low background applications. More recently, LWIR HgCdTe FPAs have shown tremendous improvements, most pronounced for lower background applications, in both pixel response and dark current uniformity. "LW HgCdTe" may soon compete with IBC silicon for applications with wavelength response shortward of approximately 12 microns, given the higher operating temperature (40 Kelvin or high for LW HgCdTe vs. 10 Kelvin for IBC silicon). The results of recent characterizations carried out at Phillips Laboratory confirm the high levels of performance mentioned above. Also, IBC silicon detectors have recently been employed in a variety of space surveillance and related applications. An acquisition camera based on a 128x128 IBC silicon FPA was developed for the Phillips Laboratory 1.6 meter telescope as a pathfinder for the utilization of this technology for ground-based space surveillance. In addition, Phillips Laboratory sponsored the engineering proof of concept for, and export of, IBC silicon detectors for use with the European Space Agency's Infrared Space Observatory (ISO). These detectors were retrofitted into ISO, which is currently in orbit and acquiring celestial background data. Finally, IBC silicon FPAs have been chosen for both the multispectral radiometric and LWIR imaging sensors under construction for the new 3.6 meter telescope of the Phillips Laboratory Advanced Electro-Optical System.

64x64 MWIR & LWIR Dualband Focal Plane Array



(This is the first-ever vapor phase epitaxy HgCdTe FPA to image simultaneously in these two wavebands.)

Global Background Characterization in 4.2-4.4 μm MWIR by Using NOAA-12 Data

by
Hsiao-hua K. Burke¹, Peter Tennyson
John Kerekes, Harry Finkle and Ed Wack

MIT Lincoln Laboratory
244 Wood Street
Lexington, MA 02173

ABSTRACT

Background phenomenology databases and models are essential for the design and assessment of electro-optical sensing systems. The MWIR band has been proposed to satisfy a number of specific requirements in the DoD space based mission areas. However, the phenomenology database in the MWIR to support the design and performance evaluation is limited.

Currently the High Resolution Infrared Radiation Sounder (HIRS/2) onboard NOAA 12, an operational polar orbiting environmental and weather satellite, offers continual global coverage of several bands in the MWIR. In particular, Channel 17 operates in the heart of the 4.23 μm CO₂ band. Though with coarse resolution (~ 20 km), the vast database offers a good baseline understanding of the MWIR phenomenology related to space based MWIR systems on (1) amplitude variation as function of latitude, season, and solar angle, (2) correlation to relevant MWIR features such as high-altitude clouds, stratospheric warming, aurora and other geomagnetic activities, (3) identification of potential low spatial frequency atmospheric features, and (4) comparison with future dedicated measurements.

Statistical analysis on selected multiple orbits over all seasons and geographical regions was conducted. Global magnitude and variation in these bands were established. The overall spatial gradient on the 50 km scale was shown to be within sensor noise; this established the upper bound of spatial frequency in the heart-of-the-CO₂-band. Results also compared favorably with predictions from atmospheric background models such as the Synthetic High Altitude Radiance Code (SHARC-3.)

Keywords: MWIR Remote Sensing, Downlooking Earth Background, Clutter Characterization, Background Phenomenology

I. Introduction

The wings of the CO₂ MWIR band are being investigated for addressing DoD space based mission requirements. However, the phenomenology database in the MWIR to support design and performance evaluation is insufficient. Currently the High Resolution Infrared Radiometer Sounder (HIRS/2) onboard NOAA 12, an operational polar orbiting environmental and weather satellite, offers continual global coverage of several bands in the MWIR (Figure 1). The 20-channel HIRS/2 sounder was designed to provide global information on the vertical distribution of atmospheric temperature, moisture and cloud presence. In particular, Channel 17 operates in the heart of the 4.23 μm CO₂ band. Though with coarse resolution (~ 20 km), the vast database offers a good baseline understanding of the MWIR phenomenology related to (1) amplitude variation as function of latitude, season, and solar angles, (2) correlation to relevant features such as high-altitude clouds, aurora and other geomagnetic activities, (3) identification of potential low spatial frequency atmospheric features, and (4) comparison with future dedicated measurements.

In Section II, data processing and statistical analysis procedures are described. Section III presents the summary of the data, their means and variations, as well as the comparison with atmospheric structure model predictions.

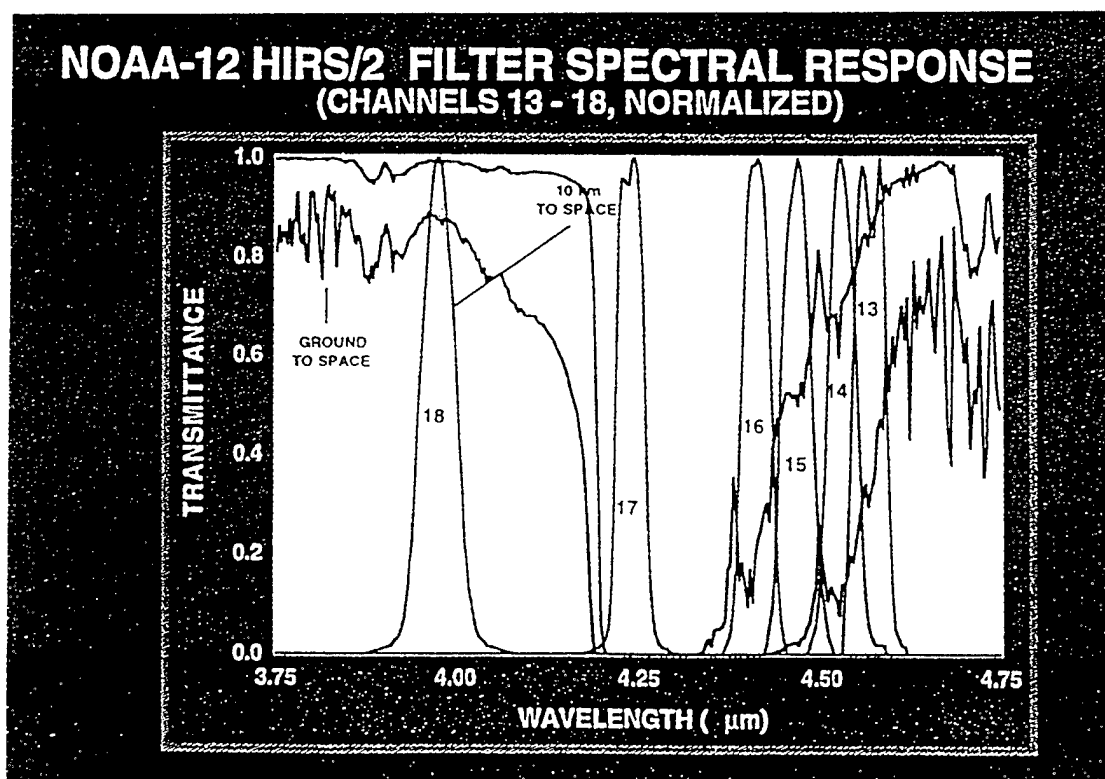


Figure 1

II. Data Processing and Analysis Approach

Various sets of HIRS/2 historical data were acquired through the National Climatic Data Center (NCDC). Thus far, four sets of 10-day global cumulative statistics were obtained and processed. Each set consists of 142 consecutive orbits; the first ten days of February, May, August and November 1995. Calibration and initial data quality check were conducted to ensure data applicability. For statistical analysis, data are limited to look angles from nadir to within 20 degrees off nadir such that uneven atmospheric attenuation effects are minimal and pixel size is smaller than 20 km by 20 km. Data were then binned to 1 deg by 1 deg in latitude and longitude grids.

Statistical analysis is then carried out which includes (1) the mean value of the ten-day samples; this establishes the global mean for each of the four seasons, (2) "temporal" standard deviation:

$$S.D. = \sqrt{N \sum I^2 - (\sum I)^2 / N} \quad N = \text{all samples}$$

which represents single cell analysis of variation of brightness at all locations over a ten-day period, and (3) "spatial" standard deviation:

$$s.d. = \sqrt{n \sum I^2 - (\sum I)^2 / n} \quad n = 9, \text{ and}$$

$$S.D. = \sum s.d. / N \quad N = \text{all samples}$$

which represents an average "in-scan" pixel-to-pixel variation within the 3 x 3 neighbors.

III. Highlights of Results

Some of the highlights of the statistical analysis results are presented here. Figure 2 illustrates the amplitude of HIRS/2 Channel 17 data for February, May, August and November. In both cases, the following can be concluded: (1) latitudinal variation is the most pronounced feature observed, (2) there is little longitudinal variation with respect to either geographical coverage or land/sea variation, and (3) the amplitude variation is generally monotonic with respect to latitude corresponding to the upper stratospheric thermal conditions.

Additionally, some stratospheric warming effects are also observed. The most evident is February in the >40 deg North Latitude and 70-135 deg East Longitude. Stratospheric warming is typically observed in January and February in the Northern Hemisphere at high latitude regions. Its persistent feature can last up to two weeks with temperature increase up to 60 deg in altitude region of 40-50 km and up to 100 km.

The range of HIRS/2 Channel 17 data is 3-12 $\mu\text{W}/\text{cm}^2\text{-sr-}\mu\text{m}$ for February, with the highest value in the Antarctic and decreasing toward the Northern Hemisphere. In

May the mean value ranges from 2 to 9 $\mu\text{W}/\text{cm}^2\text{-sr-}\mu\text{m}$, with the highest value in the Arctic region. Opposite geographical trends but with similar ranges as with February and May are observed for August and November, respectively (with the exception of November in the Antarctic where values greater than 15 $\mu\text{W}/\text{cm}^2\text{-sr-}\mu\text{m}$ were present.) These are consistent with the stratospheric thermal effect, a direct result of heating due to the absorption of solar ultraviolet radiation by ozone. A statistical representation of global zonal mean temperature is illustrated in Figure 3 for comparison.

Sample temporal and spatial standard deviation results (February and May) are shown in Figure 4. Range of temporal variation is typically $< 1 \mu\text{W}/\text{cm}^2\text{-sr-}\mu\text{m}$. In general, this represents the expected day-to-day variation. The spatial standard deviation results are indicative of the spatial "gradient" in approximately 100 x 100 km areas. Typical values are $\sim 0.05 \mu\text{W}/\text{cm}^2\text{-sr-}\mu\text{m}$.

Also conducted was the comparison with model prediction. An example of the Synthetic High Altitude Radiance Code (SHARC 3) model runs based on the Standard Atmosphere Generator (SAG) is demonstrated in Figure 5. Both nadir look and 45 deg look angle results for May are shown. The enhanced off-nadir values in the Northern Hemisphere are indicative of the non-local-thermal-equilibrium effect due to the coherent solar scattering. The agreement between data and model prediction is very good, within 20%, which confirms the capability of SHARC to predict the below-the-horizon (BTH) latitudinal and diurnal variations of the 4.23 μm mean radiance.

IV. Summary

A statistical analysis has been conducted of global MWIR data in the 4.23 μm region collected by an operational NOAA environmental and weather satellite. Initial effort includes the investigation of the global mean amplitude and standard deviations, both spatial and temporal, for all representative seasons. Results also compare favorably with model predictions. This work will be extended to analysis of other HIRS/2 bands that encompass the 4.2-4.4 mm spectral region. The data set is intended as part of the phenomenology database to aid in addressing various DoD space based system design and evaluation issues.

Acknowledgments

The authors wish to acknowledge the guidance of Capt. David O'Donnell, our program manager from the Air Force SMC/MT Office. We are grateful to Steve Nieman of the Space Science and Engineering Center, University of Wisconsin, for his assistance in calibration and navigation of the HIRS data. We are also indebted to Dr. Bill Blumberg of the Phillips Laboratory and Dr. James Duff of Spectral Sciences Inc. for the many helpful discussions and providing the model results from SHARC-3.

*Ref. Middle Atmosphere Dynamics, by D.G. Andrews, J.R. Holton and C.B. Leovy, Academic Press, 1987

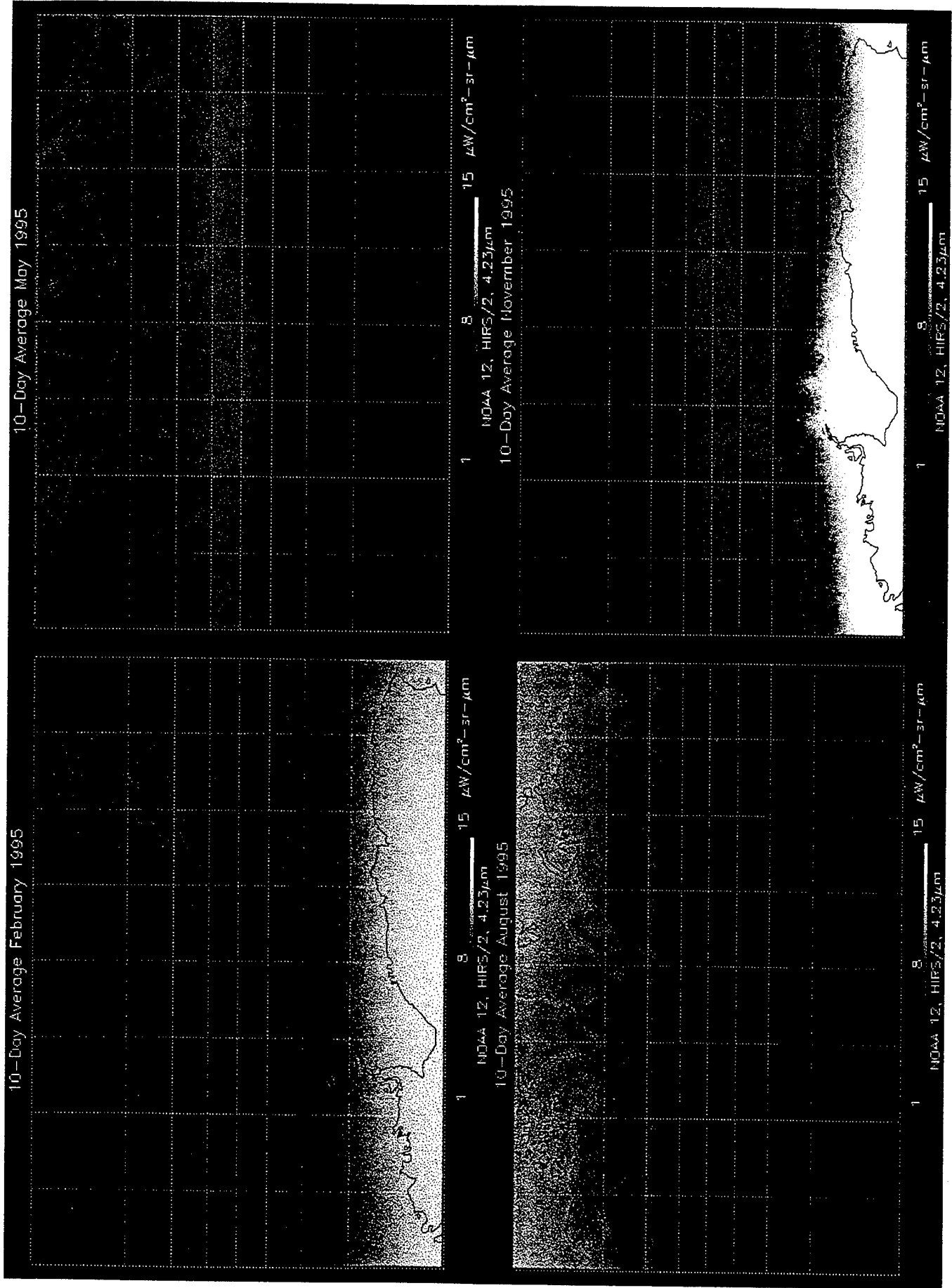
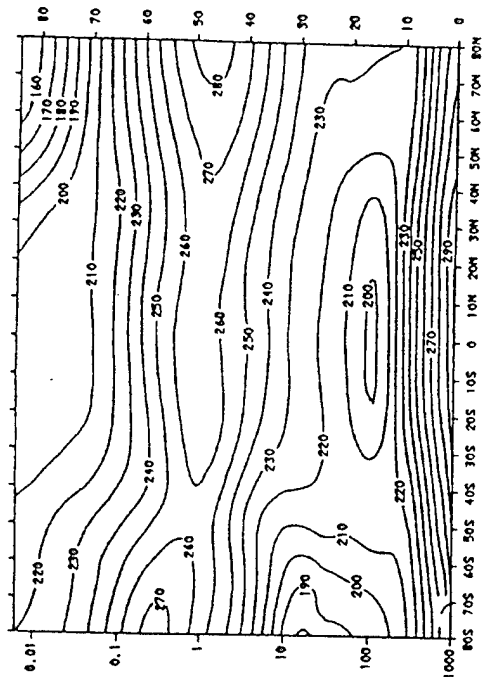
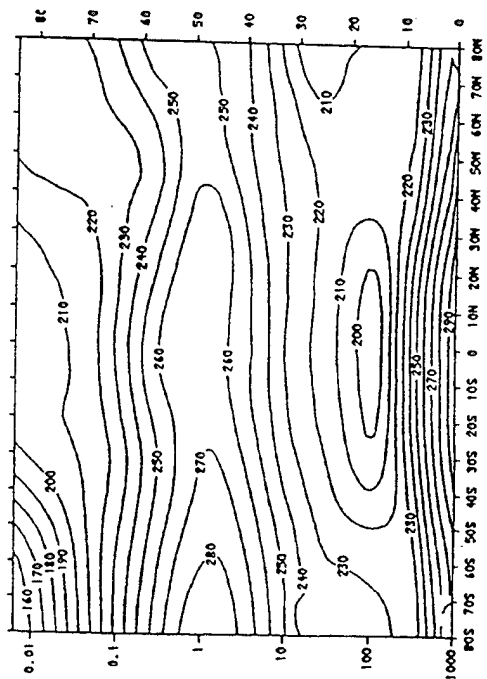


Figure 2 4.23 μm Global Averages for February, May, August and November

GLOBAL ZONAL MEAN TEMPERATURE

JANUARY

JULY

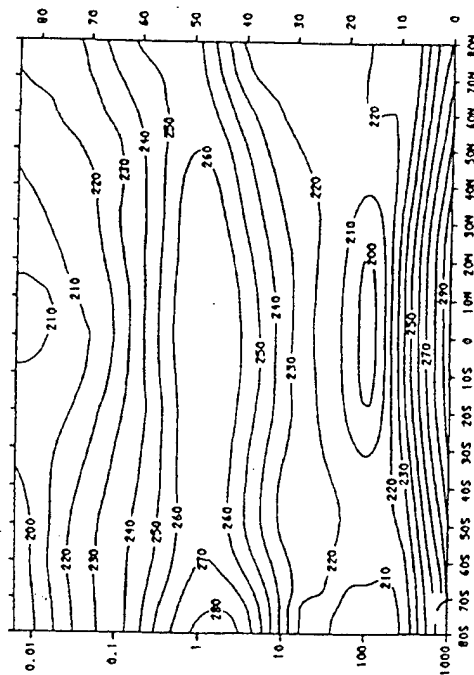
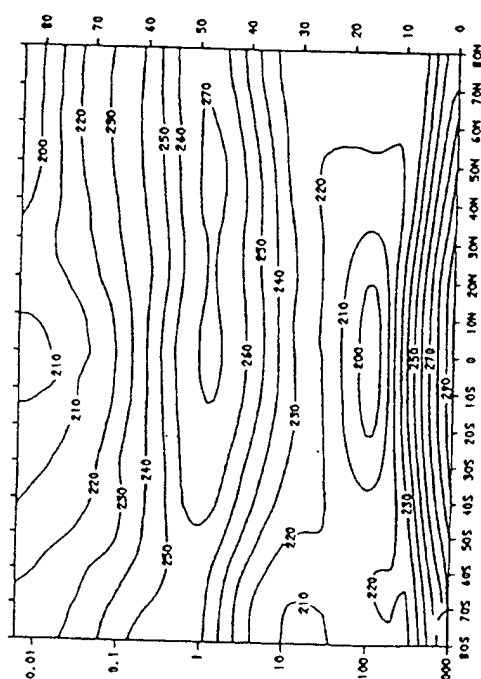


Pressure (mb)

Altitude (km)

APRIL

OCTOBER



Latitude

Figure 3

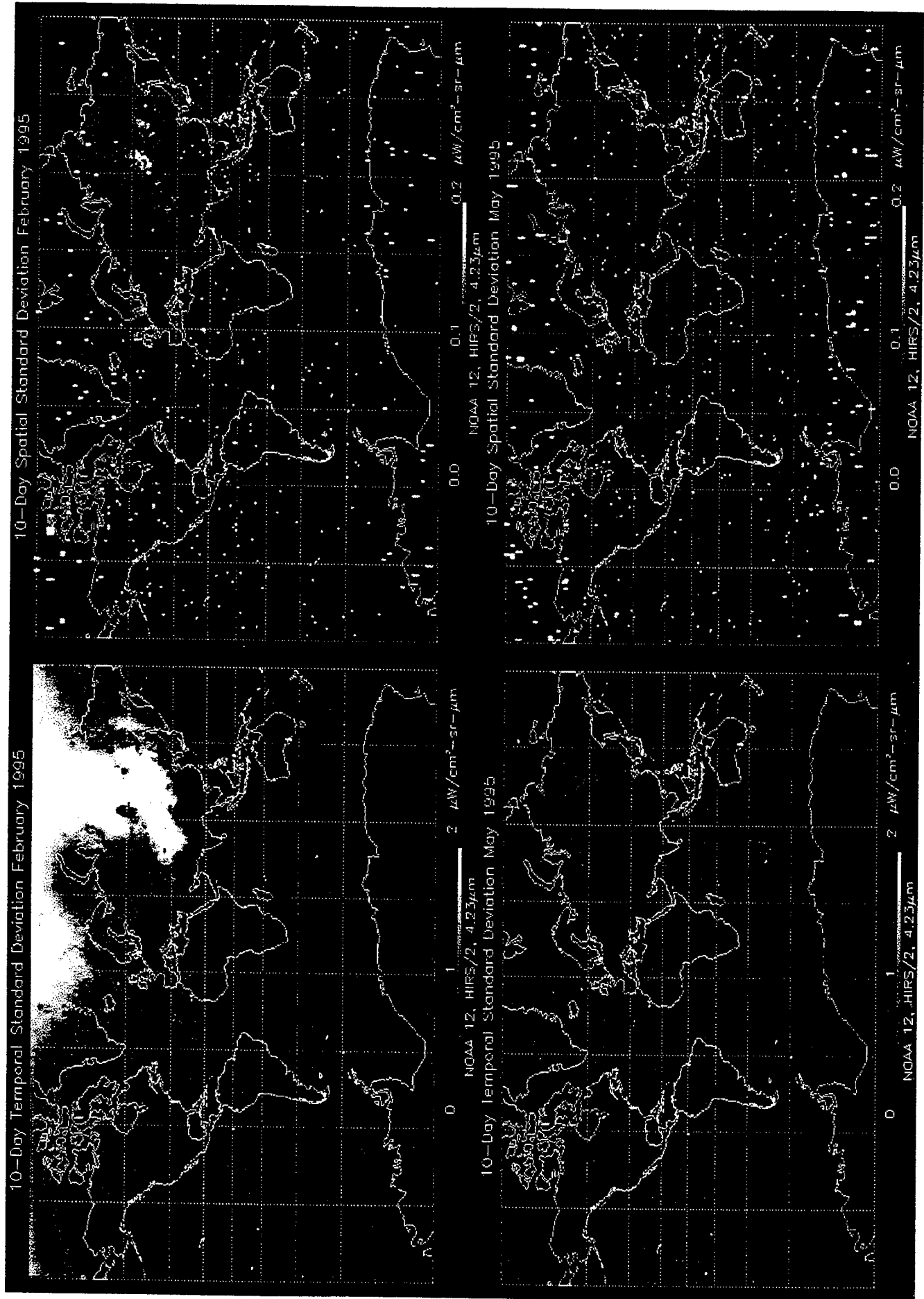
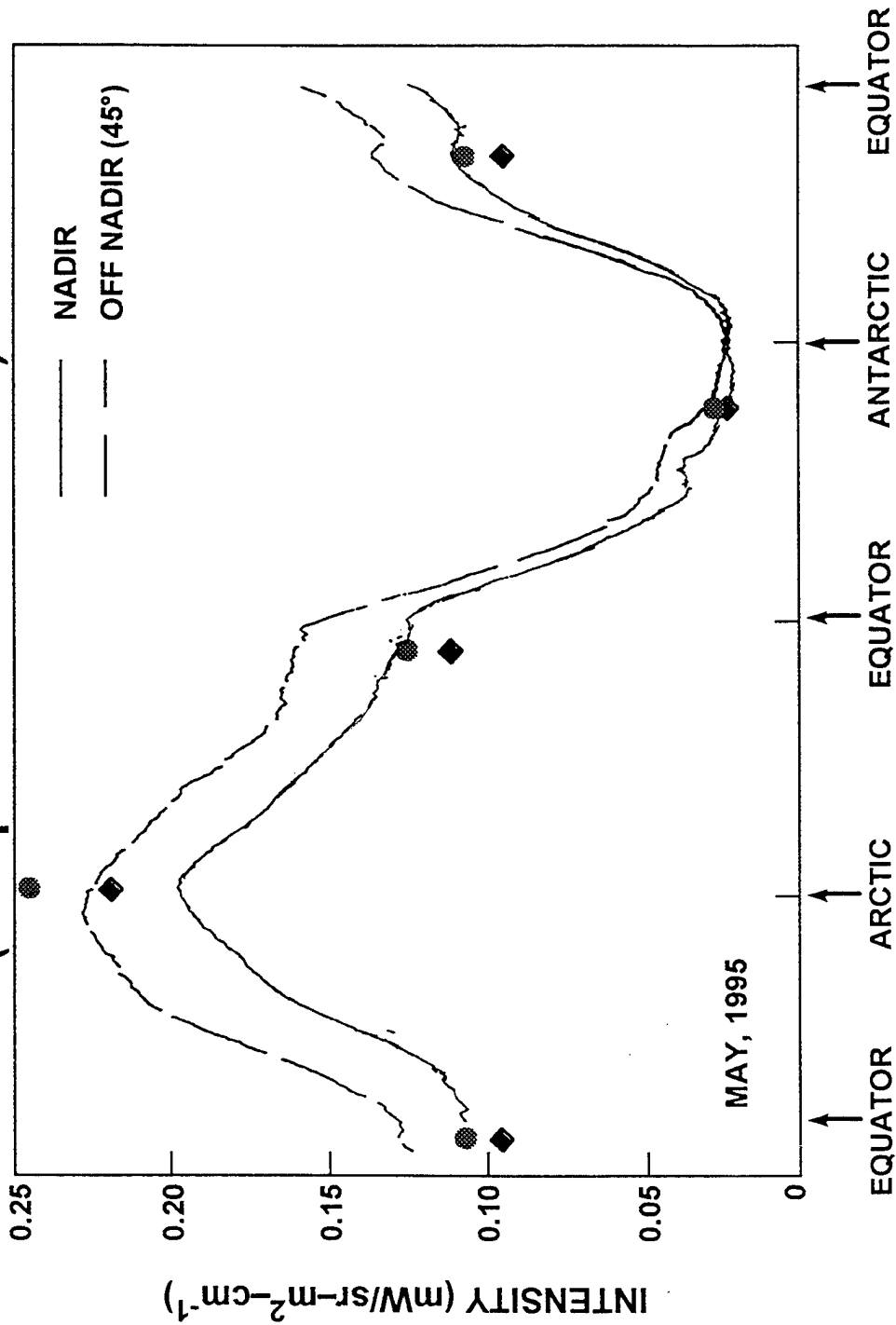


Figure 4 Temporal and Spatial Standard Deviations

NOAA 12 HIRS/2 DATA (4.23 μm) (Comparison with Model*)



*SYNTHETIC HIGH ALTITUDE RADIANCE CODE (SHARC 3)

Figure 5

Applying Electro-Optical Space Surveillance Technology to Asteroid Search and Detection

H.E.M. Viggh, G.H. Stokes, F.C. Shelly, and J. S. Stuart
MIT Lincoln Laboratory

Abstract

Lincoln Laboratory has a long history of developing electro-optical space surveillance technology for resident space object search, detection, orbit determination, and catalog maintenance. Recent advances in large format, highly sensitive CCDs make possible the application of these technologies to the detection and cataloging of Earth crossing asteroids. Preliminary search results using telescopes at the Experimental Test Site in Socorro, NM will be presented. A proposed future network of linked telescopes utilizing similar detection technology with a central tasking and cataloging facility is described.

Introduction

Recently there has been considerable discussion in both the press and in the Air Force on issues related to the detection and tracking of comets and asteroids. The interest has been generated by the collision of Shoemaker-Levy 9 with Jupiter and the realization that there are a large number of asteroids in orbits that could lead to eventual encounters with the Earth. Figure 1, adapted from the SpaceGuard Report (Ref 1), shows the estimated population of Near Earth Asteroids (NEAs) as a function of diameter. Asteroids with diameters exceeding 100 meters can cause considerable regional damage in a collision with the Earth and asteroids with diameters exceeding a kilometer may cause global effects. To avert such calamities, a system for defending the Earth would be needed.

The key enabling element of such an Earth defense system is the detection capability which allows the discovery of potentially threatening objects. This paper describes the performance of developmental GEODSS space surveillance technology, when applied to the detection and tracking of asteroids. This paper briefly describes the specifications of the new CCD detection system, compares the performance of the CCD and camera system used in the initial field trials to the specifications, presents the results of the initial system tests conducted at the ETS, and discusses how this technology fits into a concept of operations for an earth defense system based on the Air Force developed technology.

Over the past several years, the Air Force has been developing new devices and technology for the detection and tracking of earth orbiting satellites. This technology has been targeted to provide an upgraded capability for an operational space surveillance system called GEODSS. Currently, a number of GEODSS systems are deployed around the world as part of the world-wide space surveillance system operated by the US Air Force. Each GEODSS site is

currently equipped with 1-meter class telescopes and EBSICON detector systems which represent 1970's technology. The Air Force is now in the process of upgrading the GEODSS system to achieve the performance offered by state of the art detector systems. Under Air Force sponsorship, Lincoln Laboratory has developed a new generation of sensitive, large format, frame transfer CCD focal planes for GEODSS. These focal planes have been installed in a new generation of cameras and are currently undergoing testing at the Lincoln Laboratory Experimental Test Site (ETS).

When equipped with the new focal plane and camera technology, the modest sized GEODSS telescopes have considerable capability to conduct sensitive, large coverage searches for earth crossing asteroids. Field measurements have indicated that the CCD equipped GEODSS telescope is capable of achieving a limiting magnitude of 22, over a 2 sq/deg field of view, with less than 100 seconds of integration. This is comparable to the sensitivity of considerably larger telescopes equipped with current cameras. In addition to the high sensitivity, the CCD is configured for frame transfer operations which are well suited to high coverage rate asteroid search operations.

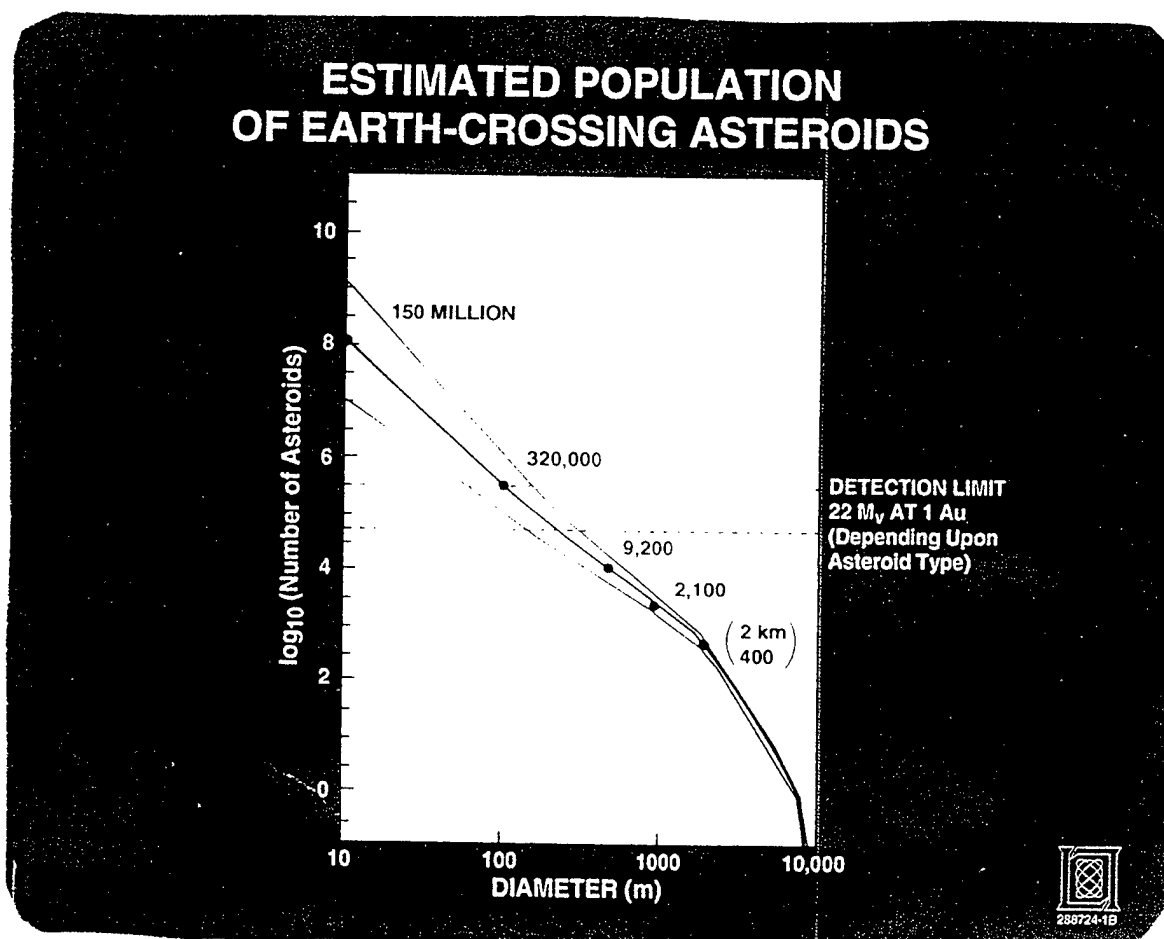


Figure 1. Near Earth Asteroid Population Estimates

Detector Technology

Under Air Force sponsorship, the Lincoln Laboratory developed CCD focal planes have been installed in a new generation of cameras which have undergone testing and validation at Lincoln Laboratory's Experimental Test Site (ETS) on White Sands Missile range. The Lincoln focal planes and camera system provide considerably improved sensitivity, which will increase the observation rate and allow tracking of fainter objects, fast frame transfer readout, which allows the integration of the next image to be started while the previous image is readout into the computer, and stringent blemish specifications which minimize the loss of detections attributed to focal plane defects. The latest generation focal plane contains an array of 2560X1960 pixels and has an intrinsic readout noise of only a few electrons per pixel. In addition, they are constructed using a back illumination process which provides peak quantum efficiency exceeding 90% and solar weighted quantum efficiency of 65% as shown in Figure 2. The figure compares the quantum efficiency of the current GEODSS EBSICON with that achieved by front or back illuminated Lincoln CCDs.

Figure 3 shows the details of the current generation 1960X2560 pixel CCD. The focal plane is equipped with 8 parallel readout ports to allow the 5 million pixel values to be read out in about 0.3 seconds. In contrast to most large format CCDs now on the market, which read directly out of the image array into the output port, the Lincoln CCD is equipped with frame store buffers. These buffers are used to store the image outside of the active area for the duration of the readout. This feature eliminates the need for a mechanical shutter to define the exposure, because the image is transferred from the image area into the frame buffer in several milliseconds. As soon as the image is transferred out of the active area, a new integration may begin. The frame store locations are identified in Figure 3.

The CCDs described above have been constructed specifically to allow large portions of the sky to be searched to find faint, moving targets. As such, they have the best combination of large format and detection performance of any CCDs that exist today. The detailed specifications for the CCD imager and the camera system are shown in Table 1.

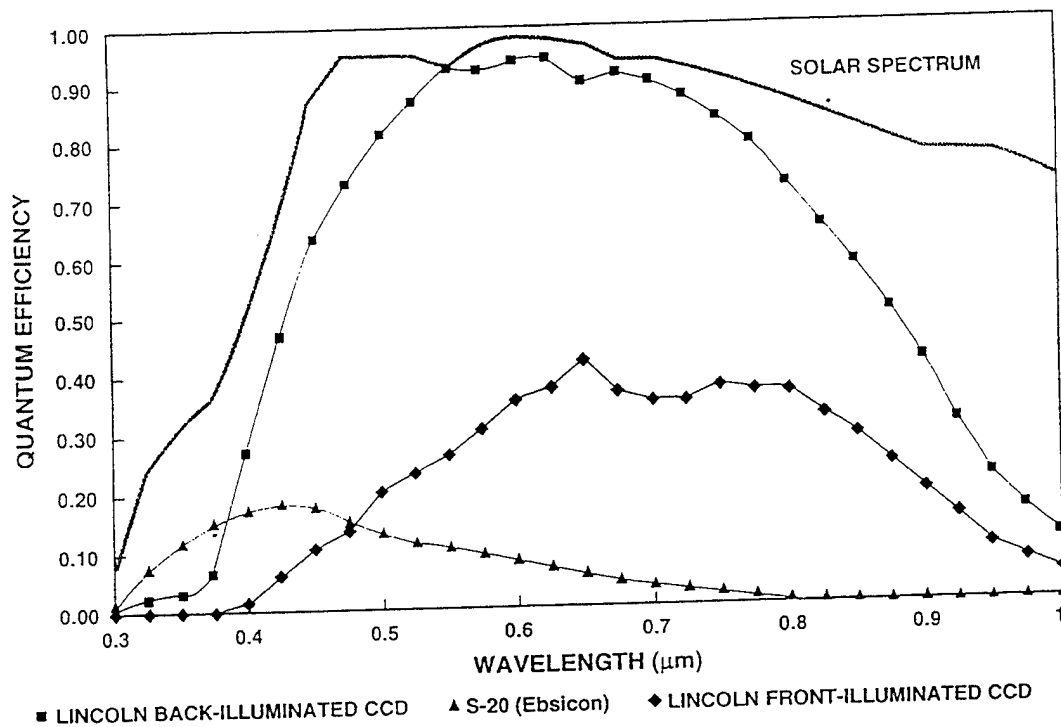


Figure 2. Quantum Efficiency of CCD and EBSICON Detectors as a Function of Wavelength

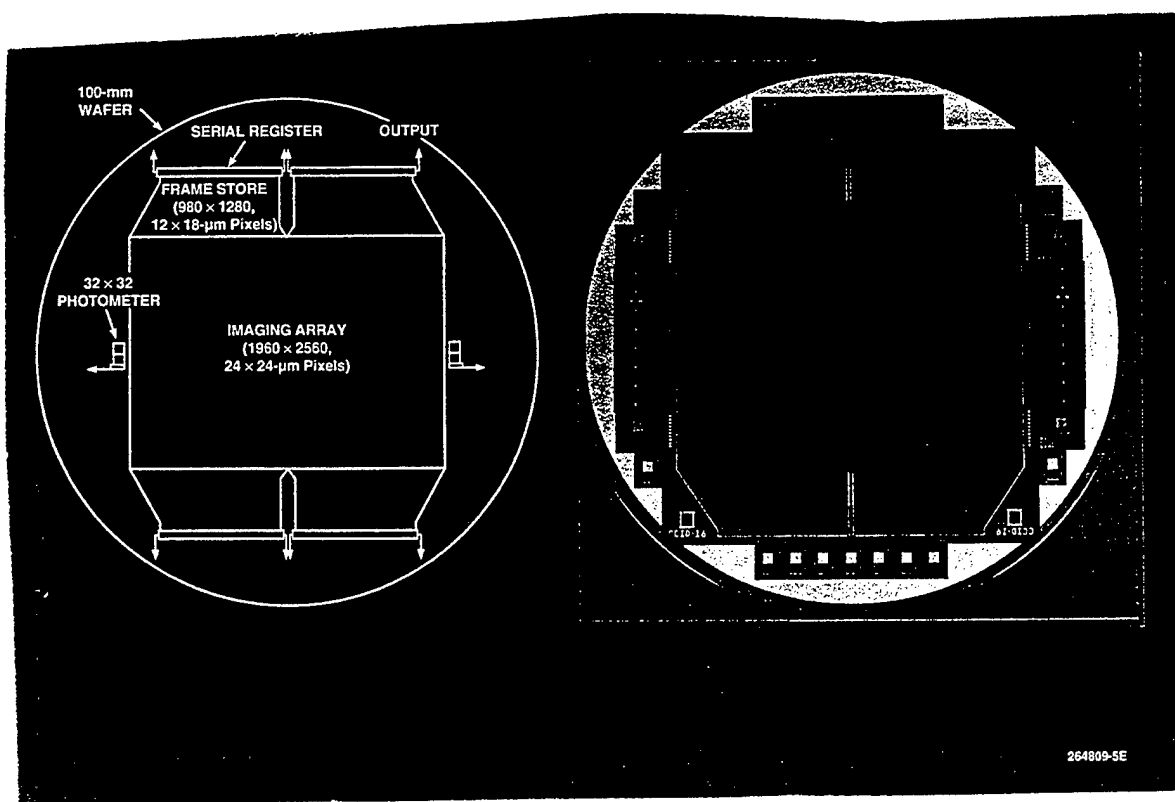


Figure 3. Lincoln Laboratory 1960x2560 pixel CCD.

TABLE 1

CCD Specifications:

# Pixels:	2560 X 1960
Pixel Width:	24 micron
Readout Method:	Frame Transfer
Focal Plane Area:	61.4 X 47 mm
# Readout Ports :	8
Highest Port Readout Rate:	2 MHZ
Highest Frame Rate:	10/s (2X2 Binning)
Readout Noise at Highest Rate:	<10 e RMS
Solar Weighted QE:	65% (Back-Illuminated)
Responsivity Variation:	<2%
Dark Current @ -40C:	<60 e/pixel/s
Dark Current Variation:	<10% RMS
Full Well capacity:	>75,000 e/pixel
% Pixel With Bright Defects:	<0.15%, All Isolated

Camera System Specifications:

Integration Times:	0.1 s to 100 s
Frame Rate:	up to 10/s with 2X2 binning
Digitization Depth:	14 Bits
Camera Noise - 1 MHZ Readout:	<6 e RMS
Camera Noise - 2 MHZ Readout:	<10 e RMS
CCD Operating Temperature:	To -50 deg C

Initial Field Test Results

Field tests of the CCD and camera system have been conducted over a period of several months starting in August of 1995. The initial efforts have been directed toward determining the capability of the camera system to meet the specifications stated in Table 1. Table 2 contains the results of the initial characterization which demonstrate that the CCD and camera are capable of meeting the specified performance requirements, with the exception of the highest frame readout rates.

TABLE 2

Test Results:

Highest Frame Rate:	5.7/s (*)
System Readout Noise at 2 MHZ:	12.7 e RMS (camera+CCD) (*)
Solar Weighted QE:	66% (Back-Illuminated)
Responsivity Variation:	0.4% (*)
Dark Current @ -50C:	10.5 e/pixel/s (*)
Dark Current Variation:	<2% RMS (*)
Full Well capacity:	75,000 e/pixel
% Pixel With Bright Defects:	0.10%
Integration Times:	0.1 s to 100 s
(*) 2X2 binned data	

In addition, the initial field tests validated the design of the system from the point of view of mechanical, vacuum and cooling capabilities.

After the initial shake-down tests were complete, the capabilities of the system to detect astronomical objects was assessed and compared to the model used to predict the performance of the system for asteroid detection. Figure 4 presents a magnified image frame containing calibration stars near galaxy M92, acquired with the camera system. A number of stars near M92 have well measured intensities, some of which are indicated by the numbers superimposed on the image frame. The portion of the frame contained in the figure is approximately $\sim 1/4000$ of the 2 square degree FOV area and was obtained by adding ten frames, each with 10 seconds of integration. Several frames of this type of data were taken over a range of integration times and the results combined with the theoretical sensor model shown in Figure 5. The results of this exercise provided convincing evidence that the camera system was performing as expected and would provide the expected capability to detect asteroids. In fact, the circled data point indicates the sensitivity required to detect a 100 meter diameter E-type asteroid at a distance of 1 astronomical unit from the earth. This sensitivity is achieved using the GEODSS telescope and the CCD camera system after about 70 seconds of integration.

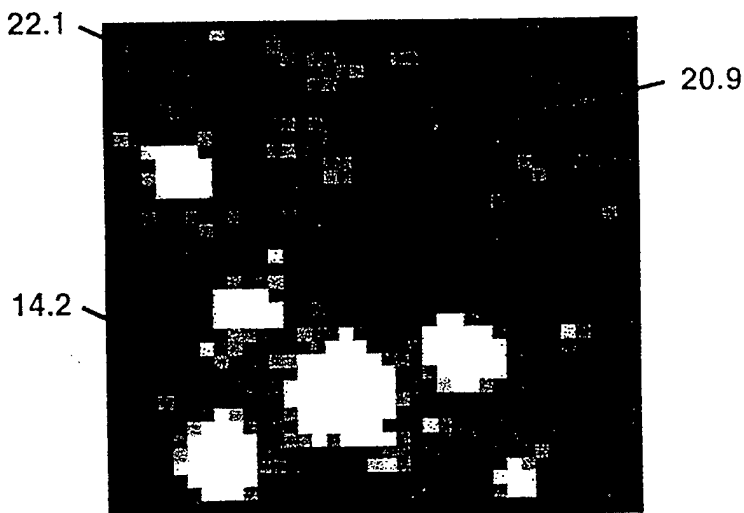


Figure 4. Image frame near M92. The magnitudes of several detected stars are indicated.

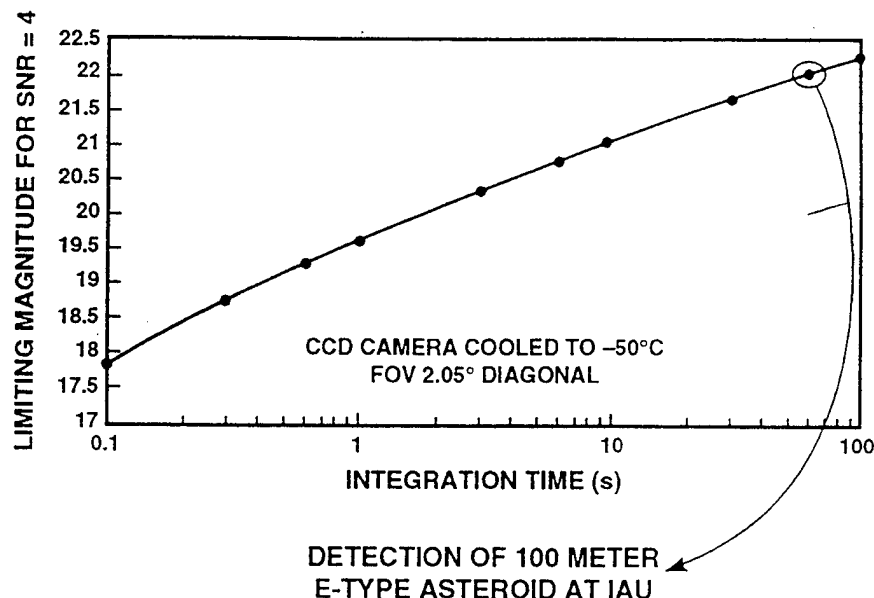


Figure 5. Comparison of the measured performance of the camera/telescope system (points) and that expected from Sensor model (solid line).

The next series of tests were undertaken to understand the capability of the camera and moving-target detection system to detect asteroids. A series of areas of the sky were surveyed repeatedly to detect moving objects. Revisit intervals spanning the range of 10 to 60 minutes between integrations were evaluated for series of between three and six revisits per area of sky. Integration times ranging between a fraction of a second and 10 seconds were employed. An existing moving target detection capability, running on a Data Cube Image Processor, was modified to detect targets moving as slowly as asteroids. A block diagrams of the site setup and the asteroid detection algorithm are shown in Figure 6. Due to equipment limitations at the site, all of the data were acquired in the 2X2 binned mode.

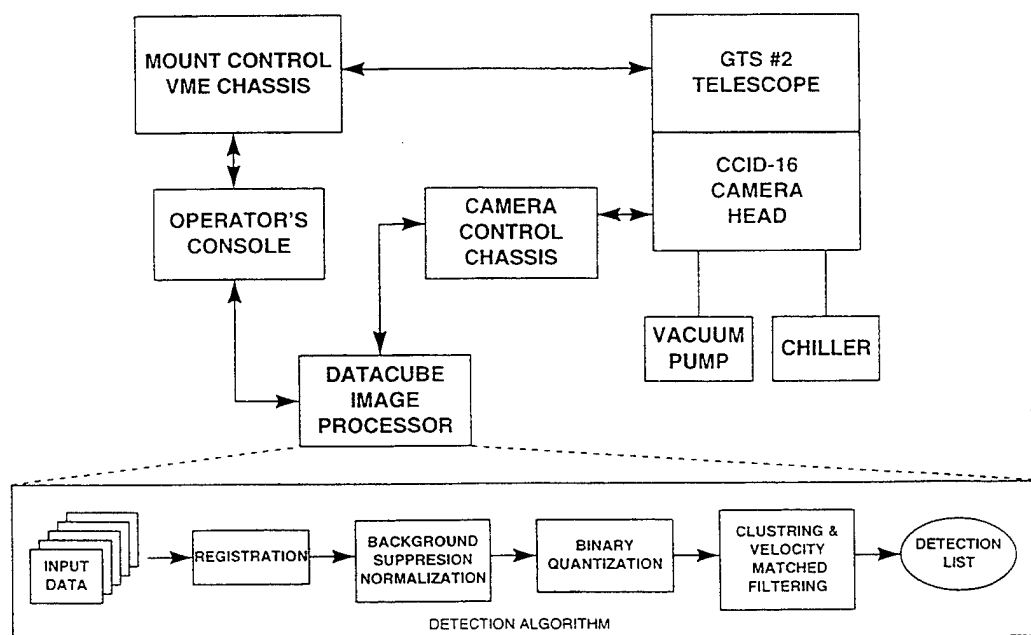


Figure 6. Block diagram of ETS system used to acquire asteroid data and detection algorithm

The detection algorithm employed has five major steps. The input data consists of five or more CCD images of the same location of the sky collected with an interval of about 30 minutes between them. Image registration is performed to correct any pointing errors between the images by shifting the second through last frames as necessary to line up their stellar backgrounds with that of the first image.

Next, the registered images are normalized to remove background noise in the clutter suppression normalization block. Estimates of background mean and standard deviation are computed at each pixel, averaging over all the frames. The data are normalized on a pixel-by-pixel basis using the local background mean and standard deviation. The normalized data are then binary quantized with a simple threshold. A threshold value of 99% is currently used.

The binary quantized data are clustered on a frame-by-frame basis to group adjacent pixels into objects. The centroids and extents of the clusters are computed. Each cluster in the first frame is paired with each cluster in the last frame that falls within a specified radius, selected as an upper limit on asteroid rates of motion. These pairs form the list of candidate detections, or streaks. Each candidate streak is assigned a velocity by dividing the displacement from the beginning to the end of the streak by the time interval which it spans. For each candidate streak, intermediate frames are searched for clusters with the appropriate displacement to match the streak's velocity. These matching clusters are added to the candidate streak. Once all of the candidate streaks have been filled out, those streaks that have too few clusters are rejected. The streaks left are considered detections which are manually reviewed to identify any false detections.

An example of the detection of an asteroid is shown in Figure 7. The data displayed is derived from five image frames made of the relatively bright asteroid 156 Xanthipe. Each frame was acquired by integrating for 0.5 seconds and the frames are each separated by 50 minutes. The top panel of the figure shows the full frame data. Below the full frame, the two panels on the left contain subsets of two of the full frames. It is obvious that there is an object that has moved during the four hours that have passed between the two pictures. The individual frames have been processed together using the automated moving object detection system discussed above to yield the output display, shown in the lower right corner of the figure. The end points of the moving object's streak are circled.

During the initial tests conducted at the ETS between August 1995 and July 1996, a total of 75 hours of observing time were dedicated to searching for asteroids. That effort yielded a total of 177 observations of asteroids which were provided to the Minor Planet Center (MPC) in Cambridge MA. A total of 49 new objects were discovered during the observing, including a confirmed Near Earth Asteroid (NEO), which was given the designation 1996MQ. In addition, observations of 79 known objects were collected.

DETECTION EXAMPLE

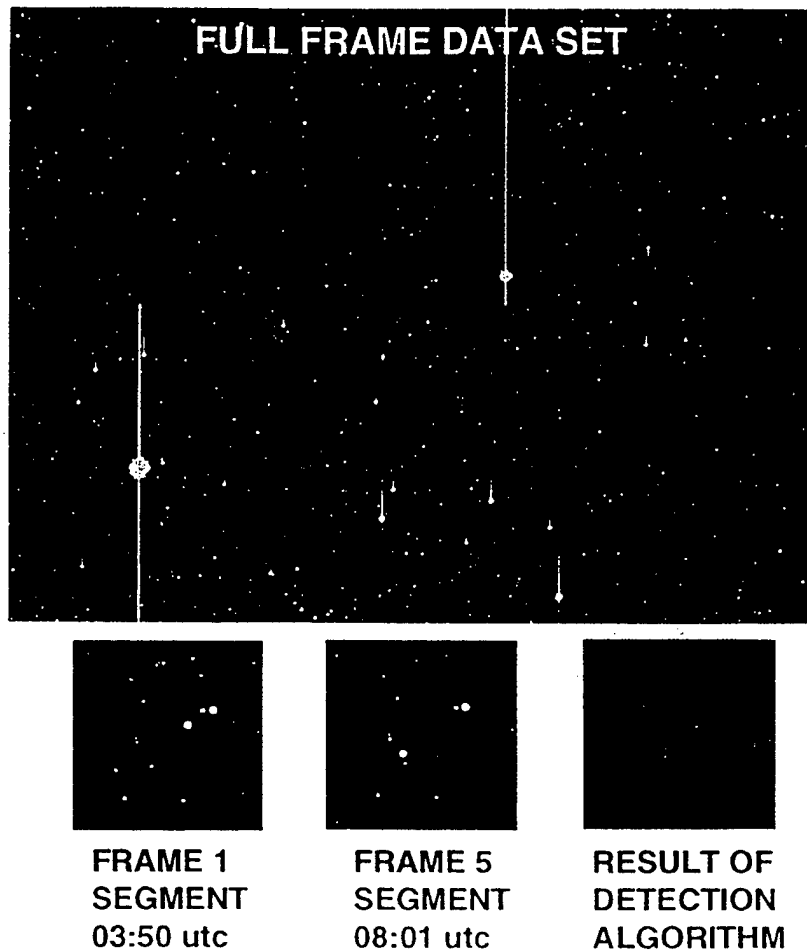


Figure 7. Detections of moving objects resulting from processing a series of image frames. The top frame shows the entire field of view of the CCD. The two subframes on the lower left show subsets of the data containing an asteroid and the subframe to the lower right displays the processed result - an asteroid detection.

These observations and new discoveries were made with a preliminary camera and datasytem that provides only a small fraction of the possible discovery rate of an operational system using the same CCD technology. With the appropriate integration of existing real time hard disk storage, unbinned read out hardware, and automation of data management tasks, a much higher rate of search, processing, and discovery can be achieved.

A second round of field tests are to be carried out beginning in early 1997. After a period of calibration tests on known asteroids, various search and follow up strategies will be demonstrated and evaluated. The emphasis will be on detecting new objects and assisting the MPC by collecting data on objects from the MPC's "critical list" of objects requiring new observations for catalog maintenance.

Air Force Asteroid System Concept of Operations

Previously, a top-level concept of operations (CONOPS) for an Air Force planetary defense system has been outlined (Ref. 2). This CONOPS is based on the experience and

technology acquired over the past 40 years of operating the space surveillance network. The detection and cataloging functions of a planetary defense system are in fact quite similar to those performed by Space Command for the earth orbiting satellite population. As a result, the technology and techniques developed over the past decades for satellite surveillance are applicable to the asteroid threat.

An overview of an asteroid system architecture is shown in Figure 8. The system consists of surveillance sensors used to detect new NEOs, tracking sensors used to gather follow-up metric and characterization data, elements for the mitigation of discovered threats, and a central control system which coordinates all of the activities of the network. The results presented in this paper provide a first look indication of the capability of the detection portion of the system, if it is based on the GEODSS upgrade technology combined with modest 1-meter class telescopes. The results are consistent with those expected at the time the concept of operations was developed.

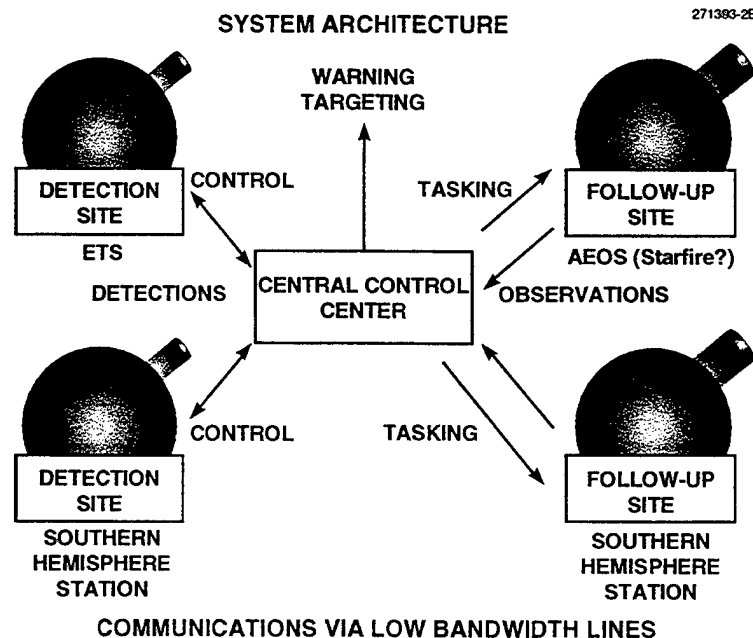


Figure 8. Architecture of possible USAF asteroid detection and tracking system.

The initial performance of the CCD camera on the GEODSS telescope has validated the capability of the upgraded GEODSS system to accomplish the search/initial detection phase of the Earth defense mission. The test-bed capability at ETS now provides the opportunity to refine the details of the CONOPS with respect to items such as the search and follow-up strategies, and more automated moving target detection architectures.

Summary

Results of system tests conducted at the ETS have been presented which validate the expected performance of the Lincoln developed CCD and camera technology. The performance demonstrated by the CCD and the camera system are sufficient for the asteroid detection application using 1-meter class telescopes, as suggested in the CONOPS under consideration by the Air Force. Field demonstration tests at the ETS have lead to the discovery of 49 new asteroids, including a Near Earth Asteroid, 1996MQ. Additional field tests are planned to further refine the use of the CCD camera and automated moving target detection technology on the GEODSS class telescopes for the asteroid detection application.

References

1. Morrison, D., Binzel, R.P., Bowell, E., Chapman, C.R., Friedman, L., Gehrels, T., Helin, E.F., Marsden, B.G., Maury, A., Morgan, T.H., Muinonen, K., Ostro, S.J., Pike, J., Rahe, J.H., Rajamohan, R., Rather, J.D.G., Russell, K.S., Shoemaker, E.M., Sokolsky, A., Steel, D.I., Tholen, D.J., Veverka, J., Vilas, F., and Yeomans, D.K., 1992. The Spaceguard Survey: Report of the NASA International Near-Earth-Object Detection Workshop (Washington, D.C., NASA).
- 2) Darrah, J., Worden, S. and Stokes, G., "*Air Force Planetary Defense Technology*", Space V, Volume 1 (Proceedings of the Fifth International Conference on Space '96), ASCE, 1-6 June 1996, pps 32-45.

REMOTE SENSING AND CHARACTERIZATION OF ANOMALOUS DEBRIS

R. Sridharan, W. Beavers, R. Lambour, J. Kansky,

Lincoln Laboratory, Massachusetts Institute of Technology,
244 Wood Street, Lexington, MA 02173

E. Stansbery

NASA/Johnson Space Center
2400 NASA Rd. 1, Mail Code SN3, Houston, TX 77058

ABSTRACT

Analysis of orbital debris data collected by the Haystack LRIR has shown a band of anomalously high debris concentration between the altitudes of 800 Km and 1000 Km. Indications from the Haystack data are that the debris range in size from 8 mm – 2 cm and that they are spherical in shape. Detective work by NASA has shown the likely origin to be the leaking coolant fluid from nuclear power sources that powered a now defunct Soviet space-based series of ocean surveillance satellites. Estimates are that there are approximately 50 – 70 thousand droplets in orbit.

A project has been in progress at MIT Lincoln Laboratory to detect, track and characterize a small sample of the anomalous debris. The primary sensors used for the purpose are the Haystack radar, the Millstone hill radar, TRADEX and the Firepond optical observatory. The major questions being addressed are:

1. What are the size and shape of the sample set?
2. Can we infer the composition of the material the droplets are made of?

The techniques being used to detect, track and characterize the sample set will be described in this paper. Results of the characterization analysis will also be presented.

The first problem addressed was the acquisition and tracking of a sample set of these small objects. Standard stare-and-chase, an innovative stare-and-detect and conventional orbit search techniques were used for finding the debris sample. These methods will be described in the paper along with the results.

One debris were in regular track, the following characterization was possible:

1. estimate of shape and size
2. estimate of mass and density
3. estimate of surface reflectivity parameters

The methods used for the characterization will be discussed and results will be presented.

1. INTRODUCTION

Remote sensing of small debris in space is a challenging task because of the low signal-to-noise (S/N) ratios that can be attained by ground-based sensors for detection and tracking. However, characterization of space debris is important as it is one of the factors affecting the short-term and long-term safety of humans in space and also of orbiting spacecraft. We present in this report techniques developed at MIT Lincoln Laboratory for remote sensing and characterization of a particular debris field and discuss the results. High power radars and high sensitivity optical systems were used for this effort because of their unique and complementary capabilities.

1.1. Debris and the Haystack Radar

NASA/JSC has been engaged in an extensive study of debris in space for over a decade. The study was triggered by the potential of significant damage to the space station and the shuttle due to impact of debris. The typical velocity of impact would be ~10 Km/s and hence even small centimeter-sized debris can cause catastrophic damage. NASA/JSC developed a model to represent the density distribution of debris in space. This model has been revised and corrected using data from actual impacts on the shuttle, the LDEF and, for the most significant threat sizes of ~5 mm. to 5cm., from the Haystack radar (Refs.1-2).

Figure 1 gives the pertinent characteristics of the Haystack radar. The radar is operated in a "stare" mode for debris data collection, *ie.*, the radar is pointed at an azimuth and elevation over a slant range extent. The earth's rotation creates a scan of space. Data are recorded whenever a preset threshold of detection S/N ratio is exceeded.

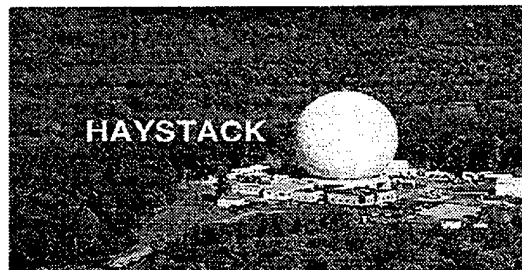


Fig. 1: Haystack Radar
[10 Ghz. X - Band Radar, 36 M. Antenna, IFOV 1 mrad,
S/N ratio of 58 dB on a 1 sq. m. target at a range of 1000 Km.]

These data are processed by NASA/JSC and result in cumulative statistics of detection as well as orbit and size characterization. One method of presenting the results is shown in Fig. 2 which is taken from Ref. 2. This figure represents the rate of detections in the Haystack beam when pointed at zenith as a function of the altitude of detection. The lower curve is a simulation of the rate for the known catalog carried by US Air Force's Space Command while the upper curve is the rate of detections processed from the Haystack data. NASA/JSC estimates that the total rate across all altitudes sampled (< 1500 Km.) is ~6.25 objects/hour.

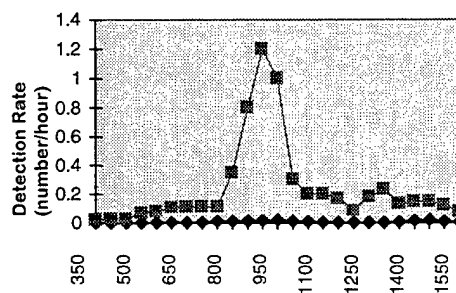


Fig. 2: Debris Detection Rate from Haystack Radar

1.2. Anomalous Debris

Most of the debris detections shown in Fig. 2 are concentrated in the altitude range between 800 Km. and 1000 Km. though there is a noticeable but smaller peak in rate of detection at ~1400 Km. The subject of this report are the debris in the 800 to 1000 Km. region. NASA/JSC has analyzed these detections extensively and concluded that (Ref. 3):

1. the debris are primarily small (< 2 cm. size) and largely spherical in shape;
2. the debris are concentrated in orbits of inclination 65° and altitudes of 900 - 1000 Km.;
3. the debris are primarily in circular orbits;

4. the debris are likely to be leaked Na-K coolant from the Bouk class of nuclear power sources of a Soviet satellite system, called RORSAT (Ref. 4) which were put into this type of orbit for long-term storage to allow the radio-activity to decay;
5. there are 50000-70000 such debris > 8 mm. in size at these altitudes and that these constitute approximately half the total debris population below 1500 Km. altitude.

This band of debris is termed "anomalous debris" in this paper because the debris density exceeded theoretical models by a large factor.

1.3. Scope of Paper

NASA/JSC funded an effort at Lincoln Laboratory to detect, track and characterize a sample set of debris in the anomalous debris band. While NASA's analysis used detection data of large numbers of debris in this band, we attempted to characterize in detail a small number of representative samples from this band using the radar and optical sensors operated by MIT Lincoln Laboratory. These sensors are located at Westford, MA, Kwajalein Atoll, Marshall Islands and White Sands Missile Range, New Mexico. The major purpose was to provide evidence supporting or contradicting the conclusions arrived at by NASA/JSC. In particular, our characterization involved the following steps:

1. Establish orbits on several debris from this band.
2. Determine the shape and size of the debris using radar data.
3. Assess the surface characteristics of the debris using visible wavelength optical data.
4. Compute the mass and density of the tracked debris.
5. Assess the state (solid/liquid) of the tracked debris.

The primary conclusion of this paper is that the properties of the debris sample tracked *are consistent with the hypothesis that they are Na-K coolant leak; and that they are likely to be in the liquid state.* The balance of this paper will describe the techniques used and individual results obtained to support this conclusion.

2. DEBRIS DETECTION

Three different strategies were used for the detection and acquisition of debris for characterization. These were:

1. Search orbits of putative parent satellites.
2. Stare and Chase using optical systems and radars.
3. Search the orbits of debris found

2.1. Orbit Search of Putative Parents

A quick assessment of the sensitivity of the Millstone radar (Fig. 3) and the putative size of the debris objects sought indicated that a new search mode needed to be created for the search. Historically the radar searches along the orbit. However, for the small objects considered here, it was better to search at a relatively low range at an elevation of approximately 30 deg.; *ie.*, search along the orbit by staring at approximately the same range and the same elevation in the orbit of an object while letting time pass. Both the Haystack and the Millstone radars modified their software to construct this search mode.

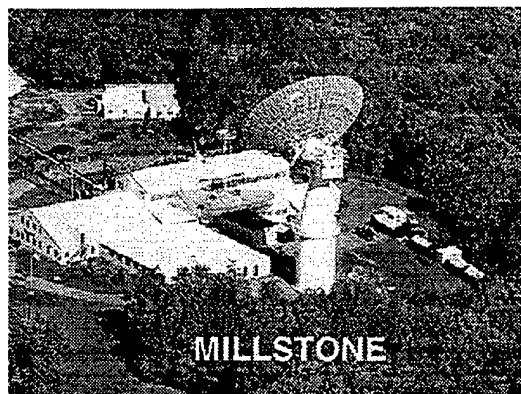


Fig. 3. Millstone Hill Radar
L-Band, 1.3 GHz., 25 m. Antenna, IFOV 8 mrad,
S/N ratio of 50 dB on 1 sq. m. target at 1000 Km.

The Millstone radar searched the orbits of ten putative parents using this technique. The search was always centered about the parent to ensure that the parent was detected and thus validate the parameters of the search. The search mode was capable of detecting a 2 cm diameter object in orbit if coherently trackable¹ and approximately a 3.5 cm size object in orbit were it trackable non-coherently. No detections resulted.

If there were any recent slow leaks of debris of the size postulated, the difference in rate of change of the right ascension of the ascending node would have been small (<0.01 deg./day). *Hence it can be positively stated that none of the parent objects whose orbits were searched had recently (within 30 days of the search) leaked any debris of size ≥ 2 cm.*

2.2. Stare and Chase - Optics and Radars

The Experimental Test System located in New Mexico (Fig. 4) is an optical system that was a proof of concept for the GEODSS. It has two 30 in. telescopes each with a FOV of $>1^\circ$ diagonal. The system uses a Vidicon camera and has a sensitivity of detection of $\sim 15.5 V_M$. The ETS conducted several stare-and-chase sessions for debris under Air Force sponsorship in 1994. The system is capable of detecting a resident space object, correlating it against the catalog and, if uncorrelated, transitioning from stare to tracking the object essentially in near-real-time (Ref. 5). ETS found one piece of anomalous debris that has been characterized extensively.

TRADEX is a L-band radar located on the Kwajalein atoll in the Marshall islands (Fig. 4). Its FOV is 0.5° . TRADEX conducted several stare and chase sessions during 1995 under NASA/JSC sponsorship. The operating principle for TRADEX is the same as for ETS. The radar points at a specific azimuth and a specific high elevation and examines a range between 500 and 1200 Km. The radar's sensitivity is such that it should detect any object >3.5 cm in diameter in this altitude range. TRADEX detected one known and one uncorrelated RSO per hour on an average (Ref. 6). The radar found four pieces of anomalous debris during its operations.

2.3. Search of Anomalous Debris Orbit Planes

If the anomalous debris were a result of the leaking of a liquid, it seemed likely that there would be many "droplets" per orbit plane. Hence the orbit planes of some of the debris pieces found by ETS and TRADEX were extensively searched with the Millstone hill radar. The sensitivity of Millstone is such that it should

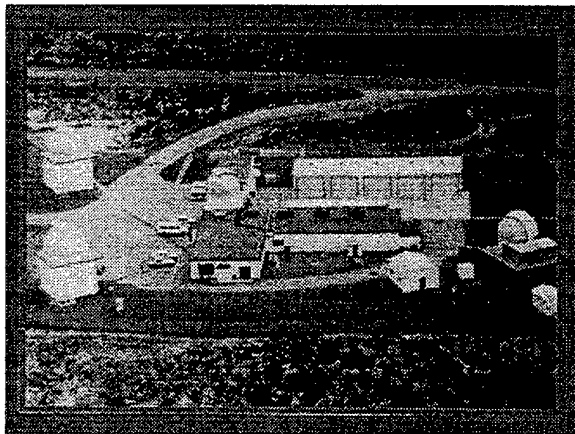
¹ The Millstone radar processes 2^N ($N < 10$) radar pulse returns together accounting for target movement during the integration interval. Were a target stable in attitude, the returns would add "coherently" yielding a combined S/N ratio of 2^N times that from a single pulse. If the target is tumbling, the returns would add "non-coherently" with a total S/N ratio of $2^{N/2}$ times that from a single pulse.

detect any metallic sphere >2 cm in diameter in the search. Millstone found six more pieces of anomalous debris.

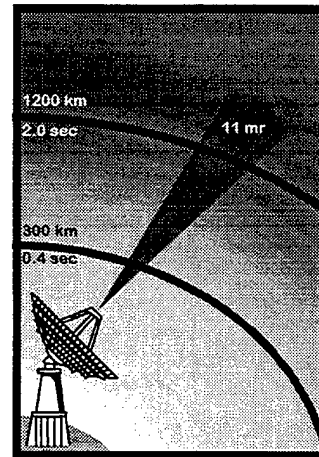
Finally, the Haystack radar searched some of the debris orbits. Haystack is the most sensitive of the radars used in this effort. It should detect debris of size >1 cm. Haystack found eight more debris objects though, unlike the eleven above, these were not completely characterized.

2.4. Results of Searches for Anomalous Debris

The purpose of this project was to characterize a sample set of anomalous debris which required finding and tracking them regularly. A "time machine" search was developed for the radars. The efficacy of the stare and chase algorithms at the



0.75 m. Telescopes with CCD Camera, IFOV 1° or 2°
Detection Sensitivity $\sim 15 - 17 \text{ m}_v$



L-Band, 1320 MHz., IFOV 8 mrad,
48 dB S/N ratio on 1 sq.m. target at 1000 Km.

Fig. 4 : ETS at White Sands Missile Base on left,
TRADEX at Kwajalein on right

radars was demonstrated. Eleven debris were found and extensively characterized. Eight more debris were found but were incompletely characterized.

A key finding is that there were multiple debris per orbit plane. This implies a common parentage and time of origin for these debris which is consistent with leaking liquid.

3. RADAR DATA ANALYSIS

Extensive data were collected with the Millstone and Haystack radars on the eleven debris found during the search. The objectives of the data collection were the following:

1. Radar signature data (radar cross-section vs. time) to assess spin period, any temporal variability and also to estimate size.
2. Polarization data (the ratio of the orthogonal polarization RCS to the principal polarization RCS) to assess the shape of the debris.
3. Metric data to support determination of accurate orbits and calculation of the area/mass ratios, mass and density of the debris.

Each of these topics will be discussed below.

3.1 Radar Signature and Polarization Data

Figure 5 is representative of the radar signature data on the debris as recorded at the Millstone radar. The radar transmits a right circularly polarized signal. The principal receive polarization (PP) is consequently left circular polarized; and the orthogonal receive polarization (OP) is right circular. The radar's tracking program dynamically selects the number of pulses integrated per signal processing cycle based on S/N ratio required for accurate metric tracking.

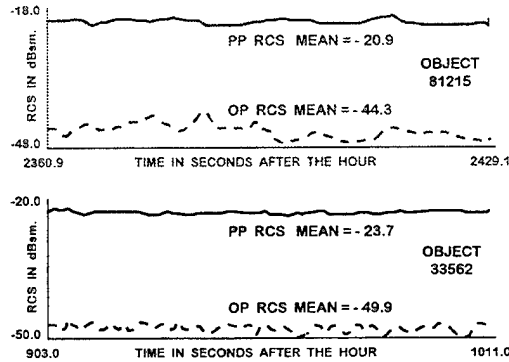


Fig. 5 : RCS signature in both polarizations of two debris

The figure shows the temporal history during a track (typically lasting 10 minutes) of the measured PP radar cross-section (RCS) for three of the debris. It is clear that the radar does not detect any temporal structure in the signal at a period longer than the integration interval which is 1 - 3 seconds. A number of tracks at a variety of aspect angles all exhibit invariant structure of the RCS at a temporal resolution of 1-3 seconds and a RCS resolution of 1dBsm. The figure also shows the temporal history of the OP RCS during the same tracks. The OP RCS is below the PP RCS by ~ -25 dB. This is quite unusual based on over 300 tracks of

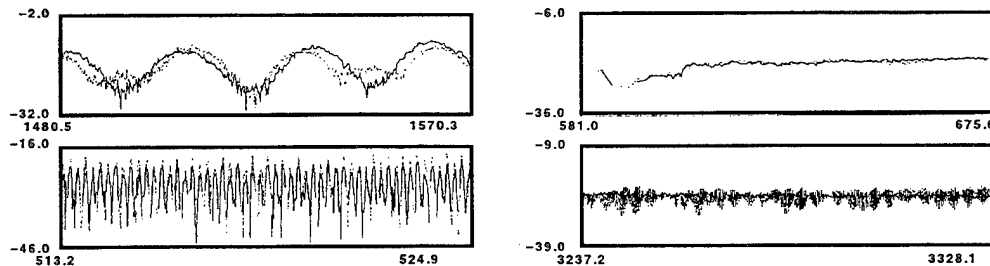


Fig. 6 : RCS signatures of typical debris at Millstone radar
[X-axis is time in secs. and Y-axis is RCS in dBsm
Solid line is PP RCS, Dotted line is OP RCS]

typical debris that have been taken by the radar. Commonly, the OP / PP ratio is of the order of a few dB and varies over tracks (Ref. 7, also see Fig. 6).

The accumulated statistics of mean PP RCS and the polarization ratio (OP RCS - PP RCS) for the eleven debris objects are given in Table 1. It is evident that, consistently, the PP RCS is < -20 dBsm, and the polarization ratio is ~ -25 dB which is close to the isolation between the PP and OP channels at the Millstone hill radar.

It is well known that the OP return from spherical objects is negligible compared to the PP return *over all aspect angles for a circularly polarized radar transmission*. Comparison of the sphere RCS signature to those of the debris leads to the conclusion that the debris objects being tracked are spherical in shape. Further, the PP RCS of the debris can be used to infer a radius of the sphere. The results are shown in Table 1 along with the formal uncertainties based on a number of tracks.

TABLE 1 : Results from Millstone Data

OBJECT NUMBER	PP RCS MEAN (dBsm)	POLRZN RATIO (dB)	SPHERE MEAN RADIUS (cm.)	STD. DEV. (cm.)
81215	-20.8	-24.2	2.84	0.09
33562	-23.6	-21.6	2.55	0.06
33609	-22.4	-23.3	2.68	0.08
33612	-22.1	-25.3	2.71	0.05
33616	-30.7	-25.1	1.94	0.09
39969	-34.3	-21.2	1.70	0.08
39970	-32.3	-25.2	1.83	0.02
39971	-21.9	-24.5	2.73	0.03
39972	-22.1	-24	2.70	0.02
39973	-25.4	-21.2	2.38	
39974	-25	-25		

A few comments are in order here:

1. The range in radius of the spheres (1.6 cm. to 2.8 cm.) represents at the lower end the detection limit of the Millstone hill radar and at the upper end perhaps the largest size of the anomalous debris detected so far.
2. The estimated sphere size to radar wavelength ratio for the Millstone radar is well in the Rayleigh region. Hence there is no ambiguity in estimating the size from the RCS. Such an ambiguity would arise if the Haystack radar with its 3 cm wavelength were used for the purpose.
3. The formal uncertainties are based on the variability of the estimated mean radar cross-section in the principal polarization channel. No calibration corrections have been applied to these values. It is believed that the RCS estimate at the Millstone radar is good to <1 dBsm generally based on frequent tracks of a large 0 dBsm sphere. The same calibration uncertainty should apply to the small spheres in question because the radar attempts to track all objects at approximately the same S/N ratio (30 - 36 dB) and, further, this high S/N ratio is achievable in the case of the small spheres because of the high sensitivity of and the low slant range from the radar.
4. It is assumed that the spheres are perfectly conducting so that the radar theory relating the size to RCS as for example in Ref. 8 applies.

3.2. Density Estimation

It is well-known that the earth's atmosphere extends beyond the 800-1000 Km. orbital altitude of the anomalous debris. Hence, with accurate metric data over many orbits, it is feasible to estimate an average area/mass ratio for the debris found in this project. Given that the debris are spherical, there is no dependence of the area/mass ratio on aspect angle. The area and volume can be calculated from the size reported in Table 1. Hence the mass and density can be computed.

The caveat in the chain of logic in the last paragraph is that the atmospheric density model at the altitudes of these anomalous debris is subject to considerable (~20%) uncertainty. This problem was solved by contemporaneous tracking of a well-characterized sphere - Lincoln calibration Sphere #4, SCC object no. 5398 - which happens to be in an orbit of similar altitude. Thus a scale factor for the atmospheric density could be estimated and used in fitting the metric data on the anomalous debris.

The metric data used came largely from the Millstone radar whose calibration is maintained extremely well. The quality of the data are shown in Table 2. The results of the procedure detailed above are shown in Table 3. It is evident that the "mean" density of the spheres is just over 1 gm/cc which is similar to that of water.

TABLE 2 : Millstone Hill Radar Data Accuracy

RCS DATA

BETTER THAN 1 dB.

METRIC DATA

RANGE : 5 METERS

ANGLES : 5 MDEG.

RANGE RATE : 10 mm/s

TABLE 3 : Mass and Density Estimates of Debris from
Millstone Tracks

Object No.	Area-Mass Ratio (cm ² /gm)	Mass (grams)	Density (gms/cm ³)
81215	0.253+0.007	100.2+9.1	1.044+0.06
33562	0.273+0.066	74.8+9.6	1.077+0.11
33609	0.225+0.011	100.2+10.8	1.244+0.10
33612	0.256+0.006	90.1+5.4	1.031+0.04
33616	0.349+0.009	33.8+4.0	1.108+0.08
39969	0.464+0.22	19.6+3.0	0.953+0.09
39970	0.545+0.043	19.3+2.1	0.752+0.07
39971	0.247	94.8	1.112
39972	0.307	74.6	0.905

"MEAN" DENSITY = 1.03 gms/cc

On the assumption that the anomalous debris are composed of Na-K, we looked up standard chemical tables for the density. The data on the Internet home page of Ref. 4 indicated that eutectic Na-K was probably used as the coolant in the nuclear power sources that were used on the Soviet satellites that are suspected to be the parents of these debris. Fig. 7 gives the variation of density of eutectic Na-K mixture with temperature drawn from Ref. 9. It is clear that the expected density of eutectic Na-K at ~300°K is 0.9 gms/cc. similar to the density of the anomalous debris given in Table 3.

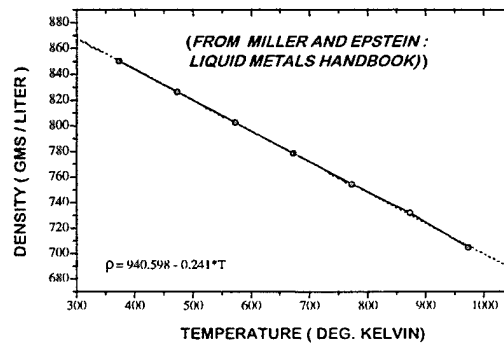


Fig. 7 : Density of Eutectic Na-K alloy vs. Temperature

3.3. Summary of Results from Radar Data Analysis

The following conclusions have been reached as a result of collection and analysis of signature, polarization and metric data from the radars.

1. The debris found and tracked exhibit without exception a polarization ratio at all aspect angles indicative of a spherical shape.
2. The debris found and tracked exhibit radii varying between 1.6 cm. and 2.8 cm.
3. The spheres have a mean density of ~1 gm./cc. consistent with eutectic Na-K at typical orbital temperatures.

4. OPTICAL DATA COLLECTION AND ANALYSIS

Earlier work (Refs. 10 - 13) has shown that some properties of the surface of debris reflecting sunlight can be derived from the analysis of photometric and polarimetric data. A photopolarimeter has been developed and fielded at the Firepond facility (Fig. 8) adjacent to the Millstone and Haystack radars.

All three sites are linked together with a real-time link such that any sensor can be driven off the pointing of any other sensor. This capability has been particularly valuable for Firepond as the photopolarimetric sensor has a narrow FOV.

Seven of the eleven debris objects have been characterized several times by the Firepond photopolarimeter. Examples of the photometric

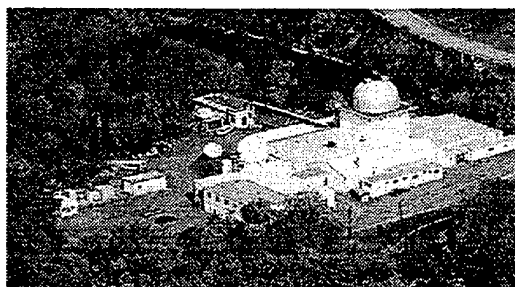
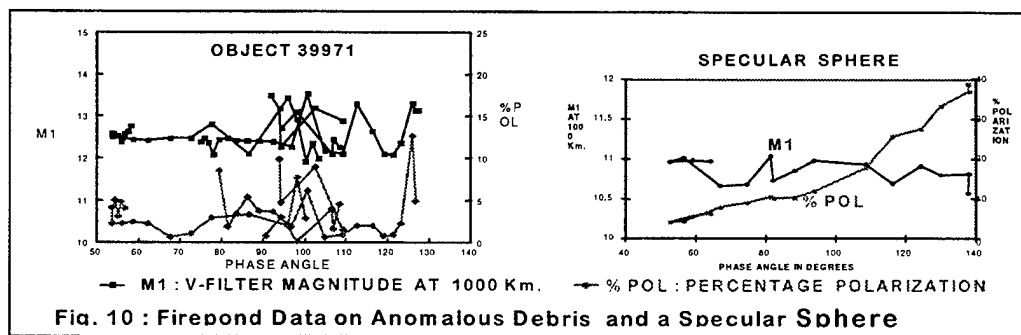
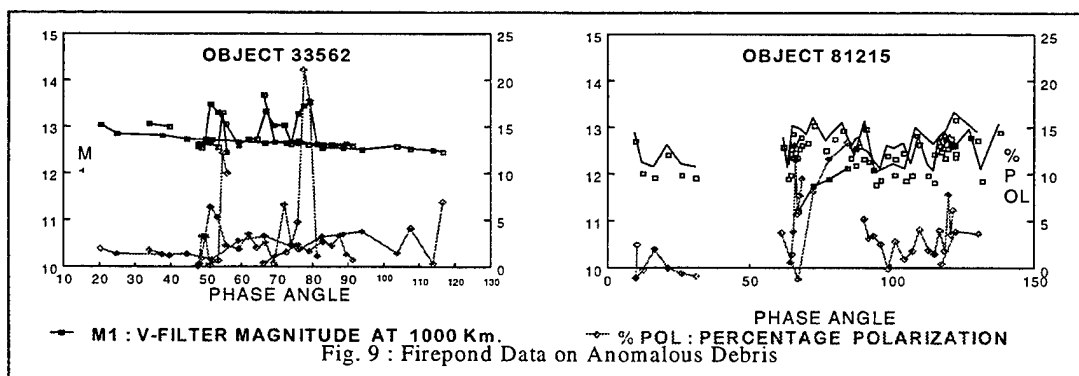


Fig. 8 : Firepond Optical Facility
1 meter optics with CCD photo-polarimeter
IFOV 1 mrad, $\sim 13 m_v$ detection sensitivity

and polarimetric signature are shown in Figs. 9 and 10. For comparison, similar data on a sphere are also shown in Fig. 10. The following conclusions can be derived from these data:



1. The photometric phase functions (ie., derived V_M at a range of 1000 Km. vs. phase angle) on all seven objects are similar to that from specular spheres. This is highly unusual as typically debris tend to have a variety of shapes and phase functions.
2. The polarization is consistently low for all these objects. There is no evidence of high polarization that would be appropriate for dielectric surfaces. Hence all these objects appear to have metallic surfaces.
3. It is possible to assign (n,k) values that characterize the reflectivity of the surface. The calculated surface reflectance from (n,k) is high (>0.8) which is consistent with a specularly reflecting metallic surface.

4. Using the fact that these objects appear to be specular spheres, we can use the average brightness (estimated V_M at 1000 Km. Range) and the reflectivity to calculate the size of the objects.

Table 4 gives the estimated M1 (V_M at 1000 Km. range) and the reflectivity of the seven objects characterized with optical data. Table 5 compares the estimated sizes of these from radar and optical data.

Table 4 : Measured M1 and Estimated Reflectance of Debris from Firepond Data

OBJECT	M1	R
33562	12.8 \pm 0.3	0.89
33609	12.5 \pm 0.2	0.84
39969	13.6 \pm 0.08	0.89
39970	13.5 \pm 0.2	0.89
39971	12.6 \pm 0.4	0.89
39972	12.7 \pm 0.3	0.89
81215	12.6 \pm 0.4	0.88

Table 5 : Comparison of Estimated Sizes : Radar and Optical Data

OBJECT NUMBER	RADAR		OPTICAL	
	MEAN	STD.	MEAN	STD.
	RADIU	DEV.	RADIU	DEV.
	(cm.)	(cm.)	(cm.)	(cm.)
81215	2.84	0.09	2.9	0.5
33562	2.55	0.06	2.6	0.4
33609	2.68	0.08	3.0	0.3
33612	2.71	0.05		
33616	1.94	0.09		
39969	1.70	0.08	1.8	0.1
39970	1.83	0.02	1.8	0.1
39971	2.73	0.03	2.9	0.5
39972	2.70	0.02	2.9	0.4
39973	2.38			

There are some features of the plots that are not yet explained:

1. There is a small variation in the photometric phase function about a mean specular sphere characteristic that could be instrument-related, medium-related or surface property related. The first cause is unlikely because the instrument is calibrated to much better than the detectable variation. The second cause is unlikely as the variation is seen over many tracks. No explanation has been found as yet.
2. There have been occasional polarimetric data points showing substantially higher polarization than normal. The cause is unknown.

5. THEORETICAL ANALYSIS

The results presented in the previous sections strongly indicate that the anomalous debris are consistent with a Na-K fluid. Given the fact that the coolant was in a liquid state in the parent spacecraft, a question arises as to its state in orbit. We computed the expected temperature of the debris spheres using the known radiation from the sun and the earth, the properties of the orbit and of Na-K. We expect the maximum temperature in sunlight to be $\sim 330^{\circ}\text{K}$ and in shadow to be $\sim 280^{\circ}\text{K}$. The melting point of Na-K mixtures as a function of the mixture ratio is shown in Fig. 11. It is evident that the anomalous debris should in general be in a liquid state. This *may* affect the computation of the area-to-mass ratio as the drag coefficient C_d has been assumed to be 2.2 which applies to solids. It is not known at the present time whether atmospheric molecular scattering from liquids is similar to that from solids. This is an open area for further research. Further, we expect that liquid droplets will deform at some natural frequency but measurement has not been done to date.

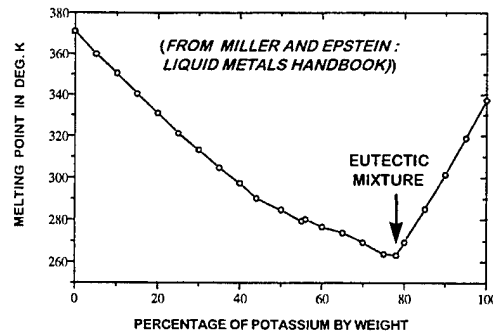


Fig. 11 : Melting Point of Na-K Mixtures

Another question is the lifetime of liquid Na-K droplets in orbit due to evaporation. This has been modeled using data available in Chemistry handbooks (Ref. 10) and our calculation show that the lifetime for a 2.5 cm. diameter sphere is > 10000 years if the debris were made of either pure Na or pure K.

A third question is the orbital lifetime of the Na-K spheres due to atmospheric drag. In particular, are these debris likely to pose a hazard to humans in space at 300-500 Km. altitudes? Given the calculated area-to-mass ratios of the detected spheres and extrapolating to 1 mm. radius debris, the orbital lifetime is well over 50 years.

6. SUMMARY

The project has demonstrated a powerful capability for remote sensing and characterization of orbital debris using ground-based radar and optical systems. A small sample from a particularly profuse debris field has been characterized with the following results:

1. The nature of the debris is consistent with leaked Na-K fluid but remote sensing done to date cannot prove this unambiguously.
2. The debris cluster in several orbit planes with many pieces of various sizes in each plane. Both of these features are consistent with a leaking liquid from a set of parents from the RORSAT set of Soviet satellite systems.
3. No recent leak has been detected. Further the last such satellite was launched in 1989. These facts would seem to indicate that the leaks occurred soon after the nuclear power sources were put into their rest orbits as inferred by NASA/JSC.
4. All the debris detected and tracked were spherical in shape with radii < 2.8 cm. The sphericity is again consistent with a leaking liquid.
5. The estimated density of the sample set is ~ 1 gm/cc which is consistent with Na-K mixture.
6. The debris are highly reflective and exhibit characteristics of specular metallic spheres - again consistent with droplets of Na-K.
7. If the debris are indeed Na-K and if, as indicated by the Russian manufacturers, it is an eutectic mixture, then the droplets are expected to be in liquid form due to heating by the sun and the earth.
8. If the debris are droplets of Na or K, the rate of evaporation is so low that their lifetimes exceed 10000 years.
9. The combination of orbital altitude and area/mass ratio is such that the orbital lifetime due to atmospheric drag is expected to exceed 50 years for even a 1 mm. size particle.

To reiterate, analysis of all the measurements done to date on the sample debris are consistent with leaking liquid Na-K but do not unambiguously prove the assertion.

7. REFERENCES

1. E.G.Sansbery *et al* : "Haystack Radar Measurements of the Orbital Debris Environment", JSC-26655, NASA/JSC Space & Life Sciences Directorate, May 20, 1994.
2. E.G.Sansbery *et al* : "Haystack Radar Measurements of the Orbital Debris Environment: 1990-1994" , JSC-27436, NASA/JSC Space & Life Sciences Directorate, 20 April 1996.
3. E.G.Stansbery *et al*: "Orbital Debris Studies Using the Haystack Radar", presented at the 1995 Space Surveillance Workshop, 29 March 1995.
4. Internet address, Russian RORSAT contacts, <http://www.rssi.ru/ippe/general/spacer.html>.
5. Private communication.
6. Ray LeClair, et al: "Improvements in TRADEX Debris Capabilities", presented at the 1996 Space Surveillance Workshop, 3 April 1996.
7. R. Sridharan, "Characteristics of Debris and Implications for Detection and Tracking", AAS 96-117, presented at the AAS/AIAA Space Flight Mechanics Meeting, Austin, Texas, 12-15 February 1997.
8. Radar Cross-Section Handbook, Editor: George T. Ruck, Plenum Press, New York – London, 1970.
9. R.R. Miller in, Liquid Metals Handbook, Sodium (NaK) Supplement, C.B. Jackson (ed.), Atomic Energy Commission and the Dept. of the Navy, 1955.
10. Smithsonian Physical Tables, W.E. Forsythe (ed.), Smithsonian Institution, Washington, DC, 1964.
11. Private communication.
12. Private communication.
13. Private communication.

Radar Measurement Campaigns in Europe

R. Jehn (European Space Operations Centre, Darmstadt, Germany), D. Mehrholz, L. Leushacke (Research Establishment for Applied Sciences (FGAN), Wachtberg-Werthhoven, Germany)

Introduction

This paper presents an overview on radar measurement campaigns which are made with FGAN's Tracking and Imaging Radar (TIRA) at Wachtberg-Werthhoven, Germany. The purpose of these campaigns are to measure the space debris environment and to validate the Meteoroid and Space Debris Terrestrial Environment Reference (MASTER) model.

First a description of TIRA is given. For space debris observations TIRA is mainly operated in two different modes: In a tracking mode and in a beam-park mode of operation. Methods and algorithms were developed to analyse raw radar data, to compute radar images, and to estimate physical characteristics of space objects like size, shape, attitude, orbit, mass and material composition.

Then two 24-hour experiments will be described. One was performed on 13/14 December 1994 and the second one on 25/26 November 1996. In December 1994 during a 24-hour extended staring experiment 350 GByte of radar data was collected. TIRA (located at about 51° N latitude) has a field-of-view of 0.5°. It was staring at a fixed direction towards the North with an elevation of 80° and the slant range spanned from 150 to 4050 km. This was the first time in Europe that such measurements were made.

On 25/26 November 1996 a 24-h cooperative beam-park experiment (COBEAM-1/96) was performed where the FGAN L-band radar transmitted (and received) at 1.33 GHz and the Max-Planck-Institute for Radioastronomy (MPIfR) radio telescope located at Bad-Münstereifel-Effelsberg (20 km distance to the FGAN radar) received the echos. Due to the large 100-m antenna of MPIfR the sensitivity of the experiment was enhanced as compared to the first experiment. Objects as small as 0.9 cm were detected.

TIRA's L-band radar detection performance

The Research Institute for High Frequency Physics (FHP) of the German *Forschungsgesellschaft für Angewandte Naturwissenschaften* (FGAN) is operating a high power radar system. It consists of two monostatic coherent radars supported by one 34-meter parabolic antenna: a narrowband L-band tracking radar and a high resolution Ku-band imaging radar. Both radars may operate simultaneously on the same object.

The performance of both radars are to be seen in Fig. 1. The dashed line shows the performance of the L-band radar before the recent modifications which were implemented in

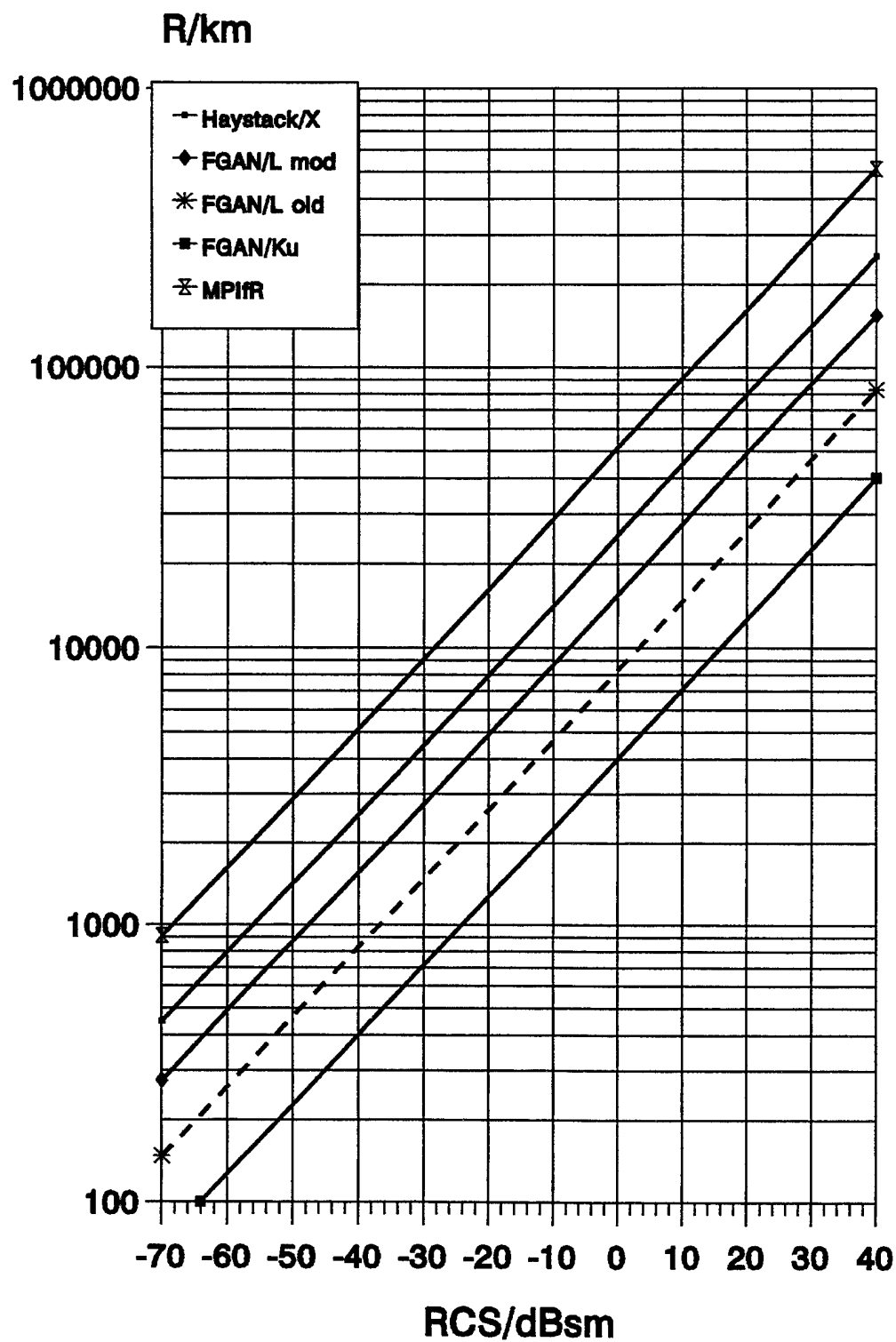


Figure 1: Radar detection performance of FGAN/Effelsberg system (top curve), Haystack/X-band (second curve), upgraded FGAN/L-band (third curve), previous FGAN/L-band (dashed curve), and FGAN/Ku-band (bottom curve).

the course of an ESA study "Advanced Radar Techniques for Space Debris Detection". An object with a RCS of -50 dBsm could be detected at a distance of 500 km. -50 dBsm at L-band corresponds to a perfectly conducting sphere of about 2 cm diameter, as it can be seen in Fig. 2. As it was demonstrated during the ODERACS experiments, 5 cm spheres with -24 dBsm were tracked at a range of 2000 km.

During 1995/1996 the following modifications were implemented:

- L-band receiver: new low noise amplifiers with 0.3 dB noise figure were moved forward to the receiver front end and directly connected to the switched limiters,
- L-band transmitter: two modulation decks were reconstructed in order to operate the transmitter at higher peak power levels (increase from 1 MW to about 2.5 MW) with reduced interpulse noise.

The performance of FGAN's upgraded L-band radar can be seen in the middle curve of Fig. 1. Spheres of 2 cm diameter (-50 dBsm) can be detected at a distance of 900 km and 5 cm spheres (-24 dBsm) at 4000 km. The modifications roughly doubled the range where objects can still be detected.

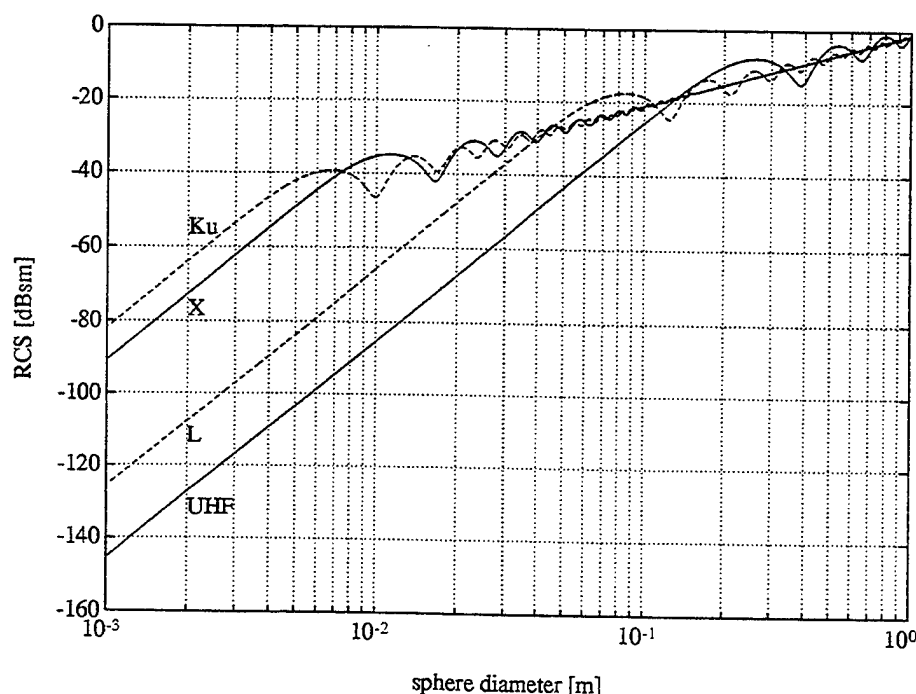


Figure 2: Radar cross section (RCS) of perfectly conducting spheres as function of sphere diameter; parameter are four different radar carrier frequencies: UHF (430 MHz), L-band (1333 MHz), X-band (10 GHz), and Ku-band (16.7 GHz).

Beam-Park Experiment 1/94

Between 13. Dec. 1994, 8:00 UTC and 14. Dec. 1994, 8:00 UTC the first European radar campaign for space debris observation was performed. The TIRA L-band radar was in beam-park mode pointing North at an elevation of 80° and an azimuth of 0° . The Fylingdales phased array radar (UK) was operating simultaneously for 24 hours pointing South-East in order to have an overlapping observation volume. Two optical stations at Zimmerwald (Switzerland) and Herstmonceaux (UK) were also involved. At Herstmonceaux observations were made during about 3 hours in the evening and morning (looking East towards the common observation volume). However at Zimmerwald, the observation conditions did not allow to make measurements.

At FGAN, a total of 350 GByte of data were collected and stored on Ampex tapes. Only a part of that data, a selected *processing window* was analysed. The processing window extends in range from 560 to 1460 km and in range rate from -11.3 to 11.3 km/s. From the three channels, sum (Σ), delta-elevation (Δ_E), and delta-transverse (Δ_T), 9.6 million pulse periods were processed. With a fixed 32-pulse incoherent integration, 1/4-shift range gating and 1024-FFT Doppler filter, and setting a 3 dB threshold/noise ratio, the total number of threshold crossings was 67 600. After post-processing a total of 255 detections remained, 72 of them could be identified in the USSpaceCom catalogue.

The results of that experiment were mainly used to gain experience in such radar campaigns, especially the data handling, data post-processing and development of target detection algorithms. The ultimate objective which is to validate the ESA MASTER model was the goal of the next experiment: COBEAM-1/96.

COBEAM-1/96

On 25/26 November 1996 a 24-h cooperative beam-park experiment was performed where the FGAN L-band radar transmitted (and received) at 1.333 GHz and the Max-Planck-Institute for Radioastronomy (MPIfR) radio telescope located at Bad-Münstereifel-Effelsberg received the echos. In Fig. 3, the configuration of the two systems is depicted. As it can be seen in this figure the two beams were completely overlapping from an altitude of 750 to 980 km altitude. This volume was observed from 25 Nov. 1996, 11:30 UT until 26 Nov. 1996, 12:00 UT.

The observation parameters of this experiment are summarized in Table 1.

The upper curve of Fig. 1 shows the detection performance at the 100-m telescope at Effelsberg. At a range of 900 km objects as small as -70 dBsm can be detected. This corresponds to a size of 9 mm (see Fig. 2). Since the data analysis is still going on at the time of the production of this report, only some preliminary results can be reported here. More results will be presented at the Space Control Conference itself.

	Parameter	TIRA	Effelsberg
Centre of observation volume (COV)	h_{cov}	850 km	850 km
	R_{cov}	875 km	880 km
	El_{cov}	76.12°	75.00°
	Az_{cov}	93.00°	90.00°
Antenna beam	3dB beam width	0.5°	0.165°
Radar transmitter	Frequency	1.333 GHz	
	Peak power	1.6 MW	
	Pulse length	1 ms	
	Pulse period	27 ms	
Receiver	Channels	$\Sigma, \Delta_E, \Delta_T$	LCP, RCP
Data collection unit data window	Range	575 - 1175 km	705 - 1055 km
	Range rate	± 11 km/s	± 11 km/s
Tracking Filter	Range	800 - 950 km	
	Range rate	-0.5 km/s ± 56 m/s	

Table 1. COBEAM-1/96 observation parameters

From visual inspection of the monitor of the data collection unit, which displayed a range of 875 to 1025 km (altitude of 845 - 990 km) and a range-rate interval of ± 7 km/s a total of 67 detections were counted. 16 of them could be correlated to catalogued objects and 51 detections could not yet be identified.

Comparison with the MASTER model

ESA has developed in recent years the ESA MASTER (Meteoroid And Space debris Terrestrial Reference) model which is a mathematical model describing the debris population. Past breakups are simulated, the fragments are propagated to the reference epoch of 1 April 1996 and the number of simulated objects are adapted to the latest observations by LDEF, EuReCa, a solar array of the Hubble Space Telescopes or by radars. The MASTER model together with application software will be available on CD. The software allows to calculate the impact flux on a target surface in a user defined orbit as function of azimuth, elevation, true latitude, impact velocity, origin of impactor, etc.

However, still a lot of uncertainties remain, especially in the size range from 1 to 50 cm. The European capabilities do not allow to check the accuracy of the MASTER model in all altitude, latitude and size regimes. However, the FGAN L-band radar can be used to make point-checks of the MASTER model down to a size range of 2 cm and even down to 1 cm if combined with the Effelsberg radio telescope data.

The "radar option" of the MASTER model allows to estimate the number of detections per hour for radar beam-park experiments. Some simplifying assumptions had to be made in order to calculate the detection rates:

- The sensitivity of the radar beam is homogeneous within the 3dB field-of-view and zero outside (i.e. sharp cut-off at the 3dB boundary).
- The detection rates given below correspond to single-pulse detection.

With these assumptions the MASTER model predicts about 10.5 detections per hour at FGAN (in the altitude band of 700 to 1000 km) and about 8 detections per hour at Effelsberg in the smaller overlap volume. Fig. 4 shows the detection rates predicted by MASTER for FGAN and in Fig. 5 for Effelsberg.

References

1. L. Leushacke, D. Mehrholz, D. Perkuhn, H.G. Peters, "Radar Detection of Mid-Size Space Debris", Final Report of ESOC Contract No. 10182/92/D/IM, FGAN, Wachtberg-Werthhoven, Germany, Nov. 1994.
2. D. Mehrholz, "Radar Detection of Mid-Size Debris", Advances in Space Research, Vol. 16, No. 11, 1995.
3. E.G. Stansbery, D.J. Kessler, M.J. Matney, "Recent Results of Orbital Debris Measurements From the Haystack Radar", 33rd Aerospace Science Meeting, AIAA 95-0664, Reno, Nevada, Jan. 9-12, 1995.
4. R. Reynolds, M. Matney, "A Comparison of Haystack Radar Data Measurements with EVOLVE Debris Environment Predictions", IAA-95-IAA.6.3.08, 46th Int. Astronautical Congress, Oslo, Norway, Oct 2-6, 1995.
5. E.G. Stansbery et al., "Haystack Radar Measurements of the Orbital Debris Environment; 1990-1994", JSC-27436, Houston, TX, 20 April 1996.
6. H. Kaiser, R. Jehn, "Determination of Rough Orbital Elements From Radar Data in Beam-Park Mode", MAS Working Paper No. 377, ESOC, Darmstadt, Jan. 1996.
7. R. Jehn, P. Staubach, "Optimum Search Volume for the Experiment COBEAM 1/96", MAS Working Paper No. 385, ESOC, Darmstadt, Oct. 1996.
8. H. Sdunnus, "Meteoroid and Space Debris Terrestrial Environment Reference Model", Final Report of ESOC Contract No. 10453/93/D/CS Technical University of Braunschweig, IfRR, Braunschweig, Germany, July 1995.
9. H. Klinkrad, W. Flury, H. Sdunnus, D. Rex, "Use of Debris Measurement Data for Verification and Improvement of ESA's MASTER model", 1st Int. Workshop on Space Debris, Moscow, Russia, Oct 9-11, 1995.

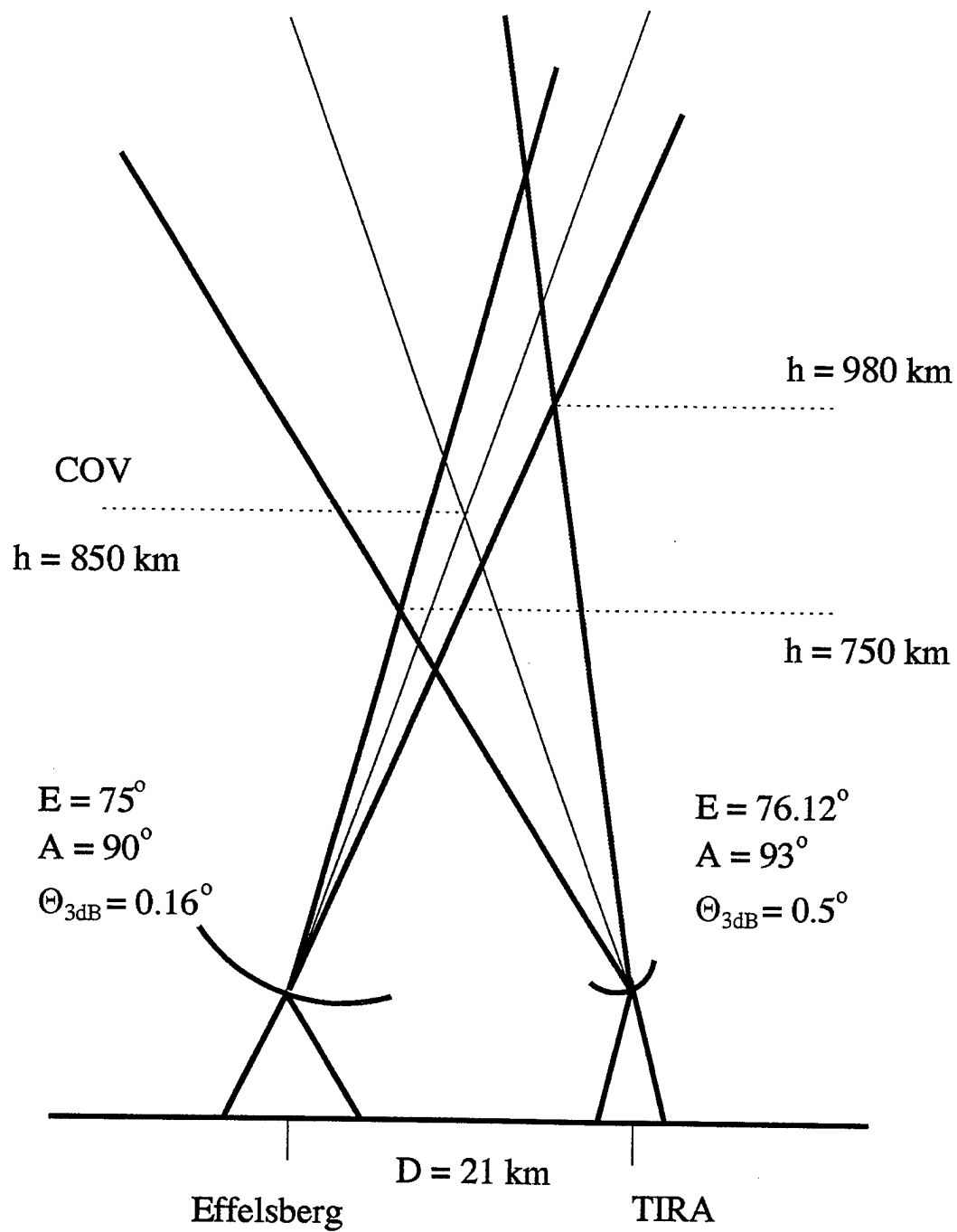


Figure 3: Overlap volume: FGAN and Effelsberg antenna pointing geometry

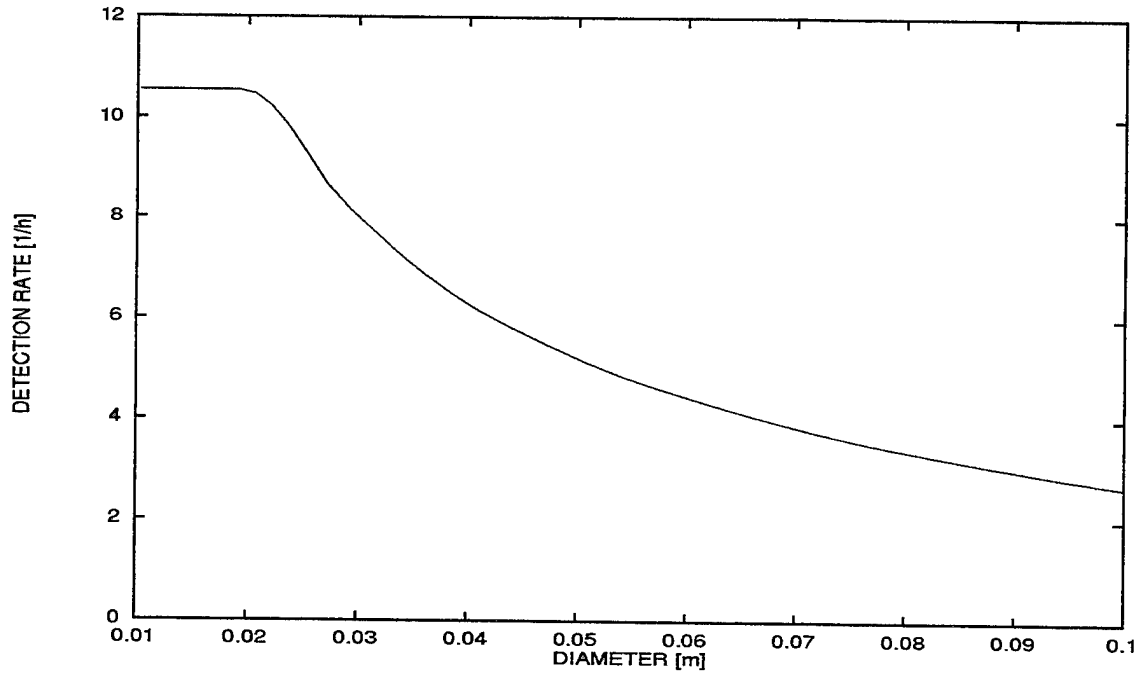


Figure 4: Hourly rate of detected objects between 700 and 1000 km with the FGAN L-band radar as function of object diameter (predictions by the MASTER model).

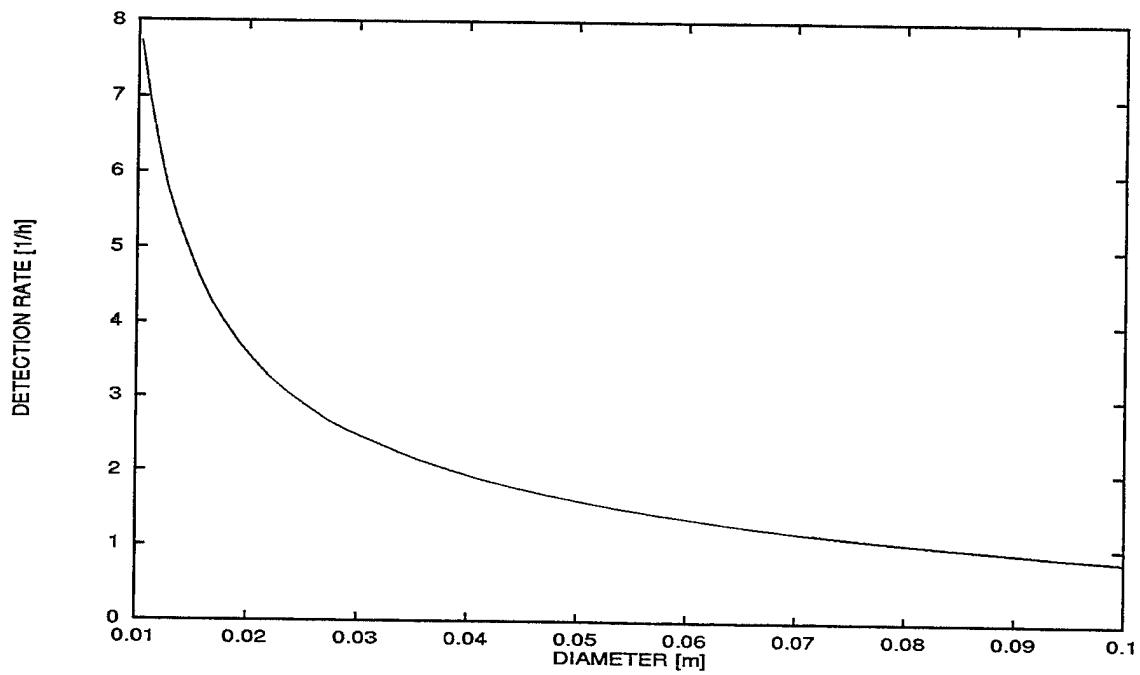


Figure 5: Hourly rate of detected objects in the overlap volume of the Effelsberg receiver beam and the FGAN transmitter beam (predictions by the MASTER model).

CALIBRATING THE NAVAL SPACE SURVEILLANCE FENCE USING SIMULTANEOUS SATELLITE LASER RANGING DATA

by

G. Charmaine Gilbreath (U. S. Naval Research Laboratory),
Paul W. Schumacher, Jr. (U. S. Naval Space Command),
Mark A. Davis (Allied Signal Technical Services), and
Edward D. Lydick (U. S. Naval Space Command)
John M. Anderson (U.S.A.F. Starfire Optical Range)

ABSTRACT

An experiment is described in which the NAVSPACECOM Fence Receivers are calibrated using Satellite Laser Ranging. We believe these are the first results presented using this method of calibration and they show the feasibility of the method as well as illustrate the powerful potential as a sensor diagnostic using this approach.

I. Introduction

This paper describes an experiment conducted with the NAVSPACECOM "Fence" and the Naval Research Laboratory's satellite laser ranging system integrated on the 3.5 meter telescope at the USAF Phillips Laboratory Starfire Optical Range (NRL@SOR). The purpose of the experiment was to show feasibility of methodology for external calibration of the receiver sensors.

Precision ephemerides for known objects were derived using SLR data from NRL@SOR as well as from other SLR sites located globally. Positions were then interpolated from the ephemeris at the times of the crossing of the Fence and at Elephant Butte in particular. This method of calibration was compared to a "direct method" where position was derived directly from SLR range and angle data obtained simultaneously with Fence crossings. Such a comparison of techniques was made possible by the proximity of NRL@SOR to Elephant Butte. Elephant Butte is located approximately 100 miles from NRL@SOR and enabled consideration of co-location issues of sensor to calibrator, as well.

Results presented will show the extent to which the Fence can be calibrated using "truth" ephemeris and post processing as well as in real-time using simultaneous range and angle data from an SLR site nearly co-located with a Fence receiver. To our knowledge, this is the first such data presented on this subject and provides the first comprehensive insight into error trends in the receiver system with significant increase in precision by the reference calibrator.

II. The Fence

The Naval Space Surveillance sensor system (NAVSPASUR Fence) operated by Naval Space Command is a continuous-wave multi-static radar deployed along a great-

circle arc across the southern United States.. This system has come to be known as "The Fence". Figure 1 shows the facilities located across the United States. The Fence provides real-time unalerted detection and metric observations for a majority of the near-Earth space object population and many high-altitude objects. The Fence detects essentially all near-Earth satellites having orbital inclinations of 30 degrees or greater. It currently records more than 80,000 station-satellite passes, and forwards more than 18,000 triangulated satellite positions to the Space Control Center (SCC) at Cheyenne Mountain, daily. The yield provides data on a majority of objects in the total space catalog.

The system is a continuous-wave multi-static radar interferometer consisting of three transmitters and six receivers located across the southern United States. The Fence uses interferometry to measure direction cosines giving the apparent angular position of space objects. A basic geometric description is illustrated in Figure 2 where cosine θ is defined in terms of the baseline orientation of the antennas.

The main transmitter radiates at the single frequency of 216.980 MHz, while the two auxiliary transmitters radiate at 216.970 and 216.990 MHz, respectively. The receivers are designed to detect signals that are Doppler-shifted by up to 15 kHz from the center frequency. By design, the transmitter and receiver beams are confined near an Earth-fixed great-circle plane inclined at about 33° to the equator, forming a radar Fence. The station locations span a 35° arc of longitude between 243° and 278° east. Coverage of satellite passes between these limits is assured for near-Earth orbits having inclinations above 33° . Over the Atlantic and Pacific Oceans, coverage is altitude-dependent because of horizon limitations, but does extend to orbits of lower inclination. Though its strength is in detection of near-Earth satellites, the system routinely makes detections at slant ranges of more than 25,000 kilometers and occasionally at ranges of more than 40,000 kilometers, giving it wide coverage in both altitude and longitude.

The primary system observables are values of east-west and north-south direction cosines measured nearly simultaneously at each of the six receiver stations. The system accuracy is among the best for high-volume space surveillance sensors. Specifically, the standard deviation of east-west cosine residuals, reckoned over the entire catalog, is less than 0.0002 rms, and it is known that orbit model errors contribute substantially to these residuals. Additionally, the system produces estimates of Doppler shift, Doppler rate and cosine rates as by-products of the primary data reduction. A more complete discussion can be found in Reference (1).

The cosine data can be triangulated, producing estimated position values, and for practical operational reasons this is done when NAVSPACCOM reports observations to the SCC. However, for updating the orbital elements, it is better to use the angles-only data themselves. The direction-cosine data are available at NAVSPACCOM where they are used for the Alternate Space Control Center (ASCC) catalog maintenance, while the SCC uses the triangulated positions in an azimuth-elevation-range format that is compatible with data from other radars in the space surveillance network.

III. Satellite Laser Ranging

Satellite Laser Ranging (SLR) is a well-known technique which can provide independent positions to centimeters for objects whose surface geometries are well known and for which orbits are well sampled. SLR uses direct detection in the optical

regime to time-tag the two way range to a given satellite. This value is then corrected for system errors and combined with range data from other sites. The ensemble of data is then reduced and analyzed using orbit determination models. NASA's GEODYN uses a batch least squares method and when the orbit is sampled properly, can produce position estimates on the order of centimeters (2). Figure 3 illustrates the technique.

In March, 1995, first returns were obtained from a new high precision SLR station for the DOD. NRL integrated a 300 mJ, 250 ps, 10 Hz, doubled-YAG system on the 3.5 meter telescope at the USAF Phillips Laboratory Starfire Optical Range (NRL@SOR). This capability presents an extremely robust link. The energy-area figure-of-merit for NRL@SOR is 2.88, which is 65 times greater than the NASA MOBLAS systems. Precisions to LAGEOS, a satellite used by the international community for geoscience and calibration, are on the order of 2 to 3 mm one sigma RMS, and accuracy is on the order of less than one cm, one sigma RMS.

This powerful capability can provide data for precision orbit estimation for spacecraft spanning ranges from 400 to 40,000 km. Specifically, returns from spacecraft as high as 22,000 km have been routinely obtained. Tracking and acquisition agility has been demonstrated against s/c as low as 380 km, enabling successful ranging against the German satellite, GFZ.

IV. CALIBRATION ISSUES

Currently, the cataloged element sets may be in error by kilometers because of the simplified orbit models used to update the catalog in real-time. Reckoned against the whole catalog, the cosine residuals usually fall in the neighborhood of 0.0002 RMS, with biases almost an order of magnitude smaller. However, because the Fence is a major contributor to the total observation base for the space catalog, the catalog residuals cannot form the basis for metric calibration. A rigorous calibration technique should use an independent data type that is at least an order of magnitude more accurate and precise than the Fence measurements.

A type of internal calibration is routinely performed at the Fence receiver stations. Every 30 minutes, a locally generated reference signal is injected into the receiver electronics downstream of the antennas themselves but ahead of the signal processing electronics. The signal simulates the antenna phases for a zenith pass of a satellite. By processing this calibration signal through the receiver electronics and interferometric algorithms, cosine variances can be derived which reflect the error contributions from these sources. Typically, these internal calibration cosine variances are about 0.00001, a value approximates the fixed error or "noise floor" of the current Fence equipment. The disparity between this internal calibration value and the nominal value of 0.0002 RMS quoted above represents the orbit model prediction error and the measurement errors due to space environmental effects along the propagation path as well as antenna and cable physical variations. Consequently, the internal cosine variance also represents a bound on the improvement that can be expected from an external calibration of the existing equipment against high-precision reference orbits and independent tracking data.

It is well known that reference orbits can be determined to a precision of centimeters for selected satellites when sufficient SLR observations are available. The internal Fence cosine variance is on the order of 10 microradians of angle or more, which is about 10 meters of position at a range of 1000 kilometers. Clearly,

reference orbits accurate to less than 10 meters can serve as a useful Fence calibration method. It is also of interest to know what level of cosine precision could be assessed by a comparison against simultaneous SLR data without a reference orbit being generated. For this purpose we have derived simple analytical formulas giving upper bounds on the cosine variance in terms of variances in the SLR range, elevation and azimuth measurements, as well as the variances in station location. In the general case when the SLR station and the Fence station are not co-located, and considering the worst possible error correlations from pass geometry, the upper bound is:

$$\text{Var}(\cosine \theta) = (1/\rho_f)^2 \{ 9 * [(\delta\rho_{slr})^2 + (\rho_{slr})^2 (\delta\varepsilon_{slr})^2 + (\rho_{slr})^2 (\delta\Psi_{slr})^2] + (\delta R_{slr})^2 + (\delta R_f)^2 \} \quad (1)$$

where $(\delta\rho_{slr})^2$ is the SLR range variance, $(\delta\varepsilon_{slr})^2$ is the SLR elevation variance, $(\delta\Psi_{slr})^2$ is the SLR azimuth variance, $(\delta R_{slr})^2$ is the SLR station position variance, and $(\delta R_f)^2$ is the Fence station position variance.

The SLR data with given variances can be expected to resolve cosine errors of this variance at least. In some cases, more accurate assessments can be made if the pass geometry and other factors are favorable. In the special case when the SLR station and the Fence station are co-located, a less conservative upper bound can be derived:

$$\text{Var}(\cosine \theta) = (1/\rho_f)^2 [(\delta\rho_{slr})^2 + (\delta R_{slr})^2 + (\delta R_f)^2] + (\delta\varepsilon_{slr})^2 + (\delta\Psi)^2 \quad (2)$$

In the previous equation, the factor of 9 multiplying SLR variances arose from worst-case correlations due to the baseline between the two sites. In the co-located case, the opportunity does not arise for such geometrical correlations to degrade the results, and the factor reduces to unity. Also, the slant range from the laser is approximately the same as the slant range from the Fence station. The result is that in this experiment, the co-located case approximates the actual situation for SOR and Elephant Butte: these two sites differ by less than 1 degree of longitude and 2 degrees of latitude. But the other stations may have slightly larger variance bounds. In both the general and co-located cases, and for all Fence stations, the contributions from the SLR angles dominate the cosine variance bound. It is apparent that collocating the laser with the site to be calibrated is desirable but not mandatory, if the SLR data is precise enough. For example, using nominal standard deviations of 2 cm in range, 5 microradians in both angles, 0.1 m in laser location and 2 m in Fence station location, together with 1000 km slant ranges, cosine errors on the order of 0.00002 in standard deviation might be resolved, for the non-co-located case. Co-location might improve this figure by a factor of three.

V. THE EXPERIMENT

NRL@SOR is located within 100 miles of Elephant Butte, where one of the Fence's most sensitive Fence receivers is located. This circumstance allows calibration using SLR measurements which are simultaneous with Fence crossings for satellites which orbit over a large range of altitudes. As shown in Figure 4, the proximity of these sites enables a comparison of the post-processed ephemeris method with the direct method of determining position using SLR range and telescope angle data only.

A total of 44 simultaneous SLR and Fence passes were obtained over the DOY 304 - 322, 1996, inclusive. Data in this paper was evaluated over DOY 318 - 322 (13 - 17 November), inclusive. Data was taken for a number of satellites, a subset of which are presented in this paper.

Fence Crossings and SLR data evaluated in this paper were correlated on satellites described in Table I.

**Table I. Spacecraft and SLR/ Fence Crossings from
13-17 November 1996**

S/C	Sat. No.	Ht (km)	Inclin. (°)	Eccen.	No. of SLR/Fence Passes
TOPEX	22076	1336.8	66.04	.00049	4
LAGEOS I	8820	5883.3	109.9	.00446	1
LAGEOS II	22195	5946.2	52.6	.01371	3
GPS 35	22779	20172.6	54.3	.00121	2

For a given crossing, a number of Fence receivers obtained data. Number of passes Fence-site-by-Fence-site are listed in Table II.

Table II. Fence Crossings Per Site from 13-17 Nov. 1996

S/C	San Diego	Elephant Butte	Red River	Silver Lake	Hawkins- ville	Tattnal	TOTAL
TOPEX	41	43	35	44	37	39	239
LAGEOS I	10	12	10	10	11	10	63
LAGEOS II	11	11	11	8	13	10	64
GPS 35	3	3	4	2	4	3	19

VI. RESULTS AND DISCUSSION

For this experiment, the SLR measurements were used in two different ways to produce a calibration reference for the Fence data. As previously noted, ephemeris solutions for the spacecraft listed were derived using GEODYN using data available from all stations, including NRL@SOR. The positions were then found based on interpolated times corresponding to the Fence crossings. At the times of the

SLR/Fence crossings, an ecf ephemeris point based on this fit was used to generate cosine residuals using SLR ephemeris as "computed" and Fence data as "observed".

For the "Direct" method, the SLR data taken at NRL@SOR simultaneously with the Fence observations and compared directly with the Fence data. Positions were estimated using experimentally measured range and angle data from Starfire and compared to the positions estimated using the Fence angle-angle data.

Tables III and IV present the sample means and standard deviations of the East-West (EW) and North-South (NS) cosine residuals reckoned against both the ephemerides and the simultaneous SLR data. In every case except one, the cosine precisions are better than the nominal 0.0002 figure from catalog-based statistics.

TABLE III. Cosine Residuals Computed from SLR Ephemeris-Based "Truth" for All Fence Receivers : 13-17 Nov. 1996

Spacecraft	EW mean	EW std.dev.	NS mean	NS std.dev.
TOPEX	.0000353	.0001708	-.0000189	.0002697
LAGEOS I	-.0000398	.0001426	-.0000379	.0001147
LAGEOS II	.0001486	.0010631	-.0000538	.0003343
GPS 35	-.0000677	.0001646	-.0000830	.0001187

TABLE IV. Cosine Residuals Computed from Simultaneous SLR & Fence Data for All Fence Receivers: 13-17 Nov. 1996

Spacecraft	EW mean	EW std.dev.	NS mean	NS std.dev.
TOPEX	.0000424	.0001574	-.0001083	.0001902
LAGEOS I	-.0000462	.0001374	-.0000053	.0001219
LAGEOS II	-.0000007	.0001348	-.0000566	.0001136
GPS 35	-.0000540	.0001647	-.0000857	.0001222

These results show that using the SLR-determined ephemeris computed from data available through the CDDIS system for satellites that pass through the Fence at a given time to compute residuals, can provide a very reliable and easily assessable means to calibrate the Fence sensor system.

A comparison between the two tables indicates very little difference in precision using the simultaneous SLR/Fence sensor technique. The advantage of the latter methodology is that it is simple to derive (position is estimated using measured SLR range and angle data), and fast, lending itself to potentially real-time calibration.

Tables V and VI present similar results receiver-by-receiver for a given satellite. Data for TOPEX has been selected as an example. The data set shows that the method can be a powerful, potentially real-time, tool to assess error trends for a given sensor.

Table V. Ephemeris-Based Cosine Residuals Per Fence Receiver for TOPEX: 13-17 Nov. 1996

Fence Rcvr.	EW mean	EW std.dev.	NS mean	NS std.dev.
San Diego	.0000613	.0001196	-.0000462	.0001897
Elephant Butte	-.0000205	.0001597	-.0000617	.0003491
Red River	.0001975	.0000723	.0002121	.0001843
Silver Lake	.0001227	.0001108	-.0000764	.0001743
Hawkinsville	-.0001932	.0001653	-.0001197	.0003558
Tattnal	.0000418	.0000726	.0000100	.0001548

Table VI. Cosine Residuals from Simultaneous Data Per Fence Receiver for TOPEX: 13-17 Nov. 1996

Fence Rcvr.	EW mean	EW std.dev.	NS mean	NS std.dev.
San Diego	.0000672	.0000609	-.0001682	.0001076
Elephant Butte	.0000111	.0000893	-.0001900	.0002629
Red River	.0001899	.0000674	.0001528	.0000939
Silver Lake	.0001415	.0001096	-.0001826	.0001281
Hawkinsville	-.0001714	.0001703	-.0001515	.0001696
Tattnal	.0000472	.0000745	.0000428	.0000920

At this writing, data was analyzed using five days of the 19-day span of the experiment; thus, the results presented here do not have high statistical confidence. Not clear at this stage of the analysis, for example, are the conditions under which co-location of the sensor and calibrator contributes significantly to accuracy. This important question requires analysis of the full body of data and is the subject of future work.

Nevertheless, a consistent and interesting picture of Fence performance emerges. As previously mentioned, more data analysis is in progress. Limited though it is in some respects, the entire data set from this experiment represents the most extensive comparison ever done between actual Fence data and high-precision external reference data. In fact, data indicates that the Fence is performing better than the traditional performance measures indicate.

A basic result of this experiment was that directly comparing Fence data and SLR data is feasible in practice and that it can be done precisely enough to establish a useful calibration of the Fence data. Furthermore, a direct comparison is easier for analysts to implement once the data is taken than is a comparison against ephemerides, because no orbit determination is involved. However, this methodology requires tasking the SLR calibrator to obtain data at specific Fence crossing times.

The data from this experiment can also help answer some important questions related to Fence operations. For example, could the current Fence data support more accurate cataloged orbit solutions if a more accurate orbit model were used? Can the residual statistics for cosines (or other Fence observables) be used to diagnose equipment problems at individual stations? To what extent should the calibrator and the Fence sensor be co-located to obtain meaningful result? These and other

questions show the need for on-going analysis of the type demonstrated in this experiment and are the subject of future work.

ACKNOWLEDGEMENTS

The authors would like to acknowledge the teams at the USAF Phillips Laboratory Starfire Optical Range and NRL for their dedicated efforts to collect the data that made this paper possible.

VII. References

1. Daniel Solomon, "NAVSPASUR Direction Cosine Processing", NRL Internal Report, available at NAVSPACECMD, August 31, 1990.
2. John J. Degnan, "Millimeter Accuracy Satellite Laser Ranging: A Review", *Contributions of Space Geodesy to Geodynamics: Technology Geodynamics*, 25, 133-161, 1993.

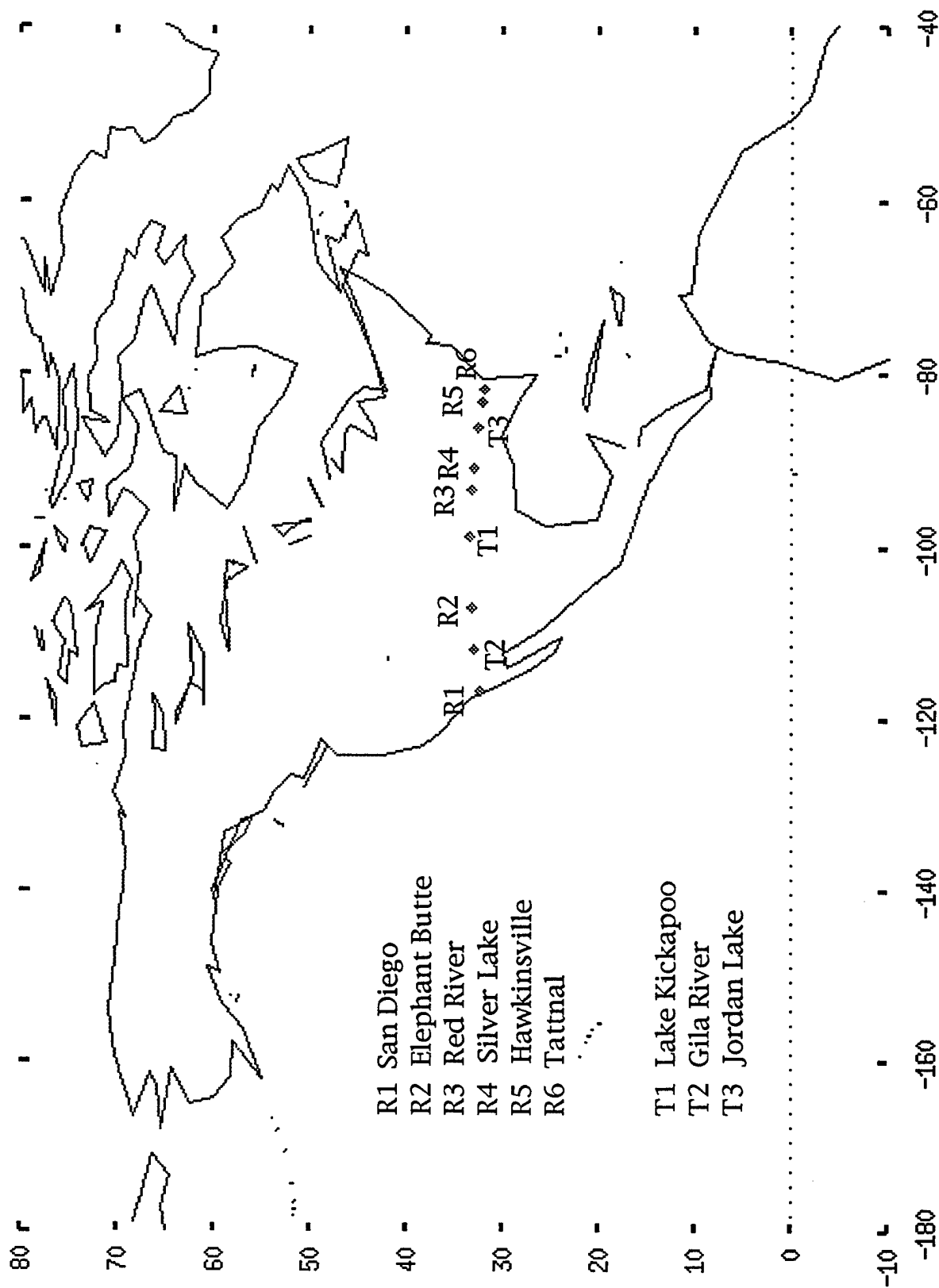
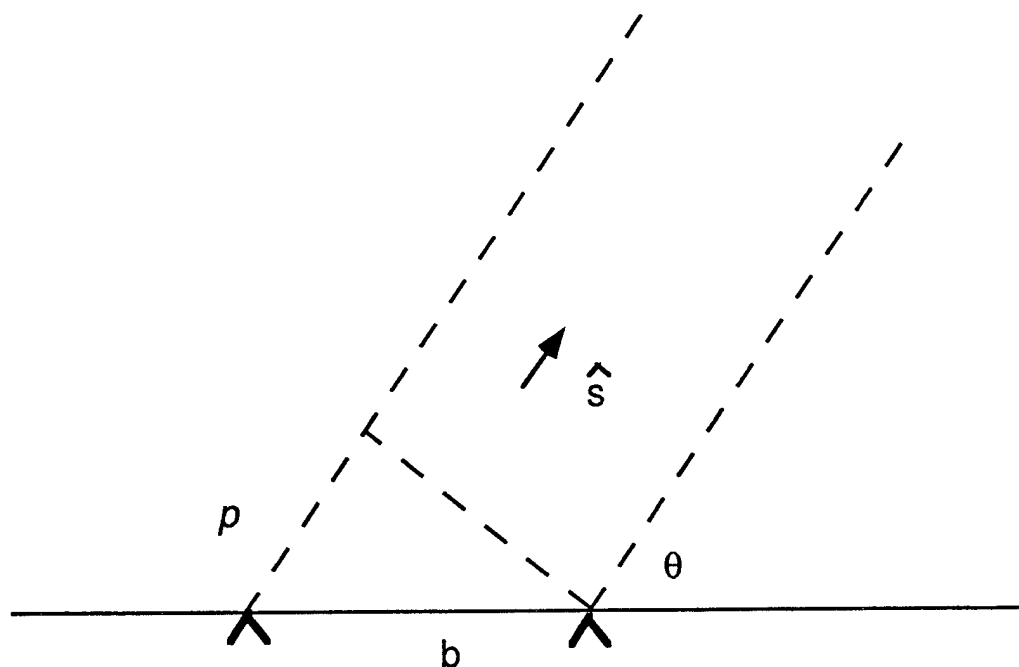


Figure 1. The NAVSPACECOM system known as "The Fence" spans the continental United States along a great-circle arc which defines an East-West baseline for the rf interferometer. A map of the facilities is shown above.



Direction cosines are defined from:

$$\cos \theta = \hat{s} \cdot \frac{\mathbf{b}}{b} = \frac{p}{b}$$

$$\cos \theta = \hat{s} \cdot \frac{\lambda}{b} \phi$$

where \hat{s} is the unit vector in the direction of the s/c; $b = |\mathbf{b}|$; and p is the path length difference from the source to the two antennas.

Error in cosine due to phase measurement error:

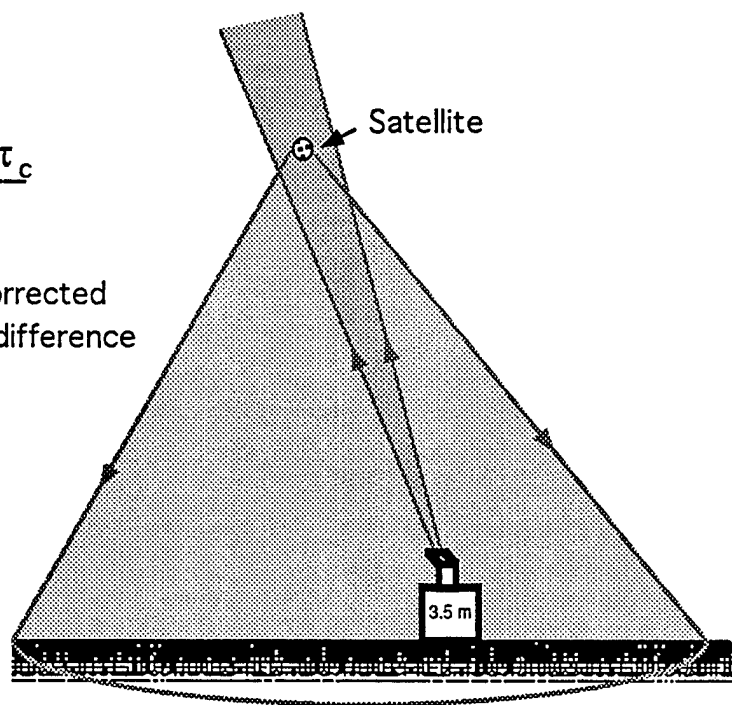
$$d \cos \theta = \frac{\lambda}{b} d \phi$$

where $2\pi\phi = 2\pi p/\lambda$.

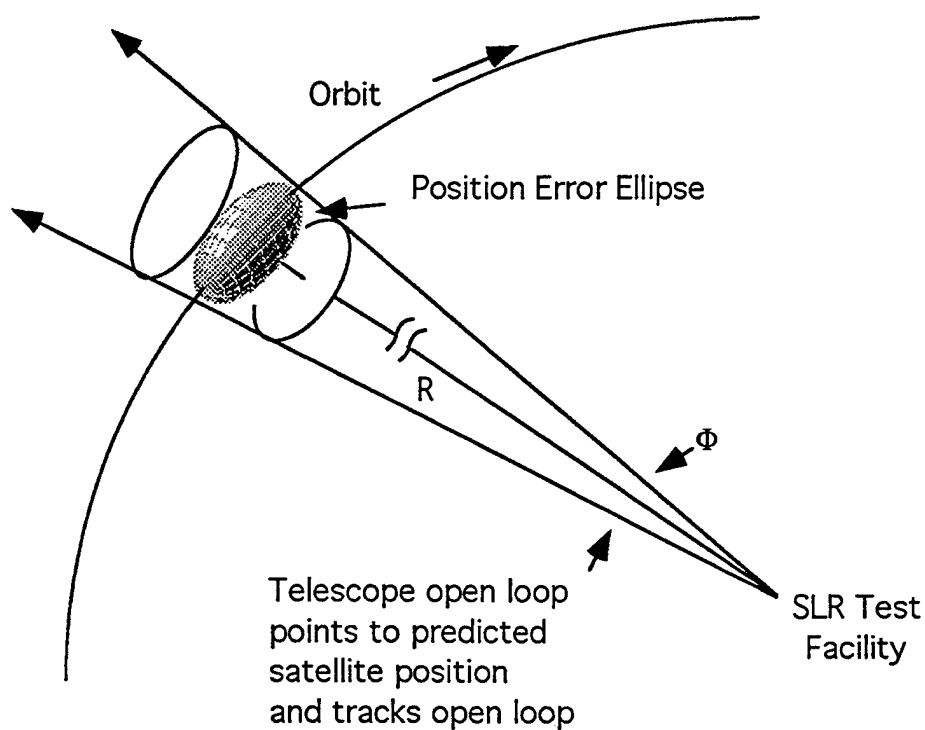
Figure 2. The basic principal of a two element interferometer is illustrated above (Ref. 1).

$$R = \frac{c\Delta\tau_c}{2}$$

$\Delta\tau_c$ = corrected
time difference



(a)



(b)

Figure 3. Satellite Laser Ranging is illustrated above. (a) A time-tagged two-way range is obtained using incoherent optical radar. (b) The range is corrected for system delays and analyzed using orbit determination modeling to finally produce a spacecraft's ephemeris.

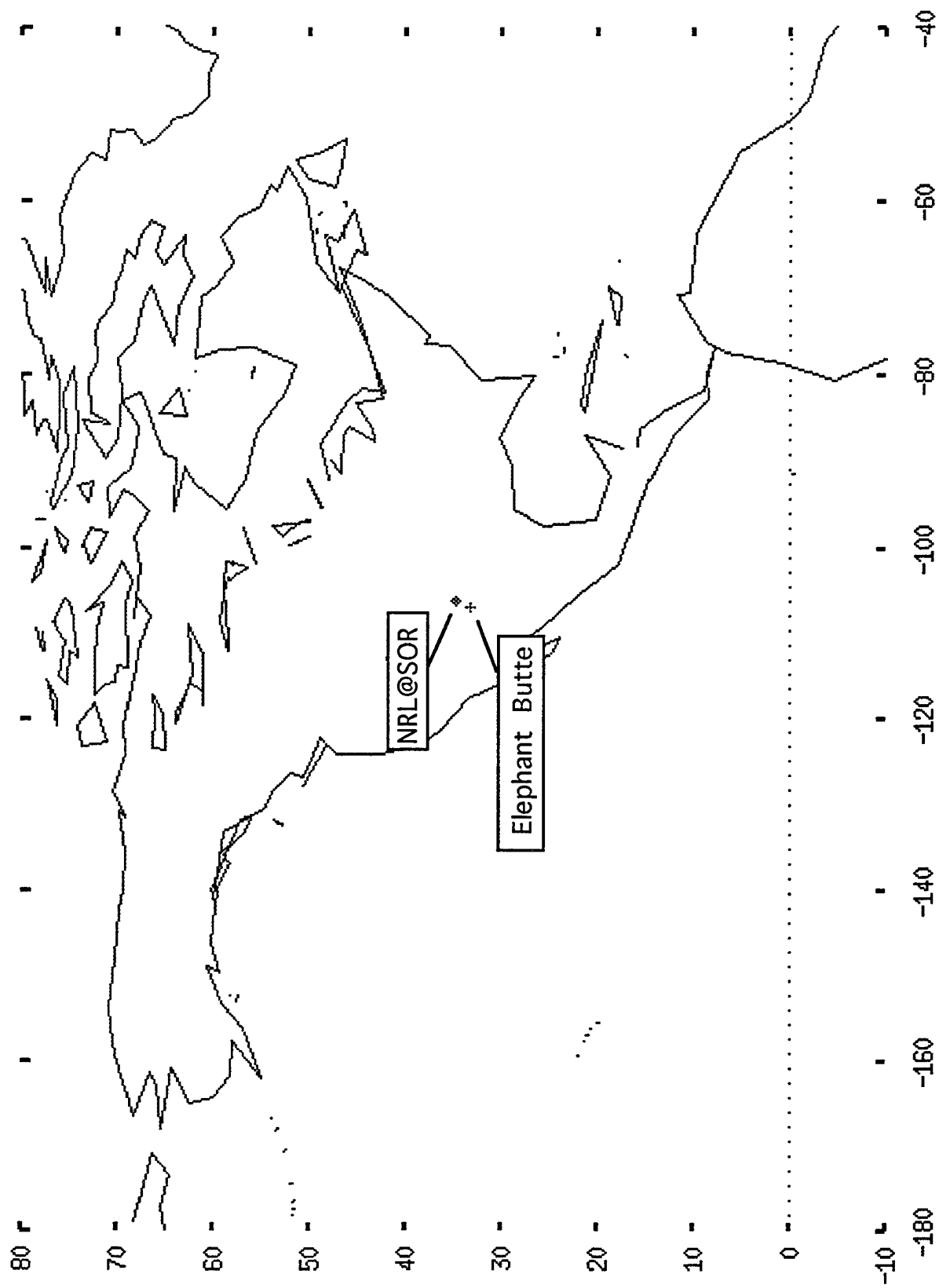


Figure 4. A map showing the geographic proximity of NRL@SOR and the Elephant Butte Fence Receiver is shown above.

TRADEX SPACE SURVEILLANCE IMPROVEMENTS, RESULTS AND PLANS

The TRADEX radar, located on the Kwajalein Missile Range (KMR), has recently demonstrated significantly improved space surveillance capabilities. During 72 days beginning in March, 1996, TRADEX assumed operational responsibility for ALTAIR, an important contributing sensor of the Space Surveillance Network, also located on the KMR. TRADEX responsibilities included support for new domestic and foreign launches and for deep space tasking. TRADEX support required 128 hour per week operations, the ability to perform five minute time bias searches and three degree scans on element sets, collect metric observations, correlate observations to the Space Control Center catalog, determine hand-over element sets and respond to fifteen minute recall notices. In addition, using a recently demonstrated local catalog maintenance capability, TRADEX detected, tracked and generated hand-over element sets on nearly 50 un-correlated targets. This paper discusses improvements implemented to support these activities, resulting operational performance and analysis of the demonstrated radar capabilities. In addition, this paper discusses an improvement plan that has important implications for future TRADEX space surveillance capabilities.

Current Capabilities and Recent Results

TRADEX, a high power instrumentation radar, operates nine degrees north of the equator on the island of Namur in the Kwajalein atoll of the Republic of the Marshall Islands. TRADEX, along with three other instrumentation radars, ALTAIR, ALCOR and MMW, compose the Kiernan Reentry Measurements Site, part of the Kwajalein Missile Range (KMR). TRADEX transmits at dual frequencies of L-Band (1320 MHz) and S-Band (2950 MHz), with full L-Band monopulse capability. The antenna produces a 0.63 deg (11.0 mrad) L-Band and a 0.32 deg (5.5 mrad) S-Band beam using an 84 ft diameter parabolic antenna with a dual-frequency focal-point feed. The antenna steers mechanically over the entire hemisphere above the horizon moving at up to 12.5 deg/sec in azimuth and elevation and accelerating from rest to full speed in under one second. Klystrons generate 2 MW peak power at each frequency

with an average power of up to 240 kW at L-Band and up to 40 kW at S-Band. These frequencies, antenna size and powers give TRADEX the sensitivity needed for single pulse S-Band detections on objects as small as 1.4 cm at 500 km and L-Band detections and tracks on objects as small as 2.7 cm at that range and on payloads in geosynchronous orbit.

As described in reference [1], during Fall, 1995, TRADEX validated a significant new capability for resident space object (RSO) characterization by the successful completion of the TRADEX Autonomous Catalog Maintenance (TRACM) experiment. The TRACM experiment built in three phases on TRADEX software which uses the AFSPACECOM propagator SGP4/DP4 and the Lincoln Laboratory catalog maintenance code ANODER. During Phase One, TRADEX maintained a catalog of 10 known objects (currently cataloged by the Space Surveillance Network (SSN)) which were reacquired as long as 10 days after their last

¹ Prepared for the Department of the Army under Air Force Contract F19628-95-C-0002. Opinions, interpretations, conclusions, and recommendations are those of the authors and are not necessarily endorsed by the United States Air Force or Army.

track and for as long as 26 days overall using only TRADEX observations and processing. During Phase Two and Three TRADEX maintained a catalog of 16 Un-Related Targets (UCTs) objects not currently cataloged by the SSN) in addition to 12 known objects which were re-acquired with a 75% overall success rate. Results from Phase Two and Three are shown in Figure 1. In the figure a successful track is shown for each object, arbitrarily assigned a number in the 43000 to 47000 range, as a function of Julian day. Dark '+'s indicate UCTs. Note that some UCTs were re-acquired as long as 10

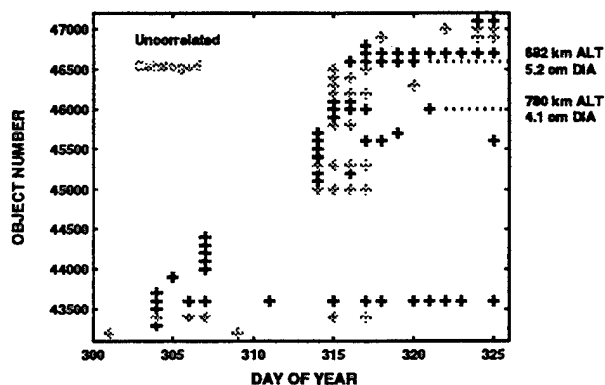


Figure 1. TRACM Phase Two and Three Results

days after the previous track. The size of two smaller objects in the 600 to 800 km altitude range is also shown. The TRACM experiment validated TRADEX capability to autonomously and reliably detect and acquire RSOs, correlate observations to the SSN Catalog, perform preliminary orbit determination, scan orbits for re-acquisition, and update orbital element sets.

In a significant operational accomplishment during 72 days beginning in March, 1996, TRADEX successfully assumed operational responsibility for ALTAIR space-track operations while modifications were made to the ALTAIR antenna. The following sections describe this activity.

TRADEX Space Detection and Tracking (TRADATS)

TRADATS denotes TRADEX Space Detection and Tracking (SPADATS), the name originally given to the ALTAIR space track activity. During periods when ALTAIR is unable to conduct normal space track operations, TRADEX provides as much of the normal Deep Space (DS) Space Control Center (SCC) tasking, New Launch (NL) and New Foreign Launch (NFL) coverage as possible. Therefore, during TRADATS, TRADEX substitutes for ALTAIR as the contributing sensor from KMR in the Space Surveillance Network (SSN).

TRADEX support for NLs, NFLs and for DS tasking required 128 hour per week operations, the ability to perform five minute time bias searches and three degree scans on element sets, collect metric observations, correlate observations to the SCC catalog, determine hand-over element sets and respond to fifteen minute recall notices. Maintaining capability to respond to recall notices can be stressing for TRADEX since scheduling downtime required advance SCC approval and careful assignment of maintenance personnel. In order to perform a significant space track role reliably, with little notice, some software development was necessary. Supporting this development during TRADATS preparation and operation required careful balancing of personnel assignment so that verification of the core requirements for TRADATS were not jeopardized. Significant coordination with ALTAIR was required, both in defining the operation and in assigning personnel. While some detailed procedures existed, many needed updating and others needed to be written, including procedures for tracking DS objects, acquiring and tracking NFLs and controlling sectors for RF safety. Training of operators in these procedures required a significant commitment of system time and careful definition of personnel responsibilities. In short, TRADATS was a demanding TRADEX operation.

TRADATS Operational Performance

USSPACECOM Regulation 55-12 establishes policy for SSN operations [2]. Metric

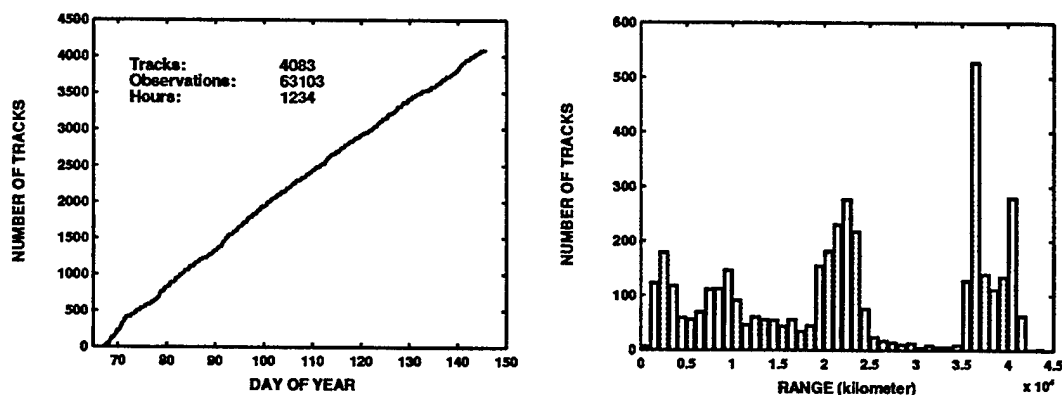


Figure 2. TRADATS 1996 Operational Performance

satellite tasking of SSN sensors is accomplished using messages which contain a category and suffix for each task. The category specifies priority and the suffix specifies the amount and type of observations required. During TRADATS, TRADEX recorded metric observations on satellites according to these tasking messages. In order to maintain the highest quality data possible, TRADEX applied a metric data quality filter, in real-time, which prevented observations from being recorded that failed to meet metric error and signal to noise standards. As a result, the ability of TRADEX to record high quality metric data of the appropriate amount and type form the primary basis for assessing TRADEX operational performance.

During 79 days of support, TRADEX tracked over 5000 objects and met the SSN requirements for a track on over 4000. These tracks were collected at an average rate of 72

per day with 52 per day meeting the SSN requirements. TRADEX supported one Chinese and four Russian launches. In addition, using a recently demonstrated catalog maintenance capability, TRADEX detected, tracked and generated hand-over element sets on nearly 50 UCTs. Millstone, an important DS contributing sensor of the SSN, acquired 90% of these hand-overs and continues to track three objects. Interestingly, five of the TRADEX discovered UCTs are in highly eccentric orbits of low inclination. Figure 2 summarizes these results. Although excellent, this operational performance could be improved by implementing improvements described in a following section.

TRADATS Metric Performance

Millstone updates precision orbital element sets weekly on six satellites using laser

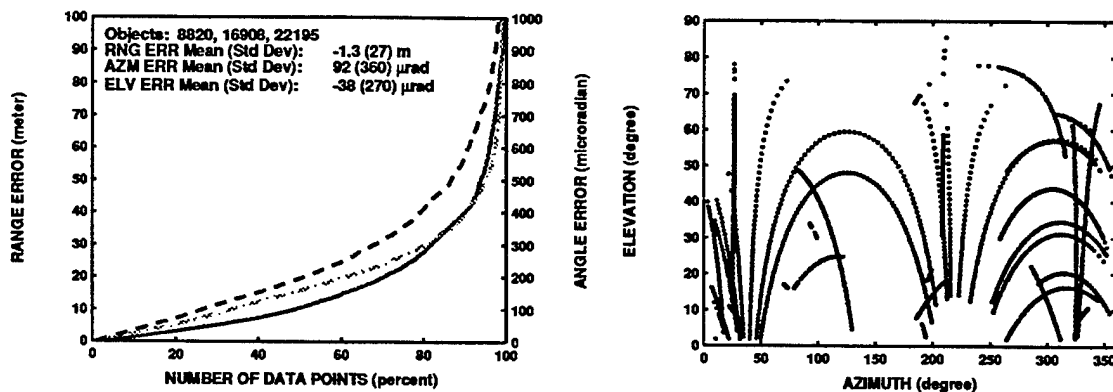


Figure 3. TRADATS 1996 Metric Performance

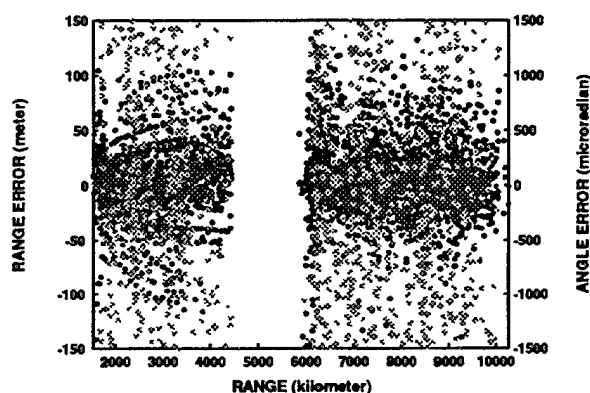


Figure 4. Range Effect on Metric Satellite Range and Angle Errors

ranging data. Data on the satellites, which have corner reflectors, has an accuracy of 10 to 20 cm and is available from the NASA Crustal Dynamic Data Information System. The satellites include near earth satellites EGP (SCC object 16908) and Starlette (7646), two deep space LAGEOS satellites (8820 and 22195) and two deep space Etalon satellites (19751 and 20026). Observations from contributing SSN sensors can be merged with this data and precision orbit fits re-computed using the general purpose numerical integration program DYNAMO [3]. The orbit fits provide individual observation residuals with an accuracy which varies from 15 cm (LAGEOS) to 70 cm (Starlette) [4]. During TRADATS, TRADEX collected observations on objects 8820, 16908 and 22195. Mill-

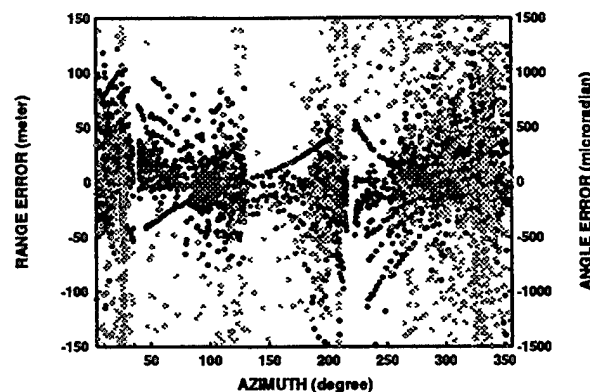


Figure 5. Azimuth Effect on Metric Satellite Range and Angle Errors

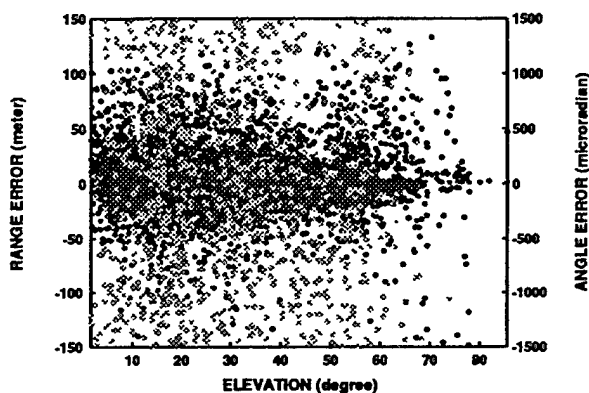


Figure 6. Elevation Effect on Metric Satellite Range and Angle Errors

stone provided TRADEX with precision orbit fit residuals on many of these tracks and the data was used to determine TRADEX metric performance. Figure 3 illustrates the angle coverage of the tracks used to produce this data and the resulting range and angle errors as a percent of the number of data points. Note that 90% of the TRADEX observations were within about 40 m in range, 400 μ rad in azimuth and 600 μ rad in elevation. Figures 4 through 6 show the resulting errors (range error shown as darkest dots and azimuth error shown as lightest dots) as a function of range, azimuth and elevation in order to illustrate systematic effects. Note that the range error decreases with elevation most likely due to atmospheric refraction effects. The range error correlation with azimuth is under investigation.

TRADATS Software Improvements

During TRADATS substantial space surveillance software improvements were completed including software for database handling, correlation, right ascension update of NFL folders, scheduling and recording. Three areas of software development are particularly significant. The first involves access to the ALTAIR database using the ALTAIR Satellite Data Server (ASDS). ASDS allows access to the ALTAIR VAX based database of element sets, observations and radar cross section (UHF RCS) data over the existing KMR secure network. Tools requiring the database, developed primarily by the Aero-

Table 1. ASDS Client Application Programs

Program Name	Use
Un-correlated Target Program (UCTP)	Unknown Satellite Identification
Callb	Radar Calibration Monitoring Tool
Work Station Satellite Data Client (WSDC)	Remote Satellite Data Base Access
Analytic Orbit Determination Revised (ANODER)	Orbit Fitting, Propagation and Analysis

space Division at Lincoln Laboratory and described in Table 1, execute on any UNIX platform on the network. ASDS consists of standard ALTAIR database access routines (LIBDAP) and network communication routines written at the socket level. AIS security requirements are satisfied by password protection and detailed logging of all user transactions.

Another important software development area interacts with ASDS and consists of the TRADEX ORB library of satellite database handling routines. Currently the ORB suite contains nine routines which are written in C, oriented for ASCII two card element set processing and described in Table 2.

Communication between the TRADEX satellite database and Real Time Program (RTP) is accomplished using the TRADEX QuickLook Library of routines. The QuickLook library permits 10 Hz recording of database items to disk or for display without modifications to the RTP. QuickLook accesses data described by a text list using an Ethernet interface between the host computer and the Encore 9780 computer running the TRADEX RTP which receives the command, collects the data and sends the requested data to the host.

TRADEX Space Surveillance Plans

TRADEX plans for space surveillance capabilities enhancement focus on improvements in three areas: routine catalog maintenance, new launch coverage (both domestic and foreign), and resident space object activities. The plan places greatest emphasis on deep space catalog maintenance and new launch coverage capabilities since funding for TRADEX space surveillance activities relates primarily to these areas. The plan also places greater emphasis on improving L-Band rather than S-Band capabilities since the L-band modifications are more economical and the majority of TRADEX space surveillance activities require the L-band sub-systems. The following sections describes these areas of emphasis and Table 3 describes the plan overall. In the table the relative value (VL) of the improvement and relative effort (SZ) required for implementation are indicated as small (S), medium (M) or large (L). Using these qualitative measures and considering personnel availability results in the nominal improvement schedule shown by quarter in the table.

Table 2. ORB Suite Routines and Use

Routine	Use
sift	Removes undesired orbital element set (OES) from ALTAIR catalog before loading TRADEX catalog.
loadoes	Creates a new OES catalog, and updates, replaces, or deletes an existing OES catalog.
orb	Responds to TRADEX Real-Time Program (RTP) requests by providing the current state vector for a cataloged object.
sitepen	Determines when a set of objects is within some pre-determined range, azimuth, and elevation box, over some period of time.
rise	Calculates directly from an OES when an object or set of objects is within some defined range, azimuth and elevation box or reads pre-calculated satellite penetration data (see sitepen).
oes	Adds, displays, updates, deletes, or prints an existing OES. Changes databases from which future OESs will be accessed or placed.
star	Calculates object position directly from the OES over some period of time, at specified intervals.
see	Prompts the user for the year, day of year, time of day, and catalog.
seenow	Prompts the user for the catalog.

Table 3. TRADEX Space Surveillance Improvements Plan

IMPROVEMENT	VL	SZ	Q1	Q2	Q3	Q4
Sensitivity						
Modified Band 1 and 4 MW Peak Power	M	S	■			
Deep Space Signal Processing Study	L	M	■			
Deep Space Signal Processing	L	L		■		
Optimal Deep Space Waveform	M	M			■	
Acquisition						
Alternatives to SGP4 Propagator	M	M	■			
RDIS Range Extents and Scans	M	S	■			
Optimize Track Filter Initialization	M	S	■			
Maximize Scan Angle Limits	M	S		■		
Minimize Latencies	M	S		■		
UCTP features at TRADEX	M	M			■	
Metrics						
Comprehensive Angle Bias Model	M	M	■			
Real-Time Ionospheric Refraction Model	M	L				■
Operations						
SSN Database Access	L	M	■			
Optimum Scheduler	L	S	■			
IOD and Differential Correction	L	S	■			
OBS Labeling / ID Processing	M	S		■		
Automated System Diagnostics	M	S		■		
Enable Remote Operations	S	M				■

Routine Catalog Maintenance Objectives

The single most important factor limiting TRADEX routine DS catalog maintenance capacity continues to be sensitivity. Comparing TRADEX with Millstone, TRADEX single pulse sensitivity in L565W (a 565 μ s pulse of 1.6 MHz chirp bandwidth) is currently 8 dB less. By either increasing the maximum pulse length to 1 msec (utilize all of the current video-on time) or raising peak transmitter power to 4 MW (achievable with a PRF band below the current Band 1), TRADEX single pulse sensitivity would increase by 3 dB. One of these changes will be made soon after an upcoming L-band rotary joint replacement is completed during the Spring 1997 shutdown. In addition, a few dB of loss should eventually be eliminated when TRADEX completes planned upgrades to digital receivers. While single pulse sensitivity is less, the TRADEX L-band transmitter average power capability is 4 dB higher than Millstone (240 kW rather than 115 kW). Assuming minimal integration loss, this advantage should enable TRADEX to overcome the single pulse sensitivity deficit. The on-

going Real Time Data Integration System (RDIS) project addresses these signal processing upgrades which will incorporate proven detection and integration methods similar to those already in use at ALTAIR and Millstone. Therefore, with longer pulse duration, increased peak power and improved coherent integration methods, TRADEX DS sensitivity should become comparable to Millstone.

Support for routine SCC tasking at KMR is coordinated through ALTAIR. Simultaneous participation in these operations by TRADEX would currently require a separate operations crew stationed at TRADEX. However, with a dedicated high bandwidth link to ALTAIR and upgraded TRADEX antenna control and transmitter consoles hosted on SGI platforms, these operations could be conducted remotely in the ALTAIR console room. In this way, spacetrack operations would continue to be coordinated and conducted from a single location by the existing dedicated spacetrack crew and efficiency and tasking capacity of KMR would be maximized.

New Launch Coverage Objectives

Although the TRADEX antenna has a relatively fast mechanical slew capability (12.5 deg/s, 13.5 deg/s²), due to a narrow beamwidth (0.63 degree L-band beamwidth) the sensor has a limited NL and NFL scanning capability. Large position uncertainties which may be associated with some NLs and NFLs could produce total probable angle errors which are larger than TRADEX scans. A system engineering investigation considering the quantitative errors which can be expected and optimization of the TRADEX orbital scan parameters to enlarge the scan is required.

Conclusions

TRADEX has developed and demonstrated a set of tools which enable the sensor to participate successfully in a wide variety of space surveillance activities. Current capabilities include catalog database handling, scheduling, observation filtering and transmission, observation correlation, orbital scans and stare and chase acquisition. Through past involvement in these activities many aspects of routine space surveillance operations at TRADEX have been automated or simplified, however, enhanced capabilities are possible. Several candidate enhancements have been identified which would maximize detection sensitivity and increase automation and efficiency, thus improving the quality and increasing the capacity of future TRADEX space surveillance support. If implemented, these improvements would enable TRADEX to take on a substantial portion of routine ALTAIR SCC tasking, free resources at ALTAIR for other tasks and increase the tasking capacity of KMR.

Acknowledgment

The authors express genuine appreciation for David L. Greene who made considerable contributions during TRADATS.

References

1. R. A. LeClair, D. L. Izatt and S. W. Six, "Improvements in TRADEX Debris Capabilities," *TRADEX Technical Report* (United States Army Kwajalein Atoll, Kwajalein Missile Range, March 1996).
2. Headquarters United States Space Command, "Space Surveillance Network (SSN) Operations," *USSPACECOM REGULATION 55-12* (Peterson Air Force Base, Colorado, 1 June 1992).
3. E. M. Gaposchkin, DYNAMO User's Guide, *Technical Report* (Lincoln Laboratory, Lexington, Massachusetts, December 1991).
4. L. E. Thornton, E. M. Gaposchkin, A. J. Coster and K. P. Buchmann, "AN/FPS-85 Calibration Assessment (1992-1996)," *Project Report* (Lincoln Laboratory, Lexington, Massachusetts, To Appear).

GEOSYNCHRONOUS SATELLITE MONITORING USING GEODSS PHOTOMETRIC SIGNATURES*

T. P. Wallace, M. A. Kosik, and M. A. Rawizza
MIT Lincoln Laboratory, Lexington MA

ABSTRACT

It is difficult to monitor stable geosynchronous satellites with currently available sensors and methods. The lack of rotational motion prohibits radar imaging. The range is too great for optical imaging. Wideband radar range profile-based monitoring is useful, but currently only the Long Range Imaging Radar can perform this monitoring.

The Ground-based Electro-Optical Deep Space Surveillance (GEODSS) sensors monitor most of the geosynchronous belt and produce photometric signatures, but these are currently used only for detection of tumbling objects. A loss of stability manifested in incorrect orientation or very slow rotation cannot be detected. Building on our work in both narrowband radar monitoring of low-earth-orbit (LEO) satellites and wideband radar monitoring of geosynchronous-earth-orbit (GEO) satellites, we are investigating the use of GEODSS signatures for GEO monitoring. We are developing a signature-comparison-based system, in which new signatures are compared to historic signatures.

There is significantly less information available in GEODSS GEO signatures than in the other signature types we have previously exploited. This talk will characterize that information, and describe methods for automatically extracting it and presenting it to the user.

1. INTRODUCTION

U. S. Space Command has several responsibilities for satellite monitoring in general and geosynchronous satellite monitoring in particular. They need to monitor the health of operating satellites. They need to identify new launches, as well as the occasional uncorrelated target (UCT) representing a detection by the space surveillance network which did not correlate well to any existing catalog object.

In the geosynchronous case, range-doppler radar imaging cannot be used since there is ordinarily no rotation of the target and hence no doppler. We are left with a range profile, giving the target cross-section in range bins which can be useful but is not as easily interpreted as an image. Similarly, the range from a sensor to the GEO belt of about 40,000 km is too great for ordinary optical imaging to be effective. Exotic methods such as compensated imaging, interferometry, or speckle imaging may give limited information, but these are not used operationally at present.

At previous workshops, we have reported on methods of geosynchronous satellite monitoring using wideband range profiles from the Haystack radar. This method has good monitoring capability, but the Haystack radar operates only about 12 weeks a year so it does not provide continuous coverage. Also, a single site is unable to cover the entire geosynchronous belt so we miss the entire Eastern Hemisphere.

Narrowband radar signatures of geosynchronous objects provide limited information, and are presently only used at the Millstone radar. These can detect some malfunctions but again are limited geographically.

This work was sponsored under Air Force Contract F19628-95-C-0002.

The GEODSS system collects photometric signatures on deep space objects which include the geosynchronous belt. The three sites provide good coverage of the geosync belt; interestingly enough, the only gap is over the Atlantic where the Haystack and Millstone radars can assist. The data is also sent directly to U.S. Space Command, so a system for information extraction similar to our narrowband radar monitoring system is conceptually possible. Getting the assessments quickly to the user is the best way to determine the operational utility of this kind of monitoring.

2. SIGNATURE COMPARISON-BASED MONITORING

We have previously developed and reported on methods for satellite monitoring based on signature comparison. These have been applied to narrowband radar signatures of low-earth-orbit (LEO) satellites in a system operational since 1992. The same approach has proven useful for GEO satellite monitoring using wideband range profiles from the Haystack radar, even though the data is substantially different from the narrowband radar LEO data. This system is presently operated at the Haystack radar due to the large data volume required to make range profiles.

The signature comparison monitoring algorithm proceeds as shown in Fig. 1. A database of validated historic signatures, representing data collections during times at which satellites of the same class were stable and in a normal operational configuration, is central to the processing. The new signature entering at left is compared to selected signatures from the historic database which are expected to be comparable to the new signature. The comparison algorithm is tailored to the particular data being processed, and is completely different for the different data types discussed here. The resulting vector of correlated distances represents multiple pieces of evidence for the status of the satellite. Small distances suggest good similarity to the database signatures which implies that the new signature is probably stable.

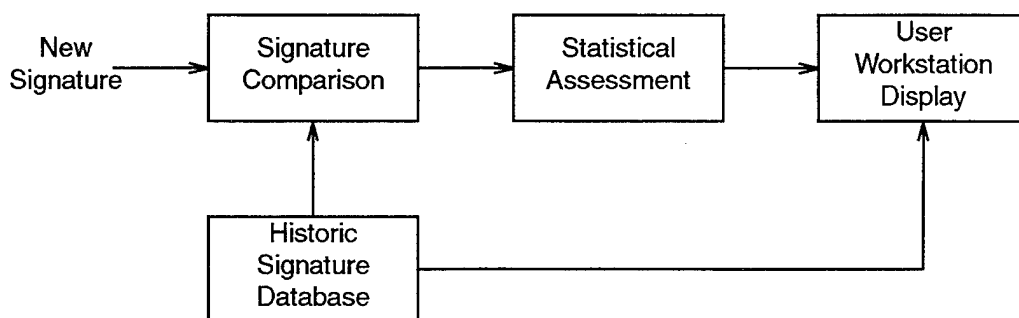


Figure 1. Signature comparison-based monitoring.

The combination of these multiple distances into a single numeric confidence is a non-trivial problem which has been described in a recent report.¹ This is necessary to summarize the assessment for the user. The user views the signature and the numeric confidence; if desired, the matching (or non-matching) database signatures can be displayed to better understand the supporting evidence for the assessment.

The previous two applications of this method involved signatures containing substantially more information than do GEODSS signatures. Preliminary results suggest that the method will indeed work on GEODSS data, and we plan to deliver a system to U.S. Space Command for test and evaluation in October 1997.

A validated database is clearly central to this algorithm, and Fig. 2 shows our database of GEODSS signatures as of December 1996. We have data going back to 1993, and the breakdown by sensor shows that Diego

Garcia is the largest contributor. Some GEODSS signatures are of high-earth-orbit (HEO) satellites which are not geosynchronous; these are not relevant to the present GEO monitoring problem.

SENSOR	GEO SYNC	TOTAL	YEAR	GEO SYNC	TOTAL
Maui	1113	1690	1993	288	851
Diego Garcia	4688	5179	1994	1125	1979
Socorro	1301	3189	1995	2986	3942
Total	7102	10058	1996	2703	3286

Figure 2. GEODSS database.

3. PRELIMINARY GEODSS DATA ANALYSIS

3.1 Photometric Signature Examples

In the following plots, the x-axis shows time since the start of the pass, while the y-axis shows brightness in optical magnitude referenced to a range of 1000 km. The actual brightness was much less due to the great distance to the GEO belt. Note that since a larger optical magnitude corresponds to dimmer objects, the lower regions of the curves represent brighter portions of each signature.

Figure 3 shows four sample GEODSS signatures. The first one is a tumbling Raduga, which is clearly evident from the periodic repetition of a large magnitude excursion of about two magnitudes. To the right is a signature which is more difficult to analyze. Is it bad weather, or is the satellite doing some strange maneuver? The two signatures below seem pretty stable, although it is difficult to say whether or not they are oriented properly.

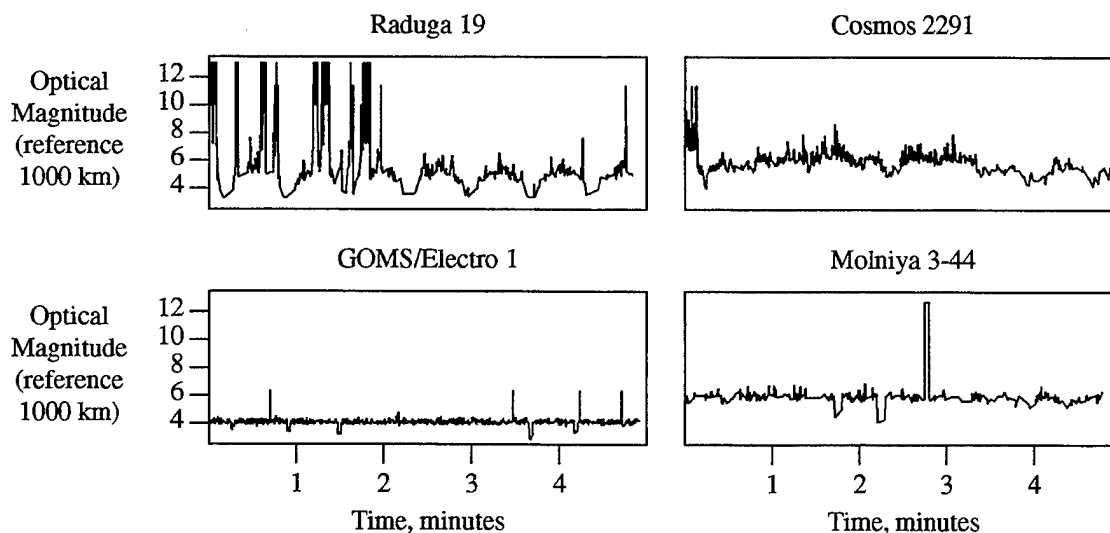


Figure 3. GEODSS signature examples.

This type of visual assessment represents the current state-of-the-art in GEODSS signature analysis. Unless a clearly repetitive signature is observed indicating tumbling, not much information can be extracted from the signatures. The goal of this effort is to extract information from more signatures, specifically those representing apparently stable satellites.

Figure 4 takes a closer look at a couple of signatures representing a variety of phenomena. The top signature shows an episode of apparently bad tracking, where the brightness drops precipitously, and then recovers perhaps 6 or 7 seconds later. There are what are probably multiple stars crossing the photometer field of view, with squared-off bottoms. One possible glint is visible around the 180 second mark. In the bottom signature again a few stars are visible, but the dominant feature is a region of substantial and irregular decrease in brightness. This might be associated with clouds or some other atmospheric effect.

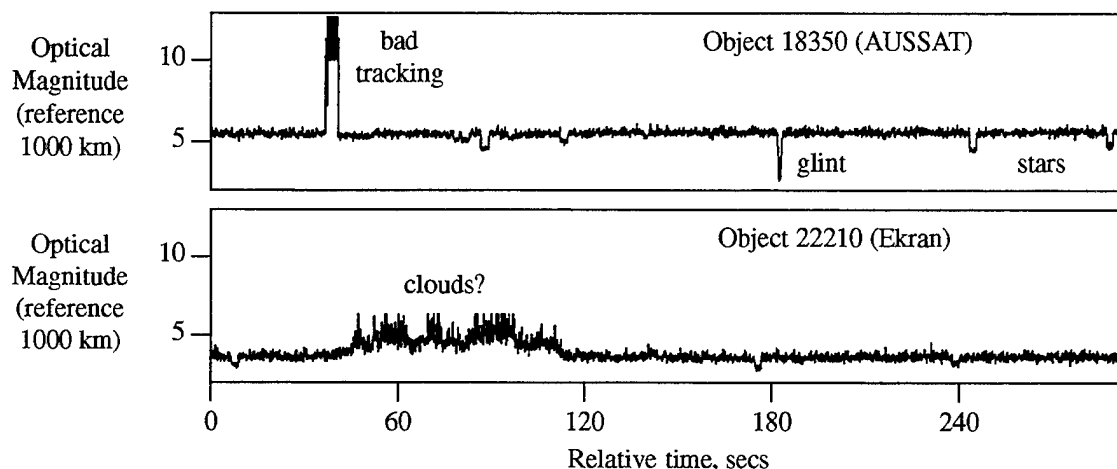


Figure 4. Annotated signature examples.

3.2 Signature Feature Extraction

There are a couple of potential useful features which might be extracted from the signatures and used to characterize the satellite. First, there are the glints. These represent a solar flash from some surface, so presumably either missing expected flashes or existing unexpected flashes could represent evidence of unusual orientation or configuration, or that a satellite is mis-tagged. Unfortunately, glints are not found in most signatures, so this approach would limit the number of signatures which could be analyzed. Also, a rather small surface can produce an observable glint, so it might be difficult to identify or predict glints except by examining a large database. Although there may be certain satellite classes which can be monitored by glints at certain times of year, this approach has significant problems.

The alternative is to use the relatively straight signature regions representing some average level of diffuse reflection. These regions have the advantages of being fairly dependable; most stable satellites will produce identifiable diffuse scattering regions. They also give confidence in data quality, telling us that we are likely tracking a stable satellite. They should be a viable method of characterizing many different satellite classes.

To characterize these regions we are considering the average optical magnitude, as well as the magnitude rate-of-change. Most signatures change very little over the average five minute signature duration, but the exact value of this variation might be useful. The problem we face is to automatically locate the straight regions of the signature, rejecting stars, glints, bad tracking, and all other disturbances. We then can fit a line to those regions,

using the slope and y-intercept as our desired magnitude and magnitude rate-of-change. This process must be fully automatic.

Figure 5 shows the algorithm used to perform the feature extraction. First, the signature is partitioned into overlapping segments of perhaps 20 or 30 seconds. Currently an overlap of about 2/3 is used. Then a line is fit to each segment, from which we derive an average magnitude, a slope (magnitude rate-of-change), and a fit error. Those segments whose fit is very bad are rejected at this point; this effectively rejects major stars, glints, and tracking problems.

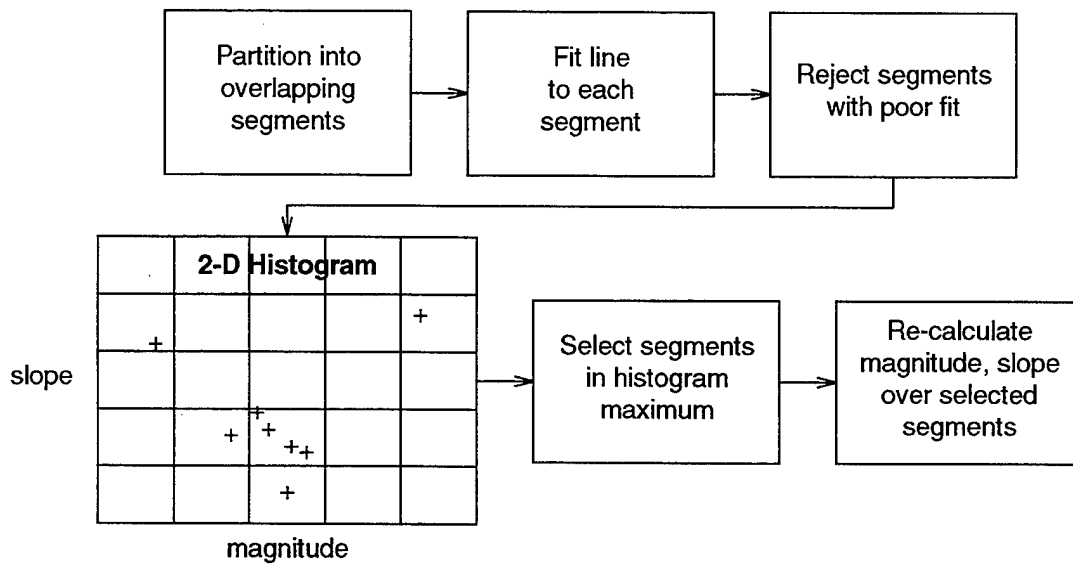


Figure 5. Feature Extraction.

The remaining segments have their magnitude/slope pairs treated as x-y coordinates and histogrammed into a 2-D histogram. The histogram bin with the most hits is taken to be the line representing the diffuse scattering region; all points included in at least one segment in this bin are taken as the diffuse reflection set. Lastly, a line is fit to these points to obtain a more accurate overall magnitude and slope.

Figure 6 shows an example which perhaps will make the operation of this algorithm clearer. At top, we see a signature with the original segments of length 20 secs, overlapped by 2/3. The segments are shown below the actual signature so that they can be easily distinguished; in reality they would lie right on top of the data. Although the fit errors are not shown, the slopes and y-intercepts of the curves are obviously affected by disturbances such as bad tracking. This causes them to fall outside of the selected 2-D histogram bin. The lower signature shows only the selected segments, illustrating the algorithm's ability to reject various disturbances and accurately identify the desired points.

As an example of monitoring, consider Fig. 7, in which a satellite was observed on two consecutive nights at exactly the same time. The resulting magnitudes are quite close, around 6.0, demonstrating repeatability. The magnitude rates are also quite close, but our preliminary assessment suggests that the rates are not repeatable unless the sun angles (and hence collection times) are extremely close. This is the case in this example, but the database as a whole does not support this type of monitoring, unless special tasking is done in an attempt to duplicate the exact parameters of an existing database signature. Hence we concentrate on the magnitudes for the rest of this paper.

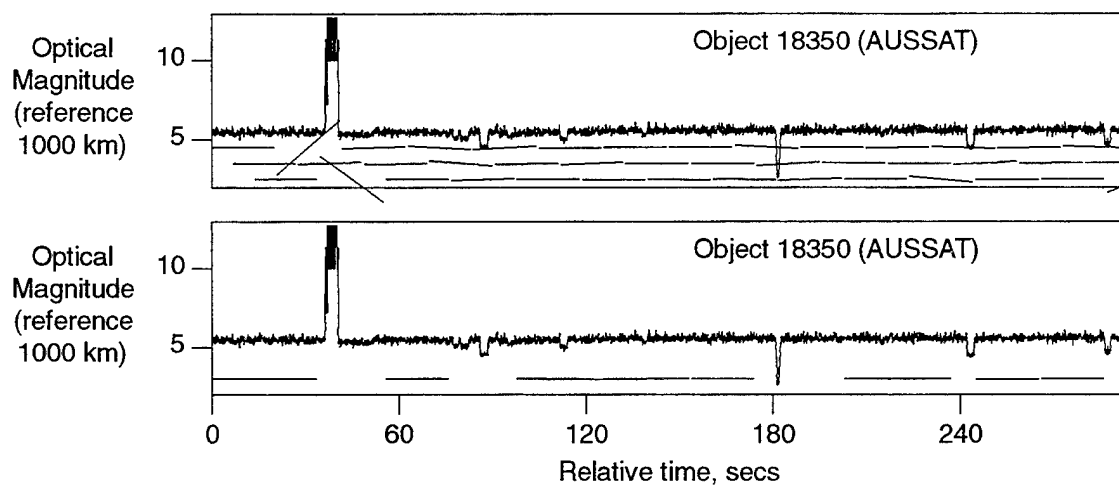


Figure 6. Segment Selection.

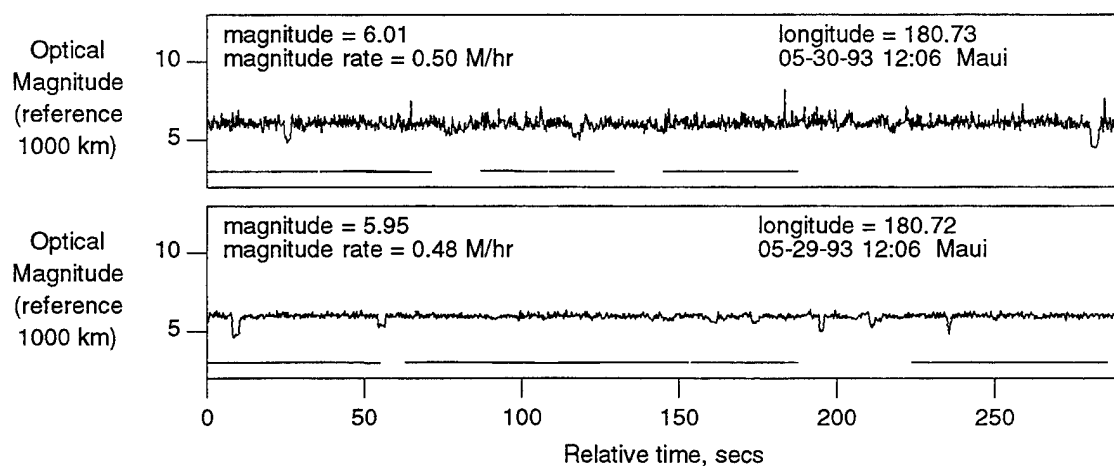


Figure 7. Object 9478 (Marisat).

3.3 Statistical Analysis

To understand our preliminary statistical analysis, consider the following monitoring concept. We hypothesize that the magnitude of the diffuse component of reflectivity is a continuous function of two sun angles. In that case, we have an ϵ - δ type argument in which magnitude differences are expected to be small if the individual sun angle differences (and viewing angle differences) are small. Translating this idea into the signature comparison environment, we hypothesize that two signatures will have similar magnitude if both signatures:

- (a) are from the same object, or the same class
- (b) are collected from the same sensor

- (c) are collected at times when the sun angle differences are small
- (d) are collected when the object(s) are at the same GEO belt position

If any of these properties are not satisfied, we expect that the magnitude difference will be larger.

Consider the following experiment. Let the distance between two signatures be defined to be the absolute value of the difference between the magnitude estimates. Calculate all inter-signature distances from the database which satisfy the four properties above. Histogramming these 8000 distances gives us a simple estimate of the probability density function (PDF) for the hypothesis that a satellite is good. Now, calculate all inter-signature distances in which the objects are of different classes, or have substantially different sun angles, etc. Histogramming these approximately 8 million distances gives us a PDF for the hypothesis that the satellite is cross-tagged (or oriented strangely).

Note that at this point in our research, the database is not validated, and there are significant numbers of cross-tagged or unstable signatures included. These will add noise to our estimates, but we expect that a repeatability "signal" should still be visible in this "noise" if there is significant hope for monitoring using this method.

Figure 8 shows the result of the experiment. The ratio of the two PDF estimates is an estimate of the likelihood ratio, giving the odds that a signature represents a stable satellite of the same class as the database signature. For example, a distance of 0.5 gives odds of 0.62/0.36 or 63% that the satellite is stable, while a distance of 2.5 gives odds of 0.08/0.18 or 31%. This result shows that significant information is contained in the magnitude estimates, and is based on a single distance. When evidence from multiple distances is combined, we hope the system will perform better and give higher (and lower) confidences to the user.

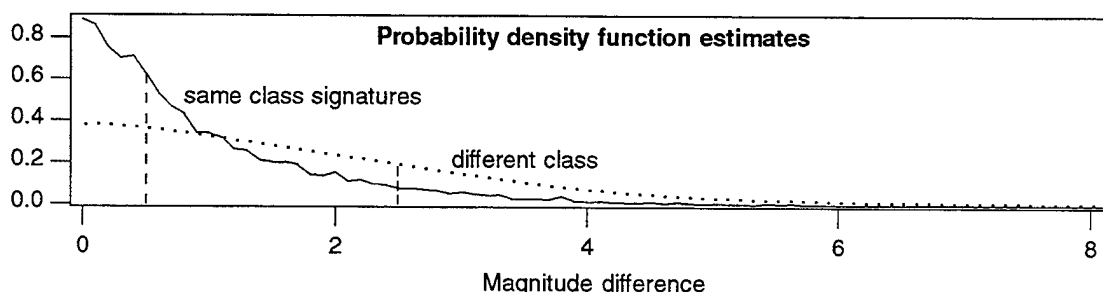


Figure 8. Single distance statistics.

4. MAJOR GEODSS MONITORING ISSUES

There are a couple of major outstanding issues, the first of which is sensor calibration. Since we are using absolute optical magnitude in signature comparisons, good absolute sensor calibration is required. Our preliminary results show that useful levels of calibration are being attained, but certainly better calibration will improve monitoring performance. As part of this project, Phillips Laboratory conducted a study of GEODSS calibration, investigating both the procedures and the software used operationally. This type of study is crucial to improving calibration; our data analysis can only give some estimate of how good calibration is at present.

Recall that in the previous section we discussed the use of magnitude rate-of-change as a feature characterizing a satellite. If this could be used, then absolute calibration would not be necessary, just short-term stability. As mentioned above, the database is presently insufficient to enable us to use rate-of-change, but this option will be studied as further data is collected. An optimum system would doubtless make use of both pieces of information, unless the sensors were completely uncalibrated, so that is the direction we will be heading in the future.

The other major issue is database validation. All assessments are ultimately derived from database comparisons, with the assumption that the database signatures represent stable satellites with correct identification. A small percentage of bad or cross-tagged signatures is tolerable, but it will of course hurt performance somewhat. It is critical to the overall success of this project to remove bad signatures from the initial database. After this, system assessments of new signatures should help the user to maintain a good database as new signatures are collected.

We can group bad signatures into three classes: cross-tags, atmospheric problems, and miscellaneous defects. The latter class would include sensor problems, tracking problems, etc. The approach we have taken to validate the database starts with the construction of a small signature assessment system, which starts with a partially-validated database. Each signature is compared to all signatures which are comparable in terms of satellite type, sun angles, ground longitude, and sensor. The resulting set of distances is combined into a single confidence that each signature represents a satellite is stable and of the proper class.

The initial performance of the system is rather poor, but some information is being extracted. At this point, we concentrate on those signatures whose confidence is very low. We may display this signature together with its cohort of comparable signatures. We have found cross-tags in this way, for example when the signature shows the periodic variations of a tumbling object. We can also display a signature along with all of the signatures collected by that sensor on that night. If many of these signatures have poor assessments, that suggests that atmospheric problems such as haze or cirrus clouds may have been present, and so certain signatures are deleted.

After deletion of some signatures, the signature assessment system is re-run, but this time without the newly discovered bad data. The performance is somewhat better; again the signatures with poorest assessments are investigated for possible deletion. This procedure is iterated as bad data is deleted and new data is collected.

5. SUMMARY AND FUTURE WORK

This project involves developing a GEO satellite monitoring system based on GEODSS signatures. The preliminary results are encouraging, and show that optical magnitudes derived from apparently stable objects are repeatable.

We have a very aggressive schedule in which we plan to deliver a prototype monitoring system to the sponsor in October 1997. Our current efforts are concentrated on database validation, as well as algorithm and software development.

REFERENCES

1. T. P. Wallace, "An All-neighbor Classification Rule Based on Correlated Distance Combination," Technical Report TR-1030, Lincoln Laboratory, M.I.T., (1996).

A FRAGMENTATION EVENT DETECTION SYSTEM

G. Zollinger and R. Sridharan
Lincoln Laboratory, Massachusetts Institute of Technology

1. INTRODUCTION

One of the best ways to detect the fragmentation of resident space objects is to continually process and analyze the uncorrelated target (UCT) detection data from the FPS-85 radar. This radar, located on the Panhandle in Florida, operates a surveillance fence continuously and is hence able to detect new objects in low altitude orbits fairly rapidly. The fragmentation detection system developed at Lincoln Laboratory uses these data.

The Fragmentation Event Detection System (FEDS), is designed to automate the detection of breakups of resident space objects (RSOs) in orbit. By processing the data daily, this system can improve the response time for tracking debris pieces from a fragmentation event. The system also produces output that minimizes the amount of time analysts need to spend determining which events are the result of a fragmentation event and which are a false alarm.

The FEDS uses historical UCT data from the FPS-85 radar to generate a model of the statistical likelihood that a fragmentation event has occurred. Data are evaluated daily by a three-stage process based on this model. Element sets that pass all three stages are considered possible evidence of a fragmentation event. When an event is detected, three types of reports are generated: 1) a list of the element sets involved in the event, 2) information about the location of the event, and 3) VRML code for the three-dimensional graphic display of the event. The current automated system generates output daily so that the Millstone radar may be used for tracking debris pieces shortly after the event is detected.

The FEDS has been successful at detecting fragmentation events ranging in size from the small COBE breakup and events including as few as three pieces to the recent PEGASUS breakup that contained over 130 pieces. This paper will include a description of the algorithm used and the results from the operation of FEDS over the last nine months.

2. DESCRIPTION OF DATA

The sensor used in this study is the FPS-85 phased array radar located at Eglin Air Force Base in Florida. This FPS-85 serves as a primary sensor in the space surveillance network. The sensor is useful to this study because it is used for surveillance of both low altitude and deep space objects, and has provided data used in the detection of both near earth and deep space fragmentation events.

Each day this site provides Millstone and FEDS with a list of UCT element sets. When the site is unable to match these objects in the existing catalog, it gives them a generic object identification. When a fragmentation event occurs, all resultant pieces do not match the catalog, and consequently they are tagged as UCTs. As a result, within a day of the event the FPS-85 will report all pieces involved as UCTs. The site does not recognize these pieces as part of a breakup, but only as uncorrelated element sets.

The FPS-85 radar detects and tracks debris as UCTs. However, since the orbit propagation software at the site is somewhat limited in accuracy, the detection of a debris object falls into a cyclical pattern in which the site is able to keep track of an object for a period of time, loses track of the object for some weeks, and, upon redetection, reports it again as a new UCT..

The cyclical nature of the FPS-85 radar produces a similar effect in FEDS. Fragmentation events are filled with debris pieces that the FPS-85 sometimes loses and re-reports as new uncorrelated element sets. In some cases, FEDS is capable of recognizing these "new" element sets as part of a given event. Consequently, a similar pattern emerges in which certain fragmentation events are detected multiple times. One PEGASUS breakup has been correctly identified by FEDS 47 times over the last six months.

This study is based on over 600 days of data from the FPS-85 radar site, during which time ten distinct fragmentation events occurred.

3. ALGORITHM

The basic idea behind FEDS is the assumption that when a fragmentation event occurs, there will be a significant increase in the number of objects detected for a given day in a small region of space. By examining each of these regions (called bins) which are defined by inclination and right ascension, the system can count the number of objects detected, and determine which objects represent a fragmentation event.

By definition a fragmentation event is the result of an object splitting into multiple objects. Another factor that must be addressed, however, is whether the objects resulting from a fragmentation event will initially be found in one bin or will immediately spread out into other bins. Typically it requires a tremendous amount of energy from the fragmentation event to change the orbital plane of the resulting debris.. Over time the pieces involved will spread out from each other but initially the debris pieces should fall into one bin.

FEDS uses the historical FPS-85 data to construct the parameters of each bin and models the expected number of objects detected in a bin for a given day. Each day FEDS measures how many objects were detected in each bin, and whether or not a

fragmentation event could have occurred. This process requires three stages. Any data that passes all three stages is reported as a possible fragmentation event.

3.1 FIRST STAGE: INCLINATION & RIGHT ASCENSION BINS

The first stage is the inclination and right ascension bin test. FEDS divides space into 40 rectangular micro-bins defined by inclination and right ascension. Each of these micro-bins has a mean and standard deviation for the number of objects detected per day. If the number of objects detected for a given day exceeds the mean detection rate for that bin by three standard deviations, then that bin is a possible candidate for a fragmentation event and this information is passed on to the next stage.

The first step in this process is to separate the historical data into ten inclination bands each with nearly equal populations. Each band therefore has roughly the same number of total objects detected. The next step is to separate each inclination band into four bins defined by right ascension. Again, each bin should have roughly equal populations. The bins are constructed daily from all historical data from the FPS-85 radar omitting the data for the last 30 days. The most recent data must be excluded from the bin construction, because otherwise they will affect the event detection model.

After the bins are defined, FEDS calculates the mean and standard deviation for the expected number of objects detected daily for each bin. Then, FEDS sorts the recent UCTs into their appropriate bins and applies an exceedance test on each bin. Most bins have means and standard deviations slightly below one UCT per day, so this test typically isolates bins with four or more UCTs.

3.2 THE SECOND STAGE: NORMALIZATION

The first stage only determines that there is an unusually high number of objects detected in that bin. The second stage is an attempt to normalize the data, to overcome system irregularities in the performance of the FPS-85. There are three factors to consider: local catalog maintenance, hours of operation, and the high elevation debris fence.

As was stated before, the FPS-85 loses track of debris pieces after a few days which then reappear as new UCTs in a matter of weeks. Hence the UCT detection rate of each bin will be periodic. Therefore, it is not unusual that a bin will have zero UCTs detected over several days simply because the population associated with a given bin is being successfully tracked. Another long term aspect of the cyclical nature of the data is that UCTs will move across bins due to changing right ascension. The PEGASUS breakup in early June of last year has moved full circle across the right ascension bins. Bin movement also occurs across inclination bands, but the inclination rate of change is typically small relative to changes in right ascension. Over time the population associated with a given event will spread out over several bins, rendering it undetectable as a fragmentation event by FEDS.

Another factor to consider is the hours of operation of the FPS-85 site. It is possible that in a given day, the hours of operation of the space surveillance fence that typically detects most UCTs were considerably higher than the usual norm and as a result more objects were seen. This has the effect of increasing the number of UCTs detected.

The final factor that impacts this study is the occasional operation of a second debris fence. Most of the data used in this study are the result of the FPS-85 radar's use of a debris fence, an inverted v-type fence which peaks at an elevation of 23 degreesⁱ. However, a second high elevation fence which also tracks and locates objects is sporadically run. Consequently, the operation of the second fence can also lead to an increase in the number of UCTs detected.

All the above factors, if present, should affect the detection rates for all bins. If one or more factors influence a given day's data, then there should be a pattern in which the detection rates across all bins are higher. Since the effect should be close to uniform, each bin should have the same relative ratio of UCTs detected in the bin to total UCTs detected that day. Since there are 40 micro-bins, each micro-bin represents 2.5% of the overall historical data. On the average day, roughly 2.5% of the daily UCTs should be located in each bin. Therefore, if a system operations problem doubles the UCTs detected across all bins, then each bin should still represent 2.5% of that day's data. The relative percentage of each bin also has a mean and standard deviation associated with it. If the relative percentage exceeds three standard deviations from the mean, then FEDS passes the elements sets involved on to the third stage.

3.3 THE THIRD STAGE: CLUSTER DETECTION

At this stage, FEDS has determined that there is an abnormal number of UCTs detected in one or more bins that is not symptomatic across all bins. However, inclination and right ascension are not sufficient characteristics to determine a fragmentation event. For example, it is possible that the objects detected are not at all close to each other. The group of UCTs involved could contain both deep space and near Earth objects and still have similar inclination and right ascension. Because of this problem, the system tests to see if a cluster exists. A cluster is defined as three or more objects having a semi-major axis within .1 Earth radius of each other. If a cluster exists, then FEDS reports the element sets involved in this cluster as a possible fragmentation event. All UCTs that are not found in a cluster are not reported. Because of this definition, it is important to note that a given bin could have multiple clusters.

3.4 MACRO BINS

An assumption behind FEDS is that the energy involved in a fragmentation event is not sufficient to significantly alter the inclination of all the resulting debris pieces. The micro bins used in this process are on average 18 degrees inclination by 90 degrees right ascension, which is sufficient to encompass most fragmentation events. However, FEDS

uses fixed boundaries to define the micro bins. If an event occurs close to or on a boundary, then the resulting pieces may be scattered over several bins and as a result may not be detected as a fragmentation event. This problem is solved by establishing macro-bins. Macro-bins are created by combining four adjacent micro-bins. Every intersection of two boundary lines defines a macro-bin, and FEDS contains a total of 40 macro bins. Because of this arrangement, the data from each micro-bin is used in four different overlapping macro-bins. On average, a macro-bin will cover 36 degrees inclination by 180 degrees right ascension, and macro-bins, like micro-bins, have a mean and standard deviation associated with each bin. Once the macro-bins are created, FEDS evaluates each macro-bin according to the same three-step process meant to detect fragmentation events in micro-bins.

In cases where a breakup does not occur at a boundary, the event is still visible in both the micro-bins and macro-bins. Large breakups such as PEGASUS frequently have such a large number of detections that the event is detected both in a micro-bin and also in the four macro-bins which share that micro-bin.

3.5 END RESULT OF ALGORITHM

When a cluster is detected by FEDS, it may or may not be evidence of a fragmentation event. Detection by FEDS only signifies that in a ring-shaped region of space defined by inclination, right ascension, and semi-major axis there was a significant increase in the number of UCTs detected. The next step is to determine how the UCTs are distributed in the cluster ring. If the UCTs are distributed evenly throughout the ring, it is unlikely to be the result of a recent fragmentation event. In the case of a fragmentation event, the UCTs should be fairly close. At this point, an analysis must be performed on each cluster to determine whether or not a fragmentation event has occurred.

FEDS provides several tools to assist in the analysis of a cluster. The first is a list of EX and EY cards for each UCT in a cluster. An EX card contains information about the orbit and position of an element set; an EY card represents the rates of change of EX card attributes. This information is essential for analysis and tracking. FEDS also keeps information about all previous clusters detected. This can be useful in determining whether a cluster is a result of an older breakup. Operational experience has shown that in 31% of the cases the increase in the number of UCTs is not the result of a recent fragmentation event.

FEDS also maintains for every detected event a corresponding virtual reality modeling file (VRML). VRML is a recent standard for three-dimensional Web pages developed by SGI for use with Netscape. FEDS uses VRML files for the display of clusters. By viewing these files, analysts can determine the distribution of UCTs through a given cluster ring. This interface also allows the user to view the object identification by placing the mouse on top of the debris piece.



Figure 1. VRML file of a Pegasus breakup

Each UCT tends to have an epoch close to the times of observation, so the UCTs in a given cluster will have different epochs. Hence to accurately determine the distribution of UCTs, FEDS propagates all UCTs to a common epoch. FEDS then determines the geocentric position of each UCT and generates the VRML file. Presented in Figure 1 is a sample VRML file showing the initial results of a Pegasus breakup. In this particular example, there are 43 distinct UCTs contained in small section of a cluster ring, clearly the result of a breakup.

All output from FEDS program is accessible to analysts on-line via Netscape. These Web pages contain information about all of the events detected over the course of the data set. Such a VRML archive is extremely useful for determining if a breakup is a recent, or rather represents an older event.

4. CURRENT RESULTS

FEDS has detected nine out of the ten known fragmentation events in the data set spanning ~600 days. The detected events ranged in size from three to one hundred and thirty-three objects. The algorithm used in this study defines that the minimum size for a detected fragmentation event as three objects. Since the typical micro-bin has a mean and standard deviation of less than one, the first stage of FEDS will be triggered by four objects. The second and third stages are used to eliminate UCTs that not part of a fragmentation. Therefore the theoretical minimum of three objects required for a breakup detection is a feasible limit backed by actual data.

One interesting feature of this study shows that FEDS is capable of detecting fragmentation events over extended periods of time. This is a direct result of the FPS-85 radar's cycle of losing track of UCTs and registering them as new ones. Currently a fragmentation event is detected about once per week, but most of these events are the result of an older event. The nine events detected were visible for a combined total of 84 appearances. In the future, this particular feature of the system may be useful in modeling

the evolution of fragmentation events because of its ability to identify and track UCTs over extended periods of time.

Thirty-one percent of the clusters detected by FEDS, however, are not the result of fragmentation events. These false alarms are usually identified quickly by either VRML files or by examining the EX & EY cards. Most of the false alarms occur at the beginning of the historical data set. There has only been one false alarm in the last 200 days. As FEDS acquires more data, the number of false alarms decreases.

The one fragmentation event that went undetected resulted from the collision between the French Military satellite CERISE and debris piece from a ARAINE rocket stage. In this case, three UCTs were created - two corresponding to the two parents plus one extra fragmentation debris. However, these UCTs were detected over the course of several days. Because FEDS requires at least three objects to be detected on a given day, not over the course of days, this particular breakup went undetected. This particular problem needs to be assessed in the future.

5. SUMMARY & FUTURE PLANS

FEDS is a quick response time analysis tool for automated detection of fragmentation events. On a daily level, the FEDS program runs in under half an hour. At the end of this time period, operators have access to several products:

- A listing of all possible fragmentation events. These events are true fragmentation events about 69% of time.
- Information about the breakup that includes all element sets involved (necessary for tracking and analysis).
- VRML code that displays the event in a three-dimensional graphics mode.
- An archive containing information about all previously detected events (useful in determining whether an event is the result of a recent or older breakup).

These products serve two main purposes:

- 1) they minimize the amount of time spent in determining whether a fragmentation event has occurred and
- 2) they provide all of the information necessary for tracking the resultant debris pieces.

One feature being considered for future development is an automated attempt to perform catalog matching on UCTs detected in a cluster. This information can be extremely useful for analysts attempting to determine the parent object of a fragmentation event. This information can also be used to establish that a given cluster is not a fragmentation event. The challenge of implementing this feature, however, is that the catalog maintenance of debris pieces is difficult. This process is typically done carefully by analysts and therefore is difficult to automate.

The FEDS system itself also raises two issues for future improvement. The first addresses the problem of the CERISE/ARIANE collision. The system failed to detect this event because the UCTs detected were scattered over several days..

The other issue for improvement to FEDS is a reduction in the number of false alarms detected. The third stage, detecting clusters, is the most appropriate place to focus on improving results.

FEDS is ongoing project at Lincoln Laboratory. It will continue to be a component of debris research carried out in Group 91.

¹ W.F. Burnham and R. Sridharan: "An Eglin Fence for the Detection of Low Inclination/High Eccentricity Satellites", Proc. Of the 1996 Space Surveillance Workshop, Ed: K.P. Schwan, MIT Lincoln Laboratory Project Rept. STK-245 Volume 1, April 1996.

Abstract

We describe a model-based image analysis system which automatically estimates the 3-D orientation vector of satellites and their sub-components by analyzing images obtained from a ground-based optical surveillance system. We adopt a two-step approach: pose estimates are derived from comparisons with a model database; pose refinements are derived from photogrammetric information. The model database is formed by representing each available training image by a set of derived geometric primitives. To obtain fast access to the model database and to increase the probability of early successful matching, a novel index hashing method is introduced. We present recent results which include our efforts at isolating and estimating orientation vectors from degraded imagery on a significant database of satellites.

Introduction

Estimating the 3-D orientation vector of a satellite and its constituent sub-components by analyzing images from a ground-based optical surveillance system can be a relatively inexpensive way to support analysts in determining satellite ID, anomalous behavior, nominal configuration, and mission status, and as a way of confirming alternative pose information. However, estimating the 3-D orientation vector of any object from its 2-D image is difficult because the various 2-D images which can be formed from a 3-D object can be quite different from different viewing angles, and because ambiguities can result for objects with symmetries.

Space Object Imagery (SOI) has characteristics which allows us to take advantage of certain techniques which have been developed in other computer vision applications. Accordingly, we have developed a SOI Image Processing Architecture (SOI-IPA) which is designed to automatically estimate satellite orientation from its 2-D images. In our problem formulation, we are building the architecture so that 3-D orientation vectors are estimated from a single image of a known satellite. However, we anticipate that the system will be modified in the future to handle multiple views and a large number of satellites.

Our architecture employs two steps: pose estimation and pose refinement. Pose estimation attempts to determine the rough pose of a given satellite image by matching the image pose with previously observed (and truthed) images - usually derived from synthetic models. Pose refinement estimates the 3-D orientation vector for each component of the satellite by extracting features and analyzing the photogrammetric information which can be gleaned from the image.

This architecture incorporates several noteworthy capabilities. First, pose estimation employs use a fast eigen-indexing technique to accelerate the matching process. Second, models stored in the model-database are constructed from high-level primitives so that the representation that is concise and corresponds to satellite components. Third, the orientation vector of each satellite component is estimated by both moment based calculations and by using surface normals.

SOI Data

SOI imagery has certain characteristics, some of which pose challenges, but others can be effectively exploited to simplify the system design. The most important characteristics are: 1) Satellites are imaged in a large variety of poses, 2) Potentially both high- and low- resolution imagery, 3) Non-cluttered background, 4) Rectangles are reasonable primitives for use as descriptors of many satellite sub-components, and 5) Most satellites are symmetric with respect to their major axis.

Because some measured SOI images are degraded substantially by atmospheric turbulence and sensor mis-calibration, only a subset of the collected images are sufficiently detailed to realistically allow for orientation-vector processing, e.g., see Figure 1. Consequently, our system development has been based on the use of synthetic images. These images have no distortion and irregularity compared to their real counterparts, as

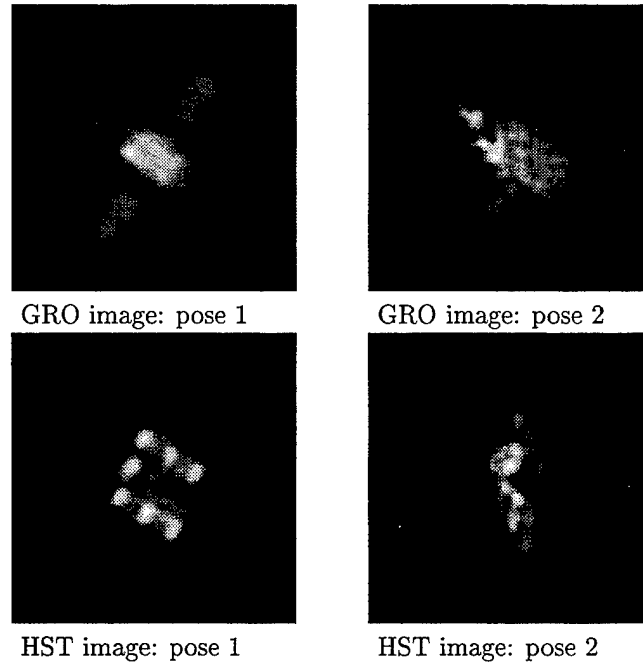


Figure 1: Measured images of satellites.

shown in Figure 2. While we report tests in which these synthetic images are degraded realistically to stress the system, we are currently collecting measured images which can be used to test the system under more realistic conditions.

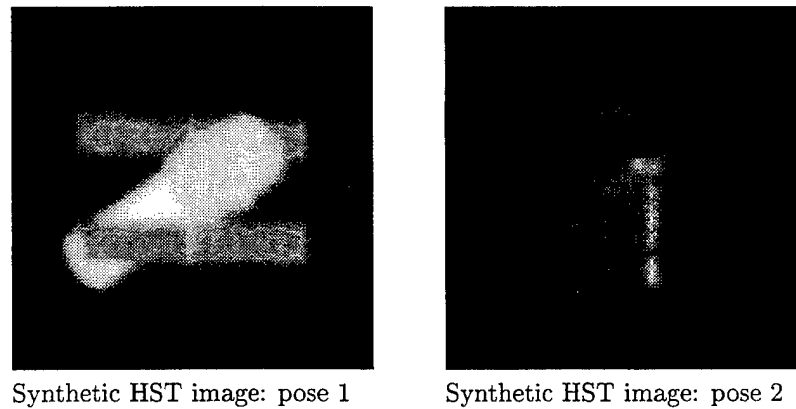


Figure 2: Synthetic images of the HST satellite

Architecture

As noted above, our model-based object recognition system uses a two step approach. Figure 3 shows the system-level block diagram.

The system consists of a number of modules. The image pre-processing, feature extraction, model-representation, eigen-indexing, and model-matching modules draw from pre-computed models in the model database to perform pose estimation. Pose refinement also uses the image pre-processing and feature extraction modules, as well as the results of the model-matching module to produce the final orientation vector.

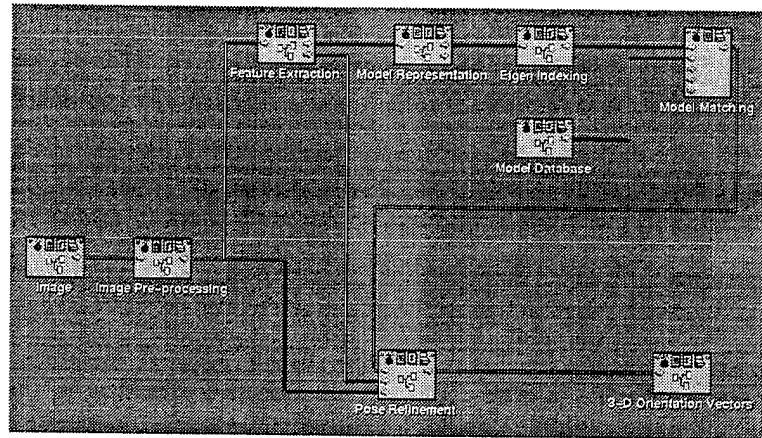


Figure 3: System block diagram

Model Database

The model-database is constructed off-line. In order to ensure that the database can be used effectively and efficiently we need to consider two issues. The first issue is model representation. Good feature representation can reduce storage requirements and provide computational advantages, and is discussed in more detail below. The second issue is model matching which determines how efficiently the model-database can be accessed. We employ an indexing technique called *eigen-indexing*, which is also described below.

Image Pre-Processing

Since any particular grey-level image may have pixel intensities which are only a subset, e.g., 32 to 138, of the full range of available intensities, e.g., 0 to 255, the image pre-processing module uses non-linear histogram stretching to expand the range of the pixel intensities of the image over the entire available range of intensities. We use a non-linear, adaptive algorithm which first determines the original range of the intensities, and then quadratically distributes these values to utilize the entire dynamic range. This process brightens the darker parts of an image disproportionately, and helps to bring out additional detail. An example is shown in Fig.4.

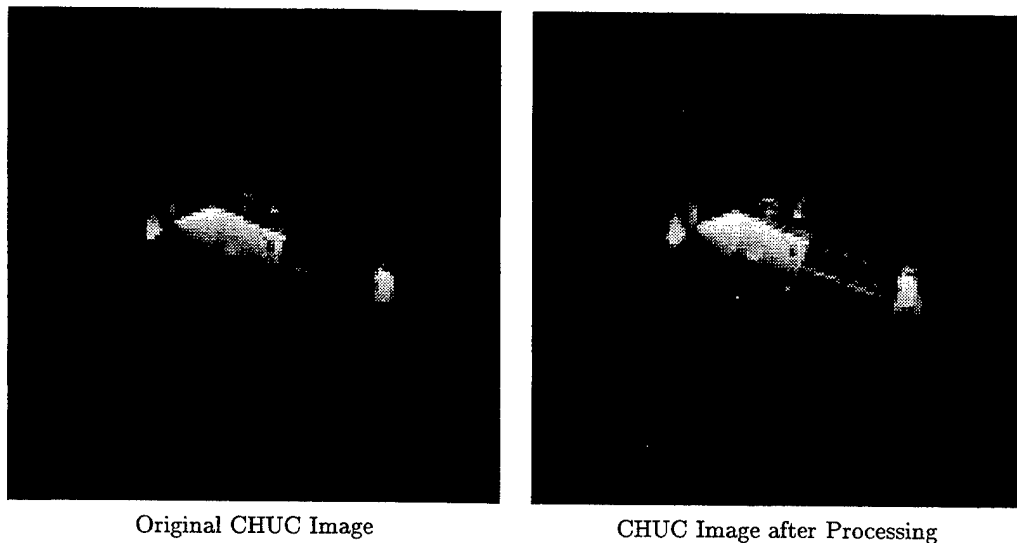


Figure 4: The results of using non-linear histogram stretching.

Feature Extraction

Most model-based object recognition systems are driven by feature extraction [1, 2, 3]. In our problem, where the orientation of satellite and its subcomponents are desired, the high-level geometric shapes which correspond to the satellite components are desirable features. To represent the satellite model we use a number of rectangles, each of which ideally corresponds to one satellite component. To extract these features, we use two steps: 1) image segmentation, and 2) rectangle extraction.

Image Segmentation

This process segments the image into a number of regions, each of which ideally corresponds to a satellite component. The process includes:

- removing the texture (2nd order intensity patterns)
- segmenting the image based on the processed histogram,
- performing an opening operation,
- performing a labeling operation,
- partitioning the image into segments based on the labels.

In order to effectively segment the images and make the segmented region interiors relatively uniform and free of holes, we use texture analysis as the first step in the processing. We use Laws matrices [4] to filter the image with a set of small convolution masks to produce filtered images. Each filtered image is processed with a local texture energy filter to generate an image with regions corresponding to specific textures, and then these images are re-combined to form a composite image. The final image will show significantly reduced 2nd order effects due to texture, and this makes locating good thresholds in the histogram of the processed images much easier. An example of the histograms for an image before and after this operation is shown in Fig. 5.

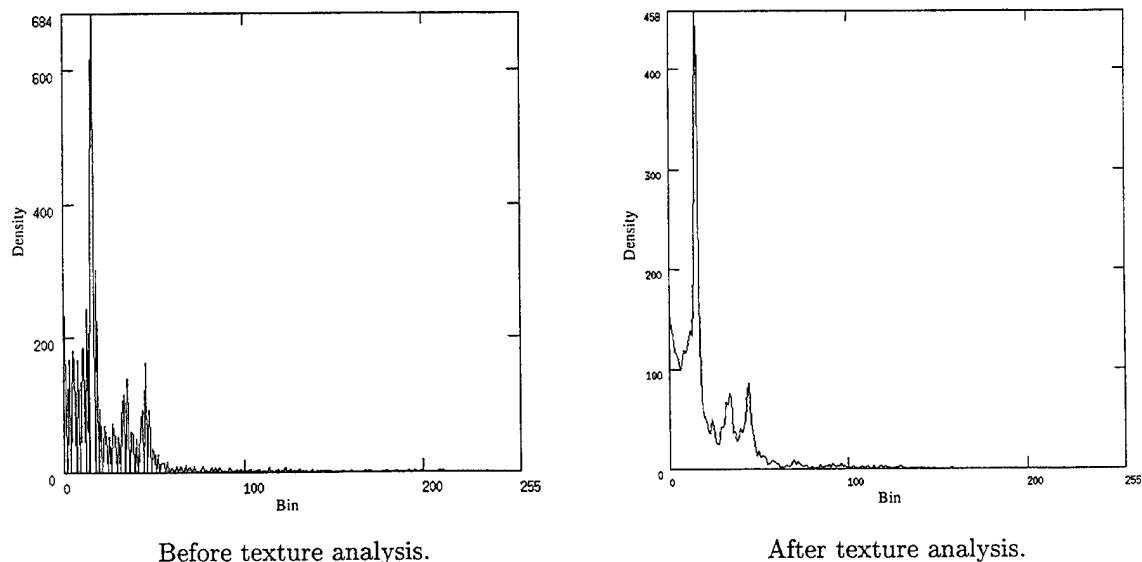


Figure 5: Histogram modification via texture analysis.

The remainder of the segmentation process is illustrated by Figure 6. Subsequently, the segmented images are presented individually to the shape extraction module from which a number of rectangles are extracted.

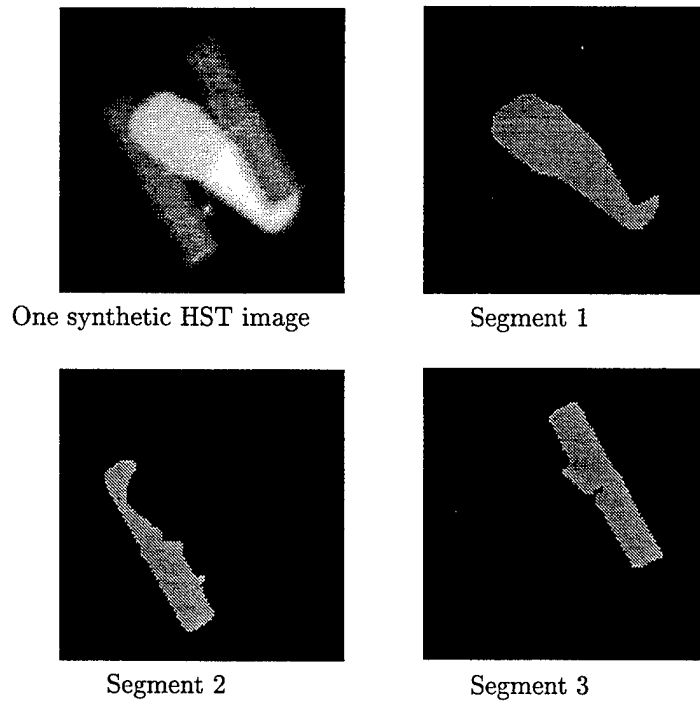


Figure 6: Image segmentation, a synthetic HST image and three segments

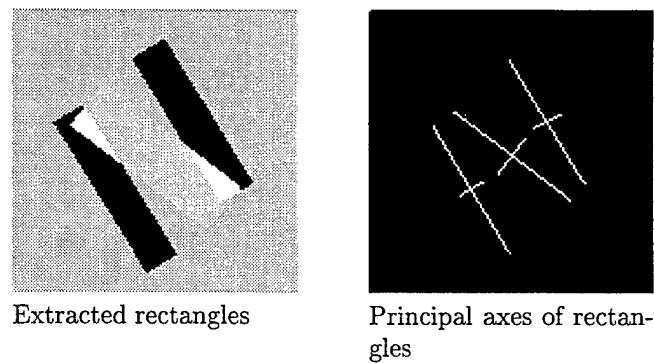


Figure 7: Extracted rectangles for the segments

Shape Extraction

To find the best fit rectangle for each segment, the centroid and central moments of each segment is calculated. From these moments, we derive the principal axes of the region. We use these two principal axes to represent the best fit rectangle. Figure 7 shows the extracted rectangles for the three segment regions. This set of rectangles is used as a model representation of the satellite.

Pose Estimation

As mentioned earlier, the pose estimation module determines the rough pose of the satellite. The rough pose should tell us 1) how many components are presented in the image, 2) how these components are organized, and 3) roughly how the components are oriented.

Feature-based model matching is a conventional method for 3-D object recognition and can be used to find the satellite's rough pose. Each entry in the model database corresponds to a particular pose of the satellite,

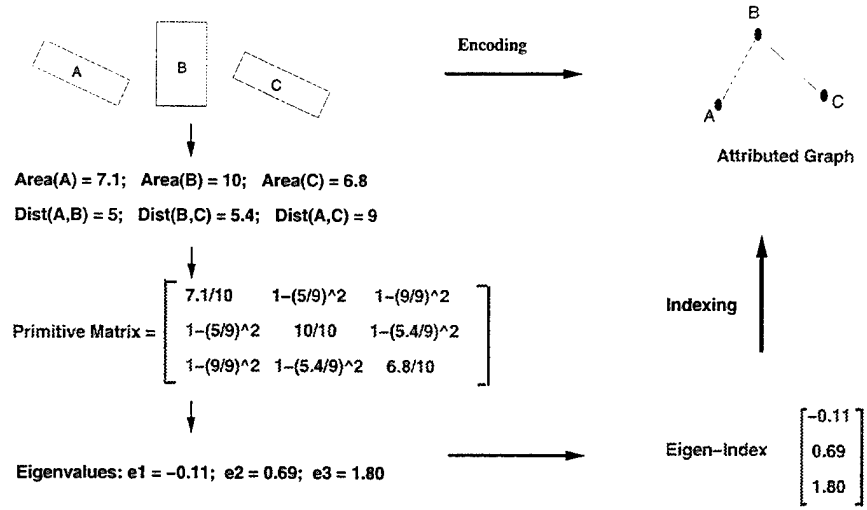


Figure 8: Procedure to form eigen-index

and features extracted from the image are matched with those of the model in the database. The best match tells us the rough pose of the satellite. However this is a graph matching problem and is known to be NP-complete. Thus, model matching across the whole model database is computationally expensive.

To circumvent this problem, a number of indexing techniques have been proposed. [5, 6] The basic idea is to associate a numerical key with each model in the database, and find the matching candidates by comparing the key for the feature representation of the image with the key of each model in the database.

Because each model in the model database corresponds to a particular pose of the satellite, in order to apply this indexing idea to our pose estimation problem we need to find some viewpoint dependent features. Such features will, hopefully, uniquely characterize the model for a given viewpoint. The most obvious feature is the number of geometric primitives (rectangles). Other features, such as the areas of the rectangles and the distances between these rectangles, are also good viewpoint dependent variables.

Based on these arguments, we define a N-by-N matrix where N is equal to the number of rectangles in the model. The entry (i, i) is equal to $\frac{a_i}{a_{max}}$, where a_i is the area of the i th surface and a_{max} is the area of the rectangle with the largest surface area in the model. The entry (i, j) is equal to $1 - (\frac{d_{ij}}{d_{max}})^2$, where d_{ij} is the distance between the center of the i th rectangle and the center of the j th rectangle and d_{max} is the maximum distance between any pair of the rectangles. Thus entry (i, j) approaches to 0 if the i th rectangle and the j th rectangle are far away from each other and approaches to 1 if they are close to each other. Consequently, the off-diagonal elements of the matrix encode adjacency information of the rectangles in the model. We then calculate the eigenvalues of this matrix and store them in an array in ascending order. This array is used as the index key to this particular model. These procedures are demonstrated in Figure 8.

The eigenvalues of the primitive matrix defined above encodes the model concisely because:

- the number of primitives in the model is equal to the number of nonzero eigenvalues of the matrix;
- the resulting eigenvalues are scale, 2-D rotation, and shift invariant;
- the eigen-index is permutation invariant (eigenvalues invariant with respect to ordering of primitives).

The eigen-indexing process is completed by calculating the Euclidean distance between the index of the model-representation of the image and those of the models in the model-database and choosing the model with the smallest distance. For two indices with different dimensions, the index with the smaller dimension is

zero padded to make the dimensions equal. Effectively, we assume that the indices with missing dimensions are projections of those with larger dimensions, as would occur with occluded sub-components.

Pose Refinement

The pose refinement module determines the 3-D orientation vector of each component of a satellite, namely the body and sub-components of the satellite. To do so we need to use the rough pose information extracted from the pose estimation module which tells us how many components are there in the image and roughly how these components are organized. The pose refinement module need to 1) identify each of these components, 2) discriminate the major and minor principal axis of each component, 3) calculate the 3-D orientation of each component.

To identify each satellite component, we use a simple technique based on moment calculation. Because each component is represented by a rectangle, the question now becomes which rectangle represents the body and which represent the sub-components. To identify the body, we use the fact that the body typically in the center of the other components. We calculate the centroid of the satellite by taking the average of the areas of all the rectangles and calculate the distance between this centroid and the center of each rectangle. The rectangle which represents the body is selected by the shortest distance. The remaining rectangles are thus sub-components. From these sub-components we further find the sub-component which has least occlusion by choosing the rectangle with the largest area. This least occluded sub-component is used to calculate the orientation vector of the collective sub-components.

To find the major and minor principal axis of the body we use the two principal axes of the body rectangle. However, the relative length of these two axes can't be used to tell which one is major and which one is minor because of the projection effect. We discriminate the major and minor axes based on the fact that the mass on each side of the major principal axis are close to each other. The mass is calculated by using the area of all the rectangles. After the major principal axis of the body has been found, finding the major principal axis of each sub-component rectangle is relatively easy because they are defined to be perpendicular to the major principal axis of the body.

After the major and minor principal axes of the body have been selected, calculation of the 3-D orientation of the body is straight forward. This is because the satellite body is typically a cylinder and rotation around the axis of the cylinder does not change the 2-D projection. The 3-D orientation of the body is defined as (θ, α) . θ is the angle between the major principal axis and the horizontal axis. α is defined as the angle between the axis of the body cylinder and the image plane, so that $\cos(\alpha) = \frac{Length/Width}{(Length/Width)_0}$, where $Length/Width$ is the measured ratio of the major principal axis over the minor principal axis and $(Length/Width)_0$ is the actual ratio of the body cylinder.

Unfortunately we can't apply the above method to calculate the 3-D orientation vector of the sub-components because satellite sub-components are typically flat plates or beam structures, and rotation around the plates' major principal axis will change its aspect ratio on the 2-D image. However the fact that most sub-components are flat (or can be adequately modeled by flat plates) means that the surface normals of each point of the plate should be close to each other. Thus using the sub-component rectangle to identify the sub-component region in the original image, and taking the average surface normal of this region will give us the estimation of the 3-D orientation of the sub-component. From this discussion, we defined the 3-D orientation vector of the sub-component as (θ, α) . θ is the angle between the major principal axis of the sub-component and the horizontal axis. α is the angle between the sub-component plate and the image plane. This angle is calculated using the surface normal technique described above.

Table 1 shows the calculated orientation vectors of both body and sub-component for the four synthetic HST image in Figure 2.

System Performance

Currently, since the measured SOI images are sometimes degraded substantially by atmospheric turbulence (seeing) and the diffraction of the telescope, only a subset of all of the collected images are sufficiently

Table 1: Estimated 3-D orientation vectors of HST in four different poses

	Main body (θ, α)	Solar panel (θ, α)
pose 1	(28.14, 52.32)	(-0.68, 6.99)
pose 2	(76.16, 67.52)	(X, X)
pose 3	(-37.89, 37.62)	(-58.78, 13.95)
pose 4	(-89.17, 56.09)	(59.25, 11.42)

detailed to realistically allow for orientation-vector processing. Consequently, our preliminary testing uses only synthetic data.

By studying the real satellite images, we find that image distortion which is due to seeing and telescope diffraction is more prominent than sensor noise. Thus, for these preliminary tests, we only test how seeing condition and telescope diffraction affects the orientation vector estimation. The image distortion due to seeing and telescope diffraction can be characterized by a point spread function (PSF).

In the following test, a Gaussian mask is used to blur the synthetic images to obtain distorted images. We use the clean images to form the model database and the blurred images to test how image distortion affects the pose estimation and pose refinement.

Evaluation of Matching Accuracy

First we evaluate the matching performance on pristine synthetic HST images. The experiment procedure is as follows:

- construct the model-database by using a set of clean images, each of which corresponds to a particular pose of the HST satellite.
- blur the clean images with a blurring mask to form a set of distorted images which are used as testing images.
- apply the testing image to the pose estimation module and find a model in the model-database.
- generate the confusion matrix.

Figure 9 shows how the synthetic HST image is distorted by a Gaussian blurring mask with $\sigma^2 = 20$. Table 2 is the matching confusion matrix generated by pose estimation module for this distortion level.

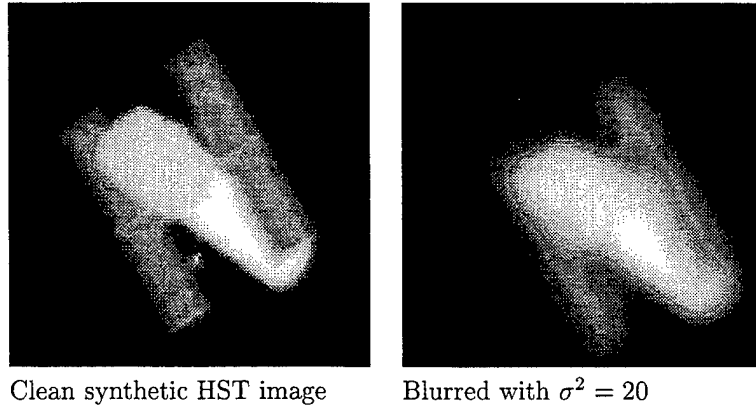


Figure 9: Comparison of clean and blurred synthetic HST images

Table 2: Confusion Matrix for $\sigma^2 = 20$

	HST1	HST2	HST3	HST4
HST1	1	0	0	0
HST2	0	1	0	0
HST3	0	0	1	0
HST4	0	0	0	1

Evaluation of Pose Refinement

We have studied how image distortion affects the orientation vector estimation. The experiment is as follows:

- construct the model-database by using a set of clean images, each of which corresponds to a particular pose of the HST satellite.
- calculate the orientation vector via the pose refinement module for each model in the database.
- blur the clean images with a blurring mask to form a set of distorted images which are used as testing images.
- apply the testing image to the pose estimation module and find a model in the model-database.
- do model matching to find the feature correspondence between the model of the testing image and the model from the model database.
- use pose refinement module to find the orientation vector.
- compare this vector with the ground-truth vector, which we know because we know the image from which the distorted image originated.

Figure 10 shows RMSE of the estimated orientation vector verses σ^2 for the four different angles of the satellite components, namely, (θ, α) of the body and (θ, α) of the solar panel. For this figure, the performance is averaged across the available CHUC images, where 45 of the 74 images have both body and panels visible.

Conclusion

We have developed a 3-D orientation vector estimation system for SOI images. For efficiency in the model matching, a novel indexing method is introduced which reduces the number of model candidates. Finally, after the correct model has been located in the model database, the 3-D orientation vector is calculated by a pose refinement module. The overall system performance in terms of accuracy indicates, at least from our preliminary testing, that the system is reasonably robust. Of course, further testing and development is needed, in particular considering:

- a larger model database with more satellites and more poses,
- degrading both synthetic and measured images by adding both distortion and noise in a more realistic way,
- investigation of information fused from multiple views.

We are now in the process of two additional refinements to the existing system. First, we are working on developing texture matrices that are tuned to the satellite images and their inherent texture. This refinement should allow us to more accurately remove the texture from the images and do a better job of segmentation. Second, we are incorporating geometric-hashing techniques into the pose refinement module to allow us to determine the affine transform which gives rise to a particular image, as compared to the stored models. This refinement should allow us to do a better job of estimating the orientation vector of those sub-components that are planar.

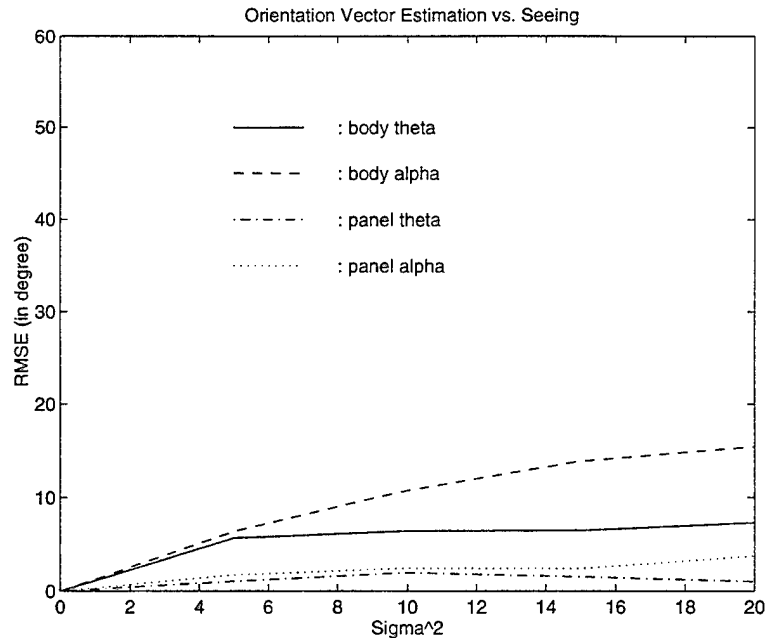


Figure 10: Performance of the orientation estimation at varying σ^2 levels

Acknowledgments

Support for this work was provided by the AMOS Research consortium.

Stan Ahalt was on sabbatical leave at University Polytechnica Madrid and gratefully acknowledges the support of the Dirección General de Investigación y Ciencia, Ministerio de Educacion y Ciencia of España.

References

- [1] R. Bolles and P. Horaud, "3DPO: A three-dimensional part orientation system," *Intl. J. Rob. Res.*, vol. 5, no. 3, pp. 3–26, 1986.
- [2] R.A.Brooks, "Model-based three-dimensional interpretations of two-dimensional images," *IEEE Trans. Pattern Anal. Machine Intell.*, vol. PAMI-5, no. 2, pp. 140–150, 1983.
- [3] P. Flynn and A. Jain, "BONSAI: 3-d object recognition using constrained search," *IEEE Trans. Pattern Anal. Machine Intell.*, vol. 13, no. 10, pp. 1066–1075, 1991.
- [4] K. I. Laws, "Rapid texture identification," *Proc. of the 1980 SPIE conference on Image Processing for Missile Guidance*, pp. 376–380, 1980.
- [5] H. Sossa and R. Horaud, "Model indexing: The graph-hashing approach," *Proc. of Computer Vision and Pattern Recognition*, pp. 811–814, 1992.
- [6] K. Sengupta, *Object Recognition Using Large Modelbases*. PhD thesis, The Ohio State University, Mar. 1996.

Data fusion experiments with metric and photometric observations.

*Dick, J., Appleby, G., Sinclair, A., (Royal Greenwich Observatory, Cambridge, UK),
Liddell, P., Seidman, P., (Defence Research Agency, UK), &
Holland, D., (Ministry of Defence, UK).*

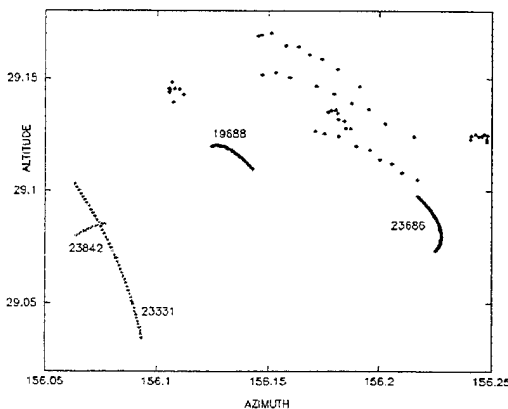
1. Introduction

The UK satellite observatory at Herstmonceux has two telescope systems. One telescope is equipped with a laser-ranger and with a co-mounted optical photometer; the other telescope is used for metric and photometric observations on GEO satellites. These three instruments are used to support in-house research work related to SOI and orbital dynamics.

Currently, part of the site's defence research programme is targeted at providing i) improved matching between ephemerides and observations, or "tagging", for GEO satellite clusters, and ii) a better understanding of satellite optical signatures. Here, we report on our work in these areas, and on our experiments in data fusion.

2. Cluster tagging

Figure 1
Observations and TLE predictions for the Astra
cluster, 96-11-09



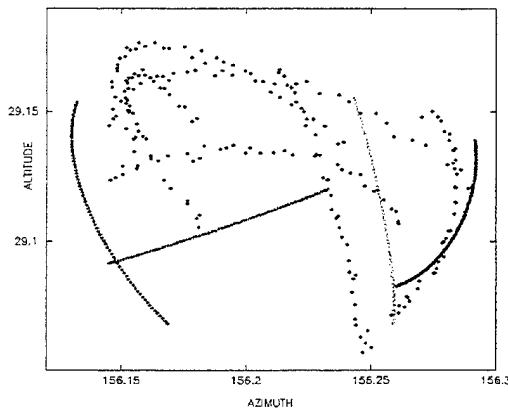
The Astra cluster is a group of six TV-relay satellites in GEO at 19° East, maintained within a box $\sim 0.15^\circ$ square on the sky. Because it is often difficult with radars to resolve the cluster (with consequent degradation of orbital information) it is useful to observe these satellites optically with consistent tagging. To improve tagging consistency, we have tried two methods: i) precision orbit determination and propagation using in-house code, and ii) linking the metric observations with photometric observations.

The Passive Imaging Metric Sensor (PIMS)^[1] at Herstmonceux was used to obtain a series of metric observations of the cluster members on six nights during November 1996. Each night, tracks up to seven hours long were obtained. Figure 1 shows as individual points, the observed positions $\{alt, az\}$ of the satellites during the night of November 9/10 compared with their tracks (full lines) predicted using two-line

elements (TLEs); SDC numbers are shown next to the tracks. The positions and motions of the satellites are only poorly represented by the predictions, with differences of up to 0.2° ; the predicted positions of two of the satellites, Astra 1B and 1C, are outside the bounds of the plot axes. The predictions offer little clue as to the correct identification of individual cluster members, because not only are the predicted tracks offset from the observations, but also the orientations and lengths of the tracks bear little resemblance to any of the observed tracks — this implies that, in particular, the orbital inclinations and eccentricities are poorly determined.

So, it follows that the predictions do not help in the difficult task of tagging of a given satellite from one night to the next, and it is impossible to tag correctly if several days elapse between sets of observations. To address this point, we carried out an experimental orbit determination process for each satellite, in a bootstrap manner, using in-house code^[2]. The differential orbit-determination scheme requires initial values of the satellites' state vectors which we derived from the TLEs, noting that for this purpose correct — absolute — identification of each satellite is not required (or possible). Orbits were computed by numerical integration of the equations of motion, using a force model which includes the the gravity field of the Earth, Sun, Moon and planets, and solar radiation pressure.

Figure 2
Observations compared with predictions for four
cluster members, 96-11-18

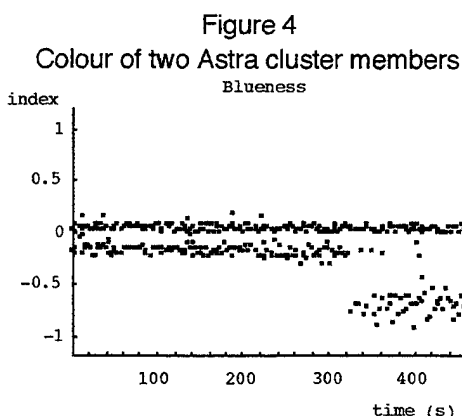
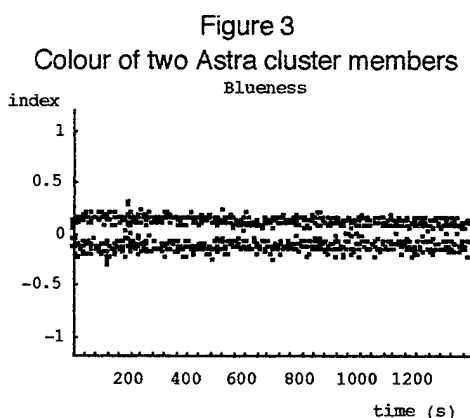


The computed orbits were then compared with PIMS observations from three nights (November 8, 9, 15), when efforts were made to identify the same satellites on the three nights, using plots similar to that shown in Figure 1. The residuals were used iteratively to improve the orbits by adjusting the state vectors, a coefficient of solar radiation, and an empirical along-track acceleration. In this way, observations of four satellites on the first night were identified with observations of the same satellites on the second and third nights, and eight-day orbits were fitted through the data.

The post-solution residual RMS values were about $6''$, close to the precision of the observations. We found that a single orbit could be fit successfully only to observations of the same satellite; the method identifies the same four satellites over the period November 8-15. We believe that the two sets of observations on each night that could not be fit by computed orbits indicate that those satellites had been maneuvered; all attempts to fit orbits to subsets of these data failed.

We tested the accuracy and predictive quality of the four successful orbits by extrapolation and comparison with the PIMS observations of November 18, 21 and 23. Two of the orbits, when extrapolated, compared well with two sets of observations taken on the night of November 18, clearly identifying the same satellites. The offset between predictions and observations on November 18 was about 1'. The other two orbits compared less well with the observations, but still well enough to identify the objects.

The results are shown in Figure 2, where the dots represent individual observations of all cluster members taken throughout the five-hour observing session. The full lines show the predicted positions of all four satellites using the extrapolated orbits. Further extrapolation of the orbits and comparison with the data of November 21 and 23 confirmed the quality of the two best orbits, which again uniquely identified the objects. However, attempts to include the data into the orbital fitting process failed, and we conclude that the two objects have been maneuvered at some time between November 18 and 21.



To help further with the tagging process and, in particular, to try to maintain tagging consistency over extended periods of time, we have taken photometry of the cluster members with the FOX twin-channel CCD photometer system^[3] to discover if useful colour differences exist between the cluster members. Simultaneous FOX observations of two satellites do show colour differences (Figure 3) but further long photometry observations on the whole cluster are required before the tagging value of colour and photometric signature can be assessed.

For example, if colour is a function, as expected, of satellite movement then sometimes quite quick changes in colour — and thus movement — can be observed (Figure 4). Whether such changes aid in, or distract from, the process of unique satellite identification remains to be determined.

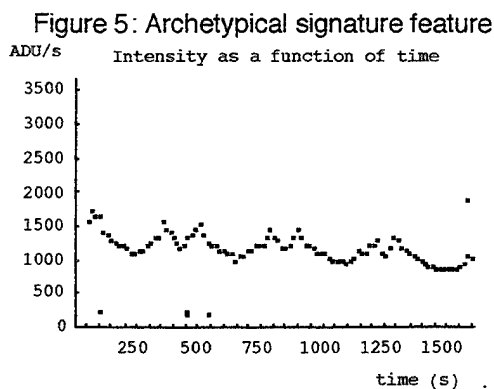
Thus, optical metric observations from a single site, combined with precise orbit determination, can help to remove ambiguity in identification, and to monitor orbital maneuvers; SOI photometry's value remains unclear at this time.

3. SOI signature interpretation

Photometry is a simple monitor of a satellite's health and an indicator of major surface features. Although optical imaging is a vastly more effective technique, no operational ground-based systems are capable of imaging deep-space targets. Radar doppler-imaging can see targets in deep-space but such work requires significant resources and is difficult against objects with minimal differential motion in range.

Over the last few years, we have used a series of photometers to gather optical signatures of satellites as a guide to their health and shape. The current generation of photometer is based around a twin-channel CCD system called FOX^[3]; the passbands of the channels are chosen to help identify different surface materials. We have an on-going programme of surface spectral characterization by laboratory measurements and results from this programme assist in the choice of photometer passband.

The interpretation of SOI signatures is quite challenging because of the number of parameters that determine the signature at any instant. In particular, the specular index of a surface, the surface's albedo, and the configuration of that surface and its light sources in the observer's image plane all affect the signature dramatically; the multitude of surfaces on even an unsophisticated satellite means that an unambiguous solution to the problem is impossible. However, we can choose to make assumptions about the principal surfaces and let them aid our morphology; observations of the same satellite — or members of the same constellation — under different Sun-satellite-observer configurations also help us work towards an understanding of a satellite's signature.



For one constellation, a archetypical signature feature is shown in Figure 5. We observe this feature often, on many constellation members, and for long periods of time.

We find the repeating nature of the feature difficult to interpret because it could be caused by a number of diffuse surfaces on a tumbling structure or by a specular surface caught on the edge of its reflection.

For example, the following two computed signatures in Figure 6 are from models i) with two diffuse surfaces and ii) a single specular surface, but with different motion models: one is tumbling, the other is rocking.

To help resolve this ambiguity, we have used simultaneously-acquired laser-ranging data to estimate the relative motion of the laser-reflecting surface to the centre of gravity. In cases where the object is tumbling, there is a clear, cyclic variation in the range residual.

Our computer model requires only a few degrees of rock to reproduce the observed signature (Figure 5); analysis with FFT techniques on the range-residuals fails to show any variation above the noise floor of the observations, implying that any relative motion is small.

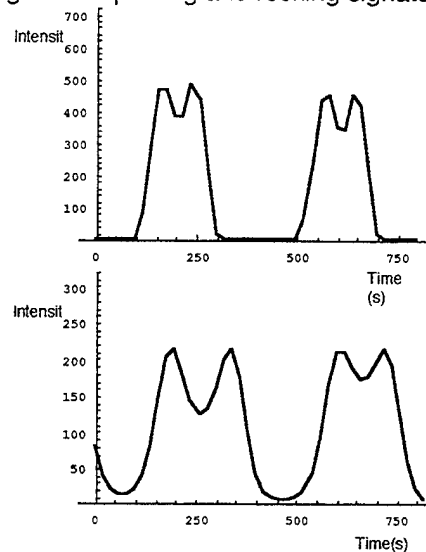
Although not proof-positive, fusing ranging and photometric observations and modelling has produced a consistent result.

Acknowledgements

The SLR is operated by the Royal Greenwich Observatory on behalf of the UK Natural Environment Research Council, the Department of Trade & Industry, and the Ministry of Defence. The FOX and PIMS systems are funded by the Ministry of Defence; their work programme is managed jointly by the Defence Research Agency and the Ministry of Defence.

- [1] Dick, J.S.B., Sinclair, A.T., Liddell, P., Holland, D., "PIMS: Progress report on a deep space metric sensor project," Proceedings of the 1996 Space Surveillance Workshop, MIT Lincoln Laboratory
- [2] Sinclair, A.T., Appleby, G.M., "SATAN — Programs for the determination and analysis of satellite orbits from satellite laser ranging data," SLR Technical Note 8, Royal Greenwich Observatory, 1986.
- [3] Dick, J.S.B., Sinclair, A.T., Greenaway, A., Liddell, P., "Initial results from a new sensor system on the UK SOI facility at Herstmonceux," Proceedings of the 1995 Space Surveillance Workshop, MIT Lincoln Laboratory

Figure 6: Spinning and rocking signatures



The Midcourse Space Experiment (MSX)

W.C. Smith (BMDO), C.S. Mansperger (PRA)

Abstract -- The Midcourse Space Experiment (MSX) is the first and only extended duration, multi-wavelength (0.1 to 28 mm) phenomenology measurement program funded and managed by Ballistic Missile Defense Organization (BMDO). During its 12 month cryogen lifetime and five year satellite lifetime, MSX will provide high quality target, earth, earthlimb, and celestial multi-wavelength phenomenology data and demonstrate space surveillance and other midcourse sensor functions and key technologies. The data are essential to fill critical gaps in phenomenology and discrimination databases, furthering development of robust models of representative scenes, and assessing optical discrimination algorithms. Eight scientific teams formulate experiments which are performed by the sensors on MSX. The satellite is in a 903 km near polar orbit (99.4° inclination), with an eccentricity of 0.001. One dedicated target mission was executed out of Kauai, Hawaii. Several cooperative target missions have also occurred. MSX has collected more than a tera-byte of high quality data as well as demonstrating the ability to track and perform target discrimination.

Introduction -- The MSX satellite began its mission on April 24, 1996. It was launched on a McDonnell Douglas Delta II booster from Vandenberg Air Force Base, CA. MSX is a multi-year space technology demonstration and data collection experiment addressing three main objectives for the BMDO:

- Functionally demonstrate the capability of midwave infrared, long wave infrared, ultraviolet, and visible sensors to acquire, track, and discriminate objects associated with the midcourse (after booster burnout and before re-entry) phase of a ballistic missile flight, and of resident space objects;
- Collect a statistically significant natural phenomenology and target signature database to improve and validate models and serve as a system design database;
- Validate key sensor technologies in an operational environment over extended periods to support technology transfer. Evaluate extended on-orbit performance data on focal planes, optics, and processors.

In the process of meeting these BMDO objectives, MSX is also contributing significantly to the understanding of scientific issues of national interest such as global change, remote sensing, astronomy, astrophysics, and orbital debris.

Program Overview -- The Midcourse Space Experiment is the first extended duration, multi-wavelength phenomenology measurement program sponsored by BMDO. The period during which the cryogenically cooled infrared sensor will operate is referred to as the cryogen phase (the first 12 months). The remainder of the mission is called the post-cryogen phase.

The Mission Operations Center located at John Hopkins University Applied Physics Laboratory (JHU/APL) contains the primary Mission Control Center, the MSX Tracking Station, the Mission Processing Center, the Attitude Processing Center, and the Operations Planning Center.

All MSX data (science data, calibration records, certified software and final calibration factors) will be archived at the Backgrounds Data Center at the Naval Research Laboratory. The Backgrounds Data Center maintains an on-line catalog to aid in data selection.

The primary sensor is the SPace InfRared Imaging Telescope (SPIRIT III), a cryogenically cooled infrared sensor. It is the most advanced infrared instrument yet launched into space. In the long wavelength, SPIRIT III has approximately the same sensitivity but 40 times better spatial resolution than the Infrared Astronomy Satellite. Developed by the Space Dynamics Laboratory of Utah State University, SPIRIT III includes a five-color, high-spatial-resolution scanning radiometer and a six-channel, high-spectral-resolution, fourier-transform interferometer-spectrometer. SPIRIT III is the primary sensor for target and background data collection. Its key features include rejection of light from sources outside the field of view, and high spatial and spectral resolution. The infrared radiometer and interferometer detector bandwidths were chosen to address particular data collection needs, including: thermal discrimination, cold target detection, earthlimb clutter measurement, and atmospheric composition measurement.

Ultraviolet and Visible Imagers and Spectrographic Imagers (UVISI) is a Johns Hopkins University/Applied Physics Laboratory built instrument system with five spectrographic imagers, and four ultraviolet and visible imagers. UVISI provides complete spectral and imaging capabilities from the far ultraviolet through visible wavelengths.

The Space-Based Visible (SBV) instrument, equipped with a charged-coupled device, is a visible band telescope with a six-inch aperture and image processing electronics. Built by MIT/Lincoln Laboratory, SBV will demonstrate an above-the-horizon surveillance capability in visible wavelengths from a space platform. The SBV sensor will also supplement the target and background phenomenology data collected by SPIRIT III and UVISI. The spectral coverage of SPIRIT III, UVISI, and SBV is illustrated in Figure 1.

The On-board Signal and Data Processor (OSDP), built by Hughes Aircraft Co., conducts real-time signal processing using data from SPIRIT III for target detection and tracking. It also provides information about radiation effects on state-of-the-art semiconductor devices.

The contamination sensors, provided by JHU/APL, include five quartz crystal microbalances, a pressure sensor, neutral and ion mass spectrometers, and flash lamps to illuminate contaminants in the sensor fields-of-view. These sensors were chosen to measure specific contaminants (such as water vapor) in the spacecraft environment. These measurements will validate the strict contamination control plan followed throughout the development of the satellite, enhance satellite contamination models, and measure contaminants in situ.

Satellite -- The MSX satellite (Figure 2) structure consists of three main sections: the instrument section, the truss structure, and the electronics section. The satellite structure was designed and built by JHU/APL. The attitude control hardware consists of four reaction wheels and three magnetic torque rods. The electronic section carries the warm electronics of all the instruments. Placing the warm electronics in this section minimizes thermal dissipation in the

instrument section, allowing the cryogenically cooled instruments to operate as cold as possible. The spacecraft weighs 2800 kg and excluding the two solar arrays measures 510 cm in length with a 150 cm by 150 cm cross section.

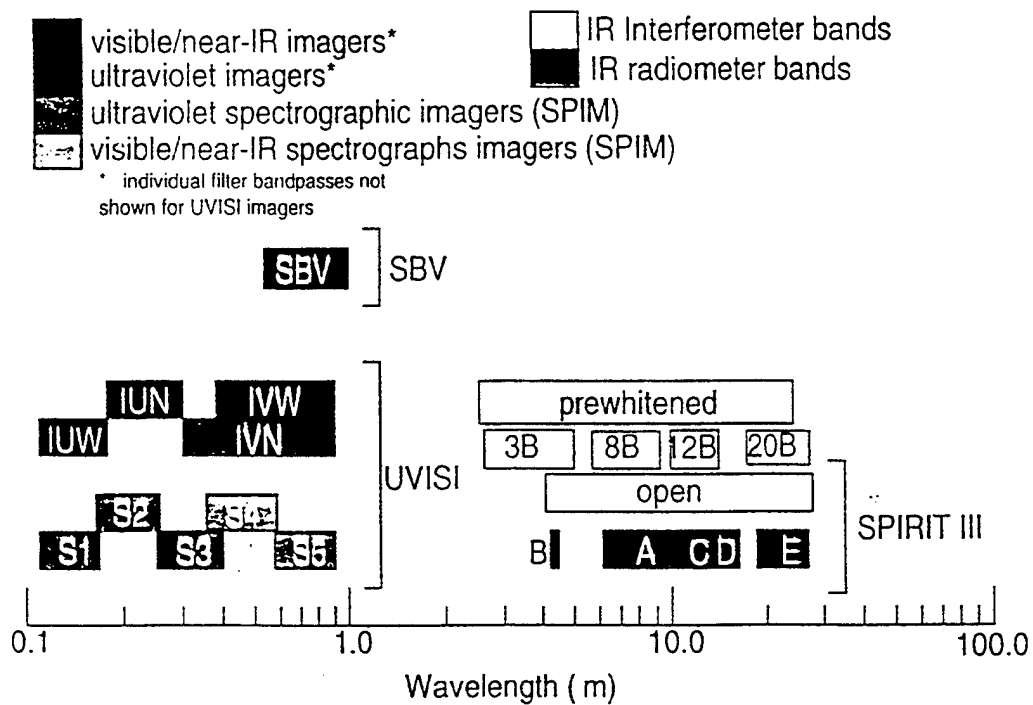


Figure 1. MSX Spectral Coverage

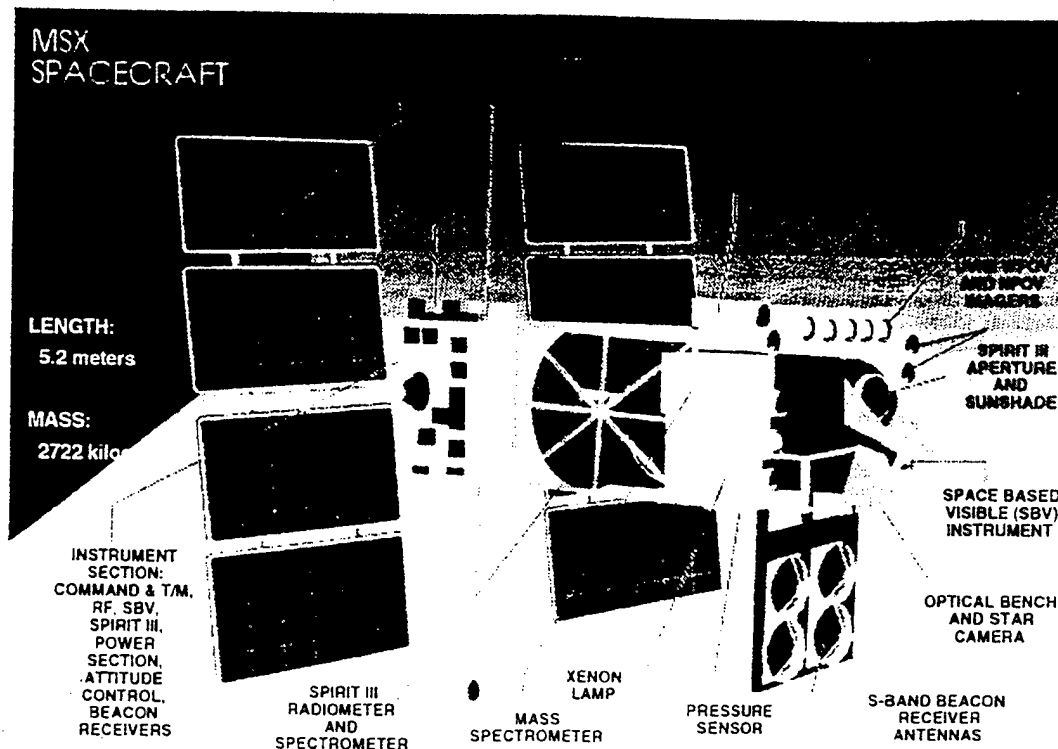


Figure 2. MSX Spacecraft

Scientific Teams -- The Project Scientist leads the experiment planning function. He interprets the MSX science objectives in light of evolving BMDO and science community requirements. The Project Scientist also chairs the Principle Investigator (PI) executive committee. This group reviews experiment plans, coordinates with the Mission Planning Team and supporting organizations to execute the experiments, and certifies the analyzed results of the experiments. Each PI and his team of experts from various organizations are responsible for defining the science and modeling requirements in their category, designing the experiments, and analyzing the resulting data to satisfy MSX mission objectives and requirements. A brief mission objective for each of the eight PI teams along with some results to date follows.

The Space Surveillance team's experiments provide a functional demonstration of the space-based surveillance capability and address the detection of space targets against stressing backgrounds. This analysis focuses on surveillance sensor performance, network integration, critical issues for space surveillance, and applications to future systems. For example, MSX will track along the orbits of three known resident space objects (RSO) that have fragmented: Cosmos 2227 in LEO, a Titan transtage rocket booster in GEO, and Cosmos 1278 in a geotransfer (highly eccentric) orbit. A search around these known objects while tracking at the rate of the parent RSO should permit identification of debris pieces generated by the fragmentation. Multi-spectral data from the SBV, SPIRIT III, and UVISI instruments can be combined to yield information about the albedo (percent reflectivity) and size of the object. These results address the existence of radar-transparent debris and provide data to update existing models at these altitudes.

The SBV hardware performance has exceeded expectation. The metric data analysis nearly meets with the desired goal. The experiment has already demonstrated search, acquisition and tracking capabilities as well as RSO metric discrimination and identification abilities. There has been successful fusion of space and ground sensors.

The Early Midcourse Target team concentrates on the phenomenology and functions associated with the boost through deployment phase of ballistic missiles. The team addresses target acquisition, deployment, and tracking against cluttered backgrounds, as well as radiometric and metric discrimination. They also will provide a definitive target signature database on NMD targets. They use the dedicated target and cooperative target missions for primary data collection. Targets of opportunity are used to supplement this data.

The MSX spacecraft is successfully collecting data on aircraft in Mid Wave Infrared (MWIR) against the hard earth and in five color LWIR on RSO's against space and earth limb background. Object sighting messages have been generated from relative target intensities, signature features and characteristics, and temperatures. MSX has demonstrated the ability to track deeper into the earth limb than expected with the appropriate clutter suppression filter. The MDT-II dedicated target mission was executed on August 31, 1996. High quality data was successfully collected in the infrared, visible, and ultraviolet. This dedicated target included a number of test objects deployed from the Operational Deployment Experiment Simulator, launched on the Strategic Target System booster. It was launched from the Kauai Test Facility in Kauai, Hawaii, and impacted in the broad ocean area north of the US Army Kwajalein Atoll. The Post Boost Vehicle launched on the STARS II booster deployed twenty-four midcourse objects. These objects represented a number of different target types and deployment techniques. All the target objects were deployed in sunlight and subsequently crossed the Earth's shadow into darkness.

The Cooperative Target team concentrates on the latter phase of a missile's exoatmospheric trajectory and demonstrates tracking and handover functions on credible targets. This PI team is concerned with payload evolution from post-deployment through reentry. They focus on thermal and dynamic discrimination, and target signature collection.

A successful TCMP 2B mission was carried out on July 15, 1996. High quality data was collected in the infrared and the visible. The signature events correlate to the maneuvers and deployments. MSLS was successfully launched on September 27, 1996. All five targets were deployed in accordance with the timeline. MSX performed to order, with all scheduled sensors operating. The Red Tigress III mission, executed on October 16, 1996, was successful. The three stage rocket obtained an apogee of about 400 km and impacted approximately 270 km downrange. Red Tigress III deployed 17 payloads consisting of over 42 objects that replicate enemy ballistic missile reentry vehicles and penetration aids. This mission was a pre-cursor experiment to the dedicated MDT III & IV flights in February, 1997. MSX performed as planned during the Red Tigress III mission. It was the only asset to collect LWIR measurements of individual payload objects during the middle of the flight.

Since targets are observed against various backgrounds, PI teams have been formulated to study terrestrial, earthlimb and celestial backgrounds. These teams make dedicated background measurements over a variety of conditions to provide real data to evaluate their impact on sensors and overall system performance. The Earthlimb team and the Short wavelength Terrestrial Backgrounds (STB) team obtain ultraviolet through very long wave infrared data which is required for evaluation of missile defense system performance against stressing earthlimb and terrestrial backgrounds. Earthlimb experiments focus on measuring earthlimb radiance, auroral emissions intensities, radiance, and structure, and on the spatial distribution and IR radiance of mesospheric clouds and terrestrial clutter. The STB team focuses on characterizing the terrestrial auroral and airglow limb and below-the-horizon spectral databases in the 110 to 900 nm wavelength range. The goal is to acquire a representative database on global, seasonal, diurnal, and temporal variations simultaneously in the ultraviolet through infrared wavelengths.

The initial measurement of infrared earth limb and infrared terrestrial backgrounds was made on 23 May 1996 at 09:30 to 10:00 UT in a push broom scan mode, observing a region from approximately 60 degrees south to 40 degrees north latitude. The spacecraft line of sight was maintained at an azimuth and elevation angle of 90 and 45 degrees in local vertical and horizontal coordinates, respectively, with azimuth referenced to the velocity vector. The infrared radiometer provided an image of the terrestrial scene in bands B1 and B2 with overall dimensions of 46 kilometers by 380 kilometers per minute. The 30 minute image created in this push broom scan included the region east of Australia, Indonesia, the Malaysian peninsula, Thailand and China. Band B2 recorded radiance contrast ratios of about 20 percent due to high altitude clouds. Band B1 showed little structure in the scene other than slow changes associated with large scale temperature changes in the atmosphere over this latitude range. Another measurement was made on August 17, 1996 in the region of eastern India north of Bangladesh. Again, Band B2 showed discrete features due to high altitude clouds. Band B1 showed significant spatial structure while both Band B1 and B2 showed a "mottled" structure.

The STB Backgrounds team has taken part in a number of Data Collection events that provided ultraviolet through near infrared observations of the earth's limb and ground in darkness and sunlight. Much of this has been taken simultaneously with the SPIRIT III mid-to-far infrared observations. The UV-Near IR data also includes stars occulted and refracted as they set below the horizon, aurora and lightning displays. Most of the data include wide and narrow field of view images in different spectral bands as well as hyperspectral spectrographic data. Analysis of the data is proceeding on different levels. Some of the imaging data is being processed for scene characteristics such as histogram moments, power spectral densities and auto-correlation parameters. Other data is being used to determine: the density of minor atmospheric constituents such as ozone, with altitude, at different locations on the earth; auroral particle energy characteristics; and temperature variations in the troposphere, stratosphere and mesosphere. Additional studies are being carried out to determine gravity wave activity in the mesosphere, ocean color, and terrain signatures and associated atmosphere corrections.

The Celestial Backgrounds team characterizes representative and stressing celestial backgrounds. The results of the celestial background experiments are upgrading the brightness/resolution databases to satisfy strategic defense system requirements.

Infrared observations have been taken of the center of the Milky Way galaxy and the Small Magellanic Cloud (SMC). The infrared is the best spectral region for measuring the thermal or heat radiation from the cool dust found in interstellar clouds and H II regions, regions of ionized hydrogen. Ultraviolet images have also been taken of the Small Magellanic cloud. While there are some UV photographic imaging of the SMC at higher spatial resolution, UVISI was the first ultraviolet instrument to image the entire SMC region with a combination of good spatial resolution and high sensitivity.

The Contamination team has oversight of contamination control and monitoring through the life of the program. They oversaw material choice and handling during hardware development and integration, through the contamination control plan. This plan has been validated by on-orbit data and is a legacy to future satellite programs. The contamination team is responsible for monitoring, modeling and documenting the effects of contamination (from the spacecraft and from the ambient environment) on optical sensors. The contamination experiments quantify contamination effects on optical sensor performance. The contamination team will update pre-launch models developed for use in predicting obscuration, measure in-flight contaminants, and characterize particulate and molecular contamination in the space environment which impair the functioning of space-based sensors and limit their effective lifetime.

The contamination instruments have been proven to be useful during the early operations when the molecular and particulate environments were utilized as inputs for decisions concerning the opening of the various optical sensors. They are also providing useful data on the cleanliness of the spacecraft during various maneuvers and will be used in predicting the cumulative effect of contamination on the quality of the optical sensors throughout the MSX mission life. In addition, a long-term database for the neutral and positive ion species in the thermosphere at the MSX attitude of 900 km is being developed for the various NASA atmospheric models.

The Data Certification and Technology Transfer (DCATT) team oversees the calibration of the sensors, certifies the quality of the data, and transfers the results of the technology demonstrations and lessons learned to other DoD programs. The DCATT team represents a unique approach to sensor characterization. The DCATT team is an integral part of sensor characterization, and as such provides the interface between the PIs and sensor vendors.

Pre-launch, the DCATT team worked with each sensor vendor to develop, implement, and document a sensor calibration plan. They also work to develop and implement in software a set of algorithms to calibrate the raw sensor data (CONVERT), and develop an automated process for verifying the quality of the data (Pipeline). This allows the production of high quality calibrated data in an automated, repeatable fashion. The certification technique used is similar to a method of process certification used in manufacturing.

Certification for all sensors based on flight data is complete. However, characterization of the instruments continues. The data from DCATT calibration and characterization experiments will be available for further analysis and processing to address other technical issues.

Summary -- MSX was successfully launched on April 24, 1996 and all sensors are operational. It is providing data to answer fundamental questions about the performance of BMDO surveillance systems, and providing environmental data of global interest.

Several successful target missions, both dedicated and cooperative, have been executed. MSX has performed well during these missions and gathered many high quality data sets. It has demonstrated the ability to track and discriminate different types of targets. MSX has also collected high quality data on background clutter against the earth, earthlimb, and celestial backgrounds.

MSX is also contributing significantly to the understanding of scientific issues of national interest, such as global change, (ozone chemistry, global warming, earth resources imagery), and basic science (astronomy, astrophysics and orbital debris, solar/terrestrial interactions, and celestial radiometric standards).

SPACECRAFT IDENTIFICATION BY MULTISPECTRAL SIGNATURE ANALYSIS USING NEURAL NETWORKS

C. J. Poelman (USAF/PL) & S. R. Meltzer (USAF/PL)

ABSTRACT

This study examines the feasibility of 1) identifying satellites by their spectral signatures and 2) developing an algorithm to automate the process. The efforts of this study focus on solving the problem of crosstaging deep space objects. Crosstaging is the misnaming of a satellite which occurs when the identity of a tracked satellite is unknown or when the identities of several satellites are commingled. This problem can occur due to variations in satellite orbits and/or delays between data collection. Sunlight reflecting off of a satellite creates a spectral signature. Satellite signatures may differ due to geometry and material properties. Spectral signatures of seven satellites were simulated using an image simulation software package and high-fidelity satellite models. These spectra took into account atmospheric degradation and were simulated for a variety of orbital parameters and different imaging times. These simulated signatures trained a neural network to identify the satellite. The trained network was able to accurately identify satellites based on their spectral signatures. This technology has application to the space analyst needing to identify satellites beyond the range of resolved imaging and detect anomalies on these objects.

1. INTRODUCTION

US Space Command is the organization responsible for tracking satellite orbits and monitoring their health and status. Occasionally these satellites are no longer in their expected positions due to maneuver, drift, or infrequent observations. Tracking radars and photometric observation systems can generally find and track the satellites, but may not be able to distinguish between the different satellites. In these cases it is possible for the satellites to become crosstaged, so that the operators are not certain of which satellites are which, or worse yet, incorrectly believe that they know the identities of the satellites. For low-earth orbit (LEO) satellites, ground-based optical imaging or wideband radar assets can help identify the satellites, but once satellites in deep-space orbits become crosstaged, there are few assets to help identify them. Deep space satellites are too distant to optically image, and generally lack sufficient rotation to form synthetic aperture radar (SAR) images.

This study explores the use of multi-spectral sensors to obtain additional information on deep space satellites, including health and status assessments in addition to satellite identification. Such sensors will be of maximum benefit to an operational user if they are accompanied by automated data analysis tools. For this reason, our study focuses on developing an automated spectral signature recognition algorithm, and showing that these algorithms can detect anomalous signatures. In addition to demonstrating the utility of the multi-spectral data to the operational users, these automated tools can identify patterns in the data which can determine important sensor design parameters, such as the choice of spectral bands.

We have chosen to use neural networks for spectral signature recognition and satellite identification for a number of reasons. Neural networks provide the ability to generalize from a set of examples and can be robust with respect to noisy input. Additionally, once trained to distinguish between a number of satellites, a neural network can be examined to determine which features of the input data most strongly contribute to its processing. By training the neural network with a number of input spectral bands and then examining the weights and internal connections of the network, we will be able to determine the most useful set of spectral bands for our sensor design. Since there are currently no multi-spectral space surveillance sensor data available, much of our effort to date has focused on generating simulated data for the training and testing of our algorithm.

The high-fidelity satellite models used for the simulations were created by the Phillips Laboratory. We began with models for Ekran, Gorizont and Molniya, three deep space satellites. The satellite models, two-line element sets, and ground station characteristics were then used by the Time Domain Analysis Simulation for Advanced Tracking (TASAT) code to simulate the satellite's spectral signature. These exoatmospheric signatures from TASAT were then atmospherically degraded using the Moderate Resolution Transmittance Code (MODTRAN).

A neural network was then trained to identify the different simulated spectral signatures. The ability of the neural network to generalize the results of the training was then tested by introducing previously unseen data. The results of this test showed that the network had the ability to differentiate between the satellites with minimal error.

This effort builds on a large body of previous research. Beavers collected multi-spectral and polarimetric data using three standard astronomical filters attached to an optical telescope.¹ He later performed similar experiments which investigated the effects of seasonal changes on the reflected spectra.² Prochko, et. al. developed non-atmospherically-degraded spectral signature simulations using the SATSIG/SATSIM simulation software, and demonstrated that the differences between the signatures of the SEASAT and DMSP satellites were substantial enough that it should be possible to distinguish between them.³ Payne used the TASAT software to predict spectral signatures and extended the simulations to include eight different satellites, showing that it should be possible to distinguish between general classes of satellites, though perhaps not between specific models of similar design.⁴ Her work also demonstrated the variation of spectral signature as a function of solar phase angle and viewing angle. Hrovat examined the use of hyperspectral imagers for observing satellites, and focused on studying the Signal to Noise Ratios (SNRs) of the expected signatures to predict that sufficient signal existed to discriminate between satellites.⁵ Caudill demonstrated the use of neural networks for identifying individual materials by simulating their reflectance as it would be observed with a Sagnac interferometer.⁶ In contrast, our project applies neural networks to the problem of recognizing atmospherically degraded signatures generated from high-fidelity satellite models.

In Section 2, we will describe the simulation process. Section 3 deals with our neural network procedure and Section 4 details our experiments. Conclusions and future work are discussed in Section 5.

2. SPECTRAL SIMULATION

Spectral simulations are computed using the TASAT and MODTRAN commercial off-the-shelf (COTS) software packages. Three additional modules, *write-taparams*, *write-tape5* and *convert*, automatically prepare the input files for TASAT and MODTRAN, and convert the outputs of these programs into a form acceptable for training the neural networks. The overall simulation process shown in figure 1 is explained in the following sections.

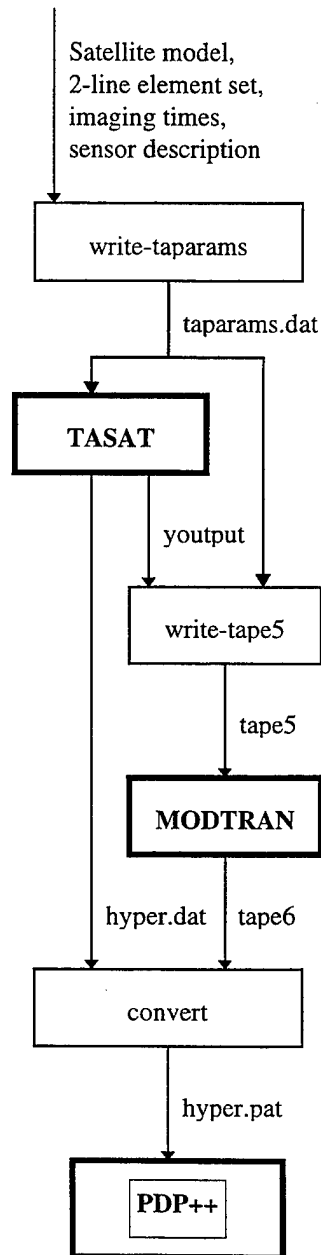


Figure 1. Simulation flow-chart

2.1 TASAT

The Time-domain Analysis Simulation for Advanced Tracking (TASAT) software was developed by Logicon/RDA under contract to the Phillips Laboratory. TASAT was developed mainly to model electro-optical imaging and laser weapon systems effectiveness⁷, but it can be used for a wide variety of simulation needs. This software provided the capability to simulate the spectral signatures we were interested in.

TASAT reads NSM satellite models, combinatorial solid-geometry (CSG) models developed by the Phillips Laboratory's Satellite Assessment Center which contain material properties and articulating part specifications in addition to basic shape information. Articulation describes the motion of certain satellite parts, such as solar panels so that they realistically move to track the sun. A separate materials database defines the wavelength dependent reflectance of each material. The quality of the simulation is limited by the quality of the information in the materials database. For some materials, reflectance values have been carefully measured and recorded in a laboratory environment over 10 nm increments, while for others, the data is only available at 100 nm intervals.

TASAT also takes as input an orbital trajectory definition in the form of a two-line element set available from US Space Command, and a series of "imaging" times. At each time step; 1) the satellite's position is propagated using the standard SGP4 propagation codes; 2) its orientation is updated based on the user-requested motion (generally nadir-pointing); 3) the position of the groundsite is computed based on the user-supplied latitude, longitude, and altitude; and 4) the sun's position is determined. A ray-tracing technique determines the spectral composition of the reflected solar light as observed at the groundsite, though the resulting signatures do not account for any atmospheric effects. Sensor parameters such as transmission of the optics and the size of the receiving aperture may also be specified to scale the resulting intensities.

The TASAT inputs are specified in the taparams.dat file. A separate defaults file referenced from the taparams.dat file contains rarely-changing program inputs and

default values for TASAT parameters in the same format as the `taparams.dat` file.

TASAT generates a `hyper.dat` file containing the specular and diffuse components of the reflected solar light as a function of wavelength at evenly-spaced 10 nm intervals from 295 nm to 1405 nm. Additionally the output file produced by TASAT (`youtput`) contains many internal values which were generated in the course of its simulation, such as the position of the sun and the position of the satellite at each imaging time. These values are necessary for conversions (see Section 2.3).

2.2 MODTRAN

The MODTRAN atmospheric simulation program is used to account for atmospheric effects on the signatures. MODTRAN uses the set of fundamental molecular constants found in the HITRAN database to accurately model molecular transitions at various temperatures and pressures.⁸

The inputs to MODTRAN include time of day, ground site location, haze model (e.g. maritime, desert, rural, etc.), meteorological model (e.g. tropical, midlatitude summer/winter, 1976 US standard), moon position and phase, and so forth. Our simulations assume no rain, clouds or volcanic particles, accept the default values of wind speed and visibility for these haze models, and ignored ground-scattered light. Our input also dictated a slant path from the ground to space, single-scattering models for both the radiance and transmittance calculations, and the use of MODTRAN's internal MIE-generated database of aerosol phase functions

MODTRAN outputs include vast amounts of chemical composition data, but the data of concern to us were the atmospheric transmittance and radiance values as a function of wave number, i.e. inverse wavelength. These output values were computed at evenly-spaced 50 cm^{-1} intervals from 7000 cm^{-1} (1429 nm) to 34000 cm^{-1} (294 nm). Transmittance is a factor from 0 to 1 specifying the fraction of light at the given wavelength which will penetrate the atmosphere. Radiance is given in units of watts per cm^2 per steradian per micron, and specifies the amount of light from the moon or the ground reradiating from the atmosphere, i.e. the basic background sky brightness at each wavelength.

2.3 PREPARATION & CONVERSION MODULES

The *write-taparams* module prepares information for TASAT. The sensor characterization information is stored in a prototype `taparams.dat` file for each sensor. Contained are the proper telescope aperture diameter, latitude, longitude, altitude, and site name, in addition to the general set of parameters necessary for multi-spectral simulation. The *write-taparams* module inserts the model file name, specific simulation times, and element set file name into the proper lines of the prototype file to form the final `taparams.dat` file used to run TASAT.

The *write-tape5* module refers to the `taparams.dat` file to obtain the sensor latitude, longitude, altitude, and simulation time needed to prepare the `tape5` input file for MODTRAN. Since MODTRAN does not propagate satellite positions or model the encounter geometry, the zenith and azimuth angles, indicating the sensor's pointing direction, are pulled from the TASAT-generated `youtput` file. The position of the moon, which MODTRAN needs to compute the

atmospheric reradiance values, is determined using the Vallado moon position propagation routine.⁹ The lunar phase angle θ is computed from the position of the moon \vec{R}_{moon} , specified in earth-centered inertial coordinates (ECI), and the ECI position of the sun \vec{R}_{sun} , determined using the Vallado sun position propagation routine, (see Figure 2) using

$$\text{the dot-product formula: } \theta = \cos^{-1} \left(\frac{\vec{R}_{moon} \cdot (\vec{R}_{moon} - \vec{R}_{sun})}{\|\vec{R}_{moon}\| \|\vec{R}_{moon} - \vec{R}_{sun}\|} \right).$$

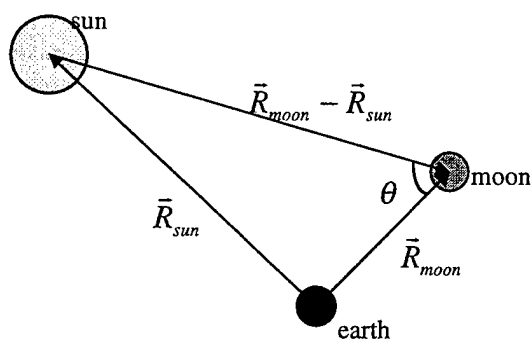


Figure 2. Lunar phase angle geometry

The *convert* module reads the MODTRAN output file, converting the radiance values from units of watts per cm^2 per steradian per micron to watts by multiplying by the sensor field of view in steradians, the area of the collector, and the spectral bandwidth of 10 nm. The exoatmospheric output signatures from TASAT are in units of watts/meter, which we convert to watts multiplying by the spectral bandwidth. The final spectral signature is computed by multiplying the exoatmospheric signatures by the transmittance and adding the radiance. Because TASAT provides data points equally spaced in wavelength and MODTRAN provides data points equally spaced in frequency, it was necessary for the *convert* module to interpolate between adjacent values in the

MODTRAN output file to obtain the atmospheric transmittance and radiance values. Each atmospherically degraded signature is normalized by dividing through its maximum intensity so that the intensity values vary between 0 and 1, before writing them to the hyper.pat file for input to the neural network software.

Images of each unclassified model along with sample exoatmospheric and endoatmospheric (and normalized) signatures are shown in Figures 3, 4 and 5.

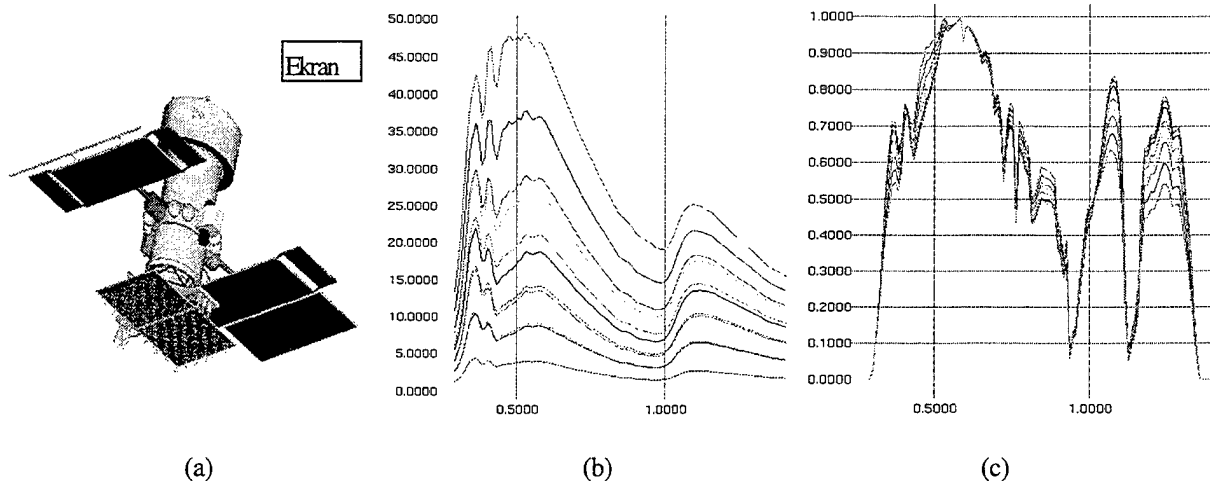


Figure 3 (a) Ekran satellite model (b) Simulated exoatmospheric signatures (in watts as a function of wavelength in microns) in a given orbit at several different imaging times (c) Signatures after accounting for the atmosphere and normalizing the intensities

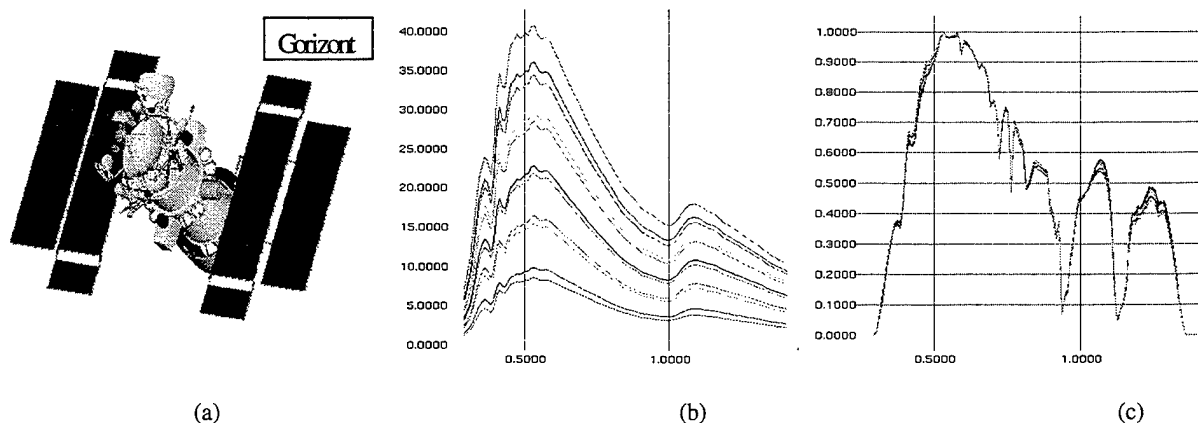


Figure 4 (a) Gorizont satellite model (b) Simulated exoatmospheric signatures (in watts as a function of wavelength in microns) in a given orbit at several different imaging times (c) Signatures after accounting for the atmosphere and normalizing the intensities

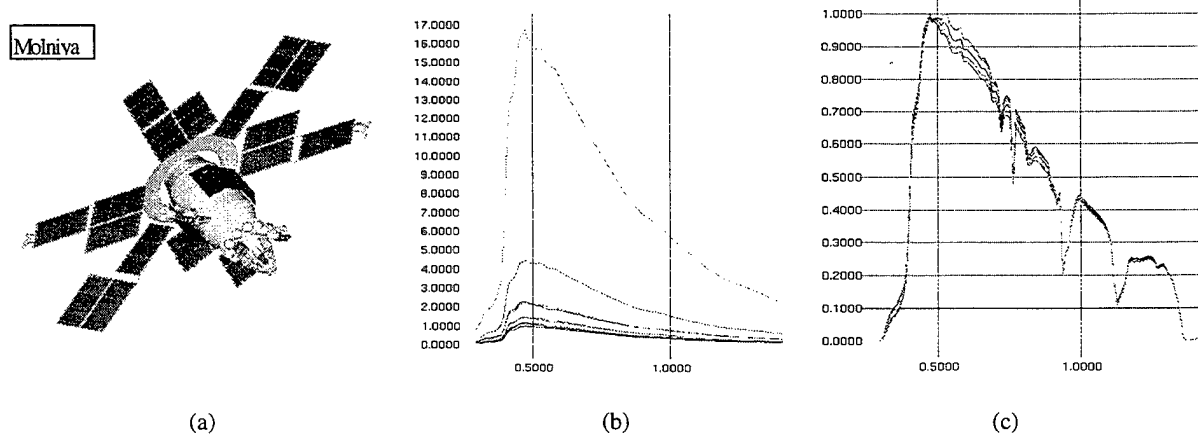


Figure 5. (a) Molniya satellite model (b) Simulated exoatmospheric signatures (in watts as a function of wavelength in microns) in a given orbit at several different imaging times (c) Signatures after accounting for the atmosphere and normalizing the intensities

3. NEURAL NETWORK RECOGNITION TECHNIQUE

3.1 NEURAL NETWORKS

Neural networks are computational devices whose basic design was inspired by neurological evidence of the computation performed by neurons in humans and other primates. They are useful computational tools which learn mappings from inputs to outputs based on training examples. Each layer of a standard feed-forward network consists of a number of nodes which are connected to each node in the subsequent layer. Each node computes a single output value by applying a simple function to its inputs, and each connection between nodes has a variable weight associated with it. During the training process, input patterns and their corresponding target output patterns are presented to the network, and the network's weights are updated via the backpropagation algorithm. The adjustment of the weights is based on the calculations of the derivative of the error in the output of the network with respect to each weight.¹⁰

3.2 PDP++

The Parallel Distributed Processing (PDP++) neural network freeware package, developed at Carnegie Mellon University, uses a backpropagation-type network like the one described above. PDP++ consists of both a C++ class library and an extensive graphical user interface which allows the user to modify the network architecture, train the network, examine specific weights, and so forth.

3.3 SPECTRAL SIGNATURE RECOGNITION ARCHITECTURE

The neural network architecture which we employed for spectral signature recognition consists of three layers. The input layer consists of 112 input nodes corresponding to the 112 wavelength bands (10 nm each from 295 nm to 1405 nm) generated by simulation. The single hidden layer consists of as few nodes as possible while still allowing for generalization. The output layer contains of a node corresponding to each satellite that the network is being trained to identify, either three or seven in our experiments.

The correct output pattern is defined by assigning the value of one to the output node corresponding to the satellite, and assigning values of zero to the other nodes. When a signature is presented to the network, the output of the network may not exactly match this pattern, so we classify the signature according to the most strongly activated output node. The degree to which the actual output pattern differs from a correct output pattern can be used as a qualitative measure of the network's confidence in its classification. The distribution of this difference for each node of the output layer can provide further information regarding the network's confidence; for example, if two nodes are highly activated and the remaining nodes are near zero, then the network is indicating that the signature may come from either of the satellites corresponding to the two highly activated nodes, but is unlikely to be from any of the other satellites.

3.4 TRAINING

Training takes place by repeatedly exposing the network to a series of events. During each event, a training signature for a given satellite is presented to the network, and the initially random weights of the connections between the nodes are adjusted in an effort to produce the correct output pattern for the satellite. The sum-of-squares error between the network's output and the correct output is measured at each time step, and training continues until the error reaches a stable and hopefully low plateau.

Various parameters can be modified to effect the training process. The learning rate (lrate) controls how fast the weights are updated along the computed error gradient. It is usually less than one, but harder problems require smaller values. The momentum parameter (mom) determines how much of the previous weight change will be retained in the present weight change computation. The momentum parameter allows learning to "pick up speed" if the weight changes all head in the same direction. This can allow the network to learn faster if the problem is a rather easy one, but may be detrimental if the problem is tough because the network may rush past an important bump in the learning curve. Typical values for momentum are .5 to .9.¹¹

A low sum-of-squares error after completing the training process indicates that the network has successfully learned to produce the correct output patterns when given an input signature from the training set. A high training error can indicate a number of things. It may indicate that the number of hidden nodes is too small, so the network lacks sufficient "memory" to learn. It may also indicate that there is not enough information in the training set to learn the differences between the satellites, possibly because certain satellites have nearly identical signatures.

3.5 GENERALIZATION TESTING

It is important to test the network's ability to generalize by measuring its performance when previously unseen signatures are introduced. If most of the unseen signatures are classified correctly, then the network has generalized from the training set. If the network performs badly when presented with the new signatures, it may indicate that the network has too many hidden nodes and has simply memorized the training set without performing any generalization. It may also indicate that the training set was too narrow, meaning that certain signatures presented during generalization testing bore little resemblance to the original signatures used for training.

4. EXPERIMENTS

Four experiments were performed, varying the number of satellites the network was trained to identify and the inclusion or exclusion of atmospheric effects, as shown in Table 2. We chose to model the three Ground-based Electro-Optical Deep Space Surveillance (GEODSS) sites because of their interest to Space Command, using the site parameters listed in Table 1.

	Aperture (m)	MODTRAN Haze Model	MODTRAN Meteorological Data
Socorro	1	desert	midlatitude
Maui	1	maritime	tropic
Diego Garcia	1	maritime	tropic

Table 1. Sensor-specific parameters

In order to train the neural network, it was necessary to generate large amounts of simulated data. Typical two-line element sets for the satellites under consideration were acquired from Space Command. These orbital trajectories were analyzed using the Satellite Orbit Analysis Program (SOAP) to determine from which ground site and at which imaging times the satellite could be viewed under proper illumination conditions. Each orbit was used to define a number of *scenarios*, (a particular orbit, ground station, and simulation time), spacing simulation times at approximately one hour intervals between the orbit's first and last valid imaging times. Signatures were then simulated by placing each satellite model in each scenario.

Half of the simulated data was used to train the neural network, while the remaining data was reserved for generalization testing. PDP++ repeatedly presented each training example to the network, updating the networks weights using the backpropagation algorithm, and displaying the resulting sum-of-squares error between the network outputs and the correct outputs. When this error reached a low and stable level, the training process was stopped. (see Figure 6)

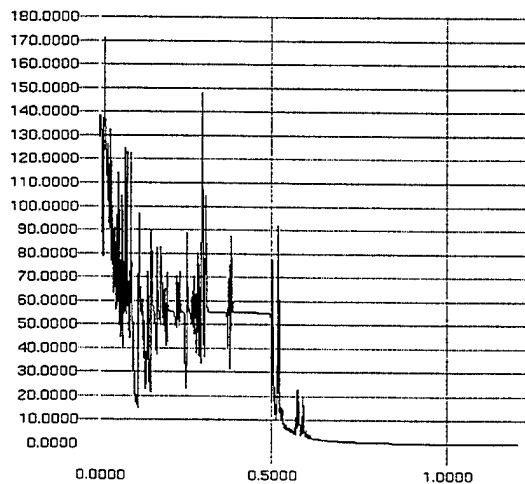


Figure 6. Network training error versus time.

Satellites	atm	hidden nodes	lrate	mom	training examples	epochs	error	testing examples	success rate
3	no	15	0.05	0.4	133	2000	0.0452	132	100%
3	yes	15	0.05	0.4	133	2000	0.0415	132	100%
7	no	20	0.01	0.4	329	10000	25.418	329	94%
7	yes	20	0.01	0.4	329	10000	21.313	377	92%

Table 2. Neural network parameters

5. CONCLUSIONS

5.1 SUMMARY

This research project has demonstrated the application of neural network techniques for the automatic identification of deep space satellites based on their multi-spectral signatures. We have developed tools for the automatic generation of large sets of simulated spectral signatures from high-fidelity satellite models and including atmospheric effects. We have demonstrated that neural networks have the ability to generalize from training examples and identify previously unseen signatures with high probability.

5.2 FUTURE WORK

Whenever a satellite's signature is observed, the viewing angle and solar illumination angles will be known but we do not provide this information to the network. Similarly, we currently normalize the intensities of the signatures but do not provide the unnormalized magnitudes of the signatures to the network. Recognition performance may be improved by adding these values as inputs to the neural network.

The simulation will be upgraded to include additional signature degradation phenomena, such as photon shot noise and any noise associated with the sensor or sensor readout. Alternate normalization techniques which are more robust with respect to noisy data will also be considered.

We are currently investigating various filter and sensor technologies in preparation for the experimental stage of our project, in which we plan to use a set of off-the-shelf filters mounted into the filter wheel of a GEODSS telescope. We are examining the weights of the network to help determine the correct filter bands to use for a multispectral experiment. We will update our simulations and neural network architecture to validate the candidate filter set.

REFERENCES

- ¹ W.I. Beavers, Optical Monitoring of Geosynchronous Satellites, MIT Lincoln Laboratories Project Report STK-233, 27 January 1995.
- ² W.I. Beavers, UBV Photometry of Geosynchronous Satellites, MIT Lincoln Laboratories Project Report STK-241, 19 October 1995.
- ³ A.E. Prochko, M. Culpepper, S. Durham, J. O'Hair, Spectral Signatures Predicted from Detailed Satellite Models, Proceedings of the 1995 Space Surveillance Workshop, MIT Lincoln Laboratories Project Report STK-235 vol. 1., 28-30 March 1995.
- ⁴ T. Payne, et al, Spectral Signatures for Deep Space SOI: A Status Report, Deep Space Spectral Sensing Working Group, 1 December 1995.
- ⁵ D. Hrovat, Hyperspectral Analysis of Space Objects: Signal to Noise Evaluation, Air Force Institute of Technology Thesis AFIT/GSO/ENP/93D-02, December 1993.
- ⁶ E.L. Caudill, Satellite Surface Material Composition from Synthetic Spectra, Air Force Institute of Technology Thesis AFIT/GEO/ENG/94-D02, December 1994.
- ⁷ Crockett, G., et al, The Time-Domain Analysis Simulation for Advanced Tracking (TASAT) Users Manual Version 6.6, Logicon R&D Associates, July 1995.
- ⁸ Anderson, G., et al, FASCONDE/MODTRAN/LOWTRAN: Past/Present/Future, "18th Annual Review Conference on Atmospheric Transmission Models", 6-8 June 1995.
- ⁹ D.Vallado, Methods of Astrodynamics: A Computer Approach - Version 4.0, 14 March 1992.
- ¹⁰ K.L. Priddy, Introduction to Neural Networks, Accurate Automation Corporation.
- ¹¹ Dawson, C., R. O'Reilly, J. McClelland, The PDP++ Software Users Manual Version 1.1, Carnegie Mellon University, 28 May 1996.

REPORT DOCUMENTATION PAGE**Form Approved
OMB No. 0704-0188**

Public reporting burden for this collection of information is estimated to average 1 hour per response, including the time for reviewing instructions, searching existing data sources, gathering and maintaining the data needed, and completing and reviewing the collection of information. Send comments regarding this burden estimate or any other aspect of this collection of information, including suggestions for reducing this burden, to Washington Headquarters Services, Directorate for Information Operations and Reports, 1215 Jefferson Davis Highway, Suite 1204, Arlington, VA 22202-4302, and to the Office of Management and Budget, Paperwork Reduction Project (0704-0188), Washington, DC 20503.

1. AGENCY USE ONLY (Leave blank)		2. REPORT DATE 27 March 1997	3. REPORT TYPE AND DATES COVERED Project Report	
4. TITLE AND SUBTITLE Proceedings of the 1997 Space Control Conference			5. FUNDING NUMBERS C — F19628-95-C-0002	
6. AUTHOR(S) L.B. Spence (Editor)				
7. PERFORMING ORGANIZATION NAME(S) AND ADDRESS(ES) Lincoln Laboratory, MIT 244 Wood Street Lexington, MA 02173-9108			8. PERFORMING ORGANIZATION REPORT NUMBER STK-249 Volume I	
9. SPONSORING/MONITORING AGENCY NAME(S) AND ADDRESS(ES) ESC Hanscom Air Force Base Bedford, MA 01730			10. SPONSORING/MONITORING AGENCY REPORT NUMBER ESC-TR-96-115	
11. SUPPLEMENTARY NOTES None				
12a. DISTRIBUTION/AVAILABILITY STATEMENT Approved for public release; distribution is unlimited.			12b. DISTRIBUTION CODE	
13. ABSTRACT (Maximum 200 words) <p>The fifteenth Annual Space Control Conference (formerly called Space Surveillance Workshop) held on 25-27 March 1997 was co-hosted by MIT Lincoln Laboratory and Phillips Laboratory and provided a forum for space control issues. This <i>Proceedings</i> documents some of the presentations, with minor changes where necessary.</p>				
14. SUBJECT TERMS			15. NUMBER OF PAGES 162	
			16. PRICE CODE	
17. SECURITY CLASSIFICATION OF REPORT Unclassified	18. SECURITY CLASSIFICATION OF THIS PAGE Unclassified	19. SECURITY CLASSIFICATION OF ABSTRACT Unclassified	20. LIMITATION OF ABSTRACT Same as report	